SYNTHESIS AND CHARACTERIZATION OF

$LiMPO_4$ (M=Mn, Ni and Fe) OLIVINE MATERIALS

BY

AZLIN SANUSI

THESIS SUBMITTED FOR THE DEGREE OF

DOCTOR OF PHILOSOPHY

DEPARTMENT OF CHEMISTRY
FACULTY OF SCIENCE
UNIVERSITY OF MALAYA
KUALA LUMPUR
MALAYSIA

2010

List of Articles Published In Journals And Presented At Conferences.

Sanusi, A., Basirun, W.J., Kufian, M.Z. and Arof, A.K., 'Redox behaviour of crystalline $LiFePO_4$ prepared by chemical precipitationand low temperature sterilization', Materials Research Innovations 13 (2009) 207-209.

Sanusi, A., Navaratnam, S., Basirun, W.J.and Arof, A.K., ' Synthesis and studies of nanocrystalline $LiMnPO_4$ prepared by sol-gel method with tartaric acid', International Conference Of Advancement of Materials and Nanotechnology 2007 (ICAMN 2007) 29 May-1 Jun 07 at Pulau Langkawi, Kedah. Malaysia.

Sanusi, A., Navaratnam, S., Kufian, M.Z., Basirun, W.J.and Arof, A.K., 'Synthesis and redox behaviour studies of Olivine $LiFePO_4$ cathode material', 2^{nd} International Conference of Functional Materials and devices 2008.16-19 June 2008 at Kuala Lumpur, Malaysia.

Sanusi, A. and Navaratnam, S.,'Nanopowder phospho-olivines cathode material for lithium batteries', 6^{th} Invention, Innovation, Design (IID 2009),From Research And Innovation To Wealth 13 – 15 Jan 2009 at Universiti Teknologi MARA, Shah Alam, Malaysia. Won Silver Medal.

Acknowledgements

Syukur alhamdulillah to Allah the most gracious and the most merciful for giving me the patience and strength to complete this thesis. I would like to take this opportunity to express my gratitude to those who has helped me directly or indirectly in making this thesis a success.

First and foremost I would like to thank my supervisor, Assoc. Professor Dr. Wan Jeffry Basirun for his support and assistance throughout the course of this research. I also wish to extend my deepest gratitude and appreciation to my co-supervisor, Professor Dr. Abdul Kariem Arof for without his patience, encouragement and guidance this thesis would not have been completed

A special thank goes to Prof. Dr Rosnah Mat Taha from the Institute of Biological Sciences and not forgetting Asmah, Norazlina, Amiruddin and Norlina who has helped me in one way or another. A note of gratitude also goes to Encik Ismail Che Lah, Encik Mohd Arof and Encik Shahril of the Physics department, Cik Nisrin and Encik Zul of the Chemistry department and Encik Mohd Said of the Mechanical Engineering Department and Encik Asin for their help and assistance in the course of my laboratory work. I also would like to take this opportunity to thank my friends and laboratory mates namely Din, Fakhrul, Hamdi, Leena, Winnie, Siti, Shanti, Ramesh, Sethu, Kumutha, Sharlina, Zuraini, Fadhullah, Mohammad and Hun Lee for all their help, ideas and suggestions that had motivate me during my study.

To Universiti Teknologi MARA thank you for the support given that enable me to undertake this work and to University Malaya thank you for giving me the opportunity to undertake this course.

Last but not least my heart felt thanks to my husband, children and my mother for their love, constant encouragement and moral support for making this thesis a success.

Abstract

Lithium transition metal phosphate, $LiMPO_4$ compounds with olivine structure namely $LiMnPO_4$, $LiNiPO_4$ and $LiFePO_4$ were successfully synthesized in the present work. $LiMnPO_4$ and $LiNiPO_4$ were synthesized by the sol-gel method with tartaric acid as the chelating agent. $LiFePO_4$ was synthesized via the chemical precipitation and low temperature sterilizer heating method. TGA was carried out on $LiMnPO_4$ and $LiNiPO_4$ samples to determine the firing temperature of the gel precursor and the thermal stability of the prepared samples. $LiMnPO_4$ was heated for 15 hours at various temperatures and $LiNiPO_4$ was formed at 1000 ^oC with firing time of 24 hours. Firing of samples in this work was carried out in air. The absence of inert gas and reducing agents made the synthesis simple and low cost which is one of the objectives of this work. Reactions mechanisms for both $LiMnPO_4$ and $LiNiPO_4$ were deduced from the TGA curves. The weight loss predicted by these reaction mechanisms agree with that obtained experimentally for the two samples. XRD reveals that both $LiMnPO_4$ and $LiNiPO_4$ samples are pure while $LiFePO_4$ was formed with minor impurities. Crystallite size of samples were calculated from Scherrer equation and both methods have proven to produce nano-size crystallites. The crystallite size was found to be in the range of 31 nm to 46 nm for $LiMnPO_4$ produced at sintering temperatures from 350 ^oC to 1000 ^oC for 15 hours, 66 nm for $LiNiPO_4$ fired at 1000 ^oC for 24 hours and 58 nm for $LiFePO_4$ produced at 121 ^oC for 5 hours. Thus, tartaric acid as chelating agent is successful in inhibiting the growth of the particle as expected since nanosized samples are obtained. Samples were also characterized by FTIR. All spectra show the presence of peaks at 1135-1138 cm^{-1},1088-1096 cm^{-1},1051-1071 cm^{-1} and 984-1040 cm^{-1} and in addition asymmetric PO bending bands in the region 550-700 cm^{-1} were also observed. These observations indicate the presence of PO_4^{3-} ions in all samples

prepared. EDX analysis confirmed the percentage composition of the samples and that Mn^{2+}, Ni^{2+} and Fe^{2+} oxidation state remain unchanged although fired in air. Cyclic voltammetry measurements gave redox peaks for all samples prepared in this work indicating lithiation and delithiation of Li^{+} ion has taken place. Oxidation peak at ~ 4.4 V and reduction peak at ~ 4.0 V was observed for $LiMnPO_4$ and as for $LiNiPO_4$ anodic and cathodic peaks are observed at ~ 4.9V and ~ 4.8V respectively. Oxidation peak at ~3.8 V and reduction peak at ~3.2 V are observed in the cyclic voltammogram of $LiFePO_4$. Diffusion coefficient calculated using CV and Randles-Sevcik equation are 3.50×10^{-11} cm^2s^{-1} for $LiNiPO_4$ and 3.09×10^{-13} cm^2 s^{-1} for $LiFePO_4$. The diffusion coefficient for $LiMnPO_4$ are 9.37×10^{-13} cm^2 s^{-1}, $8.57 \times 10^{-13} cm^2$ s^{-1} and 2.97×10^{-14} cm^2 s^{-1} for sample A3, A4 and A5 respectively indicating that smaller particles at lower heating temperature has shortened the path length and enhances intercalation.

Abstrak

Litium fosfat logam peralihan, $LiMPO_4$, dengan struktur olivine, iaitu $LiMnPO_4$, $LiNiPO_4$ and $LiFePO_4$ telah disintesis dengan jayanya di dalam kajian ini. LiMnPO4 and LiNiPO4 telah dihasilkan dengan menggunakan kaedah sol-gel dan asid tartarik sebagai agen pengelatan. Manakala $LiFePO_4$ pula disintesis melalui proses pemendapan kimia dan pembakaran suhu rendah dengan menggunakan alat pensterilan.. Analisis TGA telah dilakukan keatas bahan sampel, $LiMnPO_4$ dan $LiNiPO_4$ untuk menentukan suhu pembakaran bagi sintesis bahan dan kestabilan bahan sample. $LiMnPO_4$ telah dipanaskan selama selama 15 jam pada suhu-suhu yang berlainan dan $LiNiPO_4$ pula diperolehi dengan membakar pada suhu 1000 ^oC selama 24 jam. Bahan sampel dalam kajian ini telah dipanaskan dalam keadaan udara tanpa gas nadir dan agen penurunan. Ini menjadikan kaedah sintesis ini mudah dan jimat yang mana ini adalah salah satu dari objektif kajian ini. Unjuran Persamaan bagi penguraian prapenanda $LiMnPO_4$ dan $LiNiPO_4$ telah diperolehi dengan menggunakan lekok TGA. Pengiraan peratus penurunan berat badan menggunakan persamaan unjuran dan lekok TGA adalah sama. Spektrum belauan sinar-X (XRD) menunjukkan kedua-dua bahan sampel $LiMnPO_4$ dan $LiNiPO_4$ adakah tulin manakala $LiFePO_4$ mengandungi sedikit bahan bendasing. Saiz kristalit bahan sampel telah dikira dengan menggunakan Persamaan Scherrer dan kedua – dua kaedah telah menghasilkan bahan kristalit bersaiz nano. Saiz kristalit dalam julat 31 nm hingga 46 nm telah dihasilkan bagi sampel $LiMnPO_4$ yang dipanaskan pada suhu 550 ^oC hingga 750 ^oC selama 15 jam. Bahan sampel $LiNiPO_4$ yang dipanaskan pada suhu 1000 ^oC hingga selama 24 jam telah menghasilkan bahan kristalit berukuran 66 nm manakala $LiFePO_4$ yang mempunyai saiz kristalit berukuran 58 nm telah dihasilkan dengan membakar bahan selama 121 ^oC selama 5 jam. Maka, ini menunjukkan asid tartarik telah berjaya dalam

membantutkan pembesaran kristal seperti yang dijangkakan kerana kristalit bersaiz nano telah terhasil. Pencirian bahan menggunakan Spektroskopi inframerah (FTIR) juga dilakukan. Kesemua spektra menunjukkan jalur pada 1135-1138 cm^{-1},1088-1096 cm^{-1},1051-1071 cm^{-1} dan 984-1040 cm^{-1}.Getaran pembengkokan tak asimetri P-O pada 550-700 cm^{-1} juga diperhatikan. Pemerhatian ini menunjukkan kewujudan ion PO_4^{3-} pada sampel yang disintesis. Analisis EDX telah memastikan peratus komposisi sampel dan nombor pengoksidaan Mn^{2+}, Ni^{2+} and Fe^{2+} adalah tidak berubah walaupun bahan sampel telah dipanaskan dalam udara. Kitaran voltametri menunjukkan kelok redoks bagi semua bahan yang disintesis dan ini menunjukkan litium ion telah diinterkalasi. Bagi bahan $LiMnPO_4$ kelok oksida berlaku pada 4.4 V dan kelok reduksi pada 4.0 V. Kelok oksida $LiNiPO_4$ pula berlaku pada ~ 4.9 V dan kelok reduksi pada ~ 4.8 V . Kelok oksida pada ~3.8 V dan kelok reduksi pada ~3.2 V telah diperhatikan pada kitaran voltametri bahan $LiFePO_4$. Pekali resapan bagi $LiNiPO_4$ ialah 3.50 x 10^{-11} cm^2 s^{-1} dan 3.09 x 10^{-13} cm^2 s^{-1} bagi $LiFePO_4$ mengikut pengiraan menggunakan kitaran voltametri dan persamaan Randles-Sevcik. Pekali resapan bagi $LiMnPO_4$ adalah 9.37 x 10^{-13} cm^2 s^{-1} (A3), 8.57 x 10^{-13} (A4) dan 2.97 x 10^{-14} cm^2 s^{-1} bagi sampel A3, A4 dan A5 mengikut urutan. Ini menunjukkan suhu panas yang rendah menghasilkan bahan yang lebih kecil dan ini telah memendekkan panjang jalar dan mengukuhkan interkalasi.

LIST OF CONTENTS

CONTENTS		Page
Publications		i
Acknowledgements		ii
Abstract		iv
Abstrak		vi
List of content		viii
List of figures		xii
List of tables		xvii
CHAPTER 1: INTRODUCTION TO PRESENT WORK		
1.1:	Background	1
1.2:	Why $LiMnPO_4$ (M=Mn, Ni, Fe) as cathode material?	2
1.3:	Research objectives	4
1.4:	Scope of the thesis	5
CHAPTER 2:LITERATURE REVIEW		
2.1:	Introduction	9
2.2:	Lithium transition metal phosphate with olivine structures	10
2.3:	Lithium iron phosphate, $LiFePO_4$	15
2.4:	Lithium manganese phosphate,$LiMnPO_4$	17
2.5:	Lithium nickel phosphate, $LiNiPO_4$	19
2.6:	Lithium cobalt phosphate, $LiCoPO_4$	19

2.7: Diffusion coefficient Investigations Techniques 21

2.8: Preparation method of $LiMPO_4$ cathode materials 24

2.9: Solid state reaction 24

2.10: Hydrothermal Synthesis 25

2.11: Sol-gel method 26

2.12: Water quenching treatment 27

2.13: Summary 28

CHAPTER 3: EXPERIMENTAL METHODS

3.1: Introduction 30

3.2: Samples Preparation 30

3.3: Characterization 36

3.3.1: Thermal Analysis 36

3.3.2: X-ray Diffraction (XRD) 37

3.3.3: Energy Dispersive X-rays Analysis (EDX) 39

3.3.4: Fourier Transform Infrared Spectroscopy (FTIR) 40

3.4: Preparation of cathode electrode 42

3.5: Fabrication of test cell 43

3.6: Cyclic Voltammetry 43

3.7: Summary 46

CHAPTER 4: RESULTS FOR $LiMnPO_4$

4.1: Introduction 48

4.2: Thermogravimetric Analysis (TGA) 48

4.3: X-Ray Diffraction (XRD) 55

4.3.1:	Crystallite Size	61
4.4:	Fourier Transform Infrared Spectroscopy (FTIR)	63
4.5:	Energy Dispersive X-rays Analysis (EDX)	70
4.6:	Cyclic Voltammetry	74
4.6.1:	Redox Behaviour	74
4.6.2:	Formal Electrode Potential	80
4.6.3:	Relationship between i_p and $\upsilon^{1/2}$	81
4.6.4:	Diffusion coefficient, D_{Li}^{+}	85
4.6.5:	Cell capacity	86
4.7:	Summary	87

CHAPTER 5: RESULTS FOR $LiNiPO_4$

5.1:	Introduction	90
5.2:	Thermogravimetric Analysis (TGA)	90
5.3:	X-Ray Diffraction (XRD)	95
5.3.1:	Crystallite Size	79
5.4:	Fourier Transform Infrared Spectroscopy (FTIR)	99
5.5:	Energy Dispersive X-rays Analysis (EDX)	106
5.6:	Cyclic Voltammetry	108
5.6.1:	Redox Behaviour	108
5.6.2:	Formal Electrode Potential	113
5.6.3:	Relationship between i_p and $\upsilon^{1/2}$	113
5.6.4:	Diffusion coefficient, D_{Li}^{+}	116
5.6.5:	Cell capacity	117
5.7:	Summary	118

CHAPTER 6: RESULTS FOR $LiFePO_4$

6.1: Introduction 120

6.2: X-Ray Diffraction (XRD) 121

6.2.1: Crystallite Size 123

6.3: Fourier Transform Infrared Spectroscopy (FTIR) 124

6.4: Energy Dispersive X-rays Analysis (EDX) 127

6.5: Cyclic Voltammetry 129

6.5.1: Redox Behaviour 129

6.5.2: Formal Electrode Potential 133

6.5.3: Relationship between i_p and $\upsilon^{1/2}$ 134

6.5.4: Diffusion coefficient, D_{Li}^{+} 135

6.5.5: Cell capacity 136

6.6: Summary 137

CHAPTER 7: DISCUSSION 138

CHAPTER 8: CONCLUSIONS AND SUGGESTIONS 153

REFERENCES 158

LIST OF FIGURES

Figures	Caption	Page
Figure 2.1:	Representation of the structures of $LiMPO_4$ phospho-olivine lattice, in which $LiMPO_4$ olivine-like framework in which the P atoms occupy tetrahedral sites, the Li and Fe atoms occupy octahedral sites	11
Figure2.2:	FTIR absorption spectra of lithium metal phosphates with diphosphate ($LiFeP_2O_7$), olivine-like ($LiFePO_4$, $LiCoPO_4$, $LiMnPO_4$) and Nasicon-like $Li_3Fe(PO_4)_3$ framework .	14
Figure 2.3:	Charge-discharge of LiFePO4 olivine compounds (Salah et al., 2005;Julien, 2004).	16
Figure 2.4:	The typical cyclic voltammogram of $LiFePO_4$ at 0.2 mV/s scan rate in 2.2 to 4.5	16
Figure 2.5:	Cyclic-voltammograms for $LiMnPO_4$ film electrodes in 1 mol dm^{-3} $LiPF_6$ / (EC + DEC) at different scan rates.	18
Figure 2.6:	Charge-discharge of $LiCoPO_4$ olivine compounds.	20
Figure 3.1:	The flow chart for the synthesis of $LiMnPO_4$ and $LiNiPO_4$ via the sol-gel method.	31
Figure 3.2:	Photographs showing the solutions formed during the preparation of (a)$LiMnPO_4$ and (b) $LiNiPO_4$.	33
Figure 3.3:	A photograph of the grayish blue mixture of $LiFePO_4$.	34
Figure 3.4:	Schematic diagram for the synthesis process of $LiFePO_4$.	35
Figure 3.5:	TG curve of the precursor of $LiNi_{0.5}Mn_{1.5}O_4$ measured in air.	37
Figure 3.6.:	XRD pattern of $LiNiVO_4$.	38
Figure 3.7:	Diagram showing Bragg condition.	39
Figure 3.8:	IR spectrum of the as-prepared $LiNi_{0.5}Mn_{1.5}O_4$.	40
Figure 3.9:	FTIR spectrum of $LiNiVO_4$ powder	41
Figure 3.10:	A schematic representation of the test cell.	43

Figure 3.11:	Basic shape of a cyclic voltammogram.	44
Figure 3.12 :	Autolab PG STAT 30 instrument.	46
Figure 4.1:	TGA thermogram of lithium hydroxide.	49
Figure 4.2:	TGA thermogram of ammonium dihydrogen phosphate.	50
Figure 4.3:	TGA thermogram of manganese acetate.	51
Figure 4.4:	TGA thermogram of tartaric acid.	52
Figure 4.5:	TGA and DTGA thermograms of lithium manganese phosphate precursor.	52
Figure 4.6:	XRD diffractogram of A0 sample	57
Figure 4.7:	XRD diffractogram of A1 sample	57
Figure 4.8:	XRD diffractogram of A2 sample	57
Figure 4.9:	XRD diffractogram of A3 sample	58
Figure 4.10:	XRD diffractogram of A4 sample	58
Figure 4.11:	XRD diffractogram of A5 sample	58
Figure 4.12:	XRD diffractogram of A6 sample	59
Figure 4.13:	XRD diffractogram of A7 sample	59
Figure 4.14:	XRD diffractogram of Manganese acetate	59
Figure 4.15:	Variation of crystallite size, L and firing temperatures at $2\theta = 35.2^{o}$.	62
Figure 4.16:	FTIR spectrum of lithium manganese phosphate precursor	64
Figure 4.17:	FTIR spectra of (a) sample A1 (b) sample A2 (c) sample A3 (d) sample A4 in the wavenumber 400 to 750 cm^{-1}.	65
Figure 4.18:	FTIR spectra of (a) sample A5 (b) sample A6 (c) sample A7 in the wavenumber 400 to 750 cm^{-1}.	66
Figure 4.19:	FTIR spectra of (a) sample A1 (b) sample A2 (c) sample A3 (d) sample A4 in the wavenumber 800 to 1300 cm^{-1}.	67
Figure 4.20:	FTIR spectra of (a) sample A5 (b) sample A6 (c) sample A7 in the wavenumber 800 to 1300 cm^{-1}.	68
Figure 4.21:	EDX spectrum of sample A3	71

Figure 4.22:	E72DX spectrum of sample A4	72
Figure 4.23:	EDX spectrum of sample A5	72
Figure 4.24:	Cyclic voltammogram of A3 material at scan rate 0.1mVs^{-1}.	75
Figure 4.25:	Cyclic voltammogram of A3 material at scan rate 1mVs^{-1}.	76
Figure 4.26:	Cyclic voltammogram of A3 material at scan rate 10mVs^{-1} .	76
Figure 4.27:	Cyclic voltammogram of A4 material at scan rate 0.1mVs^{-1}.	77
Figure 4.28:	Cyclic voltammogram of A4 material at scan rate 1mVs^{-1}.	78
Figure 4.29:	Cyclic voltammogram of A4 material at scan rate10 mVs^{-1}	78
Figure 4.30:	Cyclic voltammogram of A5 material at scan rate1.0mVs^{-1}.	79
Figure 4.31:	Cyclic voltammogram of A5 material at scan rate10 mVs^{-1}.	79
Figure 4.32:	Cyclic voltammogram of A3 material at different scan rates.	82
Figure 4.33:	Cyclic voltammogram of A4 material at different scan rates.	82
Figure 4.34:	Cyclic voltammogram of A5 material at different scan rates.	83
Figure 4.35:	Relationship between the peak currents and $\upsilon^{1/2}$ for a positive scan of sample A3.	83
Figure 4.36:	Relationship between the peak currents and $\upsilon^{1/2}$ for a positive scan of sample A4.	84
Figure 4.37:	Relationship between the peak currents and $\upsilon^{1/2}$ for a positive scan of sample A5	84
Figure 5.1 :	TGA curves of nickel acetate	90
Figure 5.2 :	TGA and DTGA curves of $LiNiPO_4$ precursor.	90
Figure 5.3 :	XRD diffractogram of B1 sample	95
Figure 5.4 :	XRD diffractogram of B2 sample	96
Figure 5.5 :	XRD diffractogram of B3 sample.	96
Figure 5.6 :	XRD diffractogram of B4 sample	97
Figure 5.7 :	FTIR spectrum of lithium nickel phosphate precursor	101
Figure 5.8 :	FTIR spectrum of sample B1 in the wavenumber 400-	102

	750cm^{-1}	
Figure 5.9 :	FTIR spectrum of sample B2 in the wavenumber 400-750cm^{-1}.	102
Figure 5.10:	FTIR spectrum of sample B3 in the wavenumber 400-750cm^{-1}.	103
Figure 5.11:	FTIR spectrum of sample B3 in the wavenumber 400-750cm^{-1}.	103
Figure 5.12:	FTIR spectrum of sample B1 in the wavenumber 800-1300cm^{-1}.	104
Figure 5.13:	FTIR spectrum of sample B2 in the wavenumber 800-1300cm^{-1}.	104
Figure 5.14:	FTIR spectrum of sample B3 in the wavenumber 800-1300cm^{-1}.	105
Figure 5.15:	FTIR spectrum of sample B4 in the wavenumber 800-1300cm^{-1}.	105
Figure 5.16:	EDX spectrum of sample B4.	107
Figure 5.17:	Cyclic voltammogram of LiNiPO4 at 0.1 mVs-1. scan rate.	109
Figure 5.18:	Enlarge (a) anodic and (b) cathodic peaks for scan rate 0.1 mVs^{-1}.	110
Figure 5.19:	Cyclic voltammogram of B4 material at 1 mVs^{-1} scan.	111
Figure 5.20:	Enlarge (a) anodic and (b) cathodic peaks for scan rate 1.0 mVs^{-1}.	111
Figure 5.21:	Cyclic voltammogram of B4 material at 10 mVs^{-1} scan rate.	112
Figure 5.22:	Enlarge (a) anodic and (b) cathodic peaks for scan rate 10 mVs^{-1}.	112
Figure 5.23:	Cyclic voltammograms of $LiNiPO_4$ at 40 mVs^{-1}scan rate.	114
Figure 5.24:	Cyclic voltammograms of LiNiPO4 at 20 mVs^{-1}scan rate.	115
Figure 5.25:	Cyclic voltammograms of $LiNiPO_4$ at 10 mVs^{-1}scan rate.	115
Figure 5.26:	Cyclic voltammograms of $LiNiPO_4$ at 5 mVs^{-1}scan rate.	116
Figure 5.27:	Relationship between the peak currents (i_p) and $\upsilon^{1/2}$ for a positive scan of sample $LiNiPO_4$.	116

Figure 6.1 :	X-ray diffractogram of $LiFePO_4$.	123
Figure 6.2 :	Infrared spectrum of $LiFePO_4$ in the wavenumber 750 cm^{-1} to 1400 cm^{-1} .	125
Figure 6.3 :	Infrared spectrum of $LiFePO_4$ in the wavenumber 400 cm^{-1} to 750 cm^{-1} .	126
Figure 6.4 :	EDAX spectra of $LiFePO_4$.	128
Figure 6.5 :	Cyclic voltammogram of $LiFePO_4$ at scan rate 0.1 mVs^{-1}.	130
Figure 6.6 :	Cyclic voltammogram of $LiFePO_4$ at scan rate 0.25 mVs^{-1}.	131
Figure 6.7 :	Cyclic voltammogram of $LiFePO_4$ at scan rate 0.5 mVs^{-1}.	131
Figure 6.8 :	Cyclic voltammogram of $LiFePO_4$ at scan rate 5 mVs^{-1} , 10mVs^{-1} , 20 mVs^{-1}, 30 mVs^{-1}, 40 mVs^{-1} and 50 mVs^{-1}	132
Figure 6.9 :	Relationship between the peak current and $\upsilon^{1/2}$ at various scan rates.	135
Figure 7.1 :	Structure of tartaric acid.	146

LIST Of TABLES

Table	Caption	Page
Table1.1:	Electronic structure of Manganese atom, nickel atom, manganese ions and nickel ions.	5
Table 3.1:	Amounts of raw materials used.	32
Table 4.1:	Calculation for percentage weight loss for equation 4.11.	55
Table 4.2:	The symbols designated to the samples fired at different temperatures.	55
Table 4.3:	XRD peaks for samples A3,A4,A5,A6,and A7 compared to the JCPDS values	61
Table 4.4:	Wavenumbers and peaks assignment of FTIR bands of $LiMnPO_4$ samples fired at 350^oC (A1),450^oC (A2), 550^oC A3), 650^oC (A4),750^oC (A5), 850^oC (A6) and 1000^oC (A7)	70
Table 4.5:	Starting composition, Atomic % of elements and mole ratio between elements in lithium manganese phosphate.	73
Table 4.6:	ΔE values for sample A3, A4 and A5 at 1.0 mVs^{-1} scan rate.	80
Table 4.7:	List of calculated formal potential for A3, A4 and A5 samples at scan rate 0.1 mVs^{-1}	81
Table 4.8:	List of data used for the calculation of the diffusion coefficient and the calculated diffusion coefficient values for samples A3, A4 and A5	86
Table 4.9:	The charge density, capacity and specific capacity for the samples A3, A4 and A5.	87
Table 5.1:	TG/DTGA results of the $LiNiPO_4$ precursor.	92
Table 5.2:	Calculation for percentage weight loss for equation 5.7.	94
Table 5.3:	The symbols designated to the samples fired at different temperatures with their impurities peaks	95
Table 5.4:	Comparison between the diffraction angles (2Θ) values of the prepared sample with the $LiNiPO_4$ JCPDS (pattern no 32-0578).	98

Table 5.5:	Crystallite size, L of samples B2, B3 and B4.	99
Table 5.6:	.List of vibration bands of the phosphate polyanions.	100
Table 5.7:	Starting composition, atomic % and mole ratio between elements in Lithium Nickel Phosphate	106
Table 5.8:	ΔE values for sample B4 at 0.1, 1.0 and 10 mVs^{-1} scan rates.	113
Table 5.9:	List of calculated formal potential for $LiNiPO_4$ at scan rate 1.0 mVs^{-1}.	113
Table 5.10:	List of data used for the calculation of the diffusion coefficient and the calculated diffusion coefficient value for $LiNiPO_4$.	117
Table 5.11:	The charge density, capacity and specific capacity for $LiNiPO_4$.	118
Table 6.1:	XRD peaks for lithium iron phosphate as compared to the JCPDS (No .40-1499)	122
Table 6.2:	Wavenumbers and assignments of the FTIR bands of $LiFePO_4$	126
Table 6.3:	Atomic % of elements and mole ratio between elements in lithium iron phosphate.	127
Table 6.4:	Peak potential difference (E_{pa} - E_{pc}) at various scan rates for sample $LiFePO_4$.	133
Table 6.5:	List of data used for the calculation of the diffusion coefficient and the calculated diffusion coefficient values for samples F.	136
Table 6.6:	Comparison of diffusion coefficient of $LiFePO_4$ in different electrolytes	136
Table 6.7:	The charge density, capacity and specific capacity for $LiFePO_4$.	136
Table 7.1:	Peaks ratio for $LiMnPO_4$	143
Table 7.2:	Comparison of crystallite size of $LiMnPO_4$ calculated by Scherrer Equation	145
Table 7.3:	Calculated E_f values for $LiMnPO_4$ and $LiFePO_4$ and experimental E_f values for $LiMnPO_4$, $LiFePO_4$ and $LiNiPO_4$.	151

CHAPTER 1

INTRODUCTION TO THE PRESENT WORK

1.1 Background

Lithium ion batteries have been widely used as mobile power sources in portable electronic devices such as cameras, cellular telephones and laptop computers. These batteries are attractive power sources due to their high energy density, high voltage and no memory effect.

The increase in market demands for portable electronic devices, transportation and energy storage has also increased interest in lithium ion batteries. Lithium ion batteries are being developed for use in electric vehicles where a high power surge is required for ignition and to power other electrical parts. For such needs high performance electrode materials with low cost and increased safety must be developed.

Intensive research is being conducted to further improve the performance of lithium ion batteries and reduce the cost of electrode materials. Among the cathode materials for Li ion battery are $LiCoO_2$ (Kim et al., 2005; Fey et al., 2005; Zhang et al., 2004; Peng et al., 1998) layered $LiNiO_2$ (Kim et al., 2007; Dompablo et al., 2003) and $LiMn_2O_4$ (Bao et al., 2005; Eriksson and Doeff., 2003; Lee et al., 1998). Investigations into new materials for the positive electrode is one of the basic lines of research.

Lithium transition metal oxides (LTMO) have found application as cathode electrode materials for high power applications. The use of $LiMn_2O_4$ solves problems related to cost and Co and Ni toxicity but the disproportionation of Mn^{3+} in the electrolyte that leads to rapid capacity fading remains a severe problem (Fu et al., 2006; Liang et al., 2006). Much effort have been made to identify new materials suitable for use as positive electrodes in rechargeable lithium batteries to replace $LiCoO_2$ as its component is toxic, requires very careful handling and disposal. $LiCoO_2$ is also expensive and this makes it unsuitable for a large volume product (Piana et al., 2004). Lithium transition metal phosphate ($LiMPO_4$) has been identified as the most promising cathode to replace LTMO. Unlike LTMO, $LiMPO_4$ does not liberate oxygen on decomposition which makes it safer to use.

1.2 Why $LiMPO_4$ (M= Mn, Ni, Fe) as cathode material?

Lithium transition metal phosphates are now known to be potential cathode materials for lithium ion batteries. This is due to their low toxicity, low cost and good chemical and thermal stability (Drezen et al., 2007). $LiMPO_4$ is more stable than layered oxides because the oxygen ions in the olivine can form strong covalent bonds with P^{5+} and PO_4^{3-} tetrahedral polyanions to form a stable three dimensional structure (Padhi et al., 1997). LTMOs such as $LiCoO_2$, $LiNiO_2$ and $LiMn_2O_4$ suffer from significant capacity fade during cycling (Drezen et al., 2007). This is attributed to the structural rearrangements caused during lithium intercalation and deintercalation. $LiCoO_2$ for example has a theoretical capacity of 273 mA h g^{-1} but only 137 mA h g^{-1} is possible since complete delithiation would lead to structural degradation (Gopukumar et al., 2003). $LiNiO_2$ on the other hand undergoes multiphase reactions during cycling that leads to structural degradation (Dompablo et al., 2003). Due to the Jahn-Teller effect,

the 3D spinel structure of $LiMn_2O_4$ undergoes change in phase from cubic to tetragonal during cycling that causes capacity fading and poor cycling behaviour at elevated temperatures (Liu and Shen, 2003).

Another advantage of $LiMPO_4$ is the high redox potential versus Li^+ that it offers. This shows that lithium batteries with $LiMPO_4$ cathodes can provide larger voltage. However $LiMPO_4$ suffers from low electronic conductivity and therefore discharge rate capability is poor. Electronic conductivity could be increased by structure modifications, doping or coating (Prosini et al., 2001; Wang et al., 2004; Roberts et al., 2008). Discharge rate capability improvement is attributed to the the partial occupancy of the dopant metal ions in lithium lattice sites, which reduces the resistance and thus improve the electrochemical properties. Coating with a conductive medium such as carbon increases the electronic conductivity. Particle size reduction is also essential to enhance the Li^+ diffusion (Kwon et al., 2006; Choi and Prashant, 2007; Salah et al., 2006; Xia et al., 2006). Smaller particles reduce the diffusion path length for electrons and lithium ions in the cathode material, thereby overcoming the low intrinsic electronic conductivity and slow lithium diffusion kinetics within the material (Wang et al., 2009). Thus the transport process of Li^+ in $LiMPO_4$ is the key step for energy storage and output. The diffusion properties of $LiMPO_4$ therefore play an important role in improving its rate capability (Tang et al., 2009).

As mentioned above many groups of researchers have focussed on improving the electrochemical properties of $LiMPO_4$ cathode material by doping, coating or reduction of particle size. However to the author's knowledge there are few reports about the chemical diffusion of lithium ion in $LiMnPO_4$, $LiNiPO_4$ and $LiFePO_4$ although lithium

diffusion in the electrode is a key factor that determines the rate at which a battery can be charged or discharged.

Numerous synthetic routes have so far been adopted (Xu et al., 2007; Choi and Prashant, 2007; Liu et al., 2006; Hsu et al 2004; Piana et al., 2004; Lee and Teja 2006; Chen and Whittingham, 2006; Tajimi et al., 2004; Arnold et al., 2003) for the preparation of $LiMPO_4$. Many of the sol-gel method reported used citric acid as chelating agent and argon or nitrogen ambient during calcinations of precursor powders. Argon and nitrogen gases were probably used to prevent the oxidation of Mn^{+2} to Mn^{+3} and Ni^{+2} to Ni^{+3}. However these gases are environmentally unfriendly.

1.3 Research Objectives

Based on the problems mentioned in the previous section, it is the task of this thesis to undertake the following objectives.

a. To produce nano-sized $LiMnPO_4$ and $LiNiPO_4$ cathode active materials via the sol- gel method in an environmental friendly and low cost conditions.
b. To produce nano-sized $LiFePO_4$ via the chemical precipitation and low temperature sterilization heating method in the absence of inert gas.
c. To characterize the samples and confirm their identification.
d. To study the redox properties of the cathode materials and thus determine the diffusion coefficient of Li^+ ion in $LiMnPO_4$, $LiNiPO_4$ and $LiFePO_4$ by cyclic voltammetry (CV).

1.4 Scope of the thesis

$LiMnPO_4$, $LiNiPO_4$ and $LiFePO_4$ are not novel materials. $LiMnPO_4$ and $LiNiPO_4$ cathode materials will be prepared by the sol-gel method using lithium hydroxide monohydrate, manganese acetate tetrahydrate, nickel acetate tetrahydrate and ammonium dihydrogen phosphate as raw materials. Lithium hydroxide is used as one of the starting reagents since it is cheap and chemically stable. Besides that it does not produce any harmful gases on heating. Tartaric acid, $C_4H_6O_6$ is used as the chelating agent. Tartaric acid is a plant acid found particularly in grapes, bananas and tamarinds. It is therefore safe and is also used as an antioxidant. Reports on preparation of $LiMnPO_4$ and $LiNiPO_4$ via sol-gel method using tartaric acid as chelating agent are rare.

No inert gas or reducing agent will be employed in the preparation of samples in this work. Inert gases were probably used by previous researchers (Dominko et al., 2006; Piana et al., 2004; Okada et al., 2001;Ma et al., 2005; Wolfenstine and Allen, 2005) to prevent the oxidation of Mn^{+2} to Mn^{+3} and Ni^{+2} to Ni^{+3}. Table 1.1 shows the electronic structure of manganese atom, nickel atom, manganese ion and nickel ion. From the table, it can be seen that the configuration for Mn^{+2} ion is [Ar] $3d^5$. This indicates that the 3d orbital in Mn^{+2} is half-filled and this configuration is stable. The $3d^5$ configuration is more stable than $3d^4$ suggesting that Mn^{+2} is more stable than Mn^{+3}. Therefore the use of air during firing in the synthesis of $LiMnPO_4$ will not affect its structure. As for $LiNiPO_4$, the $3d^8$ and the $3d^7$ electronic configuration does not make much difference in terms of stability.

Table 1.1. Electronic structure of Manganese atom, nickel atom, manganese ions and nickel ions.

Atoms/ions	Manganese atom	Mn^{+2}	Mn^{+3}	Nickel atom	Ni^{+2}	Ni^{+3}
Electronic structure of atoms / ions	[Ar] $3d^5$ $4s^2$	[Ar] $3d^5$	[Ar] $3d^4$	[Ar] $3d^8$ $4s^2$	[Ar] $3d^8$	[Ar] $3d^7$

The sol–gel method was chosen since the sol-gel synthesis ensures homogeneity of the precursors at the nanometric scale and improved reactivity, allowing to obtain very small agglomerates and crystal grain size (Piana et al., 2004). In this work the tartaric acid is expected to act not only as a chelating agent but also improve stability that limits particle growth and prohibits agglomeration. This is possible since tartaric acid has four carbon atoms in its structure while citric acid has six carbon atoms. The lesser number of carbon atoms in its structure allows a smaller ring structure to be formed when complexing with the cations and thus inhibits the growth of the particles. This phenomenon will lead to the formation of smaller particles in the synthesis. According to Hsu et al. (2004) increasing the grain size leads to a decrease in lithium ion diffusion and results in poor rate capability.

The $LiFePO_4$ cathode material will be prepared by the chemical precipitation and low temperature sterilization heating method. This method was chosen since only a low temperature of 121 ^{o}C is required. Review of previous work showed that grain size increases as heating temperature increases. In contrast to other methods, the chemical precipitation and low temperature sterilization heating method employed in this work does not require the presence of reducing agent and inert gas and thus diminishes the cost of synthesis and is environmental friendly. To the author's knowledge, no reports have been found on the preparation of $LiFePO_4$ using the above mentioned method.

In order to address the poor rate capability problem of the $LiMPO_4$ cathode materials stated earlier, the dependence of kinetics and lithium ion diffusion coefficient will be investigated by means of CV experiments. CV is an important method to determine Li^+ ion diffusion coefficient constant (D_{Li^+}). Knowledge of this parameter enables evaluation of material modification such as surface coating (Yu et al., 2007). This is to

ensure that the thickness of the coating materials does not significantly affect the electrochemical properties of the active materials. The thickness of the coating will affect the insertion and extraction of the lithium ions. To date, studies on diffusion coefficient of $LiMnPO_4$ and $LiNiPO_4$ have not been published and that of $LiFePO_4$ are few. It is the hope of this thesis to determine the diffusion coefficient of $LiMPO_4$ samples prepared with the use of cyclic voltammetry and the Randle-Sevcik equation.

An overview of the different types of cathode preparation techniques, different diffusion coefficient investigations techniques and the background study of the work available in the literature are presented in Chapter 2 of this thesis.

Chapter 3 deals with the method of preparation of the three different, $LiMPO_4$ cathode systems. The chapter also explains the experimental methods undertaken in order to structurally, electrically and thermally characterize the cathodes materials. These include the thermogravimetric analysis (TGA) to study the thermal stability of the precursors prepared and thus help to determine the suitable firing temperature for the samples. The different regions of weight losses in the thermogram also help to elucidate the reactions for the formation of the products. Literature survey shows that thermal stability analysis and mechanisms for the formation of $LiMnPO_4$ and $LiNiPO_4$ has not been published yet. The fired samples were characterized by X-ray diffraction (XRD) to confirm the identity of the products and their purity. From the various XRD diffractograms of samples fired at different temperatures, the effect of firing temperature on the purity of samples was observed. From the XRD results, the FWHM was determined and crystallite size was calculated by using Scherrer equation. This calculation was done in order to investigate the effect of firing temperature on the crystal size of the samples and Fourier transform infrared spectroscopy (FTIR) was

carried out to determine the formation of the phosphate bonds in the samples. Energy dispersive X-rays analysis (EDX) were employed to determine the elemental composition of the samples thereby confirming the material's identity.

Cyclic voltammetry experiments were carried out on the prepared samples in order to determine their intercalating/deintercalating properties and hence the ability of the samples as cathode material. From the CV curves, the formal electrode potential was calculated to identify the ion responsible for the gain and loss of electron in the respective system. The relationship between peak current, i_p and square root of the scan rate, $\upsilon^{1/2}$ will be plotted to show reversibility of the system. The Randles - Sevcik equation is used to determine the diffusion coefficient of the systems. The electricity obtained from the systems was determined from the recorded value of charge density, Q, obtained by the integration of the CV curves.

In Chapter 4 the structural properties and redox characteristics of the $LiMnPO_4$ system were analysed. The results of the investigations of the $LiNiPO_4$ system were reported in Chapter 5 and Chapter 6 deals with the results of the experiments and tests carried out on $LiFePO_4$ system. These studies were carried out in order to investigate the effect of particle size on the diffusion coefficient constant as well as the effect of preparation methods on the structure of the cathode materials. In Chapter 7 the overall results obtained were brought together and discussed and Chapter 8 concludes the thesis and suggestions for further work in $LiMPO_4$ cathode material are put forward.

CHAPTER 2

LITERATURE REVIEW

2.1 Introduction

Many people in the world today carry handphones or some kind of mobile communications. These devices make use of batteries that are expected to be rechargeable. Environmental concerns has led to the inventions and innovations of electric vehicles and these will require batteries which are more powerful and have long cycle life. Today lithium ion batteries are the state-of-the-art power sources for many portable electronic devices. This is due to the high energy density, high voltage, lightweight, longer shelf life and wide operating temperature of the lithium ion battery (Balakrishnan et al., 2006, Ferracin et al., 2000, Vincent, 2000). Lithium ion battery should be able to deliver specific capacity as high as 3680 Ah kg^{-1} (Dell, 2000). Lithium ion battery has long shelf life and can be stored for 10 years at room temperature with only 10% capacity loss (Vincent, 2000). However, since the standard potential of lithium is more negative than -3.0 V, the metal is thermodynamically unstable in protic solvents such as water, and this leads to safety problems.

Although a commercial reality, lithium ion batteries are still the object of intense research. According to Scrosati (2000) expected advancements in lithium ion technology include:

a) the replacement of liquid electrolytes with a plastic membrane which may act as both separator and electrolyte, with the aim of improving battery's design and reliability.

b) the replacement of carbonaceous materials with alternative low-voltage, Li-accepting anode compounds with the aim of improving safety characteristics;

c) the replacement of cobalt with nickel or manganese in the cathode structure, with the aim of reducing cost and environmental impact, that is why $LiNiPO_4$ $LiMnPO_4$ and $LiFePO_4$ are prepared in this work as they have the potential to reduce cost and may improve the environmental compatibility.

2.2 Lithium transition metal phosphate with olivine structures

Among the typical positive electrode materials for lithium-ion cells, three-dimensional (3D) materials containing PO_4^{3-} anions in their structure have attracted particular attention due to the high energy density, low cost and good environmental compatibility of its basic constituents. These compounds display high redox potentials, excellent thermal stability, and energy density comparable to that of conventional lithium metal oxides (Padhi et al., 1997). Such framework structures containing an interconnected interstitial space are potentially fast ionic conductors, especially if the substitution of the larger polyanion in an open 3D lattice helps stabilising the structure and the 3D tunnel network allowing for fast ion migration (Julien et al., 2004). Since Padhi discovered that $LiFePO_4$ could be used as the cathode material for secondary lithium batteries, lithium transition metal phosphates $LiMPO_4$ (M:Mn, Fe, Co, Ni) isostructural to olivine have been intensively studied (Franger et al ., 2003).

Crystalline $LiMPO_4$ has an ordered olivine structure (space group: Pnmb) in which MO_6 octahedra shared common corners in the bc plane as shown in Figure 2.1.

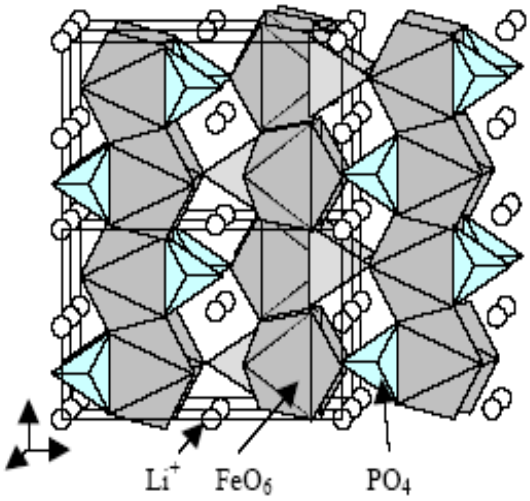

Figure.2.1. Representation of the structures of $LiMPO_4$ phospho-olivine lattice, in which $LiMPO_4$ olivine-like framework in which the P atoms occupy tetrahedral sites, the Li and Fe atoms occupy octahedral sites (Julien, 2004).

In the $LiMPO_4$ crystal structure, the oxygen atoms are arranged in a distorted, hexagonal close-packed arrangement, in which the lithium and iron atoms occupy octahedral sites, while the phosphorous atoms occupy tetrahedral sites (Wang et al., 2005). The three-dimensional framework of an olivine is stabilized by the strong covalent bonds between oxygen ions and the P^{5+} resulting in PO_4^{3-} tetrahedral polyanions (Padhi et al., 1997). This structure may be described as chains (along the c direction) of edge-sharing MeO_6 octahedra which are cross-linked by the PO_4 groups forming a three-dimensional (3-D) network. Tunnels perpendicular to the [010] and [001] directions contain octahedrally co-ordinated Li^+ cations (along the b axis), which are mobile in these cavities (Julien, 2004). As a consequence, olivine lithium metal phosphate materials do not undergo a structural re-arrangement during lithiation and de-lithiation. This means that they do not experience the capacity fade during cycling suffered by lithium transition metal oxides such as $LiCoO_2$, $LiNiO_2$, $LiMnO_2$ and

$LiMn_2O_4$ which is attributed to structural rearrangements caused during lithiation and de-lithiation (Drezen et al., 2007). Their theoretical capacity of up to 170 mA h g^{-1} provides high energy density compared to that of $LiCoO_2$, stabilized $LiNiO_2$ and $LiMn_2O_4$. In the olivine type, $LiMPO_4$ family, $LiFePO_4$ and $LiMnPO_4$, look promising because they operate at 3.4 V to 4.1 V versus Li^+/Li. This is favourable because it is not so high as to decompose the organic electrolyte but it is not so low as to sacrifice energy density (Yamada et al., 2003).

Research are being conducted to investigate the possibility of manganese disorder in $LiMnPO_4$ and its effect on the electrochemical activity. Olivine structured $LiMPO_4$ (M = Mn, Fe, Co, Ni) materials are known to have adequate intrinsic lithium ion mobility for use as rechargeable cathodes, while show only one-dimensional channel for significant lithium ion diffusion (Morgan et al., 2004). Blockages in two-dimensional and three dimensional channels are different from blockages in one-dimensional channels. In two-dimensional and three dimensional channels lithium ions can move around the blocked sites .Thus, lithium ion diffusion is extremely sensitive to the defects blocking for the olivine structured $LiMPO_4$. To understand the structure-property relationships and electrochemical behaviors of the olivine structured $LiMPO_4$ the underlying defects in $LiMPO_4$ materials are crucial. Therefore, the underlying defects in $LiMPO_4$ materials are crucial to the understanding of the structure-property relationships and electrochemical behaviors for these important compounds. A preliminary report on the possibility of Mn^{2+} disorder in $LiMnPO_4$ synthesized by a hydrothermal condition was reported by Fang et al. (2008) and it was found that the electrochemical activity of the as-prepared $LiMnPO_4$ was profoundly influenced by the extent of Mn^{2+} disorder on the Li^+ sites.

Researchers also reported that $LiFePO_4$ suffers from the limitations of poor electronic conductivity (10^{-9}-10^{-10} Scm^{-1}) (Takahashi et al., 2001; Andersson and Thomas, 2000; Padhi et al., 1997) and slow lithium ion diffusion (Nakamura et al., 2007; Padhi et at., 1997).

Various efforts were made to overcome the problem of low electronic conductivity of $LiMPO_4$. Some of the methods discovered were coating the active particles with conductive carbon (Kim et al., 2007; Shin et al., 2006; Franger et al., 2003). Shin et al. (2006) employed the mechanochemical process to synthesize the carbon-coated $LiFePO_4$ using three different carbon sources such as graphite, carbon black, and acetylene black. The purpose of the investigation was to find the effects of carbon coating on the $LiFePO_4$, which were produced by different carbon sources. The preparation of cathode active carbon-coated $LiFePO_4$ ($LiFePO_4$/C) by a modified mechanical activation (MA) process was reported by Kim et al. (2007). The electrochemical properties of $LiFePO_4$/C in lithium batteries would be decided considerably by the nature as well as the effectiveness of the conductive carbon coating around the particles. To obtain an effective coating, a uniform dispersion of carbon powder is necessary to obtain in the precursor sample before subjecting to ball milling. The modified mechanical activation (MA) method, synthesized material that had uniform carbon coating and good electrochemical properties.

The carbon coating method was further studied extensively by several researchers (Mi et al., 2005; Bewlay et al., 2004). Carbon coating the active materials not only improve the electronic conductivity between particles, but also provide electronic tunnel to complement the charge equilibrium during Li extraction/insertion (Cushing and Goodenough, 2002).

FTIR spectroscopy is one of the tool commonly used to confirm the formation of the phosphate PO_4^{3-} bond in lithium metal phosphate and lithium metal diphosphate compounds. FTIR is also used to determine the purity of the sample. Figure 2.2 shows the FTIR absorption spectra, of lithium metal phosphate, $LiMPO_4$ (M=Fe, Co, Mn) phospho-olivine phases, lithium metal diphosphate ($LiFeP_2O_7$) and Nasicon-like $Li_3Fe(PO_4)_3$ framework (Salah et al., 2005). It can be seen from Figure 2.2 that all these spectra are dominated by the internal vibrations (ν_1–ν_4) of the PO_4^{3-} units which involve the displacement of oxygen atoms of the tetrahedral PO_4^{3-} anions and present frequencies closely related to those of the free molecule.

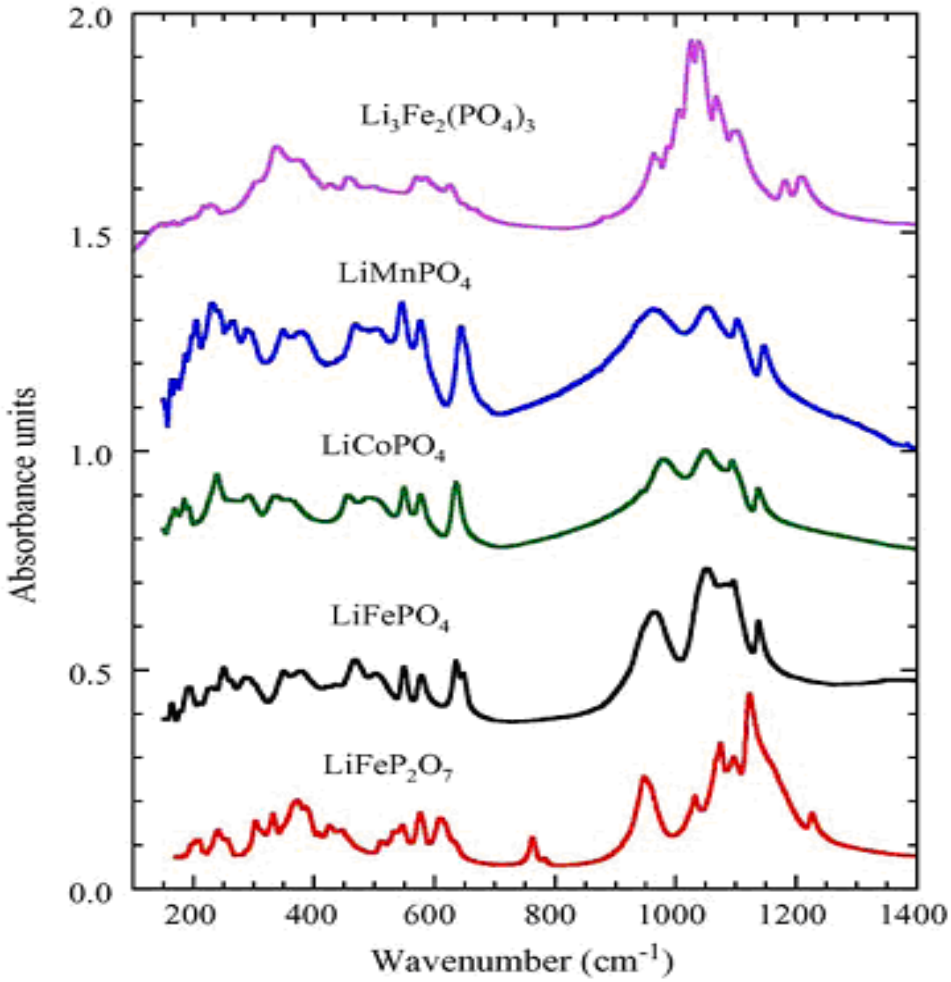

Figure 2.2 FTIR absorption spectra of lithium metal phosphates with diphosphate ($LiFeP_2O_7$), olivine-like ($LiFePO_4$, $LiCoPO_4$, $LiMnPO_4$) and Nasicon-like $Li_3Fe(PO_4)_3$ framework (Salah et al., 2005).

2.3 Lithium iron phosphate, $LiFePO_4$

Among these $LiMPO_4$ materials, $LiFePO_4$ is considered to be the most attractive candidate. This is because iron is environmentally benign, low cost, has excellent thermal stability in the fully charged state and has high capacity. Besides that $LiFePO_4$ offers advantages such as a flat discharge voltage at 3.4 V versus lithium, a wide safety margin of usage for organic electrolytes, high thermal and chemical stability, low material cost, low toxicity and improved safety (Kim et al., 2007).

Olivine-$LiFePO_4$ has orthorhombic crystalline phase with space group Pmnb. It consists of a hexagonal close packed (hcp) and the crystal skeleton consists of FeO_6 octahedra and PO_4 tetrahedra, Fe and Li occupying the space of octahedron. Among them, Fe takes M2 (010) in corner-shared octahedral and Li occupies M1 (100) in edge-shared octahedra. On the one hand, the large PO_4^{3-} polyanion lowers the Fermi energy of Fe^{2+} and enhances the open circuit voltage to application level, of 3.4 V versus Li^+/Li. On the other hand, it also separates the chain of FeO_6 edge-shared octahedra, leading to extremely low electronic conductivity (Ni et al., 2005).

The electrochemical delithiation of $LiFePO_4$ proceeds by a two-phase reaction to the isostructural $FePO_4$. It exhibits a flat discharge voltage of 3.5 V versus Li^+/Li and a theoretical high specific energy 169 mA h g^{-1}. The generation of an appropriately high voltage is due to the presence of the polyanion $(PO_4)^{3-}$ with strong Fe-O covalency, which stabilises the antibonding Fe^{2+}/Fe^{3+} state through a Fe-O-P inductive effect.

Figures 2.3 show the charge-discharge curve for the orthophosphates $LiFePO_4$ with olivine-like framework. The typical two-phase redox reaction i.e

$$LiFePO_4 \leftrightarrows Li_{1-x}FePO_4 + xLi^+ + xe- \quad (1.1)$$

is observed by the presence of the plateau at 3.5 V versus Li^+ /Li for $LiFePO_4$ in Figure 2.3. Combined with discharge voltage 2.0 to 4.3 V versus Li^+ /Li, $LiFePO_4$ leads to a high specific capacity of 150 mA h g^{-1}.

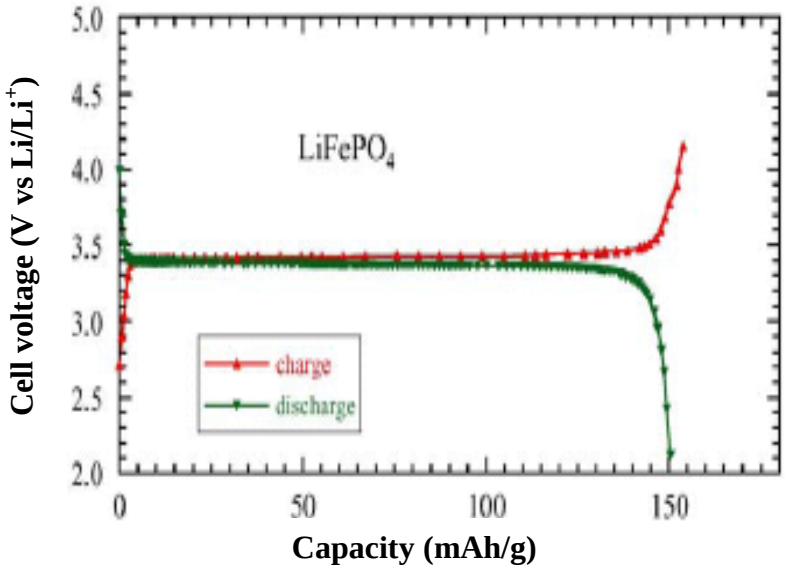

Figure. 2.3. Charge-discharge of $LiFePO_4$ olivine compounds (Salah et al., 2005; Julien, 2004)

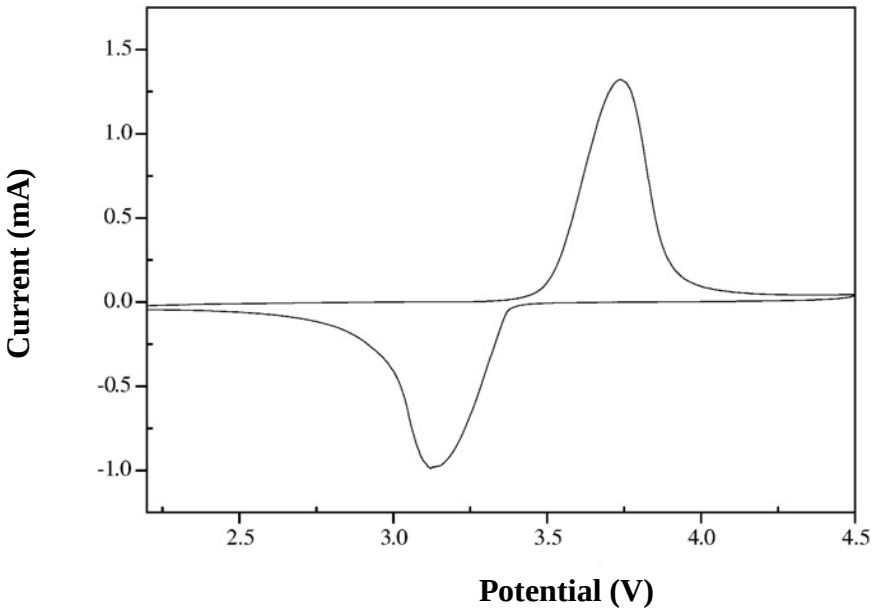

Figure. 2.4. The typical cyclic voltammogram of $LiFePO_4$ at 0.2 mV/s scan rate in 2.2 to 4.5 V (Liu and Tang, 2008).

In order to understand the electrochemical properties of $LiFePO_4$, cyclic voltammetry experiments were carried out by researchers (Yu et al., 2007; Liu et al., 2006; Wang et al., 2005; Ni et al., 2005) An example of the CV profiles of lithium iron phosphate, $LiFePO_4$ is shown in Figure 2.4. It exhibited a pair of redox peaks around 3.4 V versus Li^+/Li. There is only an oxidation peak and a reduction peak, which corresponds to the charge/discharge reaction of the Fe^{3+}/Fe^{2+} redox couple.

2.4 Lithium Manganese Phosphate, $LiMnPO_4$

Since Lithium Manganese Phosphate, $LiMnPO_4$ also exhibit the olivine structure similar to $LiFePO_4$, the success of $LiFePO_4$ as cathode material has attracted increase attention to $LiMnPO_4$. It has a redox potential of 4.1 V versus Li^+/Li (Padhi et al., 1997; Yamada et al., 2001) which is ~0.65 V higher than $LiFePO_4$, promising a great energy density and lower energy cost on a cell and system level (Wang et al., 2009). However, $LiMnPO_4$ has drawbacks i.e low intrinsic electronic and ionic conductivity and hence a poor discharge rate capability. In fact, the electronic conductivity of $LiMnPO_4$ ($<10^{-10}$ S cm^{-1}) is much lower in comparison with $LiFePO_4$ (1.8×10^{-9} S cm^{-1} at 25 °C) (Delacourt et al., 2006; Yonemura et al., 2004). Bramnik and Ehrenberg (2008) pointed out that the poor rate capability of $LiMnPO_4$ results from the sluggish electronic and /or ionic transport. The electrochemical performance is especially poor at high current densities, this is assigned to the slow lithium diffusion kinetics within the grains and the low intrinsic electronic conductivity (Delacourt et al., 2006 Yonemura et al., 2004). According to Prosini et al. (2002) the rate of performance of the olivine material can be improved by minimizing the particle size.

A lot of methods were put forward to overcome the problem. By the precipitation method, $LiMnPO_4$ with 100 nm diameter particles were synthesized. Quite recently, $LiMnPO_4$ with a platelet-like morphology (35 nm of thickness) were obtained by the polyol synthesis (Wang et al., 2009).

Recent works focused on the optimization of $LiMnPO_4$ cathode material demonstrated that intrinsic low rate capability can be overcome (at least partially) by the decreasing of the particle size and providing of good electronic contact between particles in the composite cathode (Prosini et al., 2003; Kim et al., 2004).

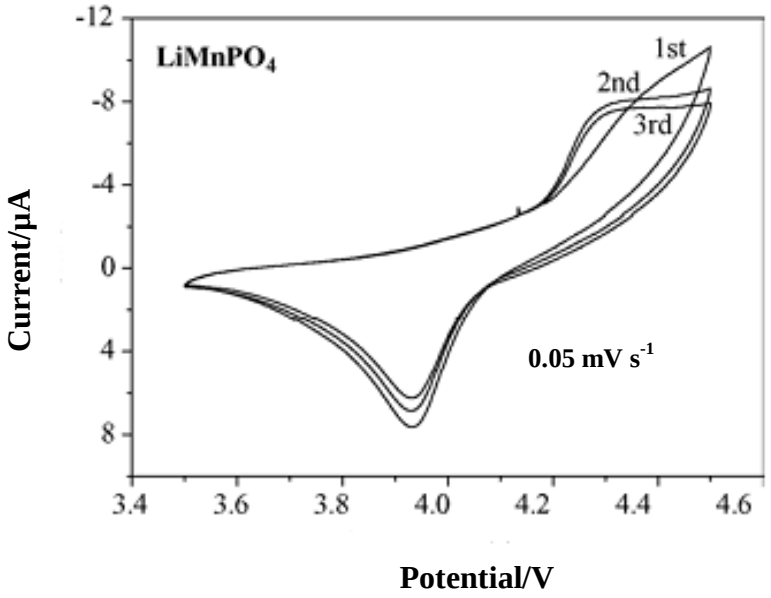

Figure 2.5. Cyclic-voltammograms for $LiMnPO_4$ film electrodes in 1 mol dm^{-3} $LiPF_6$ / (EC +DEC) at different scan rates (Ma and Qin, 2005).

Cyclic voltammetry experiments were carried out by researchers in order to determine the reversibility of a sample. The CV curves in Figure 2.5 shows the anodic peaks and cathodic peaks for $LiMnPO_4$ in the first three cycles of a 0.05 mVs^{-1} scan rate. The difference of the peak separations between the anodic and cathodic peaks was estimated to be 300 mV, indicating a strong polarization and irreversible behavior during a $LiMnPO_4$ film / Li cell cycling (Ma and Qin, 2005).

2.5 Lithium Nickel Phosphate, $LiNiPO_4$

In addition to $LiFePO_4$ and $LiMnPO_4$ there is another member of the $LiMPO_4$ series, $LiNiPO_4$, which has been postulated to have a higher redox potential ≈5.2–5.4 V than $LiCoPO_4$ and theoretical calculations suggest that the Ni^{3+}/ Ni^{2+} redox potential is above 5 V (Deniard et al., 2004; Padhi et al., 1997). Previous attempts to experimentally confirm this prediction have failed as a result of : (1) low stability electrolytes and /or (2) low rate capability of this material, which result in low electrical conductivity and slow Li-ion diffusion (Wolfenstine and Allen, 2005). Studies done by Wolfenstine and Allen (2005) suggest that the Ni^{3+}/Ni^{2+} redox potential in $LiNiPO_4$ is between 5.1 V and 5.3 V, in agreement with theoretical predictions. $LiNiPO_4$ has very low electrical conductivity, making it difficult to observe Li insertion /deinsertion.

2.6 Lithium cobalt Phosphate, $LiCoPO_4$

$LiCoPO_4$ has also attracted much interest due to high voltage (~4.7 V) and capacity

(~170 mA h g^{-1}) (Wolfenstine et al., 2007) which is predicted to be ~1.6 times the specific energy of $LiCoO_2$ (Okada et al., 2001; Wolfenstein et al., 2005). However, the presence of cobalt makes it environmentally unfriendly. Just like other orthophosphates, $LiCoPO_4$ also suffer from low electronic conductivity. However it has been shown that the electronic conductivity of $LiCoPO_4$ can be increased from 10^{-9} Scm^{-1} or lower to 10^{-4} Scm^{-1}, when when carbon-containing precursors were used (Wolfenstine, 2006).

Figure 2.6 shows the charge-discharge curve for the orthophosphates $LiCoPO_4$ with olivine-like framework. The generation of an appropriately high voltage is due to the presence of the polyanion $(PO_4)^{3-}$ with strong Co-O covalency, which stabilises the antibonding Co^{2+} / Co^{3+} state through an Co-O-P inductive effect (Salah et al., 2005; Julien , 2004).

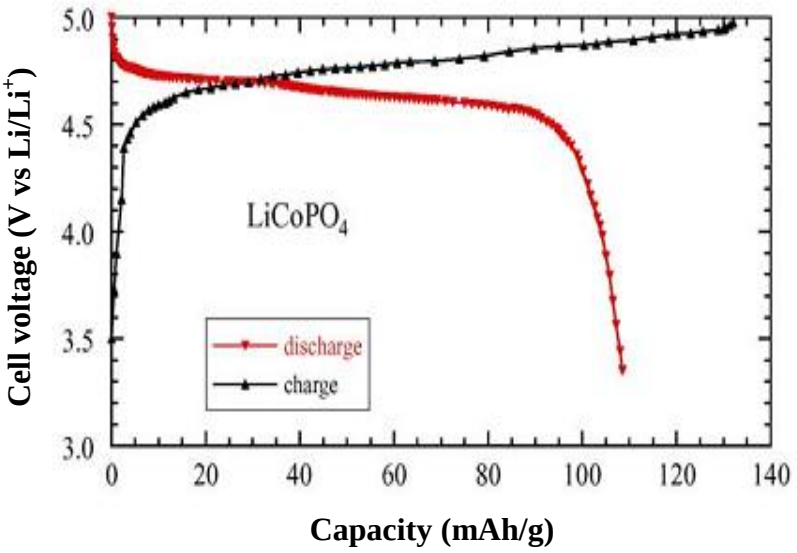

Figure 2.6. Charge-discharge of $LiCoPO_4$ olivine compounds (Salah et al., 2005;Julien et al., 2004).

2.7 Diffusion coefficient Investigations Techniques

As stated above the $LiMPO_4$ (where M=Fe, Mn and Ni) all suffer from low electronic conductivity and slow diffusitivity. To meet the requirements of high power properties, the studies on the diffusion properties becomes more important. Diffusion properties play an important role in improving its rate capability (Tang et al., 2009). Much attention has now been taken to investigate the kinetic behaviour of the $LiMPO_4$ of which the diffusion coefficient is one of the most important parameter (Gao et al., 2008, Molenda et al., 2006; Prosini et al., 2002). Some of the methods used for investigating Li^+ ion diffusion coefficient are :

(a) Cyclic voltammetry

Cyclic voltammetry has been used by several researchers for investigating Li^+ ion diffusion coefficient (Yu et al., 2007 ; Tang et al., 2009 ; Leftheriotis et al., 2007, Liu et al 2006). CV has an advantage over EIS and porous electrode theory because complicated model fitting is not necessary as long as the active area of the particle is known. CV is then a better method than potentiostatic intermittent titration technique (PITT) and galvanostatic intermittent titration technique (GITT) to obtain diffusion coefficient constants, D_{Li^+} of $LiFePO_4$ (Yu et al., 2007).

Work done using PITT and GITT showed that there are problematic within the two-phase region where the differential capacity with potential (dQ/dE) is infinite as the potential remains unchanged during charging and discharging (Prosini et al., 2002; Markevich et al., 2005). Unlike PITT and GITT , the knowledge of dQ/dE is not required for the analysis of CV profiles. Therefore, diffusion coefficient value, D_{Li^+} can be obtained with a higher accuracy using CV (Yu et al., 2007).

(b) Capacity Intermittent titration technique (CITT)

Recently a new method i.e capacity intermittent titration technique (CITT) for measurement of the diffusion coefficient by introducing the ratio of the potentio-charge capacity to the galvano-charge capacity was reported (Tang et al., 2005; Tang et al., 2004). Compared with the other methods (GITT, EIS and PITT), this method only needs one complementary parameter (the radius of insertion-host particle, *R*) and allows to continuously determine the diffusion coefficients at different state of charge and at different cycles. Tang et al. (2009) further use CITT to investigate the diffusion behavior of Li^+ in $LiFePO_4$ by taking the finite kinetics at interface into account. Results show that the approximation of infinite charge-transfer kinetics leads to a spurious value of diffusion coefficient, D which is lower than the real value, and the decreasing extent of D is relative to the galvano-charge current of CITT experiment.

(c) Electrochemical impedance spectrscopy (EIS) methods

Electrochemical impedance spectroscopy (EIS) is an important method to evaluate the diffusion coefficient of lithium ion and was used to investigate the influence of carbon content on the lithium ions transfer in the $LiFePO_4$ (Liu et al., 2006). The lithium ion

diffusion coefficient is calculated according to the following equation (Gao and Tang 2008).

(1.2)

where n, is the number of electrons per molecule during oxidization, A, the surface area of the cathode, D, the diffusion coefficient of lithium ion, R, the gas constant, T, the absolute temperature, F, the Faraday constant, C, the concentration of lithium ion, and σ, is the Warburg factor which has relationship with Z_{re}:

$$Z_{re} = R_D + R_L + \sigma\omega^{1/2} \quad (1.3)$$

Tang et al.(2009) also used EIS to investigate the chemical diffusion of lithium ion in $Li_3V_2(PO_4)_3$.

(d) Potentiostatic and galvanostatic intermittent titration techniques (PITT and GITT, respectively).

A couple of useful electroanalytical approaches, known as potentiostatic and galvanostatic intermittent titration techniques (PITT and GITT, respectively) were developed to characterize the diffusion kinetics of guest ions in ion-insertion electrodes (IIEs) (Levi et al., 2004; Kim and Pyun, 2001; Lu et al 2000 ; Shin and Pyun, 1999 ;Bae and Pyun 1996). One of the major problems related to the application of PITT and GITT to IIEs is that for a great variety of common host materials the intercalation process occurs via first order phase transition, which, at a first glance, seems to be incompatible with the approaches based on the Fickian dynamics. Some specific problems typical of a first-order phase transition kinetics,

such as a slow droplet formation of the new phase in the bulk of the old one (example: a cubic to tetragonal manganese spinel transition), for which the Fickian dynamics obviously cannot be applied, have also been reported (Markevich et al., 2005). Although concepts of the moving boundary in the two-phase systems were proposed to interpret diffusion coefficients of ions in IIEs (Shin et al.,1999; Danielewski et al., 2004), according to Markevich et al. (2005) there is serious shortage of papers considering merits, shortcomings, both theoretical and experimental limitations of PITT and GITT for a meaningful characterization of the diffusion kinetics of intercalation processes complicated by first-order phase transitions.

2.8 Preparation method of $LiMPO_4$ cathode materials

Many factors determine the performance of $LiMPO_4$. Phase purity of the active material and particle size are some of the factors. These factors are largely synthesis route dependent and thus the performance of resultant $LiMPO_4$ electrodes is strongly synthesis route dependent as well (Yang and Xu., 2004).

2.9 Solid state reaction

Lithium iron phosphate ($LiFePO_4$) cathode material has been synthesized by a solid-state reaction which uses Li_3PO_4 and $Fe_3(PO_4)_2 \cdot 8H_2O$ as starting materials (Kim et al., 2004). These materials were mixed with alumina balls and treated thermally at various temperatures in an argon and hydrogen atmospheres. The particle size increases as the heat-treatment temperature increases. Although the capacity increases as the operating temperature is raised, the degree of capacity fade also increases (Kim et al., 2004).

Okada et al.(2001) prepared four types of phospho-olivines, $LiMPO_4$ (M=Co:Ni:Mn and Fe) by the conventional solid-state reactions method. In Okada's work, the mixtures were pre-sintered at 500 ^oC for several hours and the mixtures were quenched using liquid nitrogen after firing at 780 to 850 ^oC for 2 days with an intermittent grinding.

2.10 Hydrothermal Synthesis

The hydrothermal method involves the heating of solid and liquid reagents with a suitable solvent (usually water) in a sealed vessel at temperatures of up to 250 °C. Although elevated temperatures are used and pressure is generated in the sealed container, the conditions are much less severe than the traditional ceramic methods of solid-state chemistry. These mild, solvent-mediated, reaction conditions have allowed access to many novel materials with important applications. Good examples include zeolites and other microporous materials used in gas separation and shape-selective catalysis, and layered cathode materials for use in efficient rechargeable batteries (Walton et al., 2001).

Hydrothermal methods have been successfully applied to the synthesis of lithium iron phosphates. The raw materials were mixed quickly and transferred to a Parr reactor. Crystalline $LiFePO_4$ was formed in a direct hydrothermal reaction in just a few hours. This result leads to the possibility of an easy scale-up in commercial processing. (Yang et al., 2001).

Meligrana and coworkers (2006) developed an easy, quick and low cost hydrothermal synthesis to prepare high surface area phospho-olivine $LiFePO_4$ powders to be used as cathode material for Li-ion batteries. The samples were prepared in double distilled

water starting from commercial LiOH, $FeSO_4$, H_3PO_4 and using solutions with different concentrations of a surfactant compound (CTAB), in order to increase the specific surface areas, obtaining powders with very small grain size. In the synthesis, the resulting green precipitate formed was washed to remove any excess surfactant, filtered and dried at 40 ^oC overnight. To avoid the oxidation of $Fe^{2+}$to Fe^{3+} the heating treatment was carried out in inert atmosphere. In order to obtain the crystalline phase the powders were pre-treated at 200 ^oC followed by firing at 600 ^oC in pure nitrogen for 12 hours.

Huang et al. (2005) reported that $LiCoPO_4$ with well-formed orthorhombic prism shapes was successfully synthesized by a hydrothermal method.

2.11 Sol-gel method

Sol-gel is a promising method to prepare electrode materials due to their evident advantages over traditional methods such as homogeneous mixing at the atomic or molecular level, lower synthesis temperature, shorter heating time and smaller particle size at nanometer level (Fu et al., 2005). Cathode materials including lithium cobalt oxides, lithium nickel oxides, and layered lithium manganese oxides have been synthesized by this method (Song and Lee, 2002). Various sol-gel methods have been developed to synthesize $LiFePO_4$. Hsu and group (2004) employed citric acid as the complexing agent in the sol-gel process. A new type of $LiFePO_4$ – carbon composite cathode material was prepared by a sol-gel method based with a single heating step (Gaberscek et al., 2005).

Dominko et al. (2006) prepared $LiMnPO_4$ and $LiFePO_4$ using a sol–gel method . Iron (III) citrate or manganese (II) acetate tetrahydrate and citric acid were dissolved at 60 °C in water. Separately, an equimolar water solution of LiH_2PO_4 was prepared from lithium phosphate and phosphoric (V) acid. The two separate solutions were mixed and a xerogel was obtained after drying at 60 °C for 24 hours. The xerogel was ground with mortar and pestle, and was fired in an inert (pure argon) atmosphere at 700 °C for $LiFePO_4$ sample and 900 °C for $LiMnPO_4$ sample for 10 hours.

The above examples show that sol-gel methods are an important way to synthesize cathode materials for lithium secondary batteries. In addition, the sol-gel methods can be used to prepare nanomaterials, which has become more and more important in science and technology.

2.12 Water quenching treatment

Quenching techniques are widely used in the preparation of powder materials, such as amorphous semiconductors, crystals, nanomaterials and alloys. They can produce materials with fine grains and good crystallinity by choosing a suitable sintering temperature and time and cooling modes (Gao et al., 2009).

Most research efforts have focused on synthesizing nanoparticles (Yamada et al., 2001;. Yang et al., 2002) because the diffusion path of lithium ions is reduced at the nanoscale, and thus electrochemical performance of $LiFePO_4$ can be enhanced. However, it is very difficult to prepare nanoscale particles at high temperatures without using carbon or an organic carbon precursor.

In Gao's work, the starting materials were first precalcined at 400 °C for 6 hours in flowing ultra-pure Argon in order to decompose the carbonate, oxalate, and ammonium. After cooling down, the decomposed mixtures were pressed into pellets and transferred to quartz tubes, which were then sealed in vacuum. The vacuum-sealed samples were then calcined in a muffle furnace. The quartz tubes with the samples were removed from the furnace and immediately put into water. The product $LiFePO_4$ was obtained by removal from a broken quartz tube.

Water quenching treatment provides a convenient ways for preparing samples with fine particle sizes and also decrease the iron disorder. This method has been used to prepare a series of lithium transition metalphosphate such as $LiMnPO_4$ and $LiCoPO_4$ with excellent electrochemical performance. However in this method the starting materials were precalcined in argon which is environmentally unfriendly. Various methods and technology have been developed and investigated in the search of improving the performance of $LiMPO_4$ as cathode material.

2.13 Summary

In this chapter we have looked at $LiMPO_4$ (M=Mn, Ni and Fe), as cathode material for lithium rechargeable batteries. Their structure, infrared absorption spectra and cyclic voltammograms were reviewed. Literature survey shows that the lithium metal phosphates ($LiMPO_4$) has attracted a lot of attention as an alternative cathode material due to their low toxicity, low cost, has excellent thermal stability in the fully charged state and high capacity. However, $LiMPO_4$ suffers from the poor electronic conductivity and low diffusitivity which increases the impedance of the electrode and decreases the rate capacity. This significantly limits their applications in lithium ion

batteries. The methods used to improved the electronic conductivity of $LiMPO_4$ were mentioned. Some of the methods are coating particles with conductive carbon and co-synthesizing the compounds with carbon. Literature survey also pointed out that low lithium ion diffusion can be overcome by reducing the particle size of the active material. The methods used to investigate the diffusion coefficient of Li ion were also presented. These methods include potentiostatic and galvanostatic intermittent titration techniques (PITT and GITT, respectively), capacity intermittent titration technique (CITT), electrochemical impedance spectroscopy (EIS) methods and cyclic voltammetry (CV). The methods of preparation of $LiMPO_4$ were also described and these include solid state reaction, hydrothermal, water quenching and sol-gel. It can be seen that many of the preparation methods employed the usage of inert gas in the synthesis of $LiMPO_4$.

CHAPTER 3

EXPERIMENTAL METHODS

3.1 Introduction

In this chapter the experimental techniques used to characterize the prepared samples and the methods of preparing the cathode materials are presented. The structural and thermal properties of the samples were studied by various techniques i.e. X-ray Diffraction (XRD), thermogravimetric analysis (TGA) and Energy Dispersive X-rays Analysis (EDX). The vibrational spectroscopy employed in the present study is Fourier Transform Infrared (FTIR). Cyclic voltammetry studies were also carried out to evaluate the electrochemical performance of the samples and to determine the diffusion coefficient of the lithium ions.

3.2 Samples preparation

The cathode materials prepared in this work are the lithium metal phosphate compounds with olivine structure namely $LiMnPO_4$, $LiNiPO_4$ and $LiFePO_4$. Sol-gel technique was adopted for the preparation of $LiMnPO_4$ and $LiNiPO_4$ while the $LiFePO_4$ was prepared by the chemical precipitation and low temperature sterilization method.

(a) Preparation of $LiMnPO_4$ and $LiNiPO_4$

$LiMnPO_4$ and $LiNiPO_4$ were prepared by the sol-gel technique. The flow chart for the samples preparation is shown in Figure 3.1 and the amounts of chemical used to synthesize $LiMnPO_4$ and $LiNiPO_4$ are tabulated in Table 3.1.

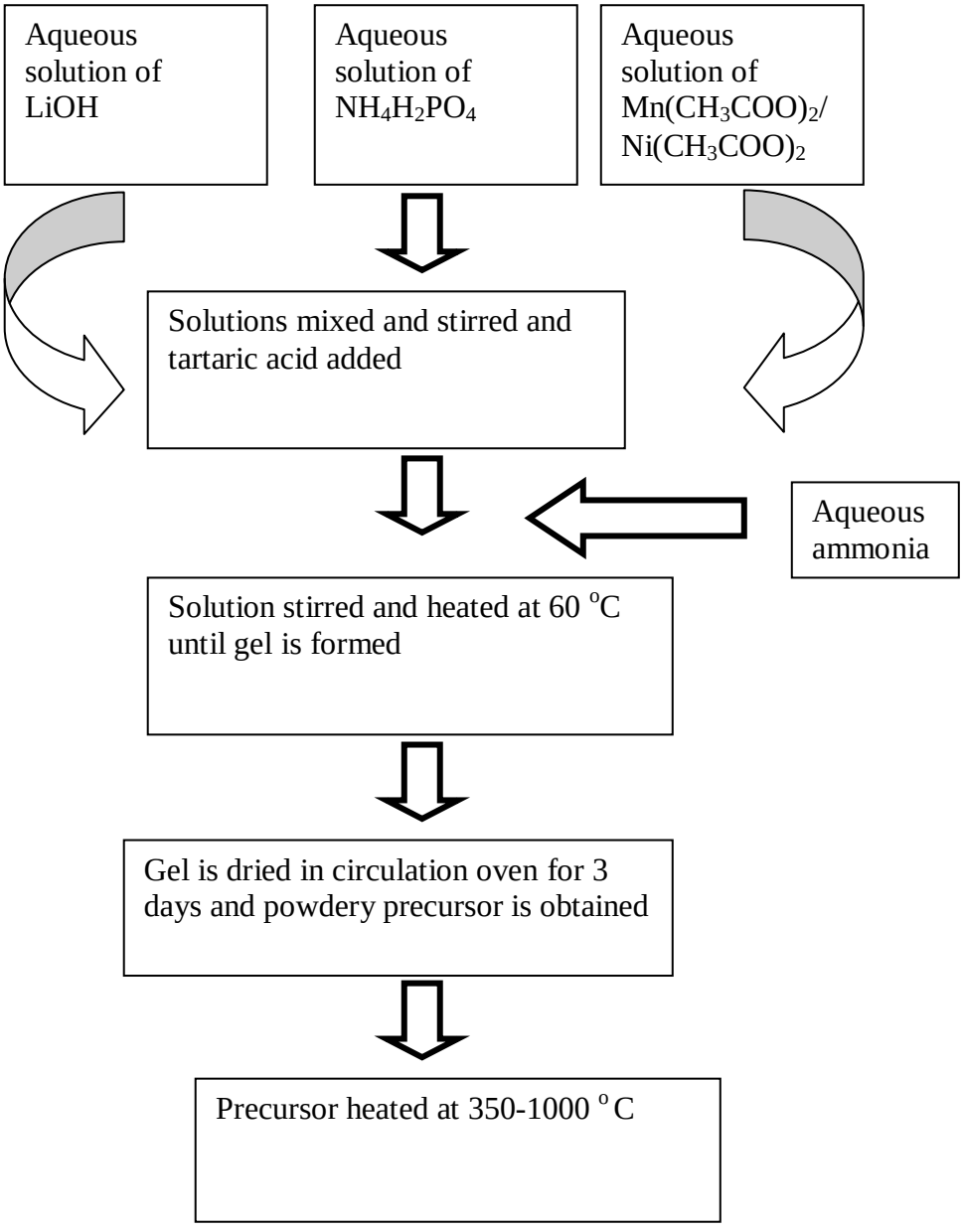

Figure 3.1. The flow chart for the synthesis of $LiMnPO_4$ and $LiNiPO_4$ via the sol-gel method.

Table 3.1. Amounts of raw materials used

Sample	Raw materials	Molecular weight, g mol^{-1}	mass used, g	mole
$LiMnPO_4$	$LiOH.H_2O$	42.96	12.53	0.30
	$Mn(CH_3COO)_2.4H_2O$	245.09	73.52	0.30
	$NH_4H_2PO_4$	115.03	34.62	0.30
$LiNiPO_4$	$LiOH.H_2O$	41.96	12.53	0.30
	$Ni(CH_3COO)_2.4H_2O$	248.86	74.62	0.30
	$NH_4H_2PO_4$	115.03	34.62	0.30

A stoichiometric proportion of high purity lithium hydroxide, manganese acetate, nickel acetate and ammonium dihydrogen phosphate were weighed and dissolved in distilled and deionised water separately in the mole ratio 1:1:1. The aqueous solutions were mixed and stirred constantly at room temperature. A whitish pink and greenish solution was obtained when preparing $LiMnPO_4$ and $LiNiPO_4$ respectively as shown in Figure 3.2. A 1.0 M tartaric acid solution was slowly added to the mixture as the chelating agent. Tartaric acid was chosen as the chelating agent and not citric acid since tartaric acid has lesser number of carbon atoms in its structure and so a smaller crystallite size is expected to be obtained in this synthesis. Ammonium hydroxide was added carefully into the mixture until a pH value of 5 to 6 was achieved. At this pH gel formation was achieved.

The mixture was stirred until a thick pinkish white gel-like mixture was obtained when preparing $LiMnPO_4$ and a green gel when preparing $LiNiPO_4$. It is expected that the carboxylic groups on the tartaric acid form a chemical bond with the metal ions and the mixture will form a gel. The gel-like mixtures were then slowly heated at

60 ^{o}C to 70 ^{o}C to remove water. The gels were further dried at 60 ^{o}C in a circulation oven for 3 days until a powdery precursor was obtained. The precursors were further fired in air in the temperature range between 350 ^{o}C to 1000 ^{o}C for 15 hours in a muffle furnace. The fired products obtained were in the form of clumps that had to be broken down by grinding with agate mortar so that it can be further characterized.

(a)

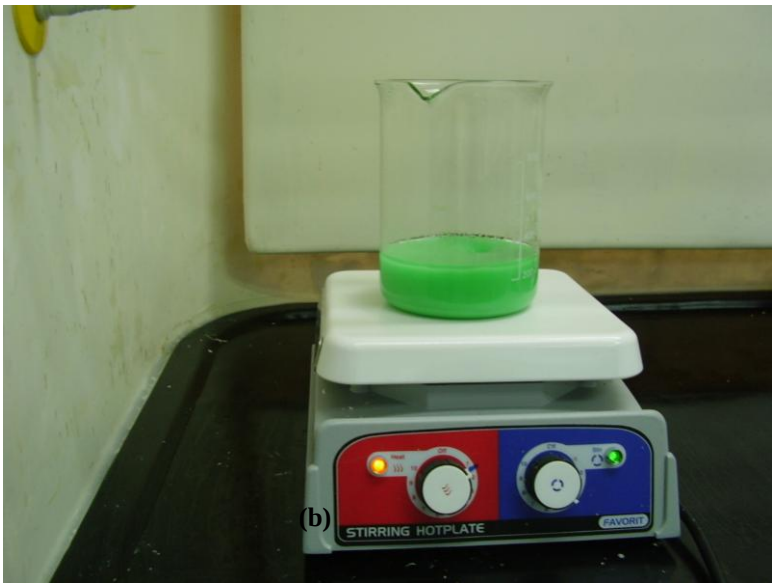

(b)

Figure 3.2. Photographs showing the solutions formed during the preparation of (a) $LiMnPO_4$ and (b) $LiNiPO_4$.

(b) Preparation of $LiFePO_4$

The synthesis was carried out in a sterilization autoclave. An appropriate amount of $LiOH.H_2O$, $FeSO_4.7H_2O$ and H_3PO_4 were weighed and dissolved separately in distilled and deionised water. Firstly, the $FeSO_4$ and H_3PO_4 solutions were mixed. This is to avoid Fe^{2+} in $Fe(OH)_2$ to be oxidized to Fe^{3+}. Then LiOH solution was added to the mixture with stirring. A grayish blue mixture was obtained. The mixture was divided into several autoclave glass jars and transferred to the sterilizer. pH of the solution was 7 and the molar ratio of Li:Fe:P was 3:1:1. The reaction proceeded at 121 ^oC for 300 minutes under 10^5 Pa pressure. The final solution was cooled, filtered and washed several times with distilled and deionised water until no SO_4^{2-} could be detected by $BaCl_2$ solution. $BaCl_2$ solution turn cloudy i.e form a white precipitate in the presence of SO_4^{2-} anion. The final product was light green precipitate and was dried in a vacuum oven at 60 ^oC for 24 hours. The final product is shown in Figure 3.3 and the synthesis is shown in Figure 3.4.

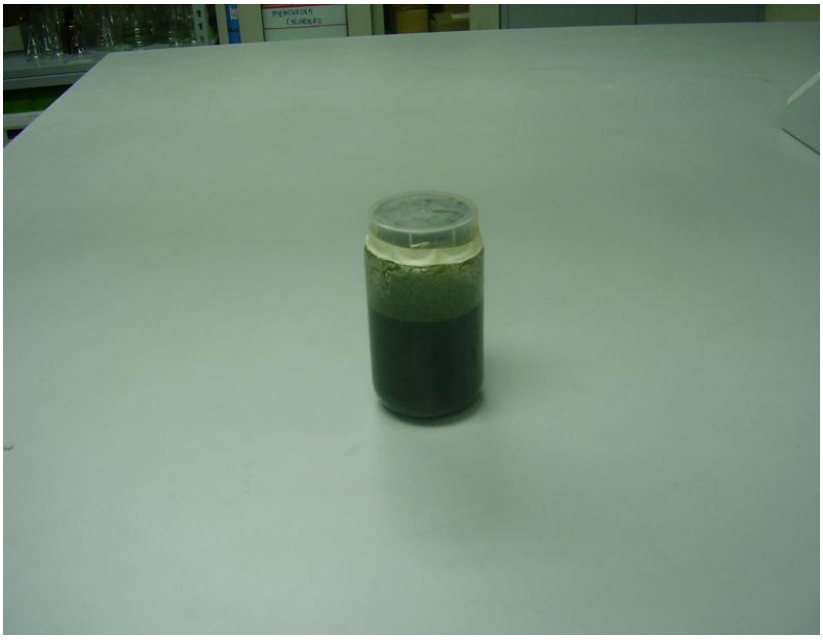

Figure 3.3. A photograph of the grayish blue mixture of $LiFePO_4$.

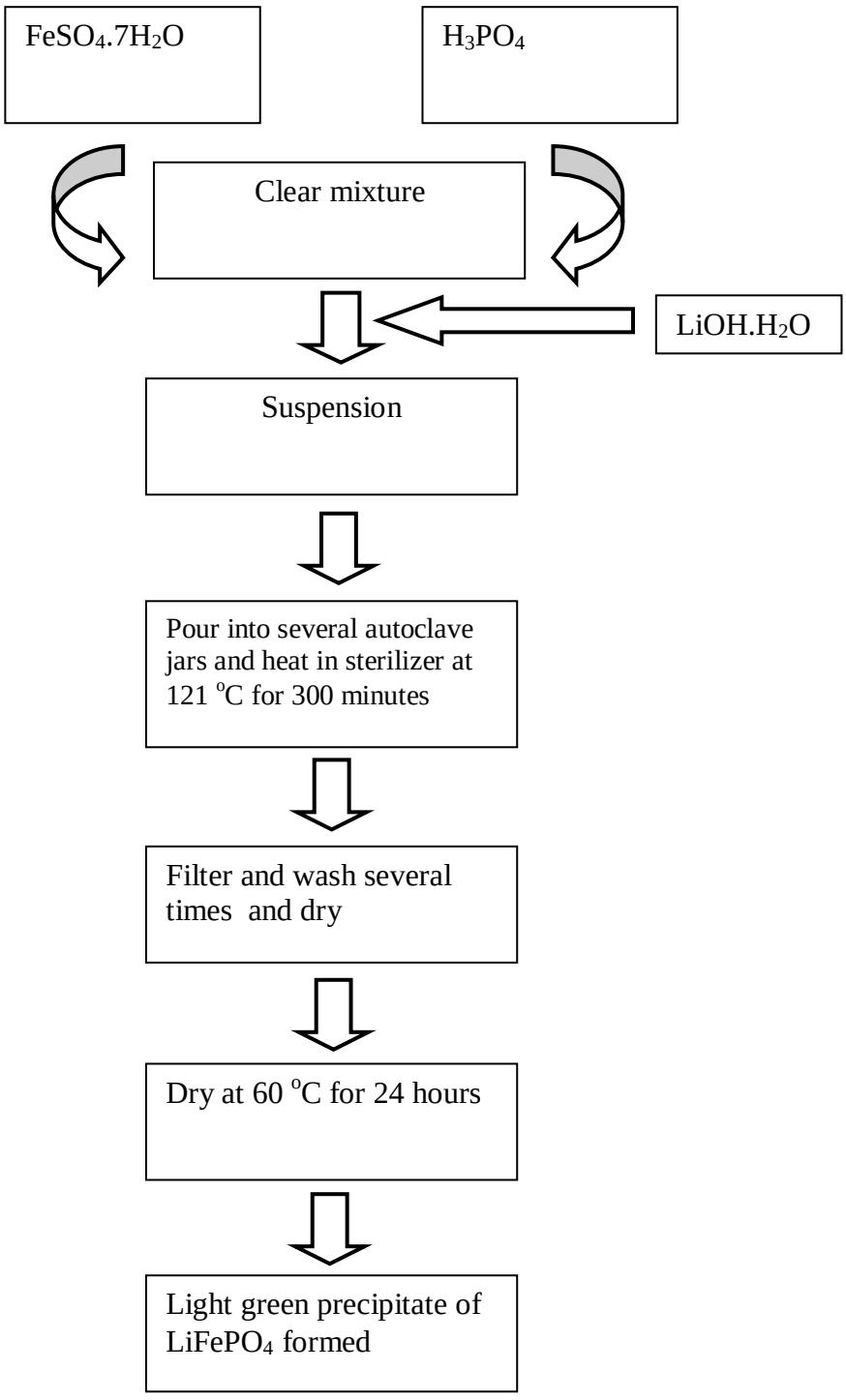

Figure 3.4. Schematic diagram for the synthesis process of $LiFePO_4$.

3.3 Characterization

Structural characterization of the samples prepared in this study were carried out by XRD, FTIR and EDX. Thermal studies was done by TGA. Cyclic voltammetry experiments were employed to obtain the electrochemical properties of the samples from the analysis of the CV profiles.

3.3.1 Thermal Analysis

Thermal analysis is a branch of materials science where the properties of materials are studied as they change with temperature. It comprises of a group of techniques which includes TGA (thermogravimetric analysis) and DTA (differential thermal analysis). Both analysis rely on samples which decompose at elevated temperature.

Thermogravimetric analysis or TGA is a type of characterization technique that is performed on samples to determine changes in weight in relation to change in temperature. TGA is also an analytical technique used to determine the thermal stability of a material. The data obtained provide information concerning the thermal stability, composition and decomposition behaviour of the original sample (Turi et al., 1988). From the thermogram the annealing temperature of the sample can be determined.

In this work, thermal analysis, thermogravimetrical analysis (TGA) was performed on the precursor to determine its thermal decomposition behaviour. Results were also plotted as a trace of differential thermogravimetric analysis (DTGA) versus temperature. The heating rate was 10 ^{o}C min^{-1} and the precursors were heated from

30 ^{o} to 1000 ^{o}C in nitrogen atmosphere. From the thermogram, the firing temperatures of the prepared samples were determined. Figure 3.5 shows an example of a TGA curve of the $LiNi_{0.5}Mn_{1.5}O_4$ spinel precursor (Fang et al., 2007).

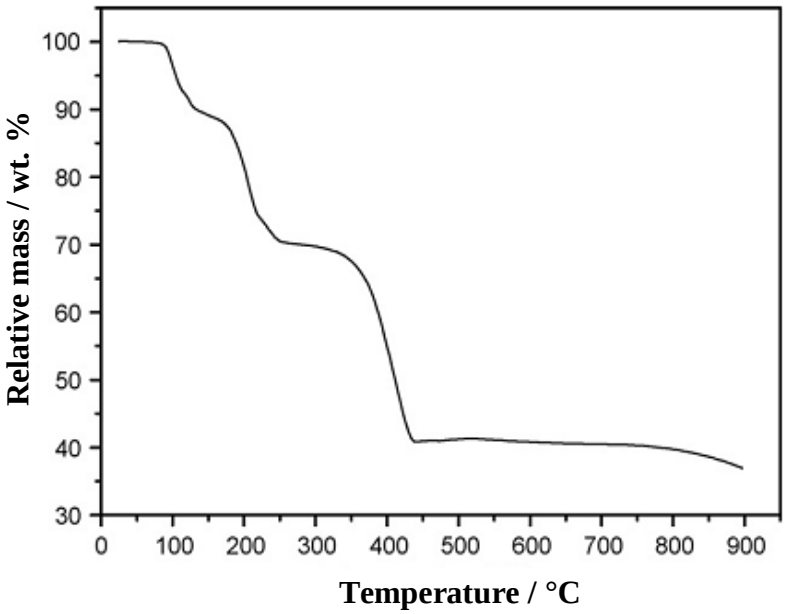

Figure 3.5. TGA curve of the precursor of $LiNi_{0.5}Mn_{1.5}O_4$ measured in air (Fang et al., 2007).

In this work, samples with the analysis was carried out at the Mechanical Engineering Department, University Malaya.

3.3.2 X-ray diffraction (XRD)

X-ray diffraction is used to obtain information about the structure, composition and the state of polycrystalline materials. The samples may be powders, solids, films or ribbons (Reidinger et al.,1988) Examples of a diffractogram of $LiNiVO_4$ which is a crystalline material is shown in Figure 3.6 (Subramania et al., 2006).

The XRD diffractogram is unique for every crystalline substance. The line position in the diffractogram depends on the unit cell size and the line intensity depends on the

type of atoms present and on the arrangement in the crystals (Whiston, 1987). Thus a sample can be confirmed from its unique powder pattern which can be obtained from the JCPDS powder diffraction file.

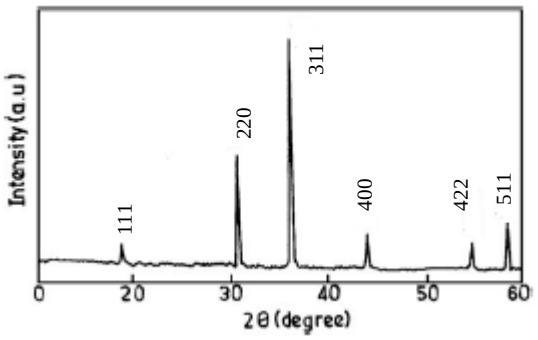

Figure 3.6. XRD pattern of $LiNiVO_4$ (Subramania et al., 2006).

In this work, the samples prepared were analyzed by the D-5000 diffractometer at the Physics department, University Malaya. The samples were scanned with a beam of monochromatic CuKα radiation of wavelength =1.5406 Å. The X-ray tube was operated at 40 kV and 20 mA. X-ray profiles were recorded for 2θ ranging from 10^o to 80^o where 2θ is the angle of diffraction. The diffraction patterns were taken at room temperature.

Diffraction would only occur if the Bragg equation was obeyed and a reflection would 'shoot out'. Thus the condition for X-Ray diffraction is,

$$2d \sin\theta = n\lambda \qquad (3.1)$$

where n is an integer (1, 2, 3 etc) indicating the order of diffraction called the order of reflection, λ is the wavelength of the reflected X-ray, d is the interplanar spacing, θ is the angle of reflection. Figure 3.7 below shows the Bragg condition (Whiston, 1987)

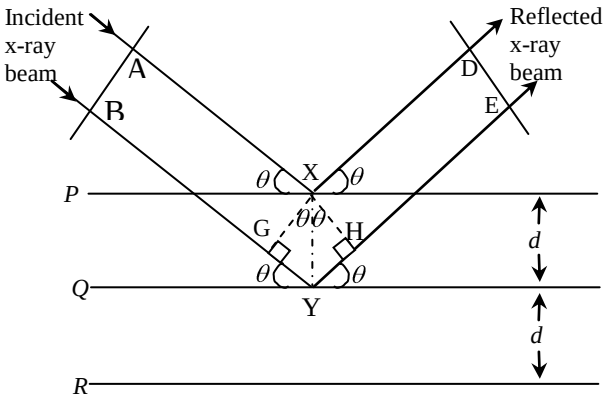

Figure 3.7. Diagram showing Bragg condition (Whiston, 1987).

3.3.3 Energy Dispersive X-rays Analysis (EDX)

Energy Dispersive Analysis of X-rays (EDAX) is a very powerful technique used in materials science. It gives useful analysis of elemental composition. Thus it can be used to determine the stoichiometry of the material It is a non-destructive technique. The analysis of the samples were carried out on the EDX LEICA S440 model instrument. Observations were made at selected areas of the samples and a fine beam of electrons was scanned across the surface of the selected area.

An electron bombarding the target may have sufficient energy to completely displace an electron from the innermost orbit of the target atom and produces an unstable ion. An electron from an outer shell could fill the vacant position. This transition is accompanied by the emission of a characteristic X-ray, a photon of definite wavelength.

The characteristic X-rays from the sample irradiated with a primary X-ray beam enter a cooled detector. It is necessary to cool the detector to liquid nitrogen temperature in order to reduce electronic noise and to ensure optimum resolution (Whiston, 1987).

3.3.4 Fourier Transform Infrared Spectroscopy (FTIR)

Infrared spectroscopy can be used to identify materials, determine the composition of mixtures and provide information useful in deducing molecular structure. Materials investigated can be solid, liquid or gaseous state. Furthermore, the frequencies of the absorption is possible to determine whether various chemical functional groups are present or absent in a chemical structure (Sibila et al., 1988).

Fourier transform infrared spectroscopy (FTIR), is the most advanced method of infrared spectroscopy. FT-IR spectrometers record the interaction of IR radiation with a sample, measuring the frequencies at which the sample absorbs the radiation and the intensities of the absorptions. For cross linked systems, which are brittle and can be ground to a fine powder, a KBr pellet or Nujol mull can be prepared. This technique has been used by many researchers (Salah et al., 2006; Burba et al., 2006; Suresh et al., 2005; Murali et al., 2000) to study the presence of various functional groups.

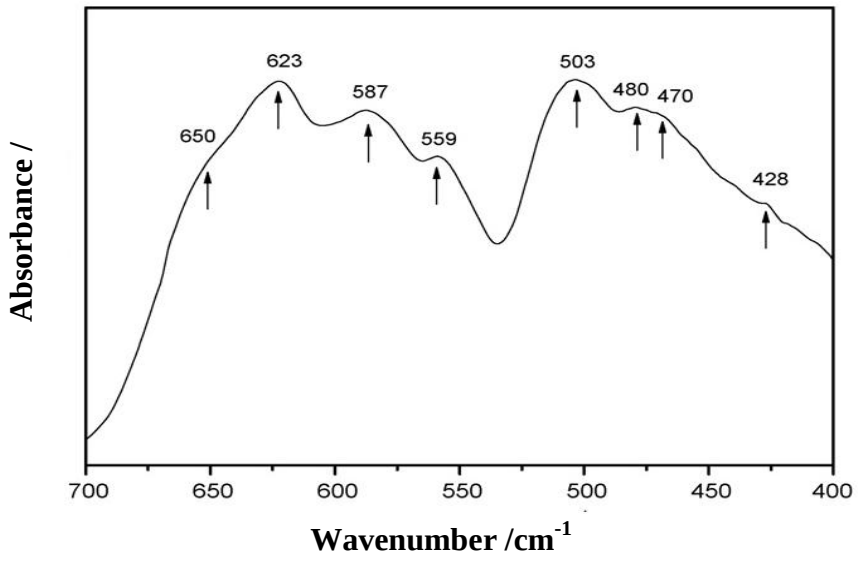

Figure 3.8. IR spectrum of the as-prepared $LiNi_{0.5}Mn_{1.5}O_4$ (Fang et al., 2007).

Figures 3.8 and 3.9 are two examples of IR spectrum exhibited by cathode materials. Fang et al. (2007) used this technique to examine the Ni ordering in $LiNi_{0.5}Mn_{1.5}O_4$. Characteristic infrared vibration bands of the M–O bonds of the sample between 700 cm^{-1} and 400 cm^{-1} were examined. As indicated by the IR spectrum in Figure 3.8, Fang et al. (2007) in their work obtained sample that showed two bands at 623 $cm^{-1}$and 480 cm^{-1} which are more intensive than those at 587 cm^{-1} and 470 cm^{-1}, respectively. In addition, two bands occurred at 650 cm^{-1} and 428 cm^{-1} which further proves a disordering distribution of Ni in the structure of $LiNi_{0.5}Mn_{1.5}O_4$. The above observations illustrate the usage of FTIR spectroscopy in identifying samples.

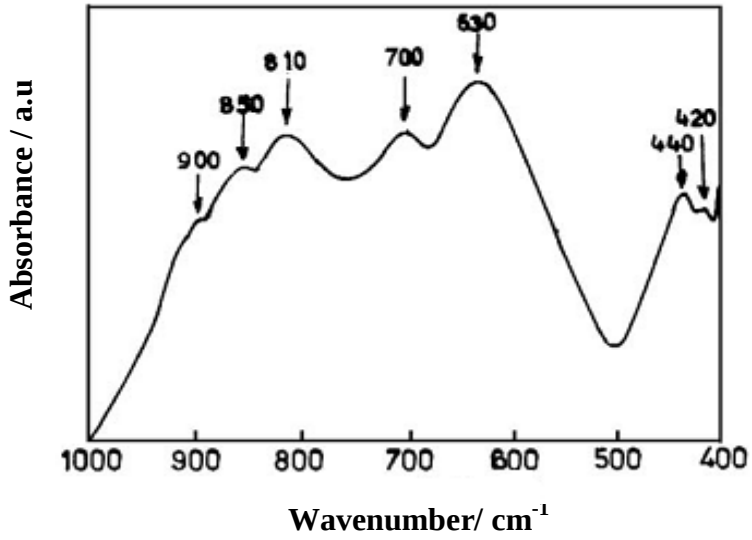

Figure 3.9. FTIR spectrum of $LiNiVO_4$ powder (Subramania et al., 2006).

Figure 3.9 shows another example of FTIR spectrum. The sample is $LiNiVO_4$ powder and the spectra obtained is recorded in the wave length range of 400–1000 cm^{-1}. The bands observed at 630, 700 and 810 cm^{-1} have been assigned to stretching vibrations of VO_4 tetrahedrons, and are found to be the characteristics vibrational bands of an inverse spinel structure (Subramania et al., 2006).Again, FTIR was used as a tool to determine the purity and identification of a sample.

When a sample is placed in a beam of infrared radiation, the sample will absorb radiation at frequencies corresponding to molecular vibrational frequencies, but will transmit all other frequencies. The frequencies of radiation absorbed are measured by an infrared spectrometer, and the resulting plot of absorbed energy versus frequency is called the infrared spectrum of the material. Analysis by infrared spectroscopy is based on the fact that molecules have specific frequencies of internal vibrations and thus different materials will have different vibrations and yield different infrared spectra. Furthermore, the presence or absence of various chemical groups in a chemical structure is possible to be determined by the frequencies of the absorptions. The IR spectra is normally taken in the infrared region of the electromagnetic spectrum in the wavenumber range from 4000 cm^{-1} to 400 cm^{-1}.

In this study the infrared absorption spectra of the cathode material prepared were recorded using the Perkin Elmer FTIR Spectrometer Spectrum 2000 at room temperature. The sample was mixed with KBr, ground to fine powders and pressed into translucent disk. All spectra were recorded in a range between 400 to 4000 cm^{-1}.

3.4 Preparation of cathode electrode

The cathode material for the test cells was prepared by grinding 25 mg of the active materials with 8 mg of mixed PTFE and acetylene black. The PTFE and acetylene black acted as a binder for the materials. The materials were ground using an agate mortar until homogeneous and a film is formed. The film was cast on a round shaped grid and pressed. All materials were transferred to the grid. The grid was heated in an oven for 200 ^{o}C for 4 to 5 hours to ensure that it is dry.

3.5 Fabrication of test cell

The test cell was made up of the fabricated cathode, a lithium metal foil anode and a separator containing the electrolyte. The fabricated cathode has a diameter of one centimetre. The separator containing the electrolyte was sandwiched between the fabricated cathode and lithium metal anode. The separator were cut into pieces which are bigger than the sizes of the anode and cathode as a precaution to avoid the contact between anode and cathode. The three layered materials was assembled in a cell holder. A schematic diagram of the cell assembled is shown in Figure 3.10. The separator was made from microporous polypropylene (pp) (Celgard 2400) and it was used to absorb and hold the non-aqueous electrolyte. The electrolyte solution used was 1M lithium hexafluorophosphate, $LiPF_6$ in a solvent mixture of ethylene carbonate (EC), propylene carbonate (PC) and dimethyl carbonate (DMC) (1:1:1 by volume). The assembling of the test cell took place in a glove box filled with pure argon.

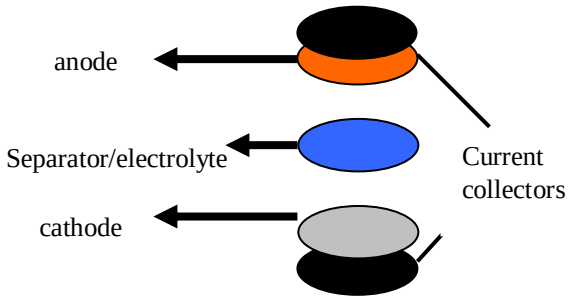

Figure 3.10. A schematic representation of the test cell.

3.6 Cyclic Voltammetry

Cyclic voltammetry (CV) is perhaps one of the more versatile analytical technique available to the electrochemist. The technique allows identification of reversible couples, study mechanisms and rates of oxidation-reduction processes and provide a

tool to help unravel complex electrochemical systems. Essentially the technique applies a linearly changing voltage to an electrode (Broadhead and Kuo, 1994). To obtain a cyclic voltammogram, the current at the working electrode in an unstirred solution was measured during the potential scan. The potential was ramped linearly to a more negative potential and then ramped in reverse, back to the starting voltage.

Consider a reversible reaction, $O + e^- \longrightarrow R$. For this reaction, during the negative scan where oxidized species are reduced to R, the depletion of O in the vicinity of the electrode is accompanied by an accumulation of R. The reduction continue until the applied potential becomes sufficiently positive to cause oxidation of the accumulated R. Oxidation of R is signaled by the appearance of anodic current, I_p^A. E_p^A is the anodic peak. The current increases as the potential moves increasingly positive until the oxidation of R depletes the region near the electrode of R to cause the current to peak and then to decrease. Thus the physical phenomena that caused a current peak during the oxidation cycle also caused a current peak during the reduction cycle. A typical, basic shape voltammogram is shown in Figure 3.11.

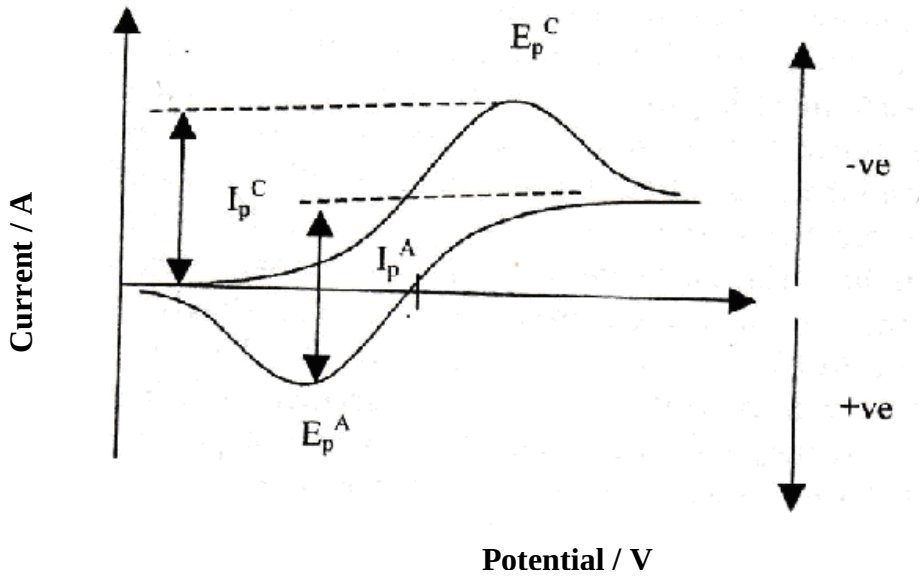

Figure 3.11. Cyclic voltammetry for a reversible process (Basirun, 2000).

For a reversible reaction, the diffusion equation can be solved under a linear voltage sweep condition to give a relationship between peak current, i_p and diffusion constant, D_{Li}^+, as shown in Equation 3.2 (Yu et al., 2007)

$$i_p = 0.4463F(F/RT)^{1/2} C_{Li}^{+} \upsilon^{1/2} A (D_{Li}^{+})^{1/2} \quad (3.2)$$

where

i_p = peak current (A)

F= Faraday's constant (96485 C/mol)

A = surface area of the electrode in cm^2

D_{Li}^+ = diffusion coefficient / $cm^2 s^{-1}$

υ = scan rate / V s^{-1}

C_{Li}^+ = concentration of lithium ion

R= universal gas constant (8.314 J/mol K)

T= absolute temperature (K)

Other parameters which characterize reversible proceses are (Yu et al., 2007):

1. The difference between the cathodic and anodic peak potentials is about 58 mV at 25°C.
2. The ratio of the cathodic to anodic peak currents is unity, i.e $i_{pa} / i_{pc} = 1$.
3. The peak current is proportional to the square root of the scan rate, based on a diffusion-controlled process.

Figure 3.12. Autolab PG STAT 30 instrument.

In this work, the CV experiments were done using Autolab PG STAT 30 instrument as shown in Figure 3.12. The fabricated cathode was used as the working electrode and Li-metal was used as the counter and the reference electrodes with a layer of separator to make the test cells. 1M $LiPF_6$ in equal volumes of Ethylene Carbonate (EC), Propylene Carbonate (PC) and Dimethyl carbonate was used as the electrolyte. Figure 3.10 shows a schematic diagram of the test cell. The cyclic voltammograms of the materials were recorded at different scan rates ranging from 0.1 mVs^{-1} to 50.0 mVs^{-1} in the potential range of 2.5 V to 5.5 V at room temperature.

3.7 Summary

The techniques used for preparing $LiMnPO_4$ and $LiNiPO_4$ and $LiFePO_4$ are presented in this chapter. Both $LiMnPO_4$ and $LiNiPO_4$ are prepared via the sol-gel techniques while the $LiFePO_4$ investigated was prepared via the chemical precipitation and low temperature sterilization method. This chapter also describes the experimental

techniques used to characterize the samples prepared such as TGA, XRD, FTIR and EDX. The electrochemical properties of the samples were evaluated by using cyclic voltammetry. The cathode material preparation and the fabrication of the test cell for cyclic voltammetry experiments are also presented in this chapter. Various properties of the cathode materials such as redox peaks, formal electrode potential and relationship between peak current and scan rates can be obtained from the cyclic voltammogram. The diffusion coefficient of the samples can be estimated by the Randles – Sevcik equation .

CHAPTER 4

RESULTS

LITHIUM MANGANESE PHOSPHATE

4.1 Introduction

Lithium manganese phosphate, $LiMnPO_4$ is one of the promising cathode materials for Li-ion batteries because of it's possibly lower cost and improved safety (Ritchie and Howard, 2006). In this work, the $LiMnPO_4$ was prepared by the sol-gel method assisted with tartaric acid. The prepared sample was then characterized by TGA, XRD, FTIR, EDX and cyclic voltammetry.

The TGA has been used to determine the firing temperatures of the samples and the thermogram was exploited to confirm the formation mechanism for the synthesis of $LiMnPO_4$. XRD analysis was performed to confirm the formation of $LiMnPO_4$ while FTIR was employed to study the vibrational modes. EDX techniques focuses on the compositional and elemental analysis of $LiMnPO_4$. The electrochemical reactions of the samples were investigated by cyclic voltammetry experiments. The results of the above analysis are presented in this chapter.

4.2 Thermogravimetric Analysis (TGA)

Thermogravimetric analysis was carried out to determine the firing temperature of the precursor. The thermograms obtained from the TGA experiments were analysed to investigate the weight loss and hence the thermal stability of sample prepared with increasing temperatures. TGA measurements were also carried out on the starting

materials i.e lithium hydroxide, manganese acetate and ammonium dihydrogen phosphate. The temperature range for this analysis was 30 ^{o}C to 1000 ^{o}C and was taken at 10 ^{o}C per minute. The thermograms of the salts which were used as reactants are depicted in Figures 4.1, 4.2 and 4.3. Figure 4.1 shows the thermogram of lithium hydroxide. The thermogram reveals that lithium hydroxide begins to decompose at 500 ^{o}C and decomposition is complete at 638 ^{o}C with lithium oxide (Li_2O) as the suggested decomposition product. The equation accompanying the decomposition process is

$$2\ LiOH.\ H_2O \longrightarrow Li_2O + 3H_2O \qquad (4.1)$$

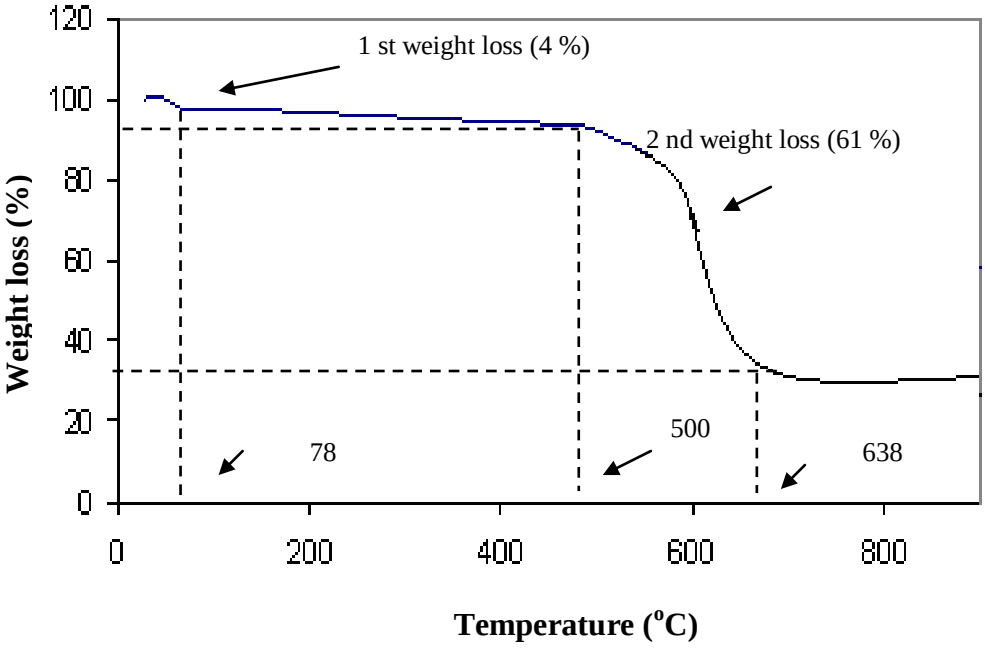

Figure 4.1. TGA thermogram of lithium hydroxide.

The thermogram of the ammonium dihydrogen phosphate salt is shown in Figure 4.2. The decomposition of ammonium dihydrogen phosphate begins at 187 ^{o}C and the decomposition is complete at 806 ^{o}C by the formation of phosphoric acid, ammonia

gas, water and oxides of phosphorous. The decomposition equation is as represented below,

$$3(NH_4)H_2PO_4 \longrightarrow P_2O_5 + 3H_2O + 3NH_3 + H_3PO_4 \quad (4.2)$$

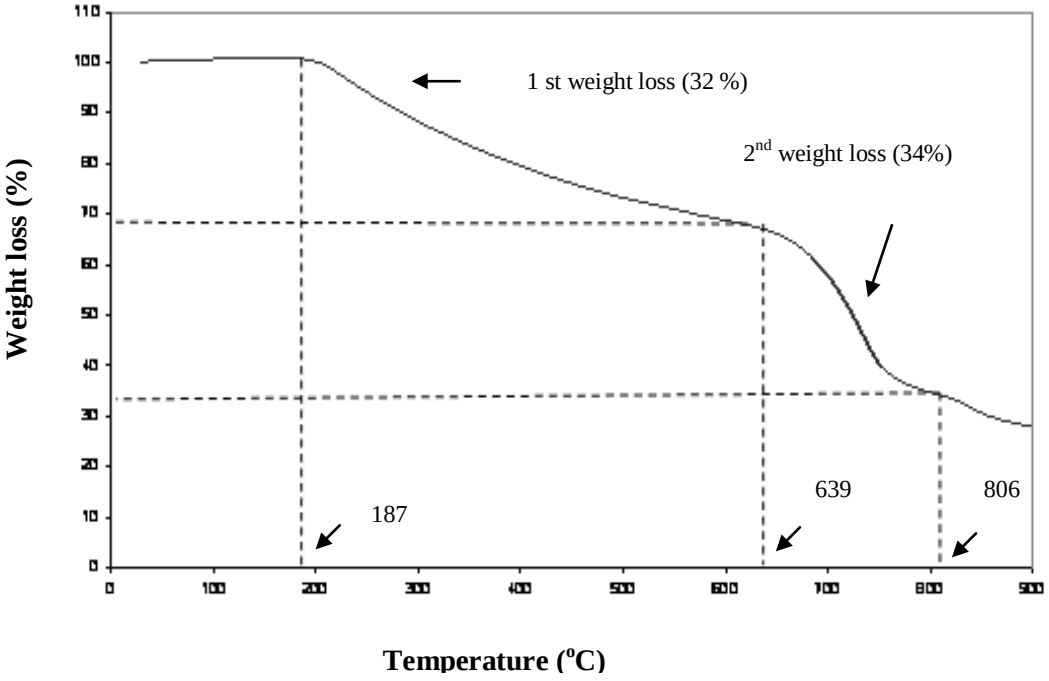

Figure 4.2. TGA thermogram of ammonium dihydrogen phosphate.

Two weight losses appeared in the thermogram of manganese acetate as shown in Figure 4.3. The first weight loss which range between room temperature to 150 ^oC is attributable to lost of water of crystallisation. Manganese acetate begins to decompose at 250 ^oC and decomposition is complete at 376 ^oC forming manganese dioxide (MnO_2) as the product. There is no more weight loss after 376 ^oC indicating that the material is stable above this temperature. The equation representing the decomposition process is:

$$Mn(CH_3COO)_2.4H_2O \longrightarrow MnO_2 + CO_2 + 3C + 4H_2O + 3H_2 \quad (4.3)$$

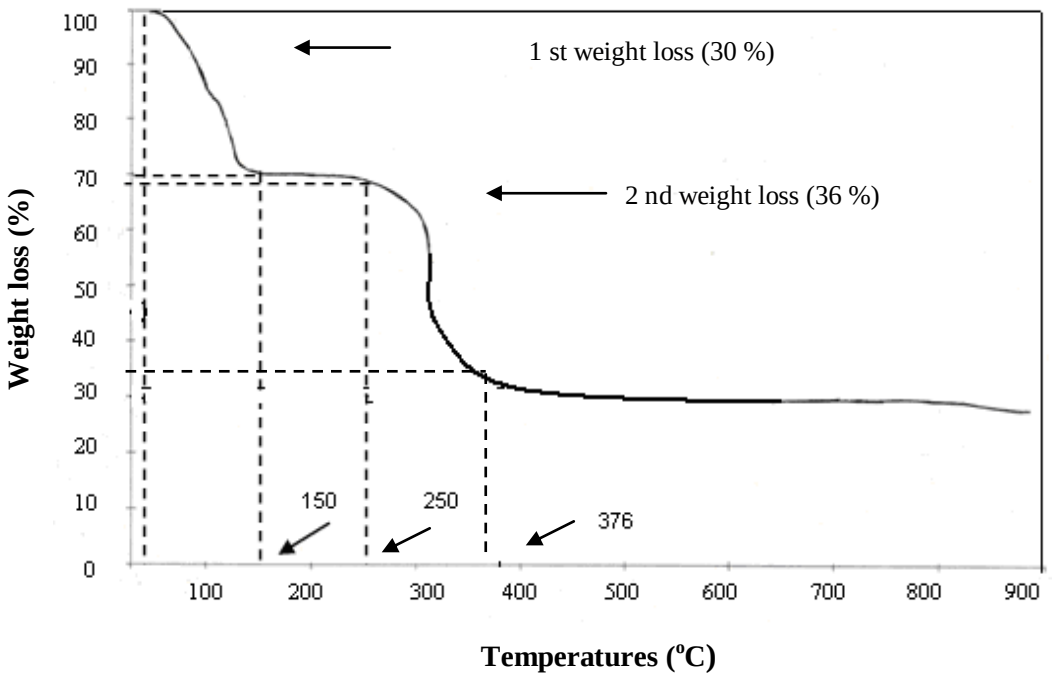

Figure 4.3. TGA thermogram of manganese acetate.

The thermogram of the tartaric acid which acts as the chelating agent in this work is shown in Figure 4.4. The tartaric acid decomposes almost completely at ~ 270 °C. The equation representing the decomposition process is:

$$C_4H_6O_6 \longrightarrow CO_2 + CO + 2C + 3H_2O \qquad (4.4)$$

Figure 4.5 shows the TGA and DTGA thermograms of the precursor of $LiMnPO_4$ (samp
TGA
the re
of an
proce
weigh
of lith
comp

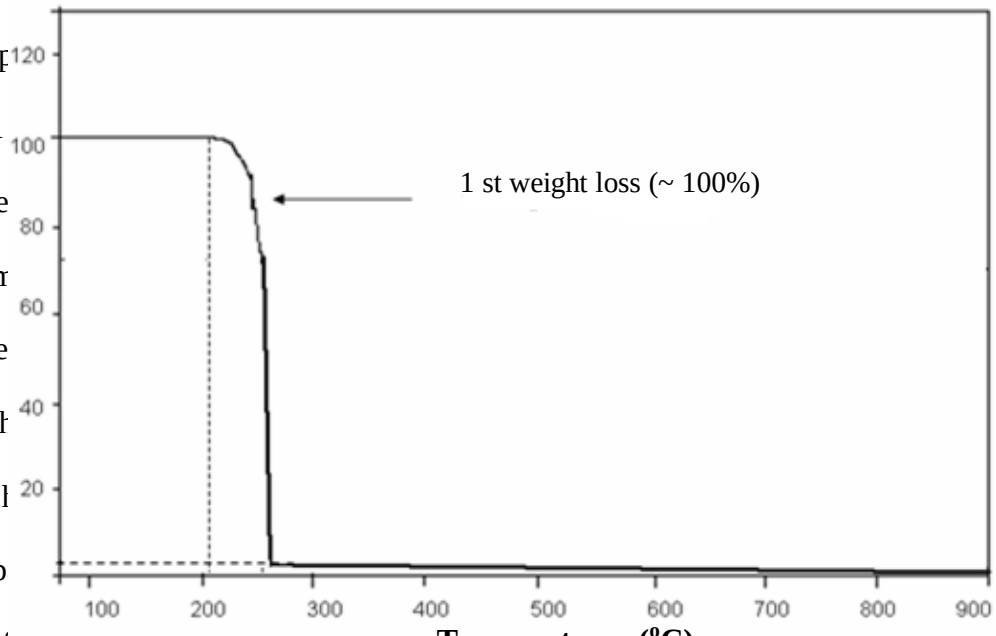

seen for manganese acetate and at around 350 °C for lithium hydroxide.

Weight loss (%)

4. TGA of tartaric acid

Figure 4.4. TGA thermograms of tartaric acid.

The small residue left as shown in Figure 4.4 is carbon.

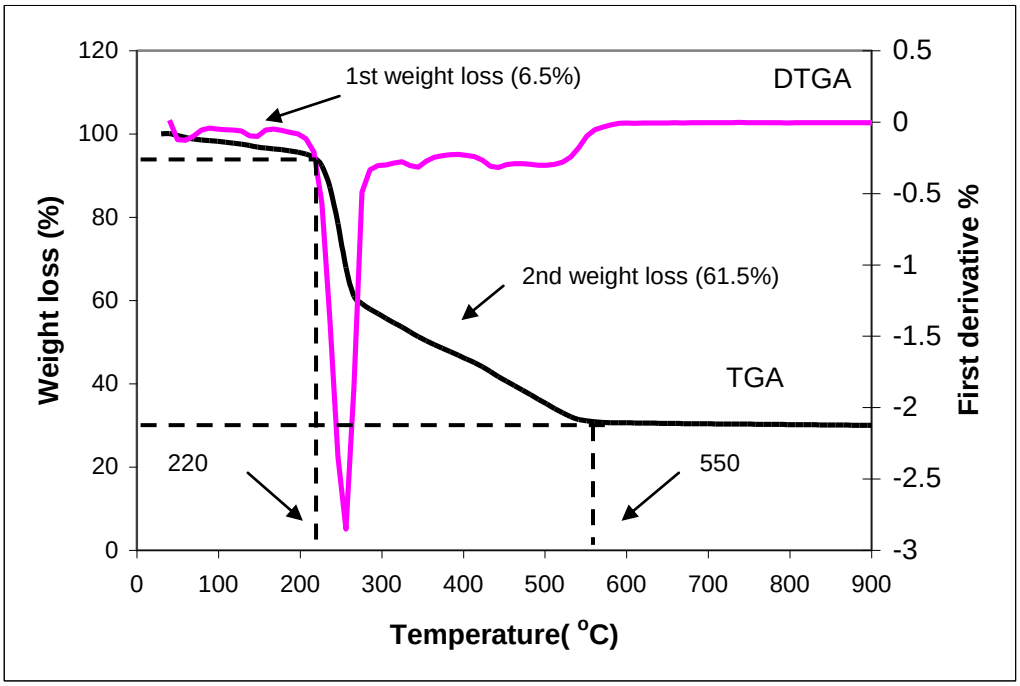

Figure 4.5. TGA and DTGA thermograms of lithium manganese phosphate precursor.

These decomposition processes are likely to be the reactions that are taking place between LiOH, MnOAc and ammonium hydrogen phosphate resulting in the formation of $LiMnPO_4$. There is no more weight loss at temperature above 550 ^{o}C

and no remarkable endothermic or exothermic peaks appeared in the DTGA curves. This indicates that the sample is thermally stable beyond 550 ^{o}C. Thus if the precursors were fired at temperatures beyond 550 ^{o}C, the final product expected is $LiMnPO_4$.

Two small endothermic peaks observed at about 61 ^{o}C and 140 ^{o}C as indicated in Figure 4.5 may be due to the loss of water of crystallization and water used as solvent in the synthesis. Also seen in Figure 4.5 is a huge endothermic reaction, which begins from 190 ^{o}C to 270 ^{o}C which is believed to be due to the decomposition of ammonium dihydrogen phosphate and tartaric acid. Oxidation-decomposition process may have taken place in this temperature range. Three small endothermic peaks are observed at 341 ^{o}C, 446 ^{o}C and 516 ^{o}C. These peaks are attributed to the decomposition of unreacted manganese acetate, unreacted lithium hydroxide and loss of oxygen. The thermal effects at temperatures higher than 500 ^{o}C can be attributed to the structural O-H evolution (Predonna et al., 2007) and $LiMnPO_4$ formation. From literature survey done by the author, TGA studies on formation mechanism of $LiMnPO_4$ has not been published. The suggested formation mechanisms of $LiMnPO_4$ are as shown below:

When tartaric acid ($C_4H_6O_6$) was added to the mixture, it is expected to react with $(NH_4)H_2PO_4$ and LiOH according to the following equations.

$$2((NH_4)H_2PO_4) + C_4H_6O_6 \longrightarrow H_3PO_4 + H_2PO_4^- + ((NH_4)_2C_4H_5O_6)^+ \quad (4.5)$$

$$LiOH + C_4H_6O_6 \longrightarrow Li\,C_4H_5O_6 + H_2O \quad (4.6)$$

LiOH also reacted with H_3PO_4 produced in equation (4.1) according to the following,

$$LiOH + H_3PO_4 \longrightarrow LiH_2PO_4 + H_2O \quad (4.7)$$

On heating,

$$2(Mn\,(CH_3COO)_2) + 2\,C_4H_6O_6 + 8O_2 \longrightarrow 2(Mn\,C_4H_4O_6) + 8CO_2 + 8H_2O \quad (4.8)$$

and

$$H_2PO_4^- + ((NH_4)_2C_4H_5O_6)^+ + C_4H_6O_6 + \frac{5}{2}O_2 \longrightarrow$$
$$((H_2PO_4)(NH_4)_2C_4H_5O_6) + 4CO_2 + 3\,H_2O \quad (4.9)$$

The overall reaction can be written as,

$$2(NH_4)H_2PO_4 + 2\,LiOH + 2(Mn(CH_3COO)_2) + 5C_4H_6O_6 + \frac{21}{2}O_2 \longrightarrow LiH_2PO_4$$
$$+ LiC_4H_5O_6 + ((H_2PO_4)(NH_4)_2C_4H_5O_6) + 2(Mn\,C_4H_4O_6) + 12CO_2 + 13H_2O \quad (4.10)$$

Equation (4.10) suggests that the dried gel precursor is composed of ,

$$Li((H_2PO_4)_2(NH_4)_2C_4H_5O_6)\;Li\,C_4H_5O_6 . (Mn\,C_4H_4O_6)_2$$

Therefore the overall proposed decomposition of the precursor in air atmosphere i.e. during firing is,

$$Li((H_2PO_4)_2(NH_4)_2C_4H_5O_6)\;Li\,C_4H_5O_6 . (Mn\,C_4H_4O_6)_2 + 10O_2 \longrightarrow$$
$$2LiMnPO_4 + 16CO_2 + 12H_2O + 2NH_3 \quad (4.11)$$

Based on Equation (4.11), the percentage weight loss is 67.0 % . The total weight loss of the decomposition process from the TGA curves is 68.0 % which agrees closely with the calculated values based on Equation (4.11) as shown in Table 4.1. The discrepancy may be due to absorbed water from the ambient.

Table 4.1. Calculation for percentage weight loss for equation 4.11.

$Li((H_2PO_4)_2(NH_4)_2C_4H_5O_6)\;Li\,C_4H_5O_6 . (Mn\,C_4H_4O_6)_2$ (precursor)				**$LiMnPO_4$**			
elements	Atomic mass	No of moles	Total mass of elements in formula (g)	elements	Atomic mass	No of moles	Total mass of elements in formula (g)
Li	6.9	2	13.8	Li	6.9	1	6.9
C	12	16	192	O	16	4	64
H	1	30	30	Mn	54.9	1	54.9

O	16	32	512	P	31	1	31
Mn	54.9	2	109.8				
P	31	2	62				
N	14	2	28				
Overall total mass			947.6				156.8 x 2 =313.6
% $LiMnPO_4$ formed after heating							33
% weight loss							67

4.3 X-Ray Diffraction (XRD)

In this work, the $LiMnPO_4$ prepared were fired at different temperatures. The samples are designated as A0 to A7 as shown in Table 4.2.

Table 4.2. The symbols designated to the samples fired at different temperatures.

Sample code	Firing Temperature(^oC)
A0	Precusor
A1	350
A2	450
A3	550
A4	650
A5	750
A6	850
A7	1000

The powdery precursors obtained were further heated for 15 hours at 350 ^oC, 450 ^oC, 550 ^oC, 650 ^oC, 750 ^oC, 850 ^oC and 1000 ^oC in a muffle furnace in air. The precursor was heated at 350 ^oC to determine if any impurities were formed at temperatures between 350 ^oC to 550 ^oC.

The XRD patterns of the fired powders were examined to obtain information on the phase of the sample and its crystallite size. The XRD patterns of the heated powder are presented in Figures 4.6 to Figure 4.13. The precursor (Figure 4.6) exhibit diffraction peaks which are not that of pure $LiMnPO_4$. The most intense peak is at $2\theta = 12^{0}$ and this peak is assigned to manganese acetate which is one of the starting materials. This can be confirmed from the XRD pattern shown in Figure 4.14.

On heating at 350 ^{o}C the peak disappeared indicating that the manganese acetate has decomposed. This agree with the TGA curve of manganese acetate (Figure 4.3) where there is a large weight loss after heating at 250 ^{o}C. It can be seen that even at temperature as low as 350 ^{o}C, the XRD peaks of the samples exhibit reflections that matches with the standard (JCPDS No:33-0803) for orthorhombic $LiMnPO_4$. However at 350 ^{o}C the peaks intensities are relatively low and broad indicating that the material is highly amorphous.

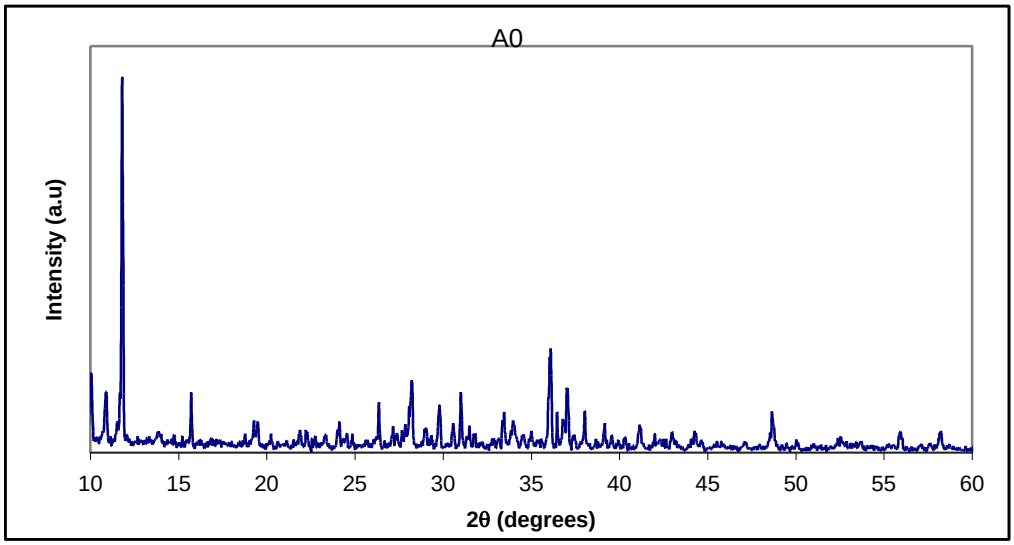

Figure 4.6. XRD diffractogram of A0 sample.

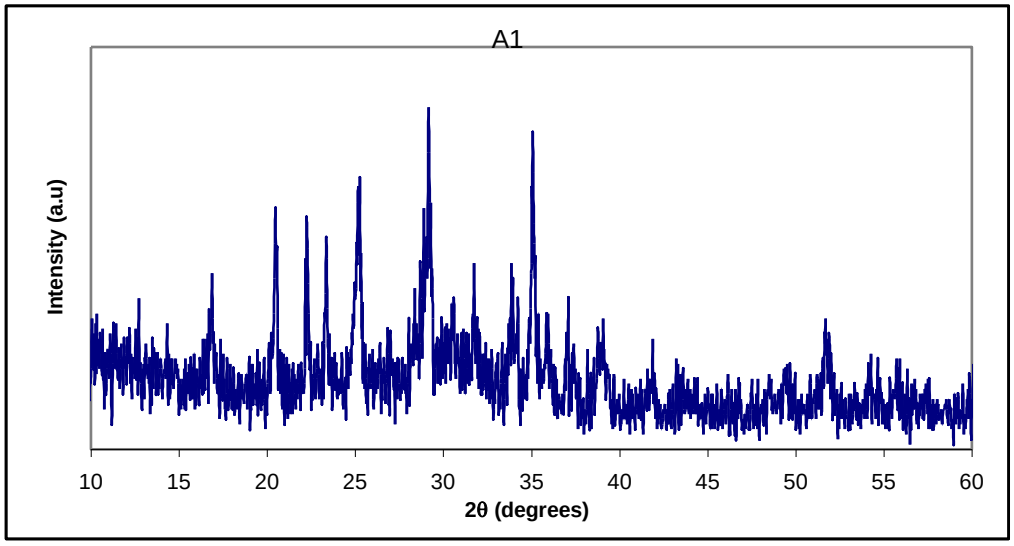

Figure 4.7. XRD diffractogram of A1 sample.

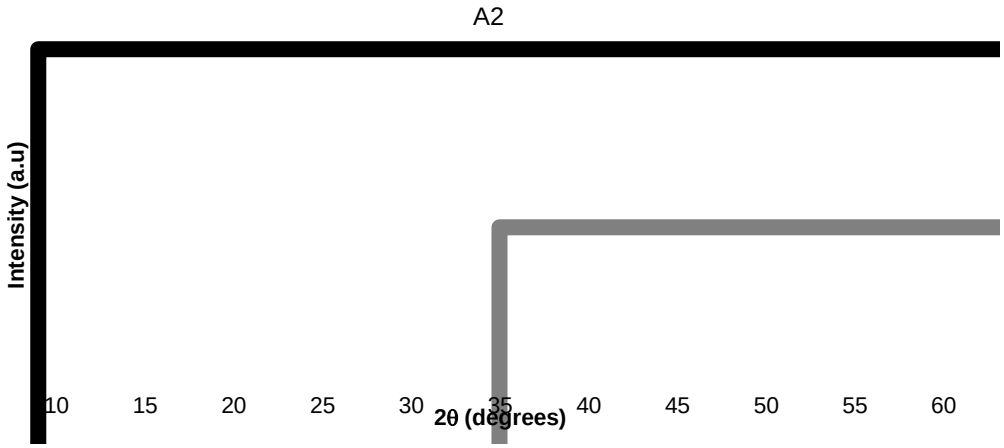

Figure 4.8. XRD diffractogram of A2 sample.

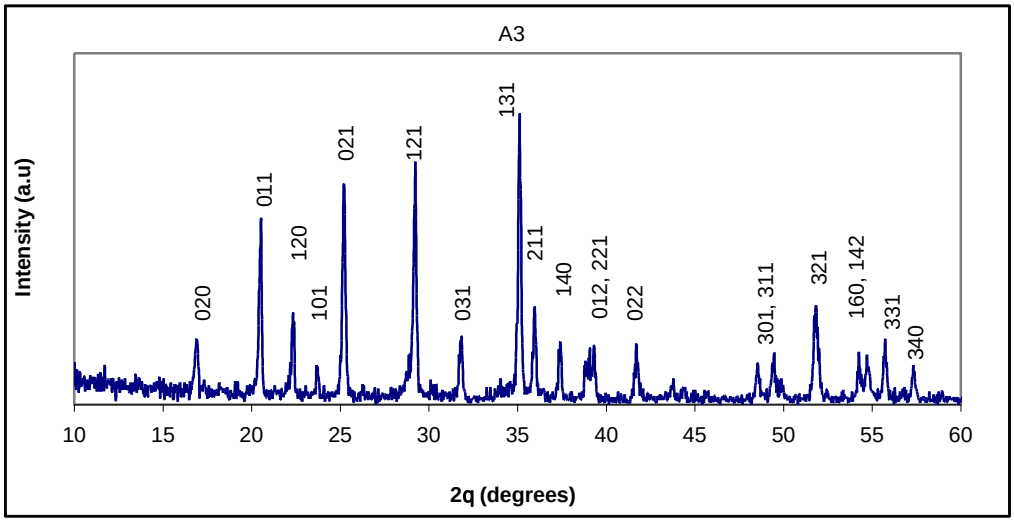

Figure 4.9. XRD diffractogram of A3 sample

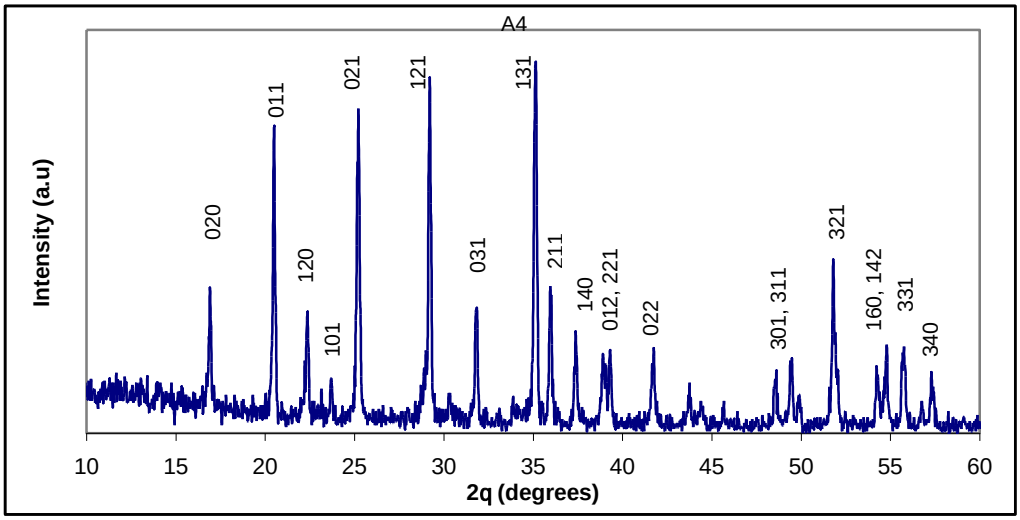

Figure 4.10. XRD diffractogram of A4 sample.

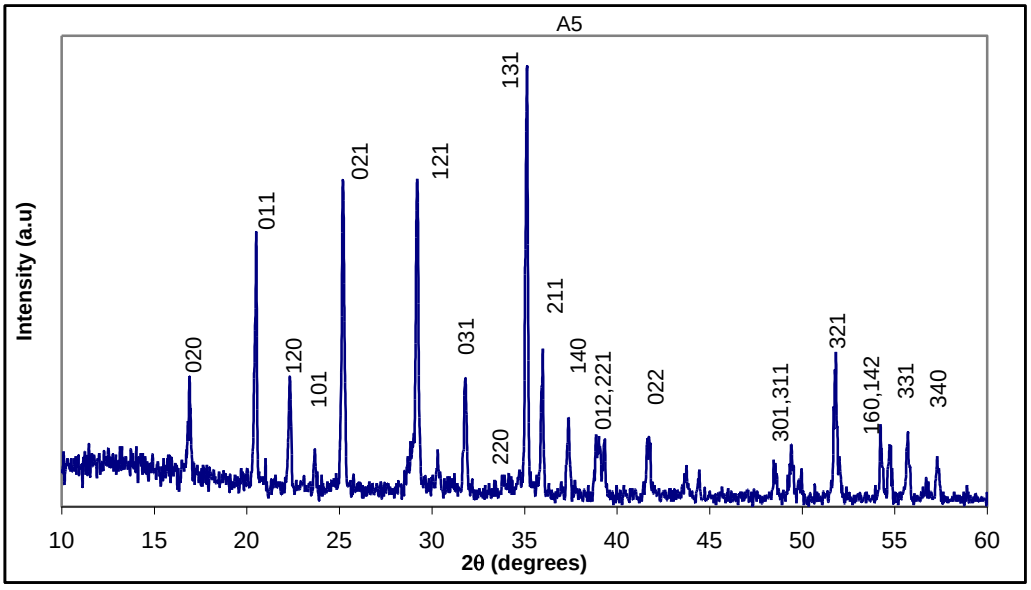

Figure 4.11. XRD diffractogram of A5 sample

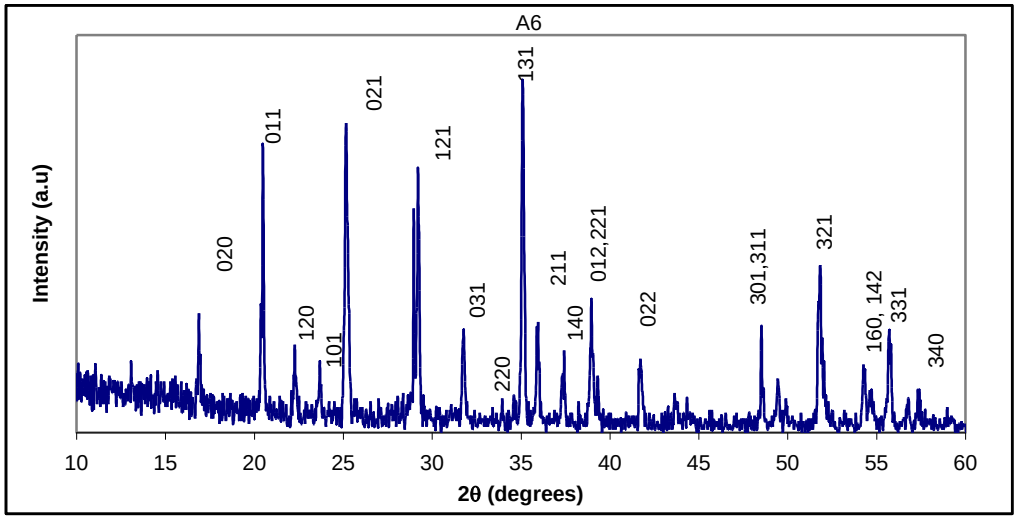

Figure 4.12. XRD diffractogram of A6 sample

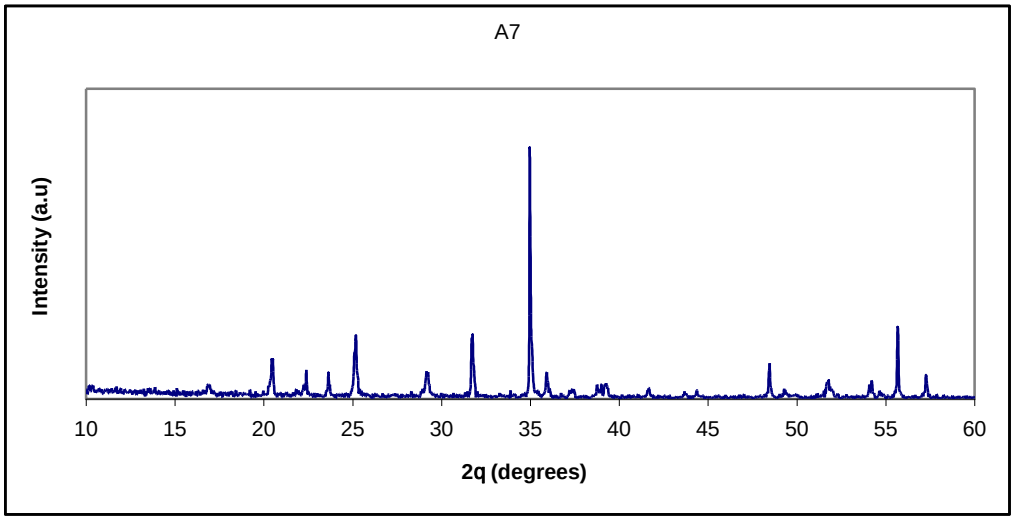

Figure 4.13. XRD diffractogram of A7 sample.

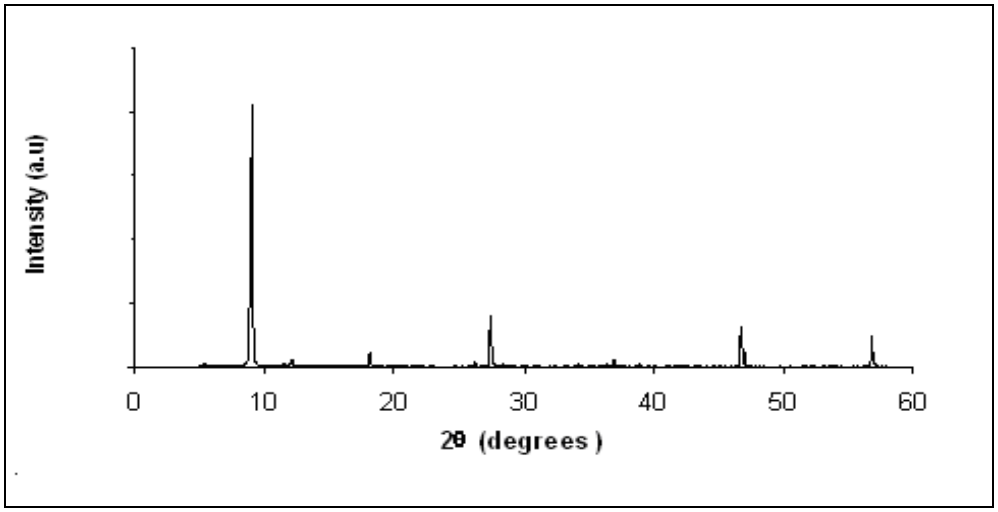

Figure 4.14. XRD diffractogram of Manganese acetate

As the firing temperature increases the intensities of the $LiMnPO_4$ peaks increases. All the seven XRD patterns are dominated by the (131), (121), (021) and (011) planes at around $2\theta = 35.2^0$, 29.2^o, 25.1^0 and 20.5^0 respectively. No impurities were detected for all samples heated at 350 ^oC to1000 ^oC and this suggests that pure crystalline $LiMnPO_4$ sample was successfully prepared. However the relative peak intensities of sample fired at 1000 ^oC decreases drastically as observed in Figure 4.13 and as shown in Table 4.3. The peaks mentioned above were also reported by Yonemura et al. (2004) who prepared $LiMnPO_4$ by the ball milling method followed by sintering at 600 ^oC for 6 hours under argon. Dominko et al.(2006) prepared $LiMnPO_4$ by firing

the precursor at 900 ^{o}C for 10 hours under argon. Ma and Qin (2005) prepared $LiMnPO_4$ by electrostatic spray deposition technique. The deposited sample was calcinated at 500 ^{o}C to 750 ^{o}C for 2 hours under pure argon. In this work calcinations or firing of precursor was done in air. The firing temperatures carried out in air agrees reasonably well with the TGA results in this work which showed complete formation of $LiMnPO_4$ at temperatures from 550 ^{o}C .

The diffraction angles (2θ) of these samples are listed in Table 4.3 and these are compared to the peaks in the JCPDS for $LiMnPO_4$ (33-0803) for 2θ angles 10 ^{o} to 60^{o}. Only the peaks for samples A3, A4, A5, A6 and A7 are listed. Samples A1 and and A2 are not listed since the peaks in these samples are relatively broad indicating the samples are not purely crystalline.

Table 4.3. XRD peaks for samples A3,A4,A5,A6,and A7 compared to the JCPDS values

EXPERIMENTAL VALUES										JCPDS (33-0803)		
A3 (550 ^{o}C)		A4 (650 ^{o}C)		A5 (750 ^{o}C)		A6 (850 ^{o}C)		A7 (1000 ^{o}C)				
2θ(^{o})	*%*	2θ(^{o})	*%*	2θ(^{o})	*%*	2θ(^{o})	*%*	2θ(^{o})	*%*	2θ(^{o})	*%*	hkl
35.123	100	35.124	100	35.113	100	35.095	100	34.979	100	***35.221***	***100***	131
29.224	83.8	29.208	95.7	29.195	75.3	29.235	75	29.200	10.8	***29.271***	***90***	121
25.201	76.3	25.191	87.5	25.208	74.9	25.164	87.9	25.162	25.3	***25.330***	***70***	021
20.499	63.6	20.506	82.6	20.491	62.9	20.476	81.5	20.469	15.7	***20.592***	***55***	011
16.905	22.7	16.889	39.7	16.911	29.7	16.891	33.9	16.912	5.8	***16.933***	***30***	020
35.981	33.8	35.957	39.7	35.970	36.3	35.951	31.5	35.925	10.8	***36.040***	***30***	211
51.803	34.3	51.852	38.6	51.807	35.5	51.779	42.7	51.751	6.6	***51.890***	***30***	321
22.344	31.3	22.344	32.6	22.315	29.7	22.286	25.0			***22.468***	***25***	120
31.806	23.2	31.813	33.7	31.808	29.3	31.771	29.0			***31.903***	***25***	031
37.404	21.7	37.400	27.2	37.372	20.5	37.384	16.9			***37.423***	***25***	140
39.297	20.2	41.733	22.8	39.314	15.4	39.316	16.1			***39.362***	***20***	012
61.157	22.2	61.130	20.7	61.176	17.8	61.184	20.2			***61.173***	***20***	113

39.050	19.2	39.170	13.0	38.933	13.9	39.316	16.1			***39.077***	***19***	221
54.739	17.2	54.752	19.6	54.273	18.9	54.310	17.7			***54.769***	***19***	160
55.722	22.7	55.743	23.4	55.699	17.0	55.737	29.0			***55.817***	***19***	331
60.600	17.2	60.646	17.4	60.594	15.4	60.583	21.0			***60.641***	***17***	312
41.720	20.7	43.737	13.6	41.710	15.8	41.708	21.0			***41.799***	***16***	022
54.263	18.2	54.291	15.8	54.733	14.3	54.310	17.7			***54.312***	***13***	142
-	-	-	-	33.876	7.3	34.629	10.5			***34.049***	***12***	220
57.332	13.6	57.330	16.3	57.315	11.6	57.370	12.1			***57.372***	***10***	340
23.716	13.1	23.720	14.7	23.680	13.1	23.693	20.2			***23.797***	***9***	101
48.542	14.1	48.585	16.8	48.553	10.0	48.555	29.8			***48.581***	***9***	301
49.448	17.7	49.446	20.1	49.440	14.3	49.464	15.3			***49.481***	***9***	311

The XRD studies show that the experimental patterns are consistent with the JCPDS implying that an orthorhombic olivine $LiMnPO_4$ structure was synthesized in this work. The peaks at $2\theta = 34^{o}$ with 12 % intensity in the JCPDS data may be too small in samples A3 and A4 such that it is not detected by the diffractometer.

4.3.1 Crystallite size

To obtain information about the crystallite size, the full width at half maximum (FWHM) of the (131) reflection plane was determined since the peak at $2\theta = 35^{o}$ has the highest intensity. The crystallite size (L) was estimated using the Scherrer equation below:

$$L = \frac{0.94\lambda}{\beta_r \cos\theta} \tag{4.12}$$

Here λ is the X-ray wavelength 1.5406 Å and $ß_r$ is the FWHM of the peak representing the (131) plane. A comparison between crystallite size (L) and firing temperatures is depicted in Figure 4.15. The plot in Figure 4.15 illustrates that the crystallite size of the $LiMnPO_4$ prepared by firing at temperatures from 350 ^{o}C to 1000 ^{o}C is between 31 to 46 nm. For comparison, average particle size of 79 nm was reported by Yonemura et al. (2004) using the conventional Scherrer equation. Average

crystalline size of 82 nm was reported by Piana et al. (2004) also calculated using the Scherrer equation.

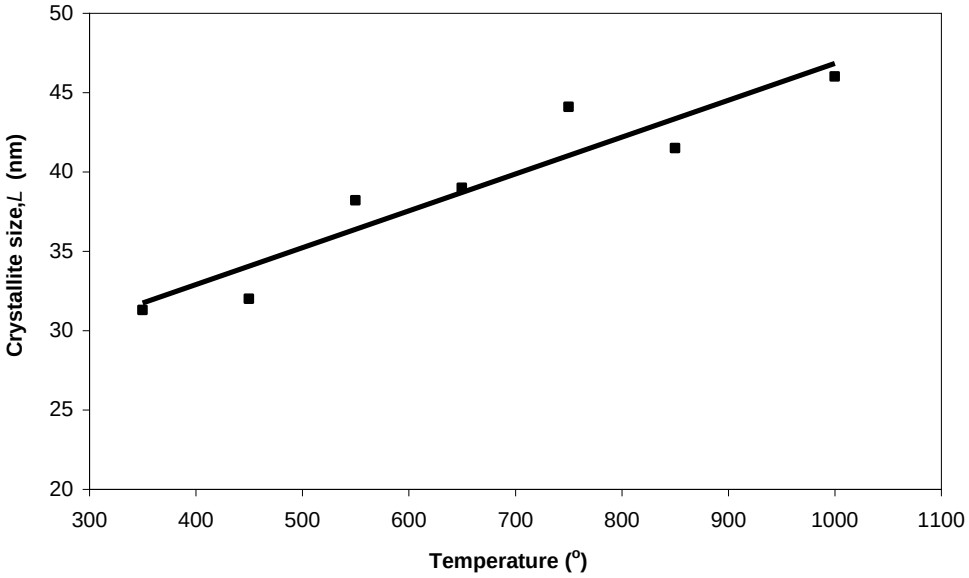

Figure 4.15. Variation of crystallite size, *L* and firing temperatures at 2θ = 35.2°.

The smaller crystallite size obtained in this work is due to the presence of the tartaric acid which limits particle growth and prohibits agglomeration since tartaric acid has only a short chain i.e four carbon atoms in its structure and the ring structure formed will be smaller when it act as a chelating agent. Thus producing smaller particles. This has been proven by calculating the crystallite size of sample A7, where even after firing at 1000 ^{o}C and 15 hours the crystallite size is still small.

4.4 Fourier Transform Infrared Spectroscopy (FTIR)

FTIR is a type of vibrational spectroscopic techniques and is a valuable analytical tool. The appearance or non–appearance of certain vibrational frequencies can provide important information on the structure of a particular molecule (Savitha et al., 2006). Thus the $LiMnPO_4$ samples prepared in this work were subjected to FTIR analysis to

study the effect of firing on the formation of the phosphate bonds. The samples were scanned at the resolution of 4.0 cm^{-1} in the transmittance mode.

Figure 4.16 represents the IR spectrum of the precursor. It can be observed that there are other absorption peaks in the spectrum besides the absorption peaks for the phosphate bond indicating the presence of impurities in the precursor. This observation agrees with the XRD pattern of the precursor where it exhibit peaks which are not that of pure $LiMnPO_4$. The peaks between 675 to 1000 cm^{-1} are attributed to the C-H bending modes while the C-O stretching mode can be related to the peaks appearing at 1130-1305 cm^{-1} (Predoana et al., 2007). The absorption peaks due to the phosphate bond exist in the range between 700 to 1200 cm^{-1} and between 450 to 700 cm^{-1} (Savitha, 2006, Salah, 2005, Julien, 2004) but are not well formed yet here in the precursor stage.

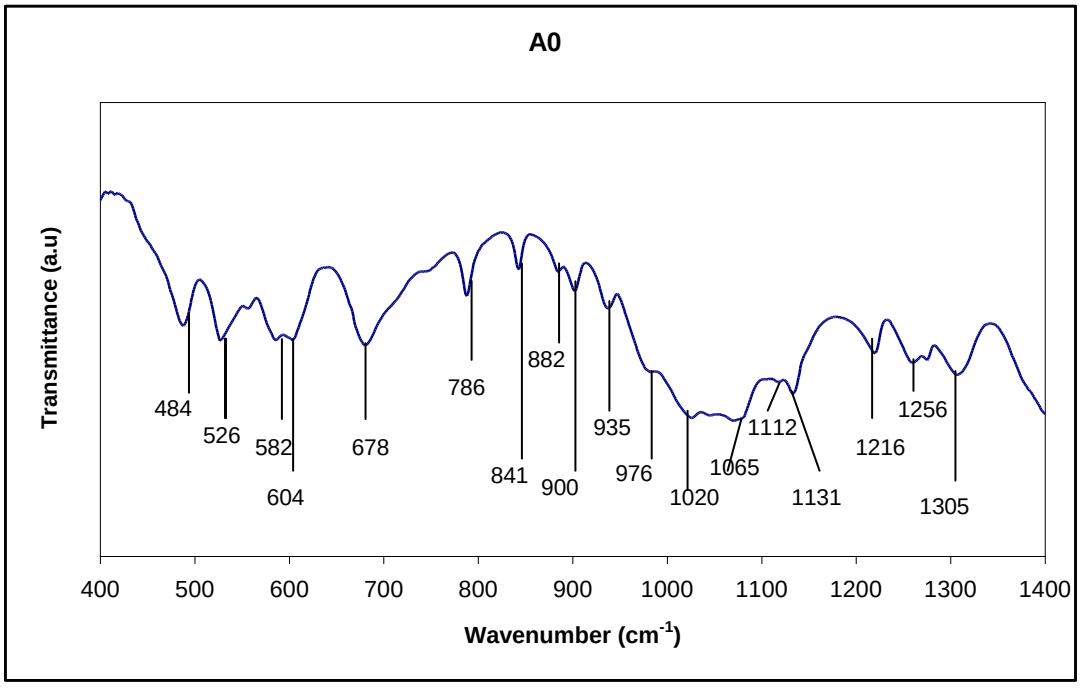

Figure 4.16. FTIR spectrum of lithium manganese phosphate precursor.

The FTIR spectrum of the samples fired at 350 ^oC (**A1**), 450 ^oC (**A2**), 550 ^oC (**A3**) and 650 ^oC (**A4**) in the wavenumber range 400-750 cm^{-1} are depicted in Figures 4.17

while the FTIR spectrum of the samples fired at 750 ^{o}C (**A5**), 850 ^{o}C (**A6**) and 1000 ^{o}C (**A7**) in the wavenumber range 400 to750 cm^{-1} are depicted in Figures 4.18. Figures 4.19 to 4.20 show the FTIR spectra of samples A1, A2, A3, A4, A5, A6 and A7 in the wavenumber range 800 to 1300 cm^{-1} . Figures 4.17 (a) shows that sample A1 has an extra peak at 670 cm^{-1} which is attributed to the C-H bending modes. This peak is also seen in Figure 4.16. The presence of this impurity in sample A1 indicates that a higher temperature is required to obtain a pure product.

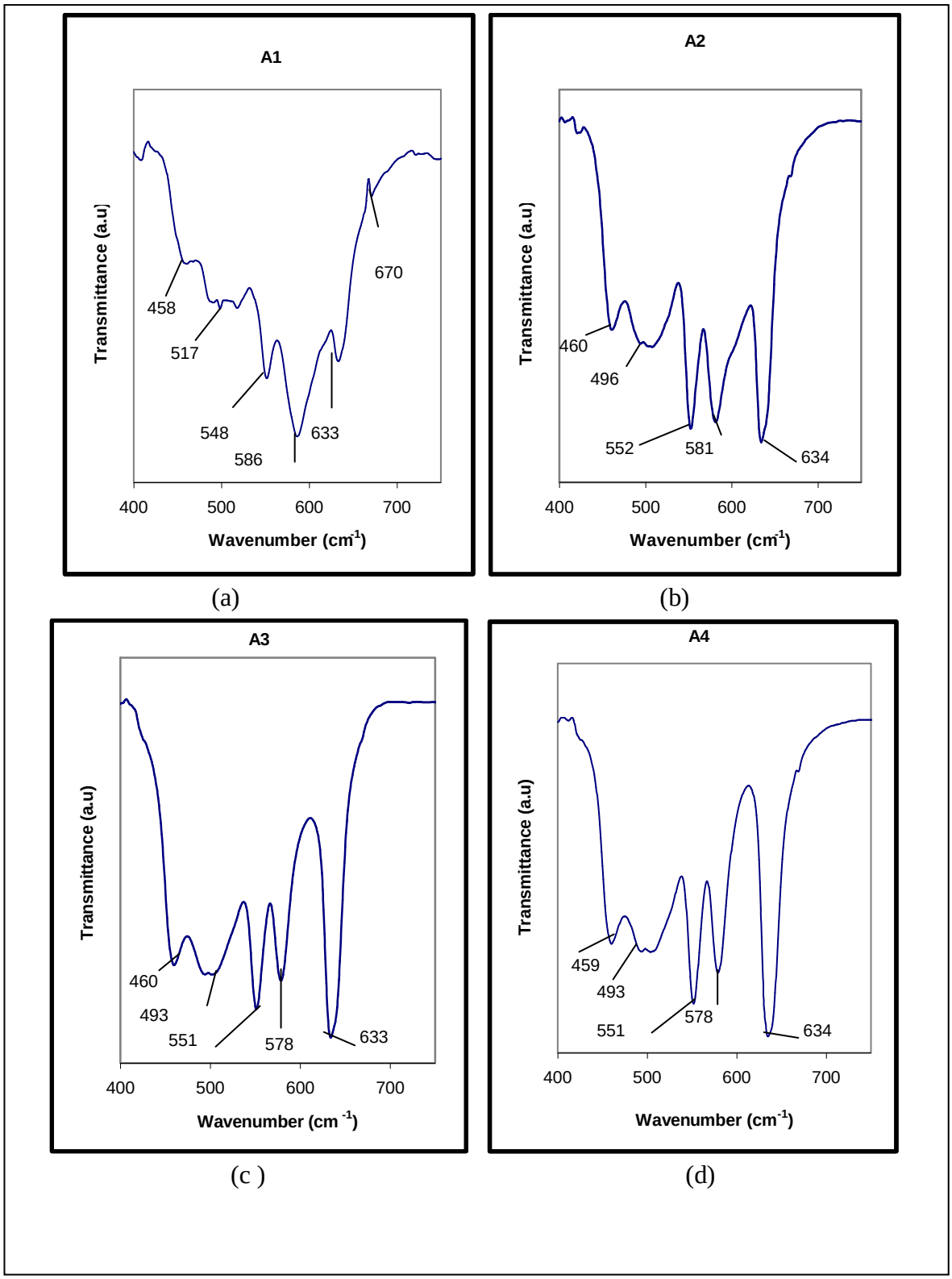

Figure 4.17. FTIR spectra of (a) sample A1 (b) sample A2 (c) sample A3 (d) sample A4 in the wavenumber 400 to 750 cm^{-1}.

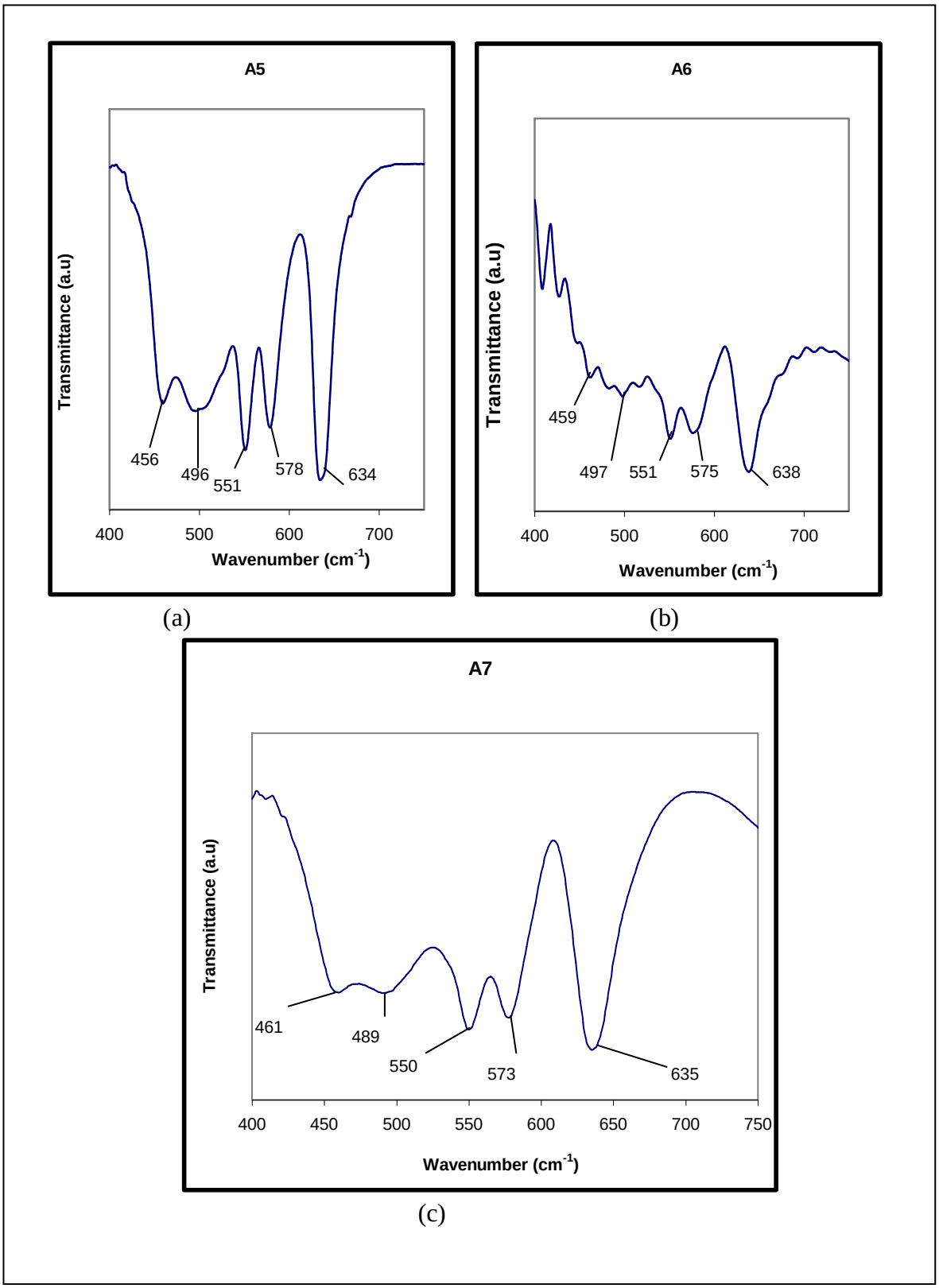

Figure 4.18. FTIR spectra of (a) sample A5 (b) sample A6 (c) sample A7 in the wavenumber 400 to 750 cm^{-1}.

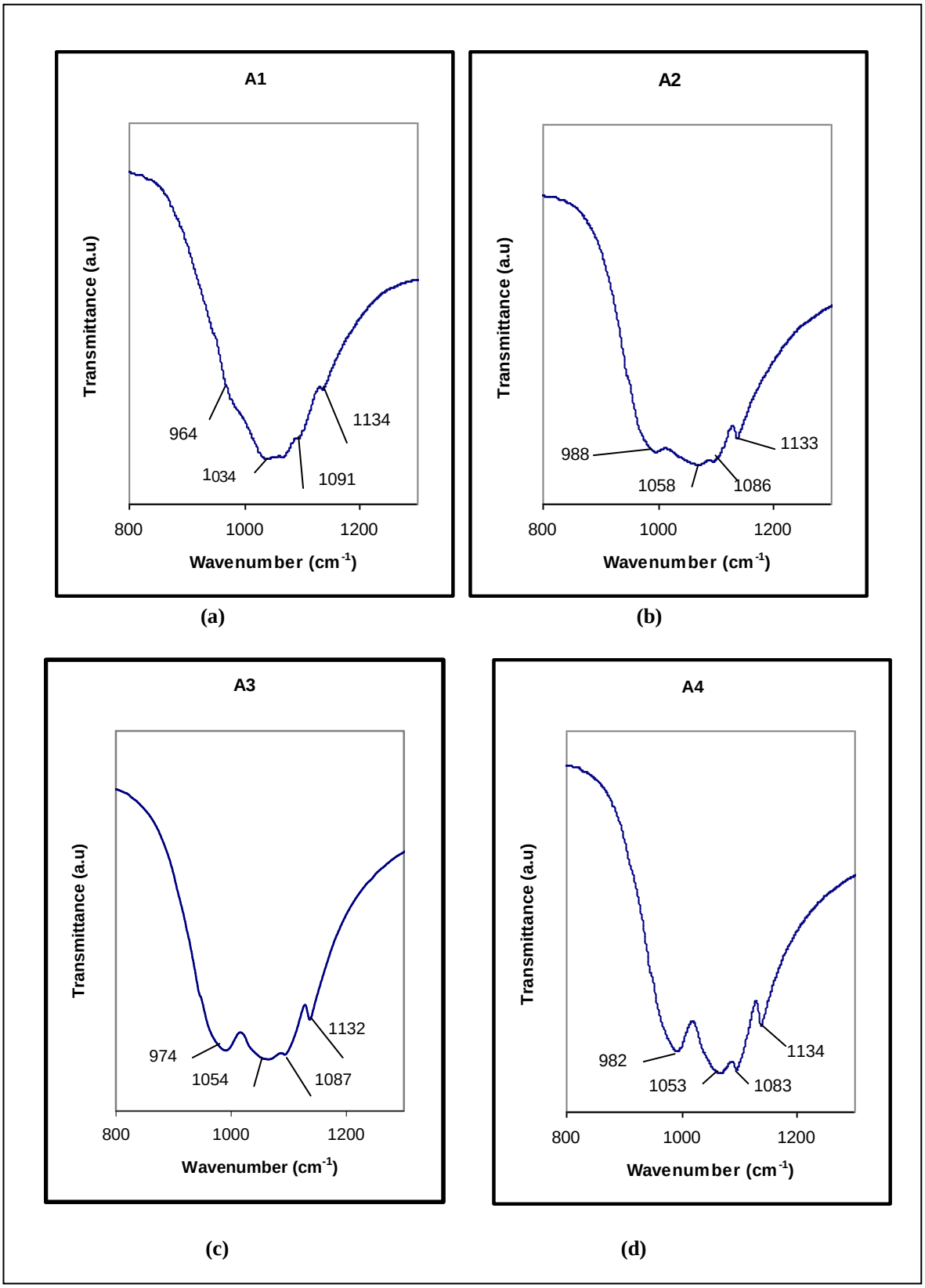

Figure 4.19. FTIR spectra of (a) sample A1 (b) sample A2 (c) sample A3 (d) sample A4 in the wavenumber 800 to 1300 cm^{-1}.

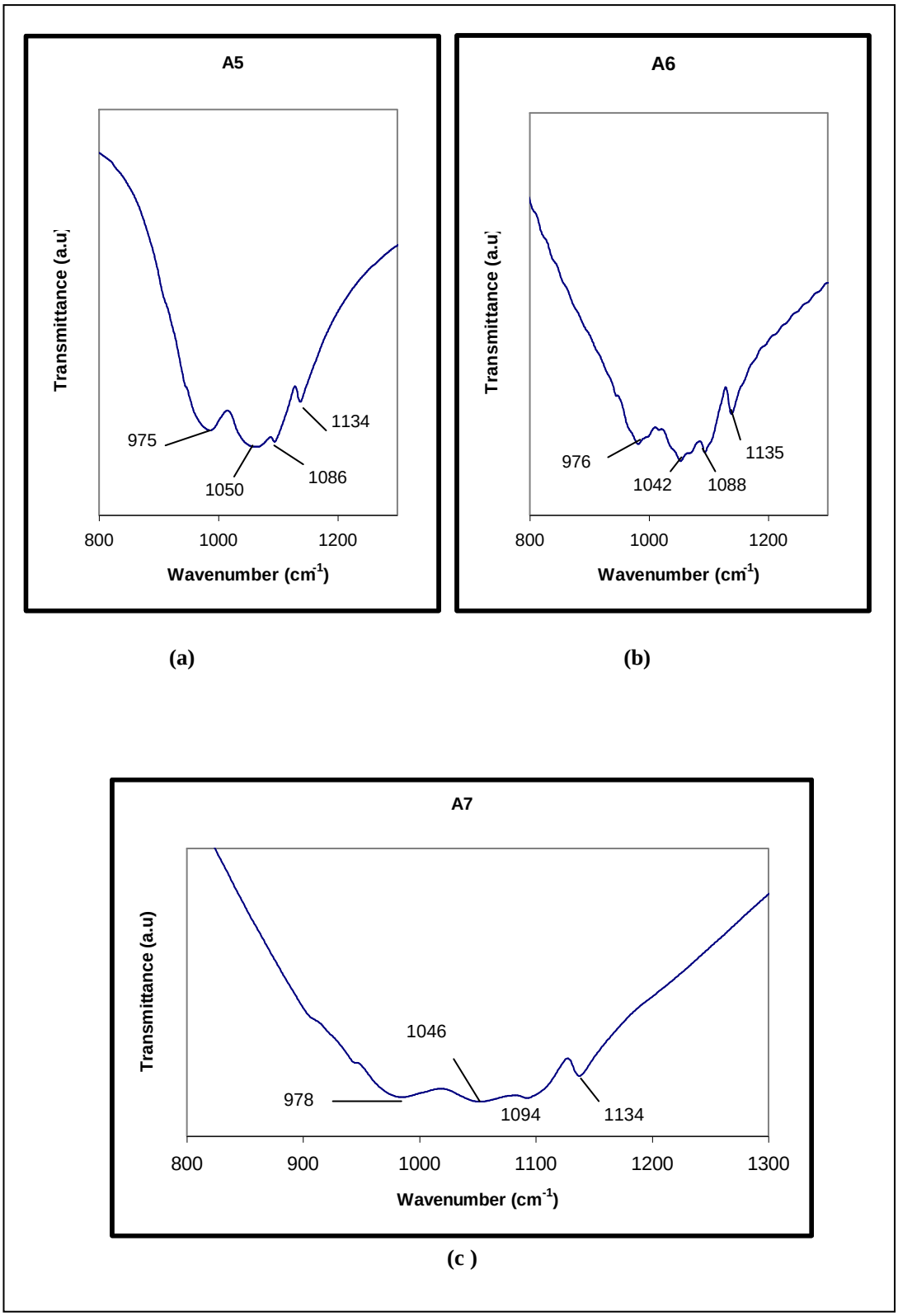

Figure 4.20. FTIR spectra of (a) sample A5 (b) sample A6 (c) sample A7 in the wavenumber 800 to 1300 cm^{-1}.

When the sample was fired at 450 ^{o}C the impurities peak is not detected anymore. Figures 4.19 to 4.20 illustrate spectrum which are dominated by intense peaks that range from 800 to 1400 cm^{-1} and while in figures 4.17 to 4.18 weaker bands between 700 and 450cm^{-1} are represented. Similar bands were observed for phosphate anions in the works of Burba and Frech (2007). The bands between 700 to 1400 cm^{-1} are assigned to the PO_4^{3-} intramolecular stretching modes (ν_1 and ν_3) whereas bands between 700 and 450 cm^{-1} region are assigned to intramolecular PO_4^{3-} bending vibrations (ν_4) (Burba and Frech, 2007).

Although all the characteristics bands for PO_4^{3-} vibrations were observed in Figures 4.17 to 4.20, their intensity differ. The FTIR spectrum shows that within the firing range of 350 ^{o}C to 750 ^{o}C the absorption peaks becomes more intense as the firing temperature increases as expected and this observation is in agreement with the XRD diffractograms analysis mentioned earlier . The absorption peaks become less intense for firing range of 850 ^{o}C to 1000 ^{o}C. This observation agree with the XRD diffractogram of sample A7 (Figure 4.13).

The FTIR spectrum observed in the present work is rather similar to the vibration bands of PO_4^{3-} anion engaged in an olivine structure i.e bands in the region 960-1200 cm^{-1} are assigned to ν_1 and ν_3 (Burba and Frech, 2006). In this work, the singlets ν_1 are observed at 974-1034cm^{-1}, while the triplets, ν_3 are observed in the regions 1033-1065 cm^{-1}, 1087-1091cm^{-1} and 1122-1134cm^{-1}. In addition, bands in the regions 550-700cm^{-1} (ν_4) and doublets in the regions 415-464 cm^{-1} which are attributed to ν_2 were also observed in Figures 4.17 and 4.18. These observations agree with the work previously reported in the literature (Burba and Frech, 2006; Julien al. 2004) indicating the presence of PO_4^{3-} ions in all samples prepared. All the characteristics

bands for PO_4^{3-} vibrations were observed in the expected regions in the FTIR spectrum of the samples in this study as shown in Table 4.4. In the following sections samples A6 and A7 will not be analysed since in sample A6 the order of intensity of the peaks is not according to the order in the JCPDS No 33-0803. As for sample A7 many peaks in the JCPDS No 33-0803 are missing in the XRD diffractogram.

Table 4.4. Wavenumbers and peaks assignment of FTIR bands of $LiMnPO_4$ samples fired at 350°C (A1),450°C (A2), 550°C A3), 650°C (A4),750°C (A5), 850°C (A6) and 1000°C (A7).

Samples/Experimental Values (cm^{-1})							Literature Values	Peak Assignment	References
A1	A2	A3	A4	A5	A6	A7			
984	988	974	982	975	976	978	υ_1 (singlet) =946cm^{-1}	symmetric stretching	Burba and Frech,2006
517 458	507 460	493 459	493 460	496 459	497 459	489 461	υ_2 (doublet) =415-464	symmetric PO bending	Burba and Frech, 2006
1065 1091 1134	1058 1086 1133	1049 1080 1121	1053 1083 1134	1050 1086 1134	1042 1088 1135	1046 1094 1134	υ_3 (triplet) = 1009-1085cm^{-1}	asymmetric stretching modes	Burba and Frech, 2006
633 586 548	634 581 552	633 578 551	634 579 551	634 578 551	638 575 551	635 573 550	υ_4(triplet) = 580-637cm^{-1}	asymmetric PO bending vibrations	Burba and Frech, 2006

4.4 Energy Dispersive X-rays Analysis (EDX)

The elemental composition of the prepared sample was analysed by EDX. The EDX spectrum for $LiMnPO_4$ fired at 550 °C, 650 °C and 750 °C fired for 15 hours are shown in Figures 4.21 to 4.23. The ratios of Mn:P was determined by this technique. Peaks attributable to manganese and phosphorous are clearly shown. The EDX spectrum indicates stoichiometries of the prepared samples. The analysis of the spectrum of the samples is presented in Table 4.5 .

For all three samples A3, A4 and A5 the total number of Li, Mn and P atoms is 5.43 $x10^{23}$. The atomic percentage of Li, Mn and P is 33%, 33% and 33% respectively. The total number of Mn and P atoms is 3.92 x 10^{23} atoms. The atomic percentage of Mn and P is 50% and 50% respectively which agrees with the results obtained from EDX. Hence the formula LiMnPOx can be assigned to the prepared sample. The starting Mn has configuration $[Ar]3d^5$ and the configuration of P is $1s^2 2s^2 2p^6 3s^2 3p^3$ .Hence it is expected that Mn and P in $LiMnPO_x$ to have oxidation state of +2 and +5 respectively. Lithium which belongs to group 1 is expected to have +1 oxidation state and oxidation state of oxygen is -2. Thus by conservation of charge, x in $LiMnPO_x$ must be 4 and the formula $LiMnPO_4$ is assigned to this sample. The comparison between the calculated and experimental results obtained from EDX is represented in Table 4.5. From these results it is shown that inert environment is not necessary to maintain the +2 oxidation state of Mn^{2+} and the starting Mn^{2+} electronic configuration $[Ar]3d^5$ does not change after firing the samples in air which agrees with the hypothesis given in Chapter 1..

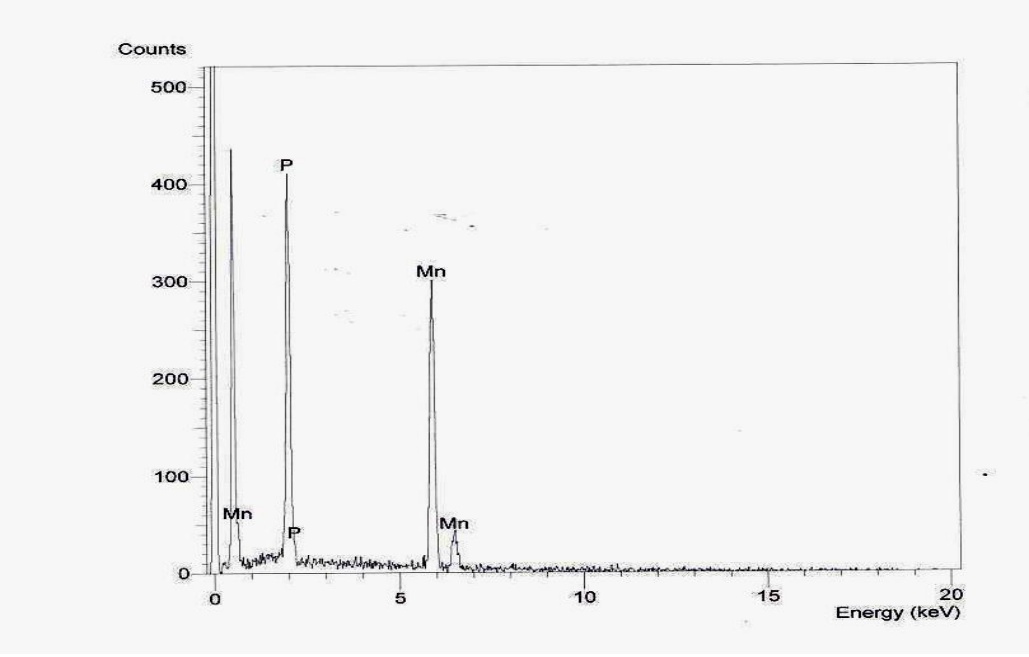

Figure 4.21 EDX spectrum of sample A3.

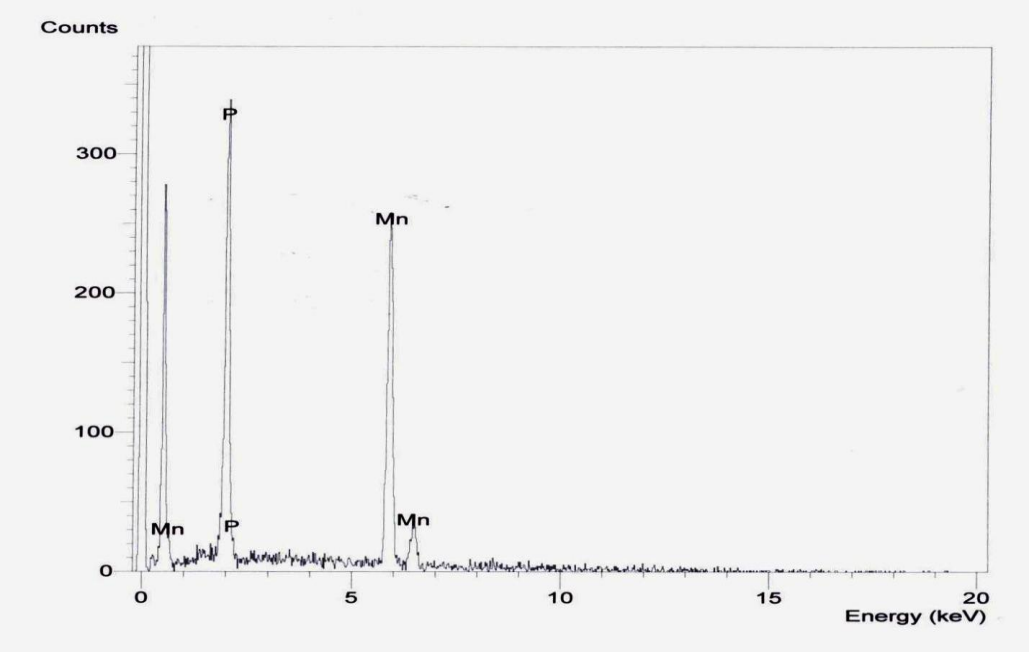

Figure 4.22. EDX spectrum of sample A4.

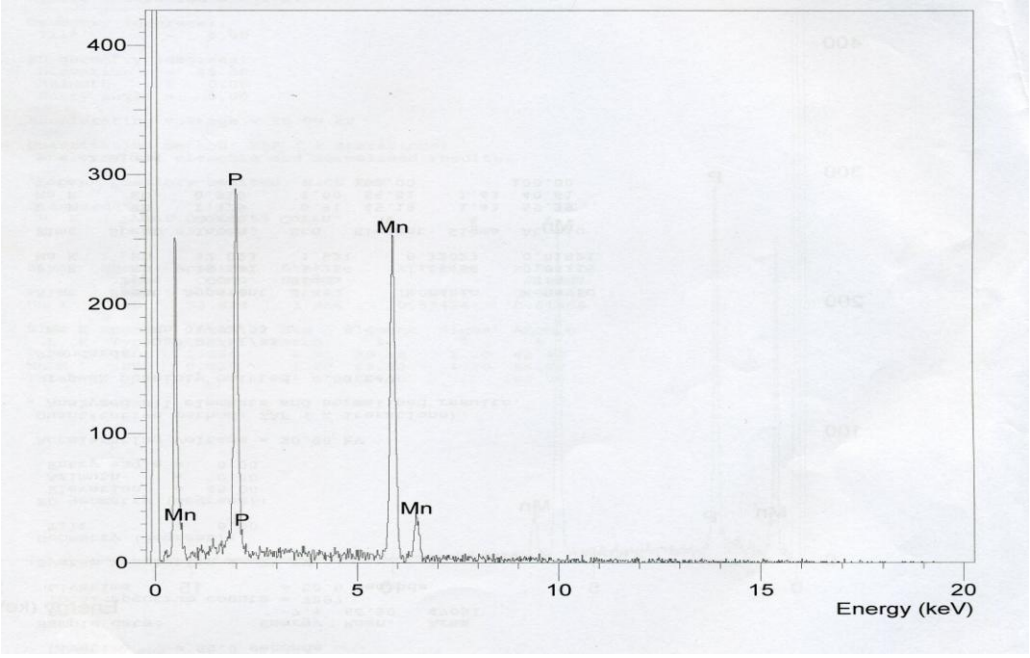

Figure 4.23. EDX spectrum of sample A5.

Table 4.5 Starting composition, Atomic % of elements and mole ratio between elements in lithium manganese phosphate.

Sample		Li	Mn	P
A3	Starting mass (g)	12.53	73.53	34.64
	No of moles	0.30	0.30	0.30
	No of atoms	1.8×10^{23}	1.8×10^{23}	1.8×10^{23}
	% expected	-	50	50
	% in EDX	-	52	48
	Mole ratio of the elements	1	1	1
A4	Starting mass(g)	12.53	73.53	34.64
	Mole	0.30	0.30	0.30
	No of atoms	1.8×10^{23}	1.8×10^{23}	1.8×10^{23}
	% expected	-	50	50
	% in EDX		49	51
	Mole ratio of the elements	1	1	1
A5	Starting mass(g)	12.53	73.53	34.64
	Mole	0.30	0.30	0.30
	No of atoms	1.8×10^{23}	1.8×10^{23}	1.8×10^{23}
	% expected	-	50	50
	% in EDX	-	56	44
	Mole ratio of the elements	1	1	1

4.6 Cyclic voltammetry

Cyclic voltammetry was used to evaluate the electrochemical performance of the prepared $LiMnPO_4$ samples. In cyclic voltammetry experiments, the electrode potential is swept linearly with a suitable scan rate over a certain potential range relative to a reference electrode. Cyclic voltammetry was carried out on samples A3, A4 and A5 at room temperature using Li as the reference and counter electrode. The working electrode was the $LiMnPO_4$ samples prepared by firing at 550 ^oC, 650 ^oC and 750 ^oC for 15 hours. The cyclic voltammograms (CV) for $LiMnPO_4$ /$LiPF_6$+EC+PC+DMC/Li cell cycled between 2.5 and 5.0 V versus Li^+/Li was recorded with scan rates at the range of 0.1 to 10 mVs^{-1}. The charge density, Q was also recorded. The characteristics of the CV curves demonstrated that lithium can reversibly intercalate and deintercalate into the $LiMnPO_4$ cathode material.

4.6.1 Redox behaviour

Figure 4.24 shows the cyclic voltammogram of the A3 sample taken at a scan rate of 0.1 mVs^{-1}. Overall there is increase in anodic current and a decrease in cathodic current. A small hump is observed at 4.41 V and 3.91 V, and is taken to be the anodic and cathodic peaks respectively. The presence of the anodic and cathodic peaks indicates a redox reaction is taking place in the cell and thus suggesting that intercalation and de-intercalation had occurred in the material .There is only one anodic and one cathodic peak indicating that the sample is stable and no other electroactive element is present. It is observed that the difference between the anodic peak and cathodic peak potentials, ΔE (E_{pa} - E_{pc}) is estimated to be 440 mV during a

$LiMnPO_4$/Li cell cycling. Ma and Qin (2005) observed a value of 300 mV for ΔE when working with $LiMnPO_4$ electrode.

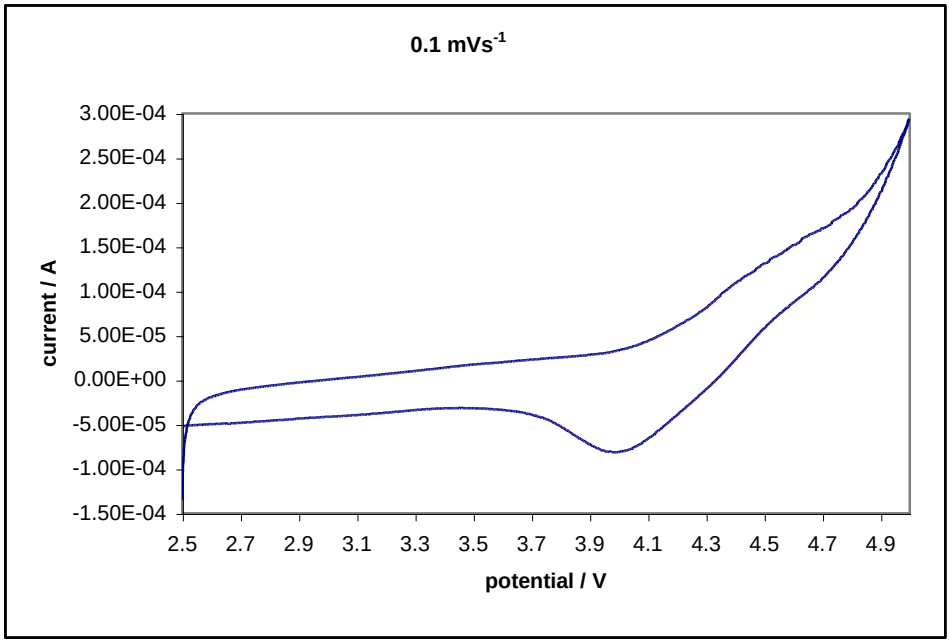

Figure 4.24. Cyclic voltammogram of A3 material at scan rate 0.1mVs^{-1}.

Figure 4.25 shows the cyclic voltammogram of sample A3 measured at 1 mVs^{-1}. At scan rate 1 mVs^{-1}, the anodic and cathodic peak was observed at 4.43 V and 3.92 V respectively. The potential difference ΔE between the two peaks is found to be 510 mV.

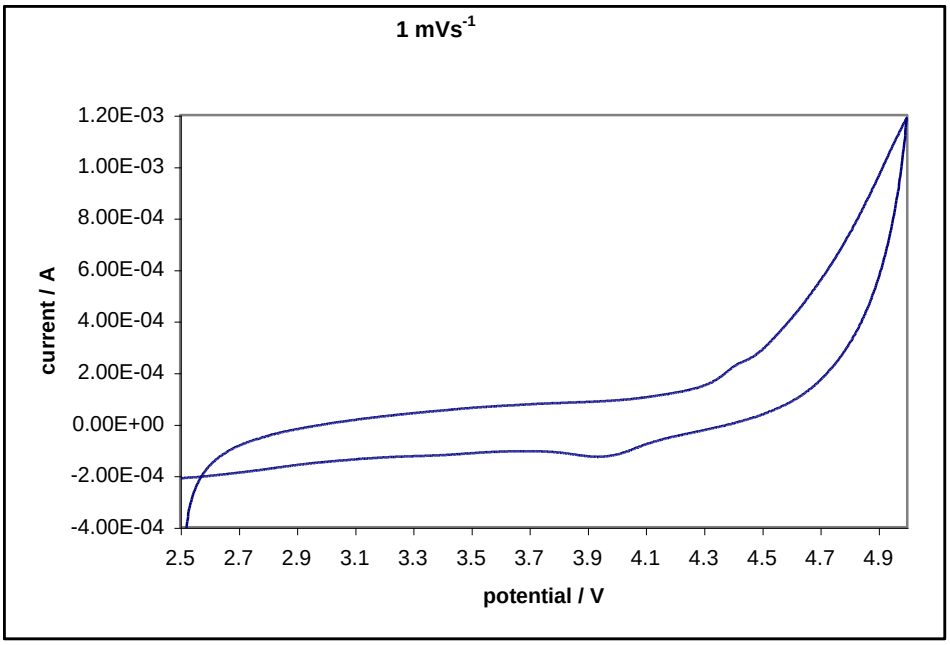

Figure 4.25. Cyclic voltammogram of A3 material at scan rate 1mVs^{-1}.

Figure 4.26 shows the cyclic voltammetry of $LiMnPO_4$ (A3) sample scanned at a rate of 10 mVs^{-1}. It is observed that the oxidation peak and the reduction peak is very small. This is expected as the Li^+ cannot completely extract/insert from/into the bulk during the time interval of a high rate scan.

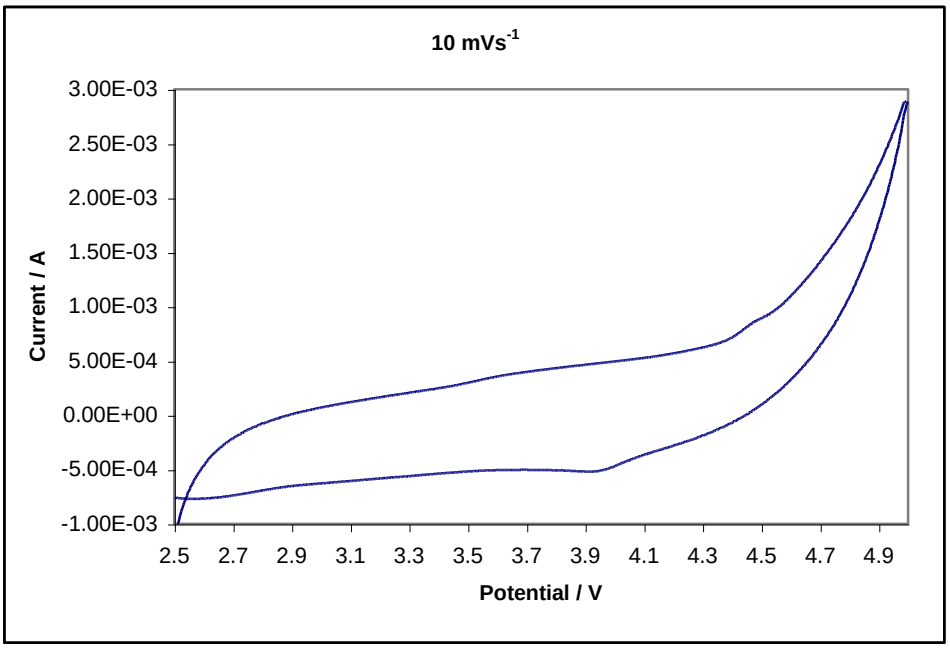

Figure 4.26. Cyclic voltammogram of A3 material at scan rate 10 ms^{-1}.

The potential difference ΔE (E_{pa} - E_{pc}) between the two peaks is found to be 550 mV. This observation shows that potential difference between two peaks increases as scan rate increases. This pattern was also observed by Mi et al. (2007) .

Cyclic voltammetry measurements was also performed on sample A4, $LiMnPO_4$ electrodes using a scan rate of 0.1 mVs^{-1},1.0 mVs^{-1} and 10 mVs^{-1}. Oxidation and reduction peaks were seen in the cyclic voltammograms of all three scan rates. Figure 4.27 shows the cyclic voltamogram of scan rate 0.1 mVs^{-1}.

During the anodic sweep, lithium ions are extracted from the $LiMnPO_4$ structure. An oxidation peak is located at 4.41 V versus Li^+/Li. When the potential was scanned from 2.5 to 5.0 V, a reduction peak occurred at 3.97 V corresponding to lithium insertion into the $LiMnPO_4$ structure.

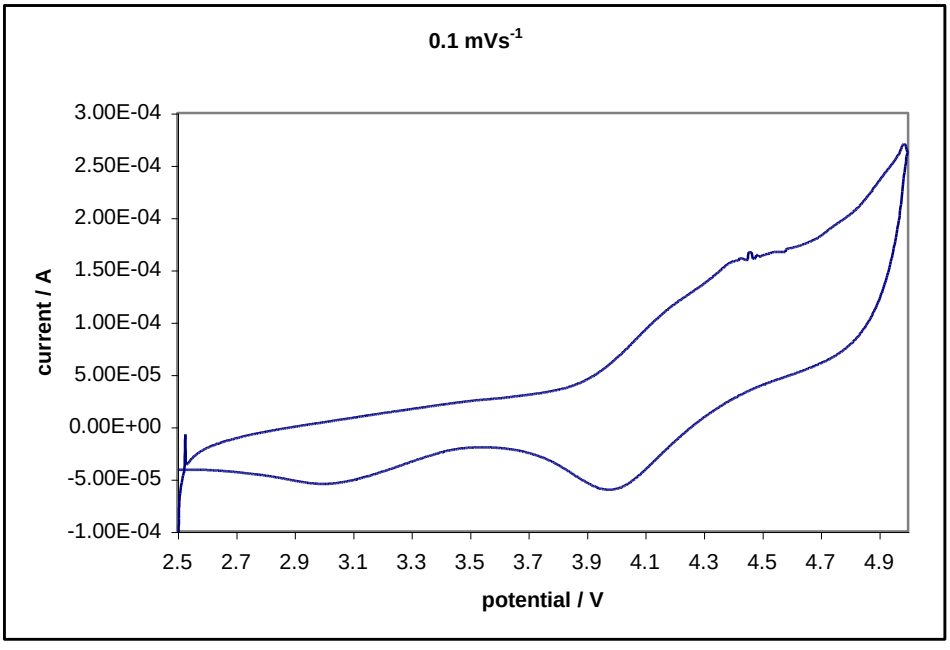

Figure 4.27. Cyclic voltammogram of A4 material at scan rate 0.1mVs^{-1}.

The cyclic voltamogram of scan rate 1.0 mVs^{-1} has oxidation peak located at 4.43 V and a reduction peak at 3.97 V (Figure 4.28). The oxidation and reduction peaks indicate the Li-ion intercalation and deintercalation. There was only a small reduction loop at 3.93 V in the curve shown in Figure 4.29 when the material was scanned at 10 mVs^{-1} scan rate. The oxidation peak is seen at 4.49 V.

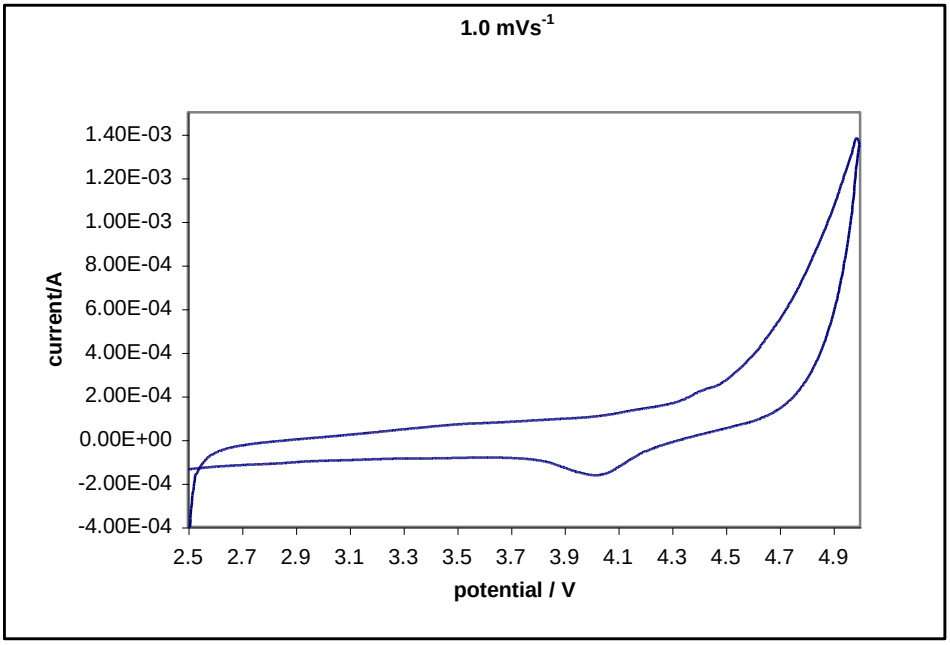

Figure 4.28 Cyclic voltammogram of A4 material at scan rate 1mVs^{-1}.

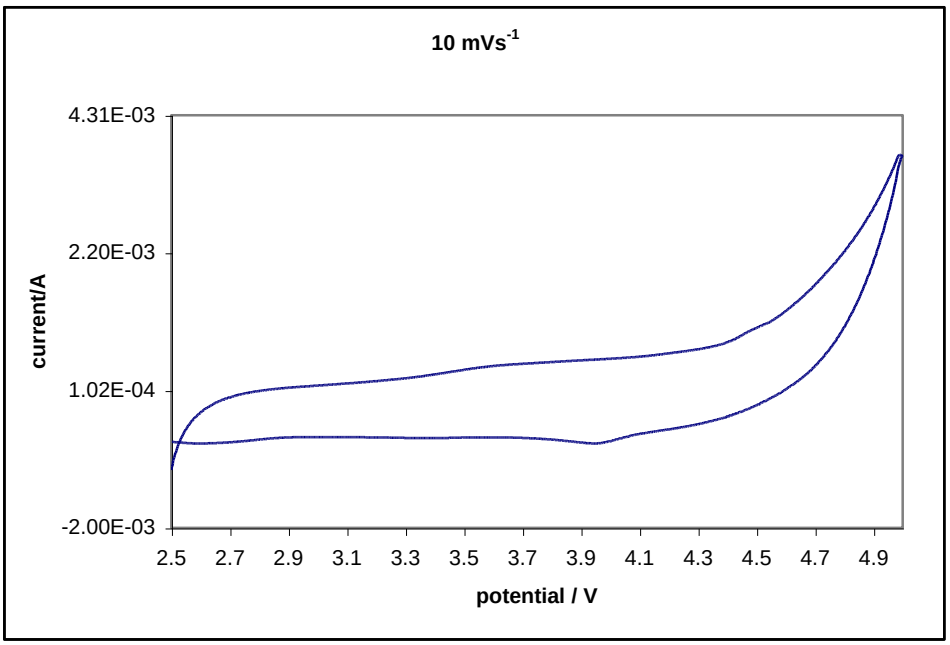

Figure4.29. Cyclic voltammogram of A4 material at scan rate10 mVs^{-1}

The cyclic voltamogram of the $LiMnPO_4$ (A5) scanned at a rate of 1.0 mVs^{-1} has oxidation peak located at 4.42 V and a reduction peak at 3.94 V as shown in Figure 4.30. The oxidation and reduction peaks indicates the lithium ion intercalation and deintercalation. A reduction loop at 3.94 V and an oxidation at 4.49 V was seen in the curve shown in Figure 4.31 when the material was scanned at 10 mVs^{-1} scan rate.

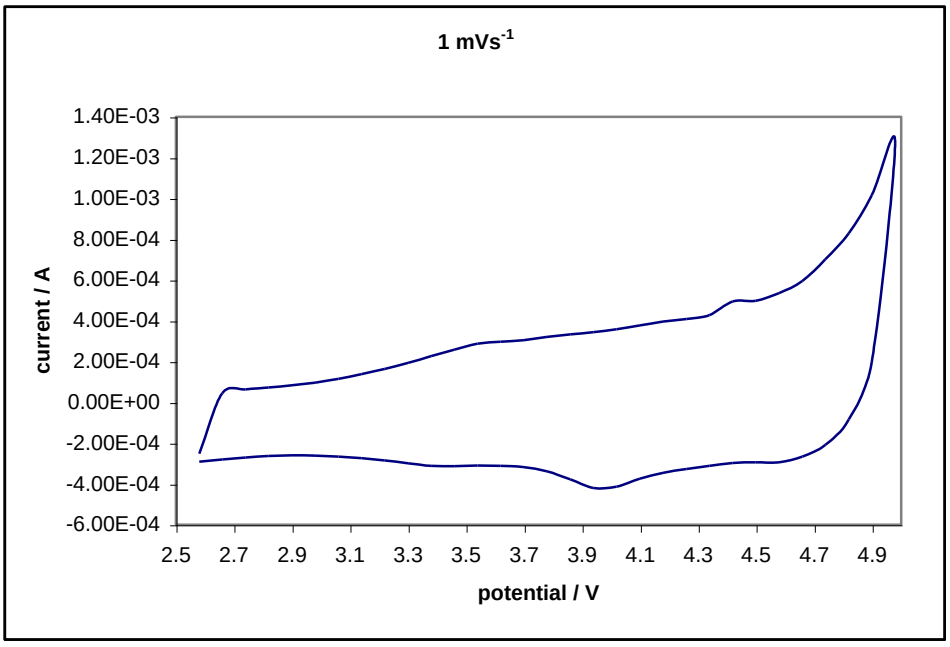

Figure 4.30. Cyclic voltammogram of A5 material at scan rate 1.0mVs^{-1}.

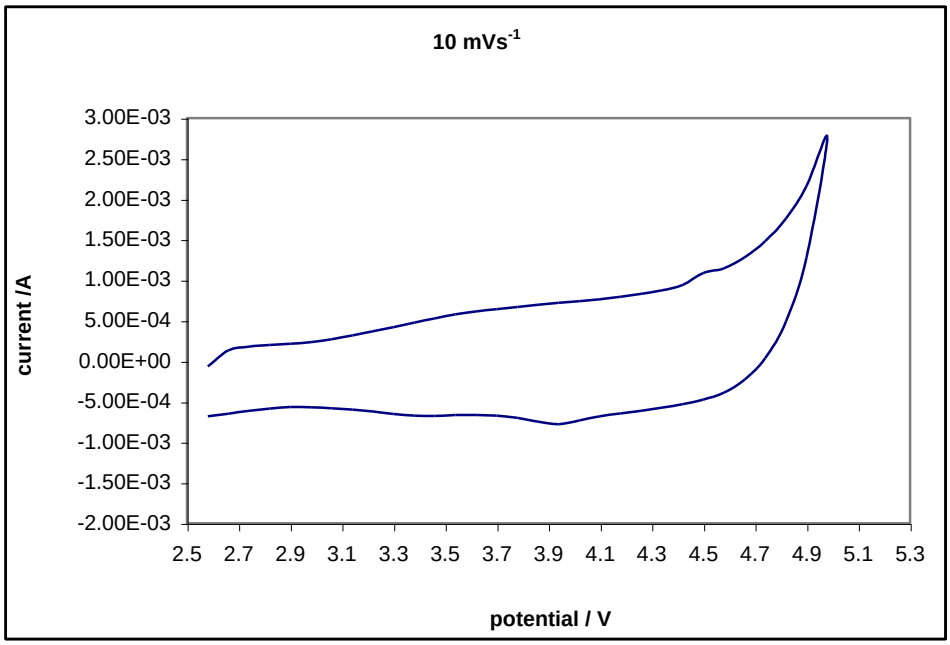

Figure 4.31 . Cyclic voltammogram of A5 material at scan rate10 mVs^{-1}.

The peak potential difference, ΔE (E_{pa} - E_{pc}) for the three samples with scan rate 10 mVs^{-1} , 1.0 mVs^{-1} and 0.1 mVs^{-1} are shown in the table below. Table 4.6 shows that as scan rate increases the difference between the two peaks increases too.

Table 4.6 . ΔE values for sample A3, A4 and A5 at 1.0 mVs^{-1} scan rate.

Sample	Scan rate (mVs^{-1})	Anodic peak, E_{pa}	Cathodic peak, E_{pc}	ΔE
A3	10	4.49	3.94	0.55
	1	4.43	3.94	0.49
	0.1	4.41	3.97	0.44
A4	10	4.49	3.93	0.56
	1	4.43	3.97	0.46
	0.1	4.41	3.97	0.44
A5	10	4.49	3.94	0.55
	1	4.42	3.94	0.48
	0.1	4.41	4.75	0.35

4.6.2 Formal electrode potential

The position of the peaks on the potential axis is related to the formal potential of the redox process. The formal potential for a redox couple is centred between the anodic peak (E_{pa}) and cathodic peak (E_{pc}). Thus the identity of the cation extraction and deintercalation can be determined by the formal electrode potential (E_f) (Mi et al; 2007).The formal potential (E_f) of the cation can be calculated from the redox peaks potentials based on the following equation:

$$E_f = \frac{E_{pa} + E_{pc}}{2} \qquad (4.13)$$

Table 4.7 List of calculated formal potential for A3, A4 and A5 samples at scan rate 1.0 mVs^{-1}.

Samples	Anodic peak potential (E_{pa}) (V)	Cathodic peak potential (E_{pc}) (V)	Formal potential (E_f) (V)
A3	4.43	3.94	4.18
A4	4.43	3.97	4.10
A5	4.42	3.94	4.18

The mean value for the calculated formal potential is 4.15 V versus Li^+/Li. At present the expected potential is 4.10 V for Mn^{3+}/Mn^{2+} versus Li^+/Li (Chang et al, 2005). The disagreement is reasonable because the structure, morphology and composition concurrently affect the electrochemistry of the $LiMnPO_4$.

4.6.3 Relationship between i_p and $\upsilon^{1/2}$

To investigate the effect of scan rate on the redox behaviours of $LiMnPO_4$, their curves at different scan rates were recorded. The cyclic voltammograms of the various scan rates for samples A3, A4 and A5 are depicted in Figures 4.32 to 4.34. To determine the reversibility in the $LiMnPO_4$ cathode material, a plot of peak current, i_p versus square root of the scan rate, $\upsilon^{1/2}$ for the cyclic voltammograms in Figures 4.32 to 4.34 were drawn**.** Figures 4.35 to 4.37 show the relationship between i_p and $\upsilon^{1/2}$ for a positive scan of samples A3, A4 and A5 respectively. The regression, R^2 lies in the range 0.93 to 0.98 and the plotted points are therefore in a straight line. It can be seen that peak current increases linearly to the square root of the scan rate as observed in Figures 4.35 to 4.37. From these results it can be inferred that the reaction that is taking place in the cell is reversible. This observation shows that the Li^+ intercalation and deintercalation processes are diffusion-controlled(Liu et al.,2006).

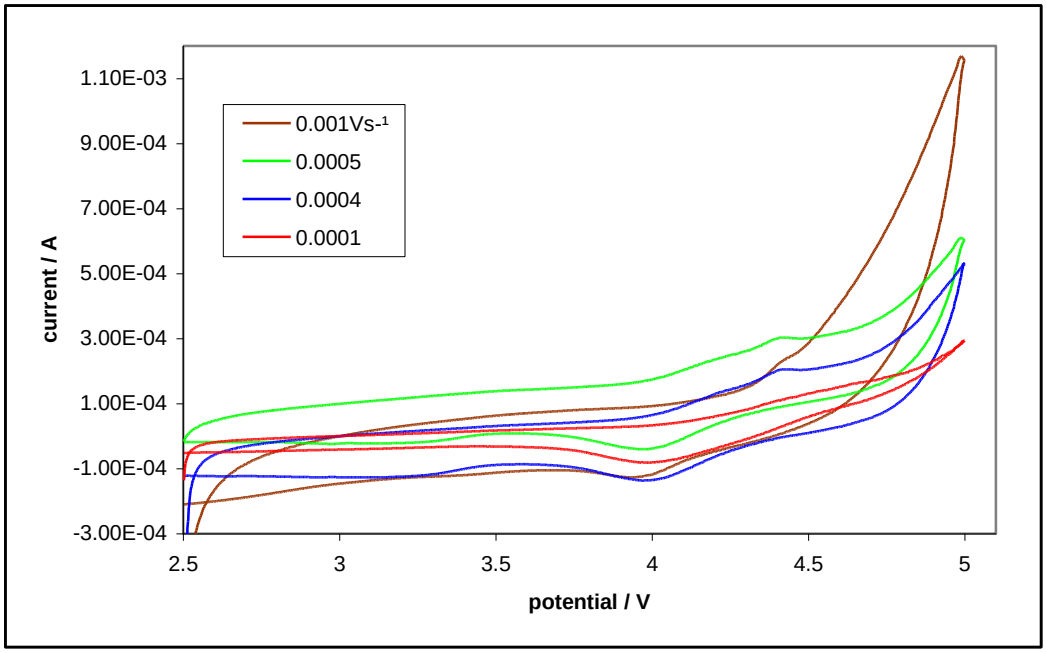

Figure 4.32. Cyclic voltammogram of A3 material at different scan rates

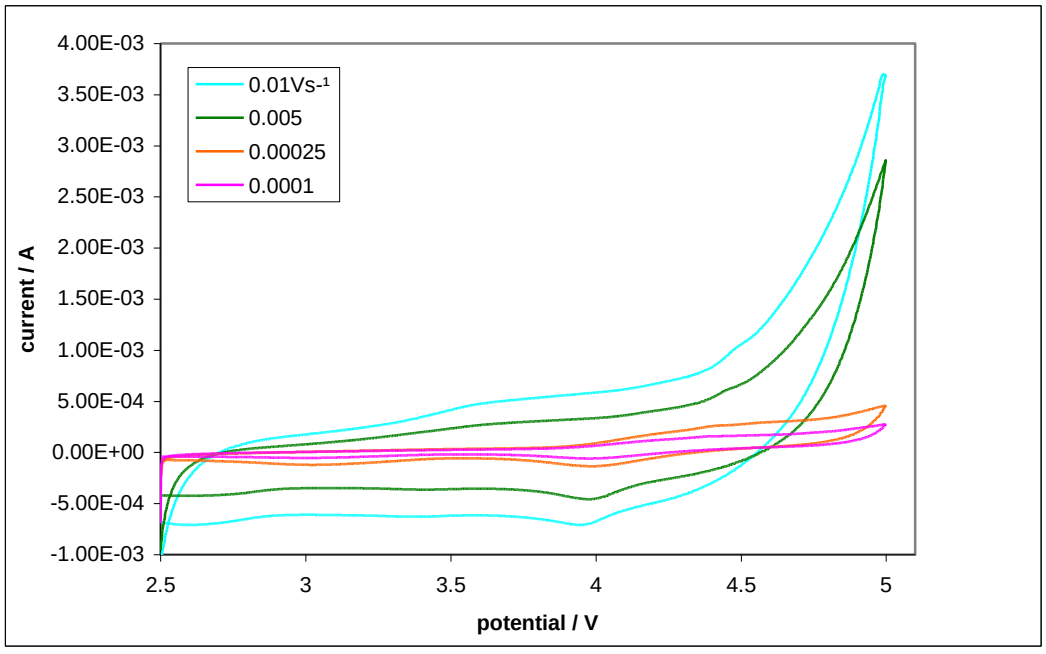

Figure 4.33. Cyclic voltammogram of A4 material at different scan rates

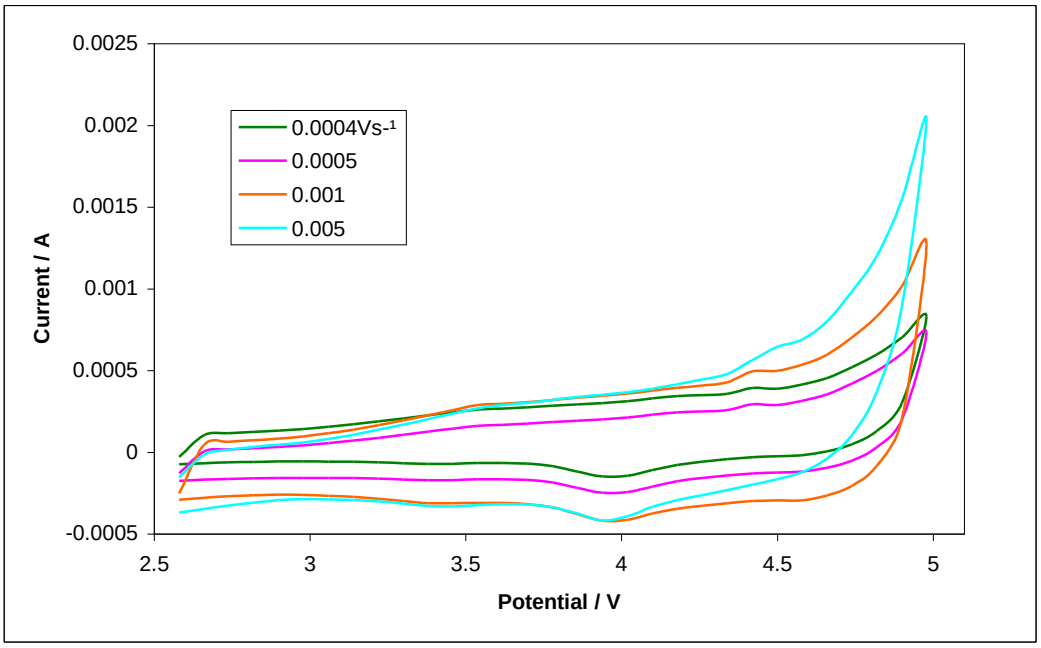

Figure 4.34. Cyclic voltammogram of A5 material at different scan rates

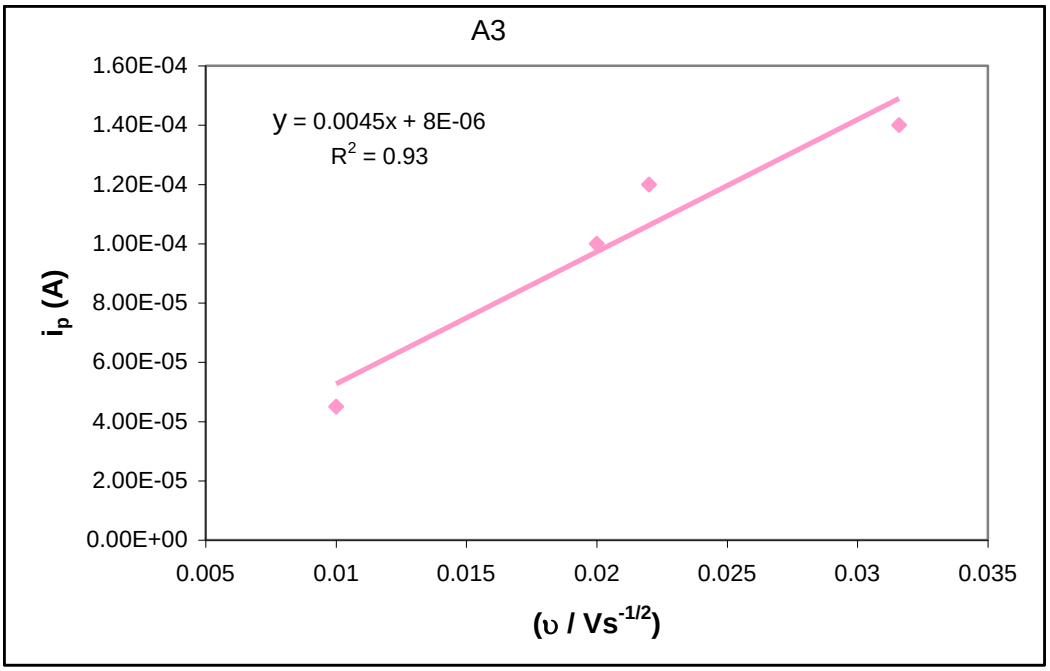

Figure 4.35. Relationship between the peak currents and $\upsilon^{1/2}$ for a positive scan of sample A3.

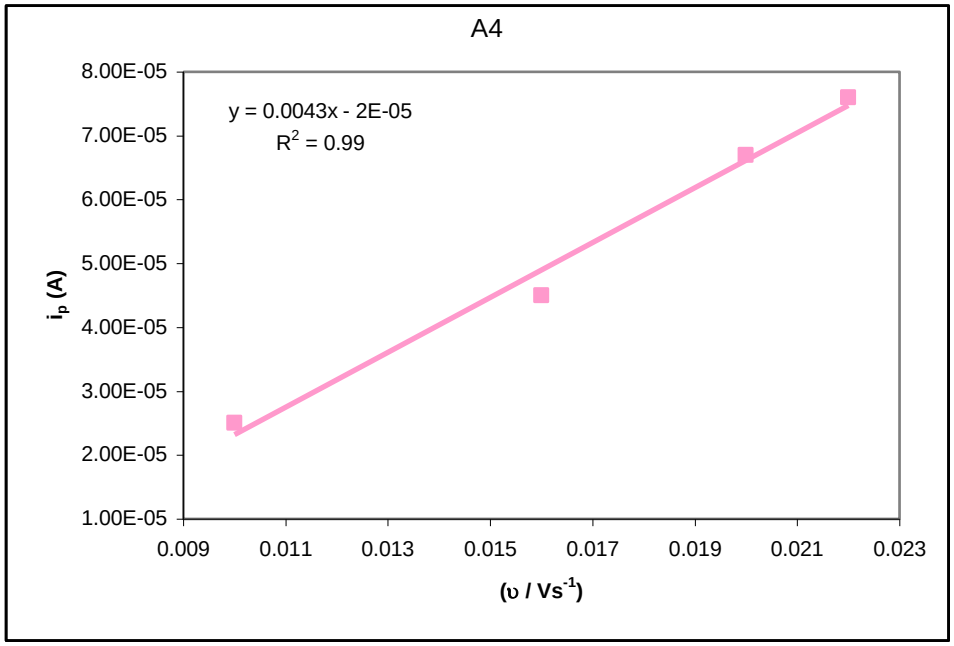

Figure 4.36. Relationship between the peak currents and $\upsilon^{1/2}$ for a positive scan of sample A4.

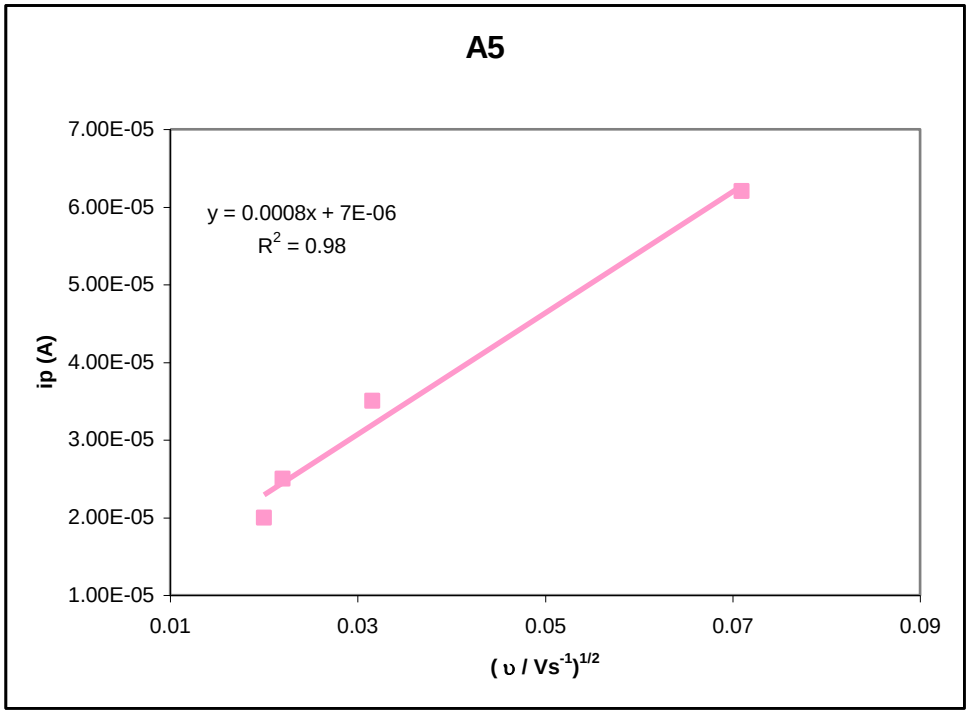

Figure 4.37. Relationship between the peak currents and $\upsilon^{1/2}$ for a positive scan of sample A5.

4.6.4 Diffusion coefficient, D_{Li}^{+}

As expected the plot of peak current, i_p versus $\upsilon^{1/2}$ yield a straight line indicating the reaction is a reversible one. The relationship between these two parameters is shown in Equation (3.2). The equation which is known as Randle- Sevcik equation ca be modified to give an expression as shown below (Yu et al., 2007).

$$i_p = (2.69 \times 10^5)\, n^{3/2} A D^{1/2}_{Li+}\, \upsilon^{1/2}\, C_{Li+} \qquad (4.14)$$

The equation can be used to determine the mean diffusion coefficient (D_{Li}^{+}) of Li^+ ions in the working electrode. From Equation 4.14, the slope of the graph can be deduced and thus the diffusion coefficient can be determined.

It is assumed that the intercalation reaction is controlled by the solid state diffusion of Li ions (Xia et al.,1995) where i_p is peak current (A), n is electrons per molecule lithium ion (n = 1), υ is scan rate of cyclic voltammetry (V s^{-1}), A is the surface area of electrode, (0.785 cm^2) and C_{Li}^{+} is the concentration of lithium ion (mol cm^{-3}). $LiMnPO_4$ has a bulk density of 3.4 g cm^{-3} (Yonemura et al., 2004) with a molar mass of 157 $gmol^{-1}$. This corresponds to a Li concentration of 0.022 mol cm^{-3}. The data used for the calculation of the diffusion coefficient of samples A3, A4 and A5 are listed in Table 4.8. For the results obtained in Figures 4.34 to 4.36, the slopes are 0.0045, 0.0043 and 0.0008 $As^{1/2}\ V^{-1/2}$ respectively. After careful substitution and unit analysis the diffusion coefficient, D_{Li}^{+} of samples A3, A4 and A5 can be determined. Table 4.8 shows that the calculated value for the diffusion coefficient for samples A3, A4 and A5 are 9.37×10^{-13} cm^2s^{-1}, 8.57×10^{-13} cm^2s^{-1} and 2.97×10^{-14} cm^2s^{-1} respectively. Results showed that diffusion coefficient of A3 >A4>A5.

Table 4.8. List of data used for the calculation of the diffusion coefficient and the calculated diffusion coefficient values for samples A3, A4 and A5.

Sample	Slope/ $As^{1/2} V^{-1/2}$	C_{Li+} / mol cm^{-3}	Molar mass g mol^{-1}	D_{Li+} / $cm^2 s^{-1}$
A3	0.0045	0.022	157	$9.37x10^{-13}$
A4	0.0043	0.022	157	$8.57x10^{-13}$
A5	0.0008	0.022	157	$2.97x10^{-14}$

To the author's best knowledge diffusion coefficient values of $LiMnPO_4$ in the literature are not available and therefore no comparison can be made.

4.6.5 Cell capacity

The charge density of the cell can be obtained by integrating the current observed for the cyclic voltammetry with the time from the moment the potential scanning was started to the time the scanning reached the potential (Takahashi et al., 2002). The charge density value, Q was then recorded and the specific capacity of the cell was calculated. The density of charge (Q) for the samples A3, A4 and A5 are recorded and tabulated in Table 4.9.

Specific charge capacity was calculated using the formula

$$Specific\ capacity = \frac{current\ (mA)\ x\ time\ (hr)}{Mass\ of\ active\ materials} \qquad (4.15)$$

The mass of the active material used was 0.025 g. Table 4.9 shows that the total electricity during the anodic scan was 25 $mAhg^{-1}$, 26 $mAhg^{-1}$ and 23 $mAhg^{-1}$ for samples A3, A4 and A5 respectively.

Table 4.9. The electrical charge density,Q, capacity and specific capacity for the samples A3, A4 and A5.

Samples	Scan rate (mVs^{-1})	Q (C)	Capacity (mAh)	Specific capacity (mAh/g)
A3	0.1	2.265	0.629	25
A4	0.1	2.362	0.656	26
A5	0.1	2.067	0.574	23

The results obtained is similar to previous work done by Ma and Qin et al. (2005) who obtained 20 $mAhg^{-1}$ as the capacity for the $LiMnPO_4$/Li cell measured by charge/discharge curves. Dominko et al (2006) obtained 40 $mAhg^{-1}$ for $LiMnPO_4$ coated with carbon. The performance of $LiMnPO_4$ prepared in this work is comparable to the scarce data available in literature.

4.7 Summary

The $LiMnPO_4$ in this study was successfully synthesized via the tartaric acid based sol-gel method. The precursor was fired in the absence of inert gases unlike other studies. Analysis of the synthesized $LiMnPO_4$ using XRD demonstrated the formation of a pure $LiMnPO_4$ phase powder without any impurities. Bands in the region 400 to 1400 cm^{-1} was observed in the FTIR spectrum indicating the presence of phosphate ion, PO_4^{3-}. $LiMnPO_4$ crystallite ranging from 31 to 46 nm were obtained at firing temperatures from 350 ^oC to 1000 ^oC in this work. The reaction mechanism for $LiMnPO_4$ was suggested and this reaction mechanism has not been published yet.

The voltammogram obtained indicates the presence of anodic and cathodic peak corresponding to the intercalation and deintercalation of lithium ion. The calculated diffusion coefficient value for samples A3, A4 and A5 are of A3, A4 and A5 are

$9.37x10^{-13}$ cm^2s^{-1}, 8.57 x 10^{-13} cm^2s^{-1} and 2.97 x 10^{-14} cm^2s^{-1} respectively and there is no data available in the literature to compare the value with. The calculated specific capacity for the $LiMnPO_4$ / Li cell obtained was 25 $mAhg^{-1}$, 26 $mAhg^{-1}$ and 23 $mAhg^{-1}$ for samples A3, A4 and A5 respectively. The performance of $LiMnPO_4$ is comparable to the scarce data available in literature. Ma and Qin (2005) obtained 20 $mAhg^{-1}$ as the capacity for the $LiMnPO_4$/Li cell measured by charge/discharge curves.

CHAPTER 5

RESULTS

LITHIUM NICKEL PHOSPHATE

5.1 Introduction

Lithium nickel phosphate in this work was synthesized via the sol gel method. During the preparation stage, pale green coloured suspensions was obtained and finally a yellow powder precursor was produced. Not many discussion have been published on this material with respect to its structure, physical and chemical properties and electrochemical studies.

The TGA/DTGA studies have been employed to analyse the reaction of raw materials during the formation of $LiNiPO_4$. The X-ray diffraction analysis was carried out to confirm the formation of $LiNiPO_4$. FTIR and EDX analysis were also performed to further characterize the samples. The electrochemical reversibility of the samples was characterized by cyclic voltammetric measurements. The results of all the analysis are presented in this chapter.

5.2 Thermogravimetric Analysis (TGA)

The thermal behavior of the prepared sample was analyzed by TGA and DTGA. The TGA and DTGA thermograms of the dried gel precursors was studied in nitrogen atmosphere.

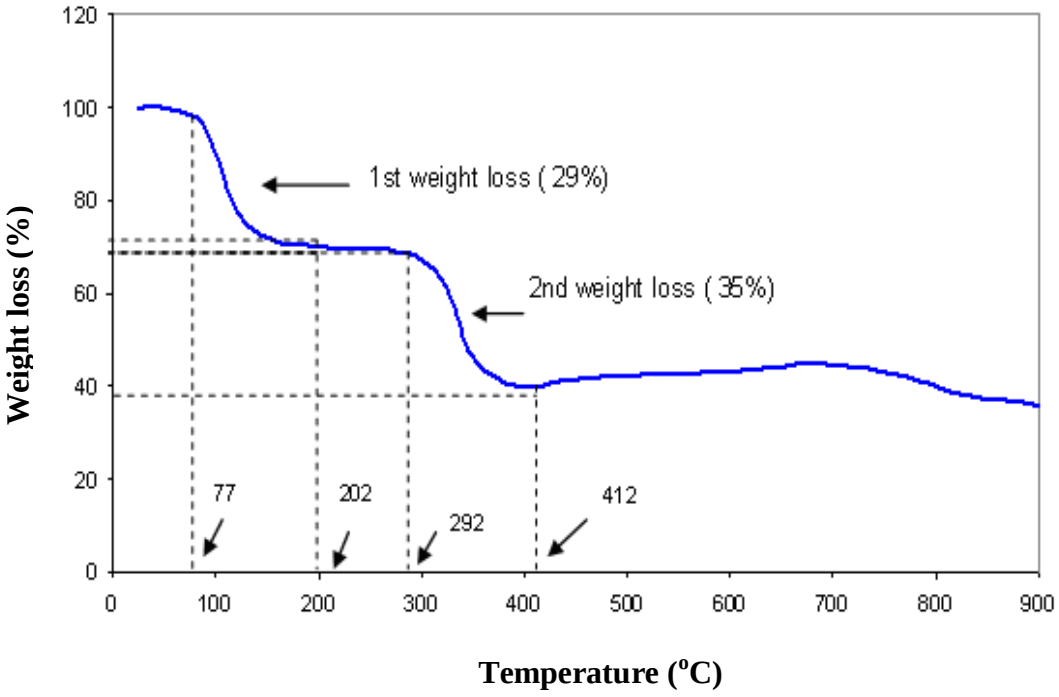

Figure 5.1. TGA thermogram of nickel acetate tetrahydrate.

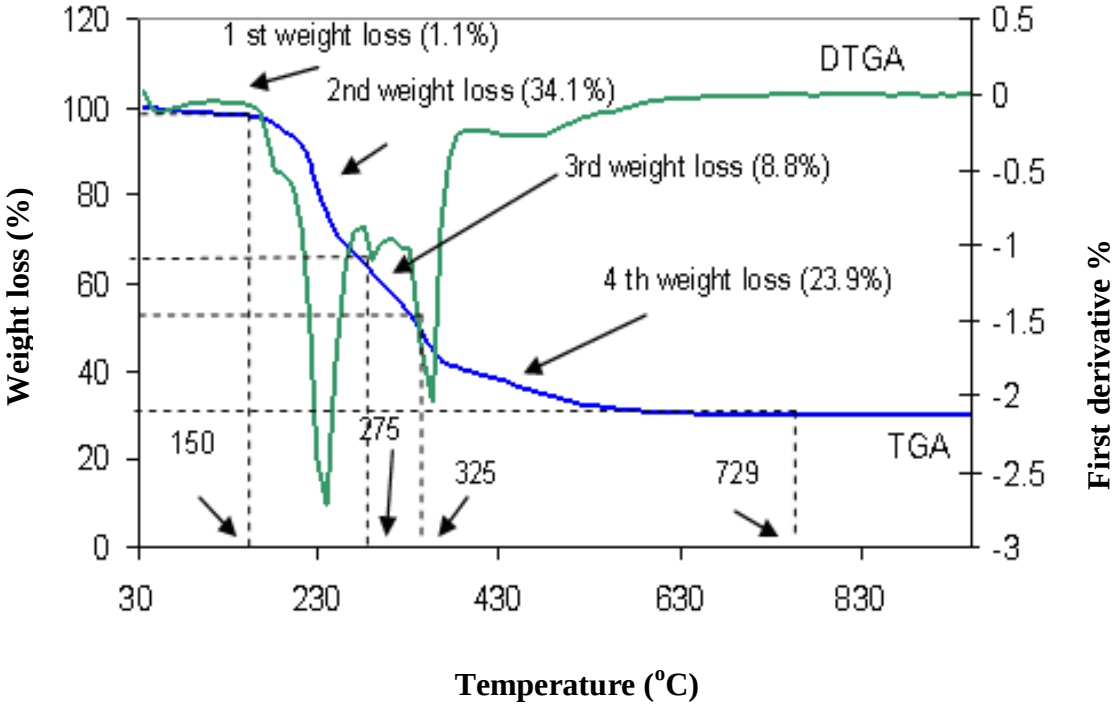

Figure 5.2. TGA and DTGA thermograms of lithium nickel phosphate precursor.

The TGA thermogram of nickel acetate tetrahydrate shows two discrete weight losses as shown in Figure 5.1. The first weight loss is attributed to the evaporation of adsorbed water from 77 ^{o}C to 202 ^{o}C and the second weight loss is due to the decomposition of nickel acetate from 292 ^{o}C to 412 ^{o}C. The TGA thermogram of the precursors revealed that there are four significant weight loss regions as shown in Figure 5.2. A weight loss of about 1.1 % ocurred slowly as the temperature was increased to about 150 ^{o}C, due to the evaporation of residual water which are still present in the sample. Rapid weight loss occurred around the temperature range between 150 ^{o}C to 275 ^{o}C and is associated with a 34.1 % weight loss. This weight loss is attributed to the decomposition of unreacted ammonium dihydrogen phosphate as it was one of the reactant materials in the sample. The removal of tartaric acid is also assigned to this region. The TGA thermogram of tartaric acid (Figure 4.4)showed that it quickly evaporates in the temperature region of 200 ^{o}C to 260 ^{o}C. The weight loss is also due to the decomposition of the Li-Ni acetate gel formed in the experiment. The decomposition process of the precursor is also accompanied by a sharp endothermic peak at about 237 ^{o}C as seen on the DTGA thermogram in Figure 5.2. This endothermic peak is probably due to the decomposition of ammonium dihydrogen phosphate.

The third weight loss occurred at the temperature range from 275 ^{o}C to 325 ^{o}C. Nickel acetate steadily decomposed in the temperature range from 272 ^{o}C to 400 ^{o}C (Lee et al., 1999). This decomposition was associated with a weight loss of 8.8 % and can be attributed to the burning out of organic residues which resulted from the Li-Ni acetate complex decomposition. The final decomposition step which is associated with 23.9 % weight loss occurred in the temperature range from 325 ^{o}C to 725 ^{o}C. The weight loss is attributed to the decomposition of nickel acetate and lithium

hydroxide. TGA of lithium hydroxide shows that the metal hydroxide decomposes in the temperature region between 450 ^{o}C and 630 ^{o}C (Figure 4.1).

The DTGA thermogram reveals a sharp endothermic peak at 354 ^{o}C indicating the rapid decomposition of nickel acetate. The weight is constant after 725 ^{o}C indicating that no heat is used for evaporation or decomposition processes and that $LiNiPO_4$ can be obtained by firing the precursor at temperatures above 750 ^{o}C. The tartaric acid is likely to act as a fuel in the pyrolysis and expedite the process of decomposition of acetate ions (Prabaharan et al; 1998; Lee et al., 1999) The corresponding weight loss, temperature ranges and their assignment are summarized in Table 5.1.

Table 5.1. TG/DTGA results of the $LiNiPO_4$ precursor.

Sample	Temperature range (^{o}C)	Effects(^{o}C)		Weight loss(%)	Assignment
		Endo	Exo		
$LiNiPO_4$ from LiOH, $Ni(CH_3COO)_2$ and $(NH_4)H_2PO_4$ with tartaric acid.	30-150	58	-	1.1	Evaporation of absorbed water.
	150-275	237	-	34.1	Decomposition of $(NH_4)H_2PO_4$ and evaporation of tartaric acid. Li-Ni acetate gel(precursor)decomposition
	275-325	289	-	8.8	Burning out organic residues resulted from the complex decomposition
	325-725	354	-	23.9	Decomposition of $Ni(CH_3COO)_2$. and LiOH. Structural OH bond broken
	725-900	-	-	-	Formation of $LiNiPO_4$
Total weight loss				67.9	

The formation mechanism for the synthesis of $LiNiPO_4$ has been proposed as shown below.

When tartaric acid ($C_4H_6O_6$) was added to the mixture, it reacted with $(NH_4)H_2PO_4$ and

LiOH according to the following equations.

$$2(NH_4)H_2PO_4 + C_4H_6O_6 \longrightarrow H_3PO_4 + H_2PO_4^- + ((NH_4)_2C_4H_5O_6)^+ \quad (5.1)$$

$$LiOH + C_4H_6O_6 \longrightarrow Li\,C_4H_5O_6 + H_2O \quad (5.2)$$

LiOH also reacted with H_3PO_4 produced in equation (1) according to the following,

$$LiOH + H_3PO_4 \longrightarrow LiH_2PO_4 + H_2O \quad (5.3)$$

On heating,

$$2(Ni(CH_3COO)_2) + 2\,C_4H_6O_6 + 8O_2 \longrightarrow 2(Ni\,C_4H_4O_6) + 8CO_2 + 8H_2O \quad (5.4)$$

and

$$H_2PO_4^- + ((NH_4)_2C_4H_5O_6)^+ + C_4H_6O_6 + \frac{5}{2}O_2 \longrightarrow ((H_2PO_4)(NH_4)_2C_4H_5O_6) + 4CO_2 + 3H_2O \quad (5.5)$$

Therefore overall reaction is given as,

$$2(NH_4)H_2PO_4 + 2\,LiOH + 2(Ni(CH_3COO)_2) + 5C_4H_6O_6 + \frac{21}{2}O_2 \longrightarrow LiH_2PO_4 + Li\,C_4H_5O_6 + ((H_2PO_4)(NH_4)_2C_4H_5O_6) + 2(Ni\,C_4H_4O_6) + 12CO_2 + 13H_2O \quad (5.6)$$

Equation (5.6) suggests that the dried gel precursor is composed of

$$Li((H_2PO_4)_2(NH_4)_2C_4H_5O_6)\,Li\,C_4H_5O_6 . (Ni\,C_4H_4O_6)_2$$

Therefore the overall proposed decomposition equation for the precursor in air atmosphere i.e. during firing is,

$$Li((H_2PO_4)_2(NH_4)_2C_4H_5O_6)\,Li\,C_4H_5O_6 . (Ni\,C_4H_4O_6)_2 + 10\,O_2 \longrightarrow 2LiNiPO_4 + 16CO_2 + 12H_2O + 2NH_3 \quad (5.7)$$

Based on equation (5.7), the percentage weight loss is 66.4 %. The total weight loss of the decomposition process from the TGA curves as shown in Table 5.1 is 67.9 % which agrees closely with the calculated values based on Equation (5.7) as shown in Table 5.2. The discrepancy could be due to the absorbed water from the ambient.

Table 5.2. Calculation for percentage weight loss for equation 5.7.

$Li((H_2PO_4)_2(NH_4)_2C_4H_5O_6)\,Li\,C_4H_5O_6 . (Ni\,C_4H_4O_6)_2$ (precursor)				**$LiNiPO_4$**			
element	Atomic mass (g)	No of moles of elements	Total mass of elements in formula (g)	element	Atomic mass (g)	No of moles of elements	Total mass of elements in formula (g)
Li	6.9	2	13.8	Li	6.9	1	6.9
C	12	16	192	O	16	4	64
H	1	30	30	Ni	58.4	1	58.4
O	16	32	512	P	31	1	31
Ni	58.7		117.4				
P	31	2	62				
N	14	2	28				
Overall total mass			955.2				160.3 x 2 =320.6
% $LiMnPO_4$ formed after heating							33.6
% weight loss							66.4

5.3 X-Ray Diffraction (XRD)

In this work, the $LiNiPO_4$ prepared were fired at different temperatures to identify the best temperature to synthesize $LiNiPO_4$. The crystalline phases of the samples were identified by the powder X-ray diffraction using CuKα radiation.

The samples were designated as, B1, B2, B3 and B4 as shown in Table 5.3. The diffraction patterns for all four samples prepared by the sol-gel method are presented in Figures 5.3, 5.4, 5.5 and 5.6.

Table 5.3. The symbols designated to the samples fired at different temperatures with their impurities peaks.

Sample code	Firing Temperature(^{o}C)	Firing time (hours)	Impurity peaks
B1	750	15	33.8^o and 43.2^o
B2	850	15	33.8^o and 43.2^o
B3	1000	15	43.2^o
B4	1000	24	None

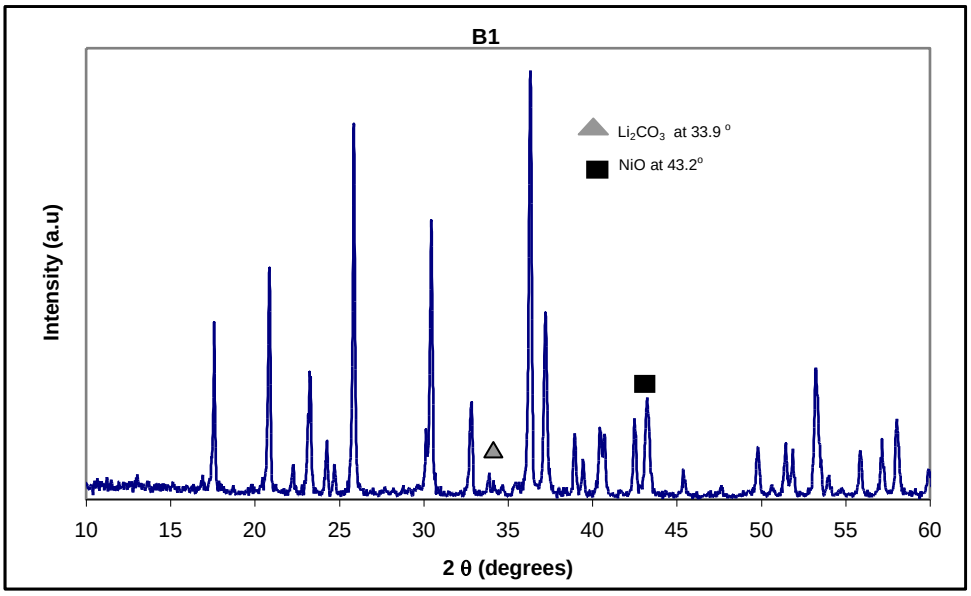

Figure 5.3. XRD diffractogram of B1 sample.

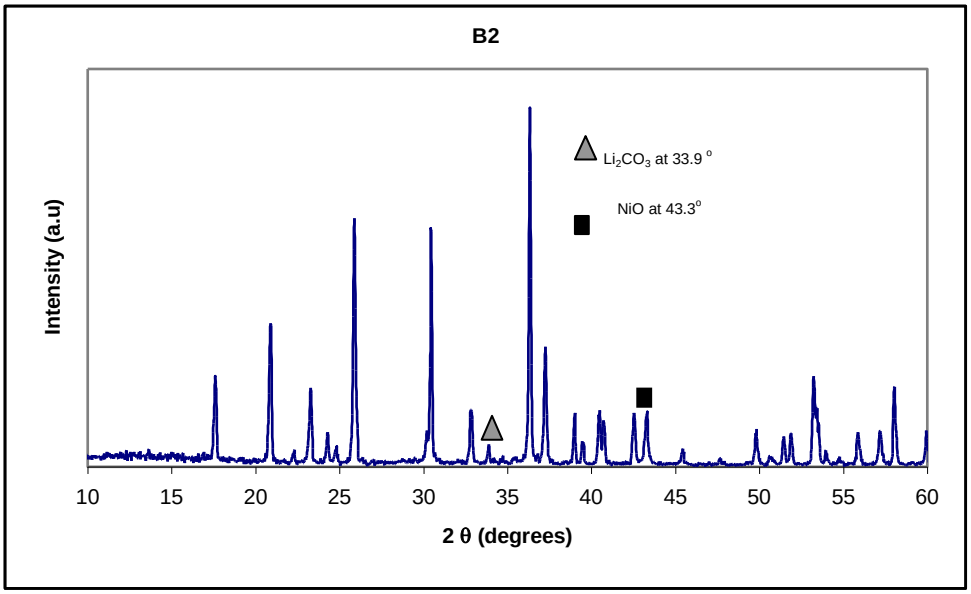

Figure 5.4. XRD diffractogram of B2 sample.

Sharp and intense diffraction lines are generally observed for all the samples indicating the crystalline nature of the materials as represented by Figures 5.3 to 5.6. All the peaks assigned to $LiNiPO_4$ appeared in these figures. However some impurities peaks are noticed in Figures 5.3, 5.4 and 5.5.

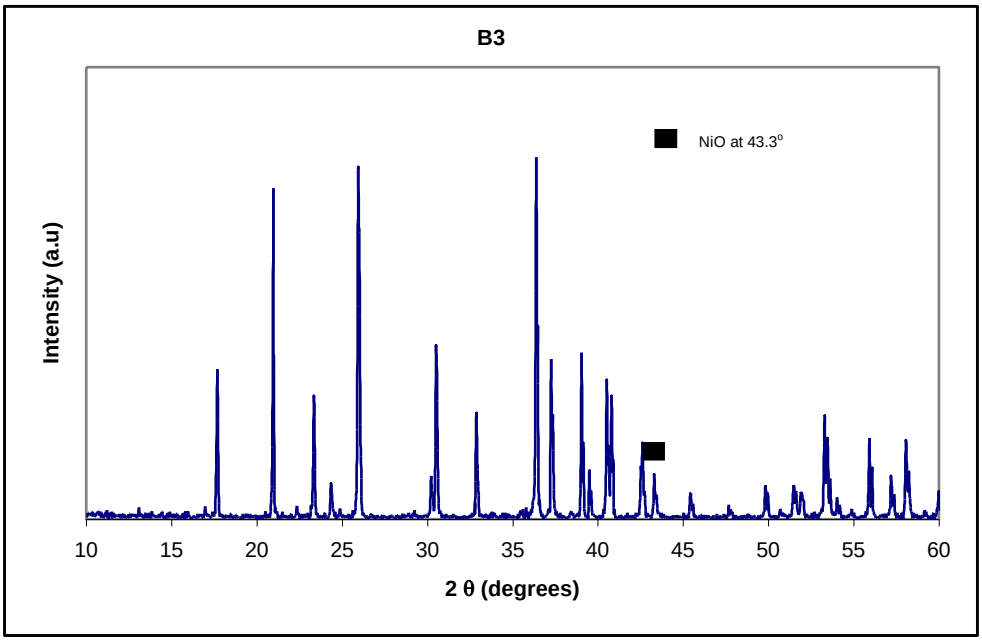

Figure 5.5. XRD diffractogram of B3 sample.

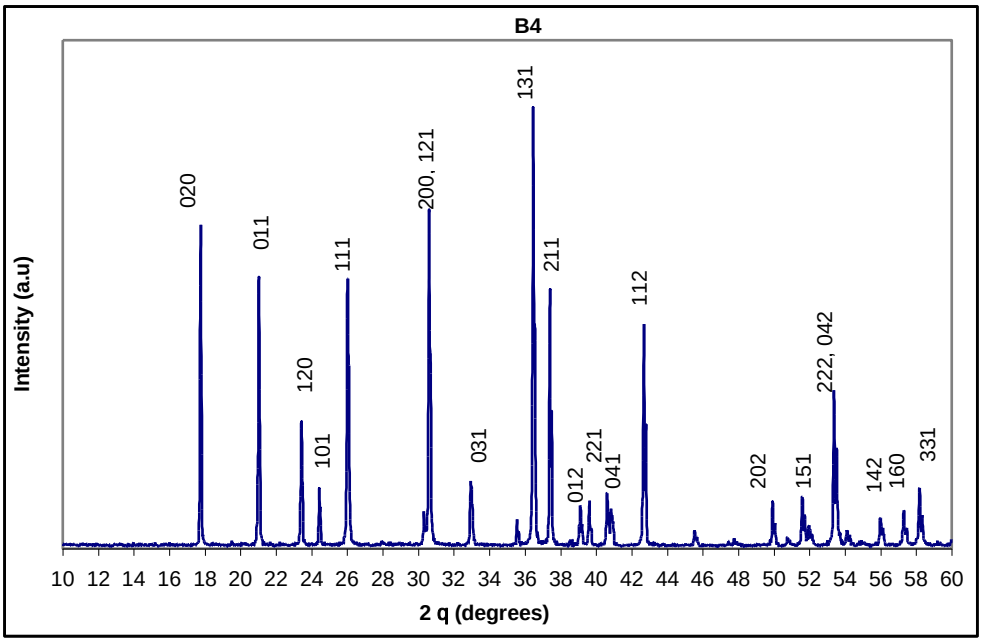

Figure 5.6. XRD diffractogram of B4 sample.

The X-ray diffraction of the lithium nickel phosphate formed by firing at 750 ^{0}C showed the presence of an impurity phase. This is apparent from an inspection of the data in Figure 5.3 where extra lines can be observed at 2θ = 33.8 and 43.2 ^{o}.The peaks at 2θ = 33.8 ^{o} are attributed to Li_2CO_3 (Arof , 2007; Song, 2002; Chang, 1998) while the peak at 2θ = 43.2 ^{o} is due to formation of NiO (Arof, 2007).

The material was then further heated at 850 ^{o}C and 1000 ^{o}C for 15 hours. The extra peaks are still observed in the XRD patterns of both samples as shown in Figure 5.4 and Figure 5.5 but are less intense. The XRD pattern indicate that firing temperature of 1000 ^{o}C and 15 hours firing time is not sufficient to get pure $LiNiPO_4$. The extra line at 43.2 ^{o} is still present. Therefore the compound was further heated at 1000 ^{o}C for 24 hours. The XRD pattern of the sample fired at 1000 ^{o}C for 24 hours exhibits the characteristic diffraction lines of $LiNiPO_4$ without any impurities and matches the orthorhombic structure listed in JCPDS pattern number 32-0578. The XRD of this

sample also agrees with the results of Ruffo and co-workers (2005). The above observations confirmed that a pure compound of $LiNiPO_4$ was successfully synthesized in the present work. Table 5.4 shows the comparison between the diffraction angles of the prepared sample with the $LiNiPO_4$ JCPDS (pattern no 32-0578). The lines due to impurities are also listed.

Table 5.4 Comparison between the diffraction angles (2Θ) values of the prepared sample with the $LiNiPO_4$ JCPDS (pattern no 32-0578).

SAMPLES								JCPDS		
B1 2θ (°)	**Int (%)**	**B2 2θ (°)**	**Int (%)**	**B3 2θ (°)**	**Int (%)**	**B4 2θ (°)**	**Int (%)**	**32-0578 2θ (°)**	**Int (%)**	**hkl**
25.9	87	25.9	69	25.9	97	25.9	61.2	25.9	100	111
36.3	100	36.3	100	36.4	100	36.4	100	36.3	100	131
30.4	65	30.4	66	30.5	43	30.5	76.4	30.5	65	200
17.6	41.	17.6	25	17.7	42	17.6	73.5	17.6	60	020
20.9	54	20.9	40	20.9	92	20.9	61.5	20.9	60	011
37.2	44	37.3	33	37.3	44	37.3	58.6	37.3	35	211
23.2	30	23.3	22	23.4	34	23.3	28.8	23.3	30	120
53.3	30	53.3	25	53.3	29	53.4	13.5	53.3	30	222
32.8	21	32.8	16	32.9	29	32.9	35.3	32.8	25	031
53.3	31	53.5	16	55.9	22	51.9	8.1	53.4	20	042
58.1	19	58.1	22	58.1	22	58.5	26.8	58.1	20	331
32.8	21	30.2	10	30.3	12	30.2	10.5	30.2	18	121
40.6	12	40.7	13	40.6	38	40.8	28.6	40.7	18	041
57.2	14	57.2	10	57.2	12	57.2	6.1	57.1	18	160
39.5	9	40.5	16	39.0	46	40.5	8.3	40.6	16	221
42.5	19	42.5	15	42.6	21	42.6	35.5	42.6	16	112
49.8	12	49.8	11	49.9	10	49.8	11.9	49.9	10	202
24.5	6	24.9	6	24.6	2.5	24.7	6.3	24.3	10	101
39.3	7	39.3	8	39.5	7	39.5	14	39.5	8	012
55.7	9	55.5	5	56	7.5	55.9	15	55.8	12	142
51.3	7.5	51.3	8.5	50	7.5	50.2	8	51.8	10	151
Impurities										
33.9	4	33.9	6							
43.3	24	43.8	15	43.4	10					

5.3.1 Crystallite size

The full width at half maximum (FWHM) of the (111) reflection plane was determined and the crystallite size (L) was again estimated using the Scherrer Equation, (Equation 4.12). Here λ is the X-ray wavelength 1.5406 Å and β_r is the FWHM of the peak representing the (111) plane. The crystallite size, L of the prepared samples B2, B3 and B4 are 61.5, 65.9 and 66.0 nm respectively as shown in Table 5.5. Could not compare crystallite size since due to lack of references reporting about crystallite size of $LiNiPO_4$. Previous literature survey indicates that in the past 10 years no reports on $LiNiPO_4$ crystallite size were published.

Table 5.5. Crystallite size, L of samples B2, B3 and B4.

Samples	Calculated, *L* (Crystallite size) nm
B2	61.5
B3	65.9
B4	66.0

5.4 Fourier Transform Infrared Spectroscopy (FTIR)

In addition to XRD analysis, further structural characterization of the prepared samples was obtained from the IR spectroscopy. Vibrational spectroscopy is one of the most powerful techniques available for materials characterisation (Julien, 2000). The IR spectrum of the as prepared $LiNiPO_4$ precursor is presented in Figure 5.7. In this spectrum vibration bands corresponding to phosphate anion was observed.

Table 5.6 . List of vibration bands of the phosphate polyanions.

Peaks cm^{-1}	Assignment	References
946	ν_1 : symmetric and stretching mode of the P-O bonds,	Julien et al., 2004, Burba et al.,2007 Salah et al.,2006
415-464	ν_2 : O-P-O symmetric bending mode	Julien et al., 2004, Salah et al.,2006
1009-1085	ν_3 : antisymmetric stretching mode of the P-O bonds,	Julien et al., 2004, Burba et al., 2007 Salah et al., 2006
580-637	ν_4 : O-P-O antisymmetric bending mode	Julien et al., 2004, Burba et al., 2007 Salah et al., 2006

.

In order to investigate the formation of phosphate bonds at different temperatures, FTIR analysis was carried out for the samples fired at different temperatures. The vibration bands of the phosphate polyanions are listed in Table 5.6

Comparing Figure 5.7 with the IR spectra of the fired samples, it can be seen that there are many extra peaks present in the IR spectra of the precursor indicating that the $LiNiPO_4$ formed here is not pure. This observation suggests that the precursor is composed of unreacted LiOH, nickel acetate, ammonium dihydrogen phosphate and tartaric acid. This agrees with the results of the TGA analysis where the rapid weight loss in the precursor occurred around 150 to 275 ^oC is attributed to the decomposition of unreacted ammonium dihydrogen phosphate and the removal of tartaric acid.

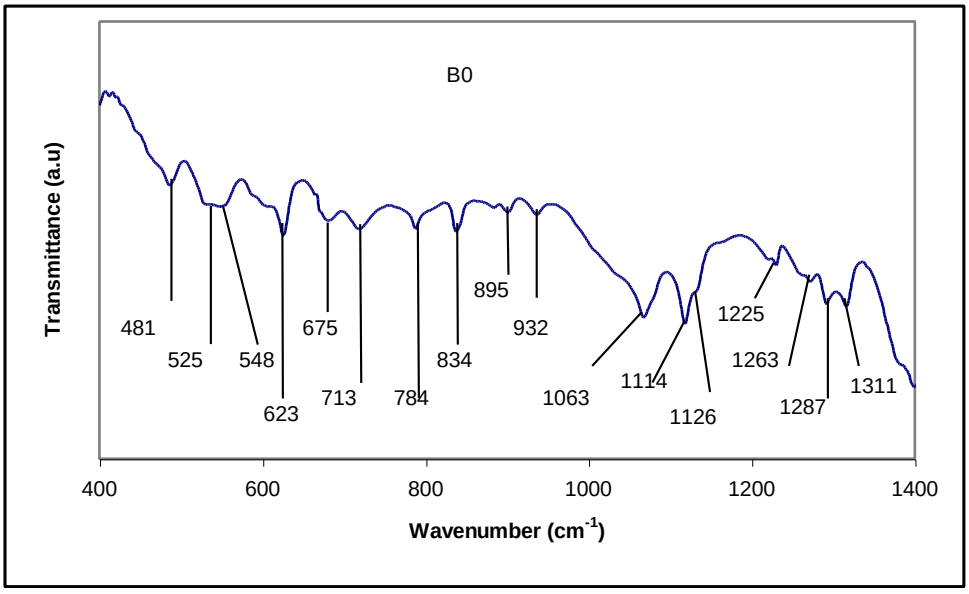

Figure 5.7 FTIR spectrum of lithium nickel phosphate precursor.

The FTIR pattern is rather similar for all phosphates and is characteristic of the PO_4^{3-} anion engaged in an olivine structure i.e bands in the region between 960 to 1200 cm^{-1} are assigned to ν_1 and ν_3.

Infrared absorption spectra of samples B1, B2, B3 and B4 in the region 400-750cm^{-1} are presented in Figures 5.8 to 5.11. In this region a triplet was observed in the range between 580 to 637 cm^{-1} and a doublet in the range between 415 to 464 cm^{-1}. These are due to ν_2 and ν_4. These absorption peaks are due to the stretching and bending vibrations of the phosphate anion.

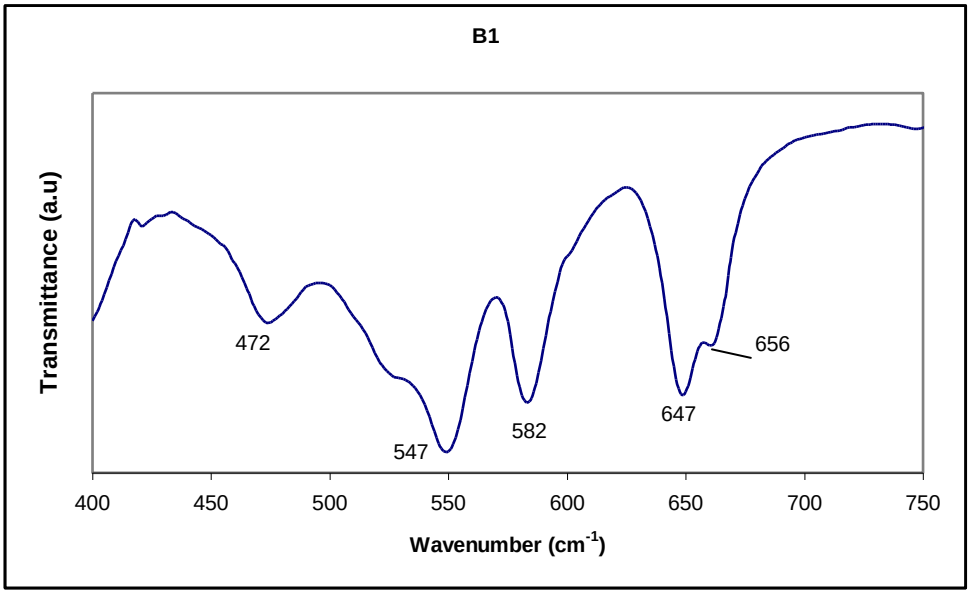

Figure 5.8. FTIR spectrum of sample B1 in the wavenumber 400 to 750 cm^{-1}.

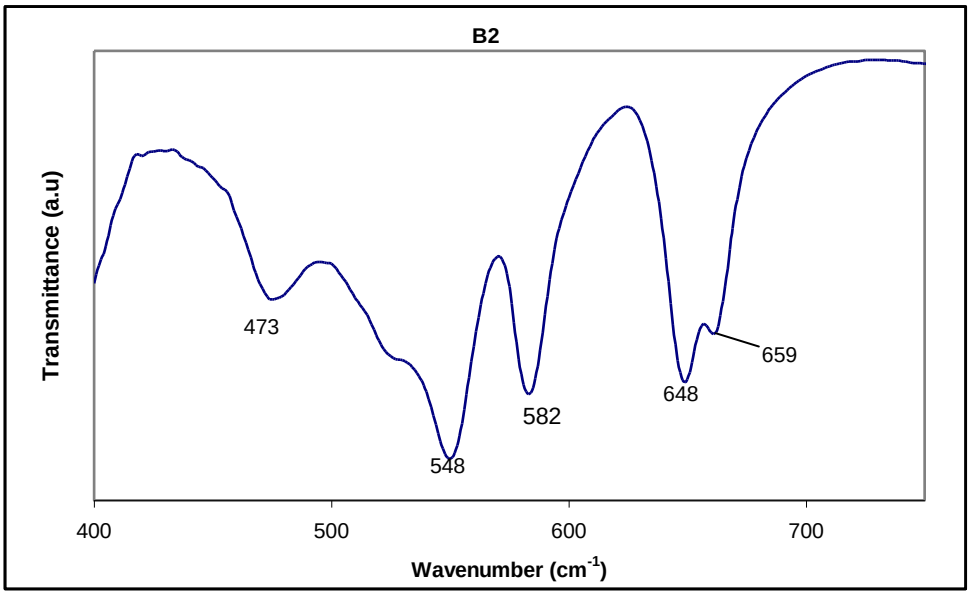

Figure 5.9. FTIR spectrum of sample B2 in the wavenumber 400 to 750 cm^{-1}.

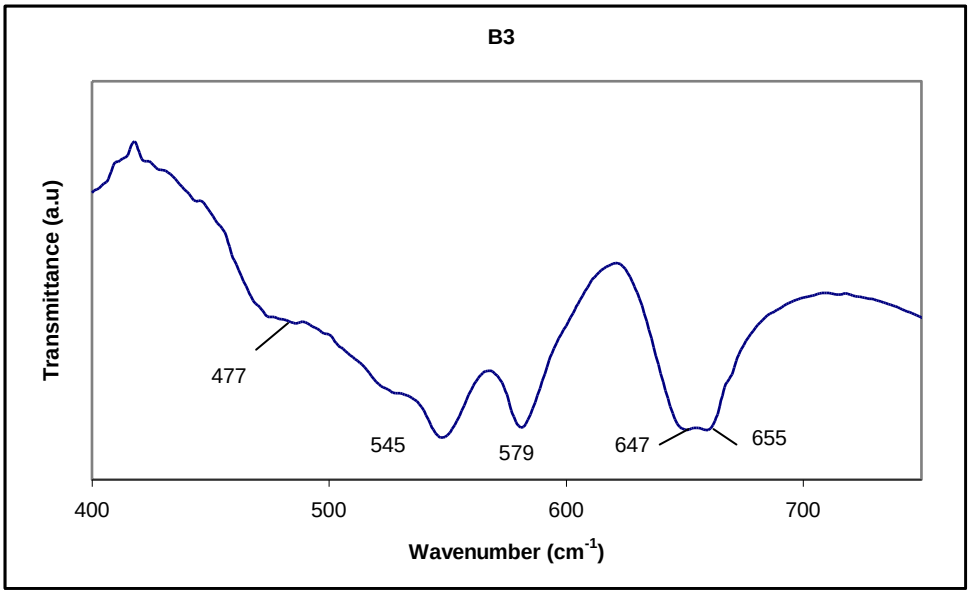

Figure 5.10. FTIR spectrum of sample B3 in the wavenumber 400 to 750 cm^{-1}.

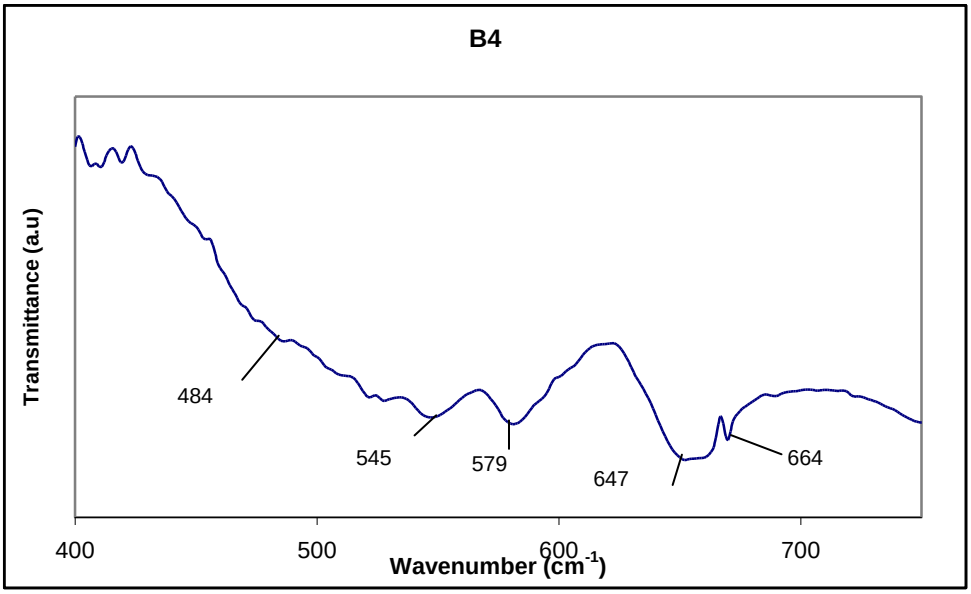

Figure 5.11. FTIR spectrum of sample B4 in the wavenumber 400 to 750 cm^{-1}.

Figures 5.12 to 5.15 show infrared absorption spectra of samples B1, B2, B3 and B4 in the region 800 to 1300 cm^{-1}. All the spectra are dominated by intense vibration bands that range from 800 to 1300 cm^{-1}. These vibration bands are attributed to intramolecular PO_4^{3-} stretching modes ν_1 and ν_3.

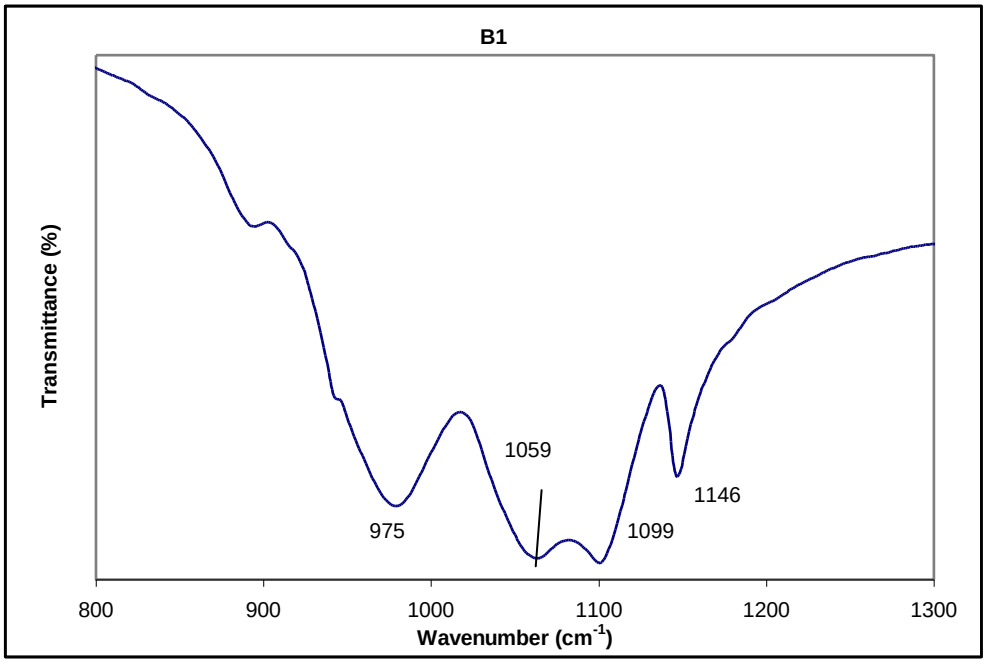

Figure 5.12 FTIR spectrum of sample B1 in the wavenumber 800 to1300 cm^{-1}.

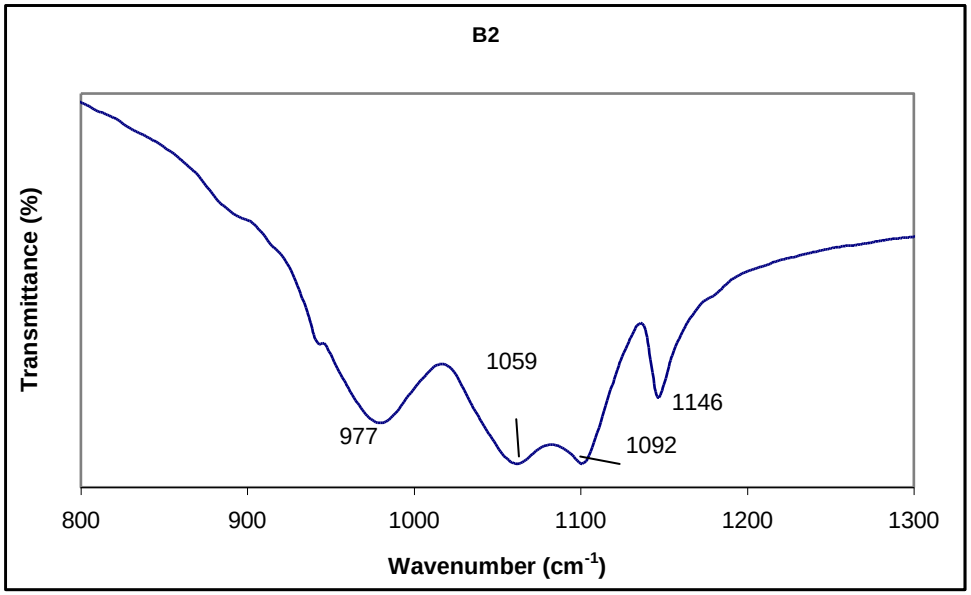

Figure 5.13. FTIR spectrum of sample B2 in the wavenumber 800 to 1300cm^{-1}.

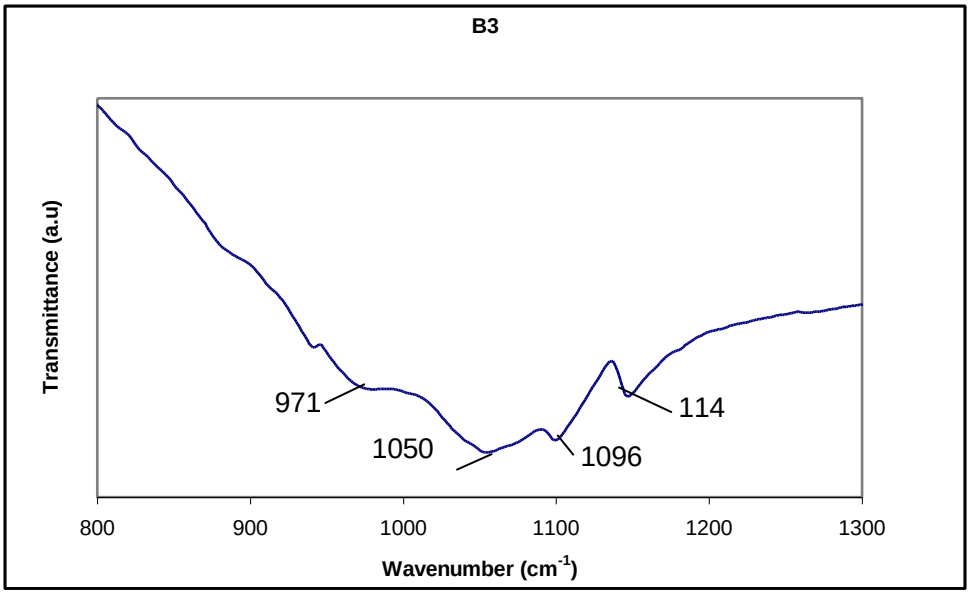

Figure 5.14. FTIR spectrum of sample B3 in the wavenumber 800 to 1300cm^{-1}.

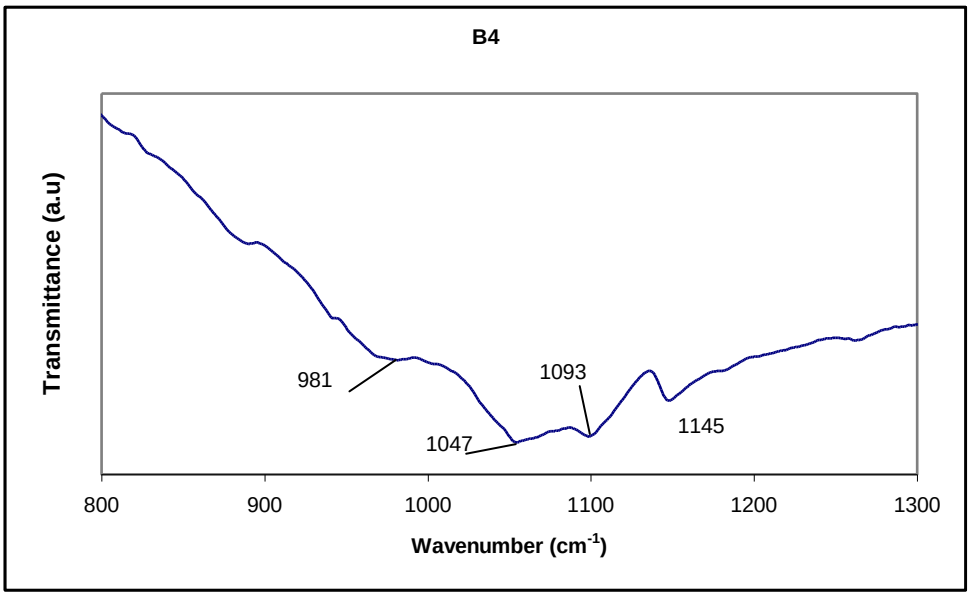

Figure 5.15. FTIR spectrum of sample B4 in the wavenumber 800 to 1300cm^{-1}.

It was reported that, in the region of the internal modes of the phosphate anion (high wavenumber region), the symmetric stretching mode at ν_1=946 cm^{-1}, the doublet at ν_2 = 415 to 464 cm^{-1} and the triplets ν_3 and ν_4 in the regions 1009 to1085 cm^{-1} and 580 to 637 cm^{-1} were observed for $LiNiPO_4$ (Julien et al., 2004). These absorption peaks are due to the stretching and bending vibrations of the PO_4^{3-} polyanions. In the present

work similar absorption peaks were observed. Most of the vibration peaks listed in Table 5.6 are observed in the IR spectra indicating the presence of PO_4^{3-} ions in all samples prepared.

No vibration bands are seen near 750 cm^{-1} in the infrared spectrum which are often due to condensed phosphate (Burba et al., 2006). The absence of vibrating bands in this region suggest that the prepared sample in this work does not contain the condensed phosphate group (P-O-P) impurities.

5.5 Energy Dispersive X-rays Analysis (EDX)

The elemental composition of the pure prepared sample was analysed by EDX analysis. Samples B2 and B3 are not pure and therefore no EDX analysis was carried out on them. Figure 5.16 shows the EDX spectrum for $LiNiPO_4$ calcined at 1000 ^oC for 24 hours. The ratios of Ni:P was determined by this technique. Peaks attributable to nickel and phosphorous are clearly shown. The EDX spectrum indicates the stoichiometries of the prepared samples. The analysis of the spectrum of the samples is presented in Table 5.7

Table 5.7 Starting composition, atomic % and mole ratio between elements in Lithium Nickel Phosphate

Sample		Li	Ni	P
B4	Starting mass(g)	12.53	73.53	34.64
	mole	0.30	0.30	0.30
	No of atoms	1.8×10^{23}	1.8×10^{23}	1.8×10^{23}
	% expected	-	50	50
	% in EDX	-	49	51
	Mole ratio of the elements	1	1	1

For sample B4, the total number of Li, Ni and P atoms is $5.43x10^{23}$. The atomic percentage of Li, Ni and P is 33%, 33% and 33% respectively. The total number of Ni and P atoms is 3.92×10^{23} atoms. The atomic percentage of Ni and P is 50% and 50% respectively which agrees with the results obtained from EDX. Hence the formula $LiNiPO_x$ can be assigned to the prepared sample. Lithium which belongs to group 1 is expected to have +1 oxidation state and oxidation state of oxygen is -2. Thus by conservation of charge, x in $LiNiPO_x$ must be 4 and the charge on nickel can be determined by charge balance between positive and negative charges. The charge balance can be calculated as shown below:

Li^{+1}	Ni^{y}	P^{+5}	=	O_4
(+1)	y	(+5)	=	4(-2)
		6+y	=	-8
		y	=	2

Thus by examining Table 5.7 and the calculation for oxidation numbers, the formula $LiNiPO_4$ is assigned to this sample. The comparison between the calculated results and results obtained from EDX is represented in Table 5.7.

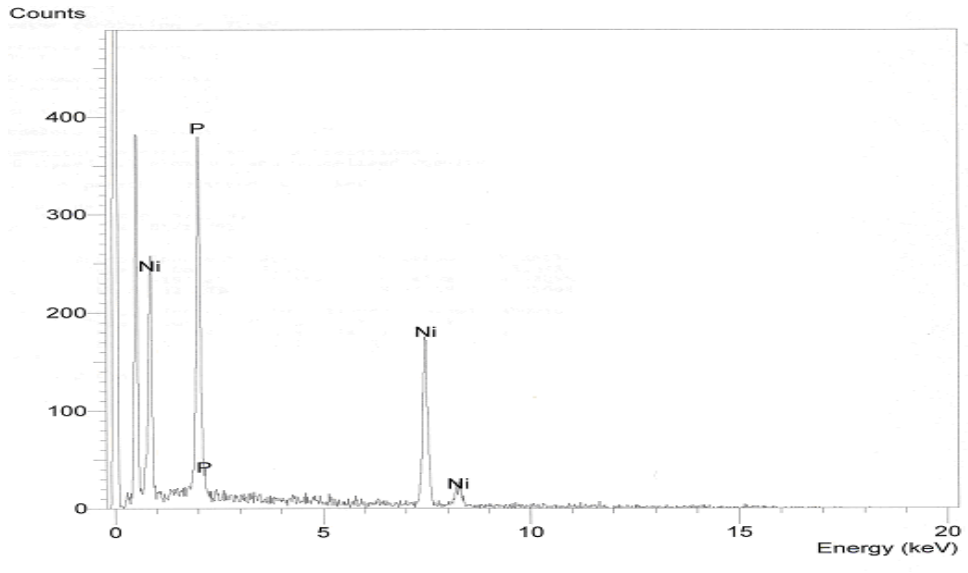

Figure 5.16. EDX spectrum of sample B4.

5.6 Cyclic voltammetry

Cyclic voltammetry was again employed to evaluate the electrochemical properties of $LiNiPO_4$ cathode material. Cyclic voltammetry has the capability for rapidly observing redox behaviour over a wide potential range. Cyclic voltammetry involves cycling of the potential electrode which is immersed in an unstirred solution and measuring the resulting current. The resulting current can be monitored as a function of time or as a function of the electrode potential (Hasel and Burgraaf, 1992). The voltammogram is a plot of current versus potential. Cyclic voltammetry was carried out on sample B4. Sample B4 was prepared by firing at 1000 ^oC for 24 hours. The cyclic voltammograms (CV) for $LiNiPO_4$ / $LiPF_6$+EC+PC+DMC/ Li cell was cycled between 2.5 and 5.5 V versus Li^+/ Li. The cyclic voltammetry experiments were carried out at various scan rates.

5.6.1 Redox behaviour

Figures 5.17, 5.19 and 5.21 show the cyclic voltammograms of the B4 samples at scan rate 0.1 mVs^{-1}, 1mVs^{-1} and 10 mVs^{-1}. During the anodic sweep, lithium ions are extracted from the $LiNiPO_4$ structure and an increase in current with a small hump (anodic peak) was seen and when the potential was scanned in the negative direction i.e from 5.5 V to 2.5 V, a decrease in current (cathodic peak) was obtained.

A pair of redox peaks were observed in all the voltammograms unlike the work done by Ruffo et al. (2005) and Wolfenstine and Allen (2004) where no significant reduction or oxidation peaks in the range 3.5 V to 6.0 V for $LiNiPO_4$. The presence of these peaks demonstrates that lithium ion can reversibly intercalate and

deintercalate into the $LiNiPO_4$ cathode electrode. The redox peaks are representing the redox reactions processes that are taking place in the cells and the suggested redox couple is the Ni^{3+}/Ni^{2+}.

Only sample B4 was analysed by cyclic voltammetry since samples B2 and B3 contained impurities as depicted by the XRD diffractogram in Figures 5.4 and 5.5. The cyclic voltammogram of sample B4 taken at scan rate 0.1 Vs^{-1} is represented in Figure 5.17. At this scan rate i.e 0.1 mVs^{-1} the cyclic voltammogram shows anodic and cathodic peaks at 4.86 V and 4.89 V respectively. However the peaks are not clear, perhaps this is why not many studies are done on this material. Therefore in this work a more detail study was done by enlarging the CV to locate the expected redox peaks. The enlarge CV are depicted in Figures 5.18 (a) and (b). The broken lines in Figures 5.18, 5.20 and 5.22 is to show the deviation from the straight line i.e a peak is possible. The potential difference ΔE between the two peaks is found to be 0.03 V.

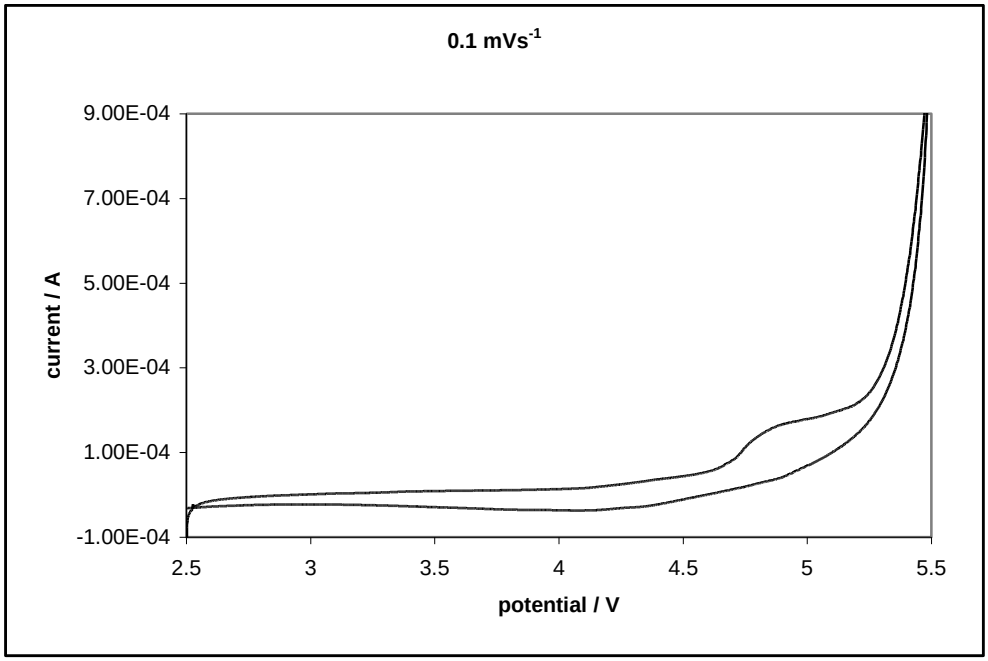

Figure 5.17. Cyclic voltammogram of $LiNiPO_4$ at 0.1 mVs^{-1} scan rate.

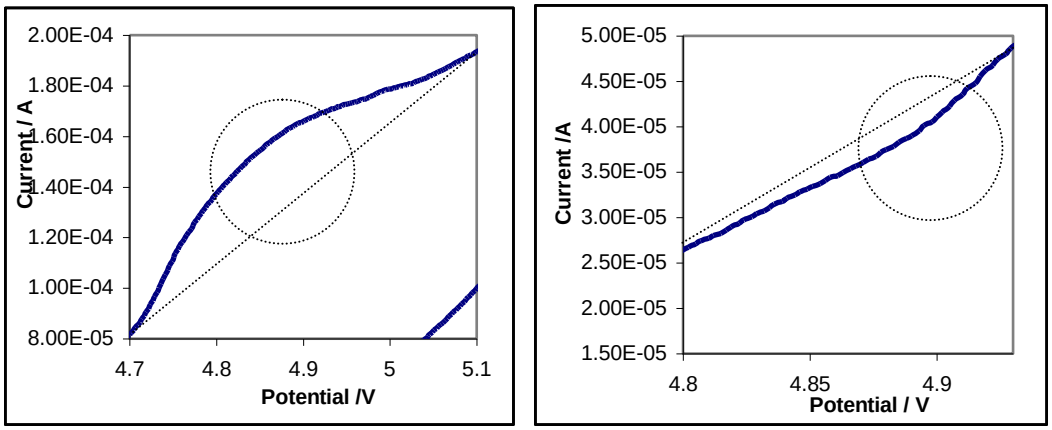

(a) **(b)**

Figure 5.18. Enlarge (a) anodic and (b) cathodic peaks for scan rate 0.1 mVs^{-1}.

In Figure 5.19 where measurements was carried out at scan rate 1.0 Vs^{-1} , there is an increase in the anodic current with a small hump observed at 4.91 V (anodic peak) and a decrease in the cathodic current with a small hump observed (cathodic peak) at 4.85 V. The oxidation and reduction peaks indicates that intercalation and de-intercalation has occurred in the compounds. The cyclic voltammogram are also enlarged to show the position of the anodic and cathodic peaks for scan rate 1.0 m Vs^{-1}. The potential difference ΔE between the two peaks is found to be 0.06V.

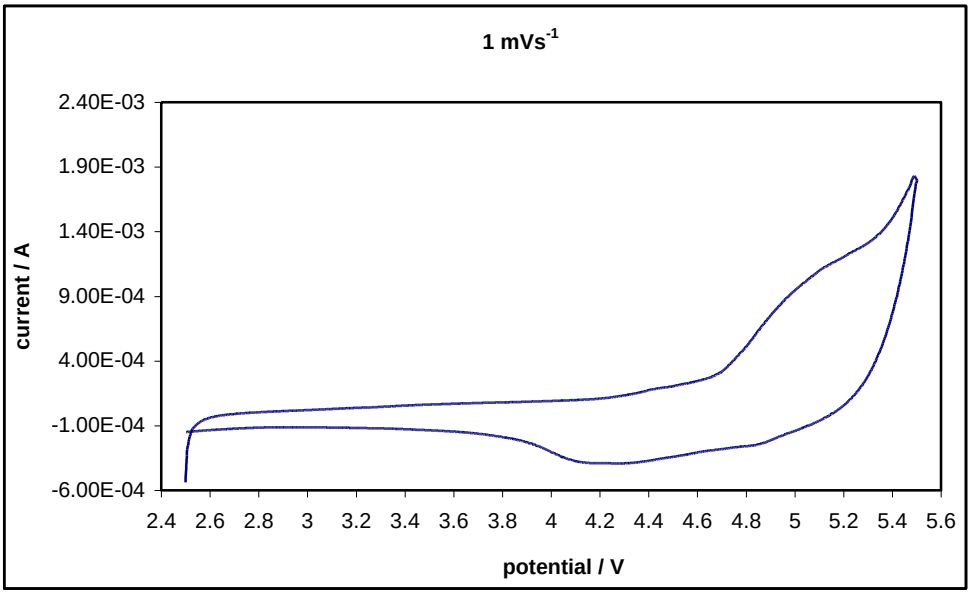

Figure 5.19. Cyclic voltammogram of B4 material at 1 mVs^{-1} scan.

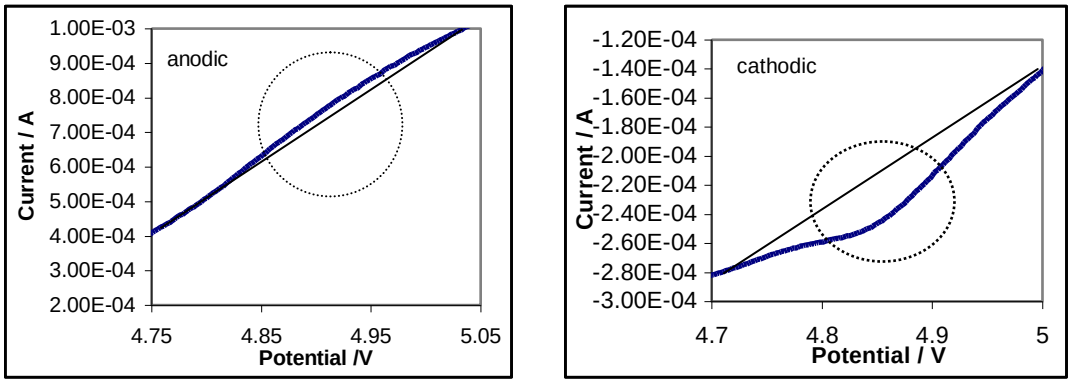

(a) **(b)**

Figure 5.20. Enlarge (a) anodic and (b) cathodic peaks for scan rate 1.0 mVs^{-1}.

Figure 5.21 shows the cyclic voltammetry of the $LiNiPO_4$ sample at scan rate 10 mVs^{-1}. A reduction loop at 4.83 V and an oxidation at 4.96 V was seen in the curve when the material was scanned at 10 mVs^{-1} scan rate. The oxidation and reduction peaks again indicate the lithium ion intercalation and deintercalation. Similar to scan rate 0.1 and 1.0 mVs^{-1}, the anodic and cathodic peaks for scan rate 10 mVs^{-1} are also enlarged as shown in Figures 5.22 (a) and (b). Again the broken lines is to show the deviation from the straight line i.e a peak is possible. The potential difference ΔE between the two peaks is found to be 0.13 V. The large difference indicates that the

electrochemical behaviour is controlled by the diffusion step (Liu et al., 2006). The pair of peaks corresponded to the two phase charge-discharge reaction of the Ni^{3+}/Ni^{2+} redox couple.

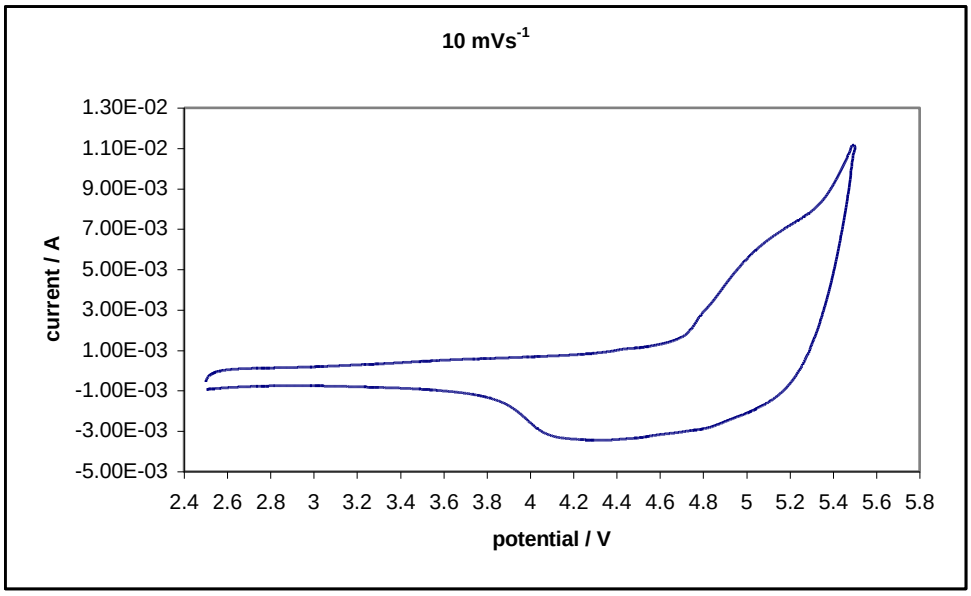

Figure 5.21. Cyclic voltammogram of B4 material at 10 mVs^{-1} scan rate.

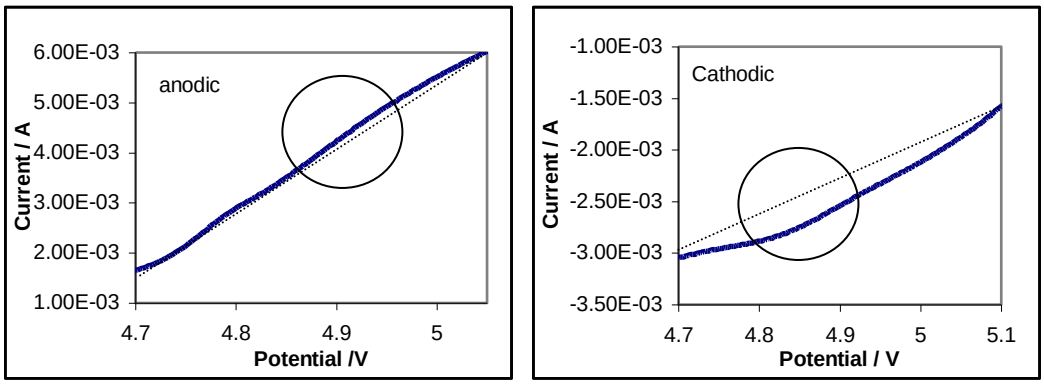

(a) **(b)**

Figure 5.22. Enlarge (a) anodic and (b) cathodic peaks for scan rate 10 mVs^{-1}.

The peak potential difference, ΔE (E_{pa}-E_{pc}) for the sample with scan rates 10 mVs^{-1}, 1.0 mVs^{-1} and 0.1 mVs^{-1} are shown in the Table 5.8 below. Similar to the trend observe for $LiMnPO_4$ in Chapter 4, ΔE also gets smaller as scan rate decreases for $LiNiPO_4$ sample.

Table 5.8. ΔE values for $LiNiPO_4$ sample at 0.1, 1.0 and 10 mVs^{-1} scan rates.

Sample	Scan rate (mVs^{-1})	Anodic peak, E_{pa}	Cathodic peak, E_{pc}	ΔE
$LiNiPO_4$	10	4.96	4.83	0.23
	1.0	4.91	4.85	0.06
	0.1	4.86	4.89	0.03

5.5.2 Formal Electrode Potential

In order to determine the formal electrode potential E_f , Equation (4.13) was employed again. The formal reduction potential E_f for an electrochemically reversible couple is centred between the anodic peak, E_{pa} and cathodic peak, E_{pc} . Table 5.9 shows the list of calculated formal electrode potential for $LiNiPO_4$. Values for anodic and cathodic peaks were taken from cyclic voltammogram measured at scan rate 1.0 mVs^{-1}. From Table 5.9 the calculated mean formal electrode potential for the system is 4.88 V versus Li^+/Li .

Table 5.9. List of calculated formal potential for $LiNiPO_4$ at scan rate 1.0 mVs^{-1}.

Sample	Anodic peak potential E_{pa}	Cathodic peak potential E_{pc}	Formal potential (E_f)
$LiNiPO_4$	4.91	4.85	4.88

5.5.3 Relationship between i_p and $\upsilon^{1/2}$

The objective of this study is to investigate the relationship between the peak currents, i_p and the square root of the scan rate ($\upsilon^{1/2}$) for a positive scan of $LiNiPO_4$ cathode material. In order to investigate the relationship between the peak currents, i_p

and the square root of the scan rate ($\upsilon^{1/2}$) various scan rates were recorded as depicted in Figures 5.23, 5.24 and 5.25. Figures 5.27 show the relationship of peak currents, i_p and $\upsilon^{1/2}$ for $LiNiPO_4$. Similar to the results obtained for $LiMnPO_4$ shown in Chapter 4 , the regression value, R^2 for $LiNiPO_4$ cathode material in this study also lies in the range 0.990 to 0.999. This indicates that all points lie on an almost perfect straight line. The linear relationship reveals that i_p is proportional to $\upsilon^{1/2}$ and these results demonstrate that Li^+ ions are intercalated and deintercalated reversibly in this material .

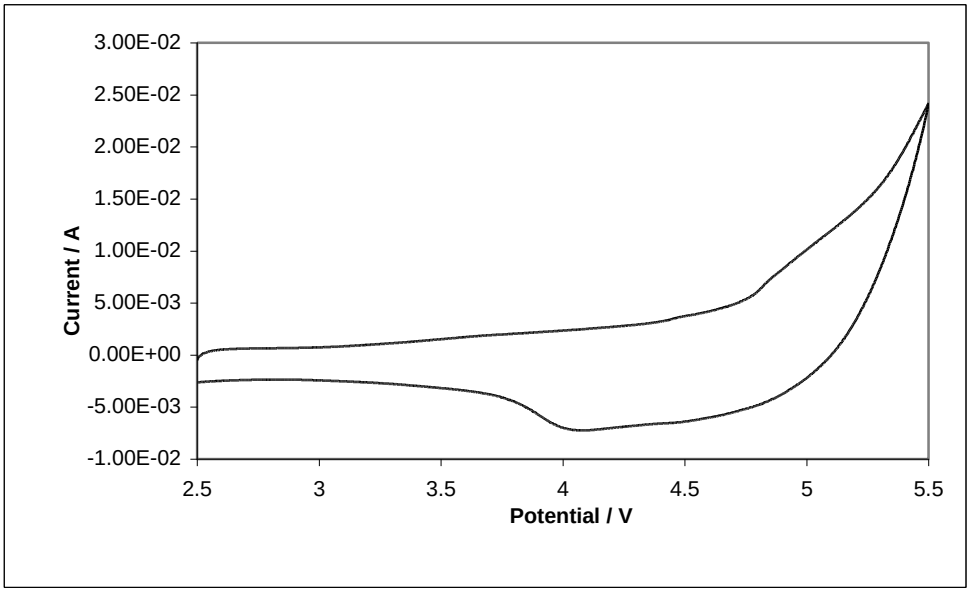

Figure 5.23. Cyclic voltammogram of $LiNiPO_4$ at 40 mVs^{-1} scan rate.

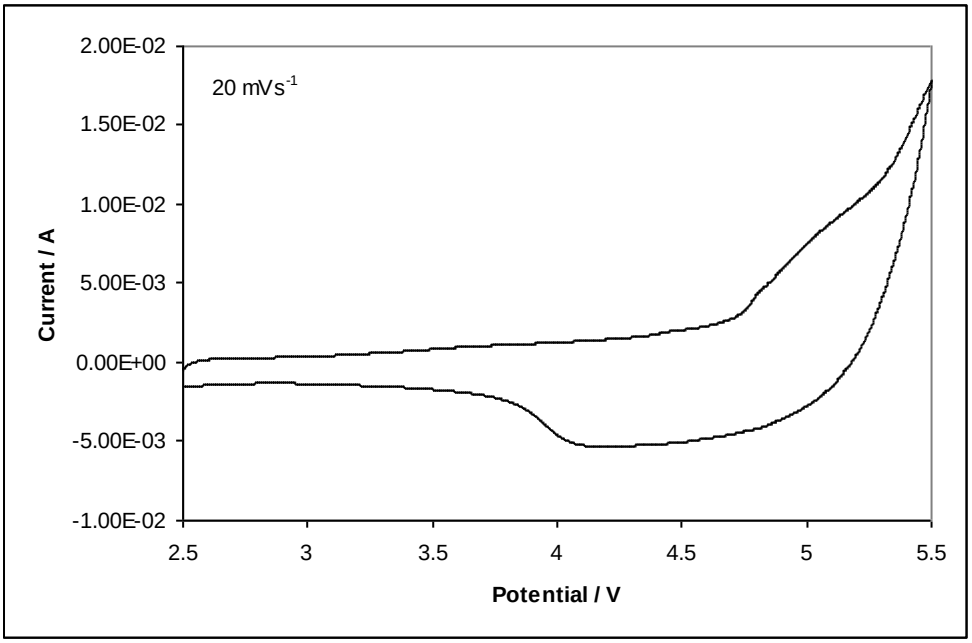

Figure 5.24. Cyclic voltammogram of $LiNiPO_4$ at 20 mVs^{-1} scan rate.

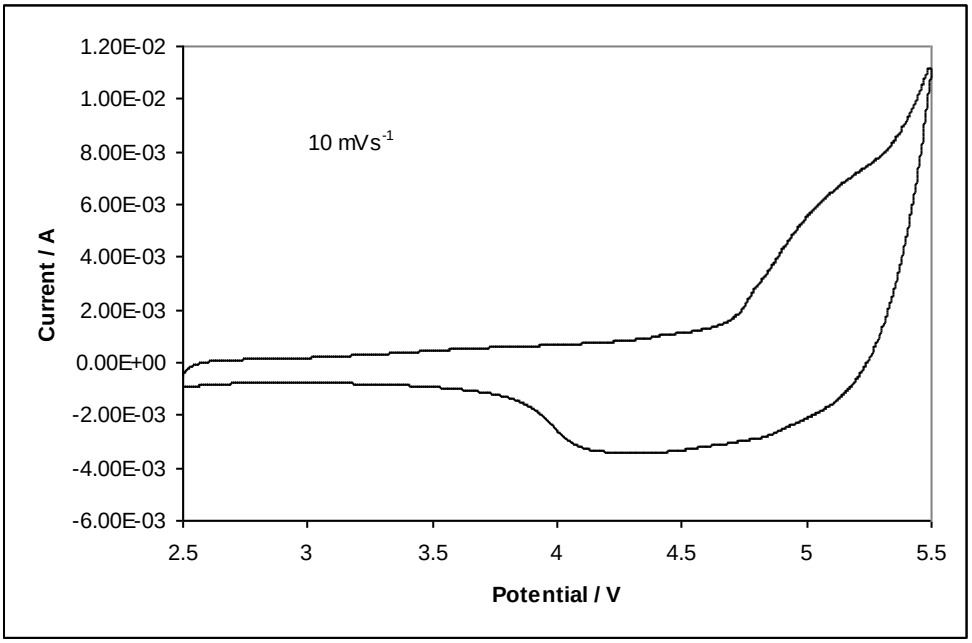

Figure 5.25 . Cyclic voltammogram of $LiNiPO_4$ at 10 mVs^{-1} scan rate.

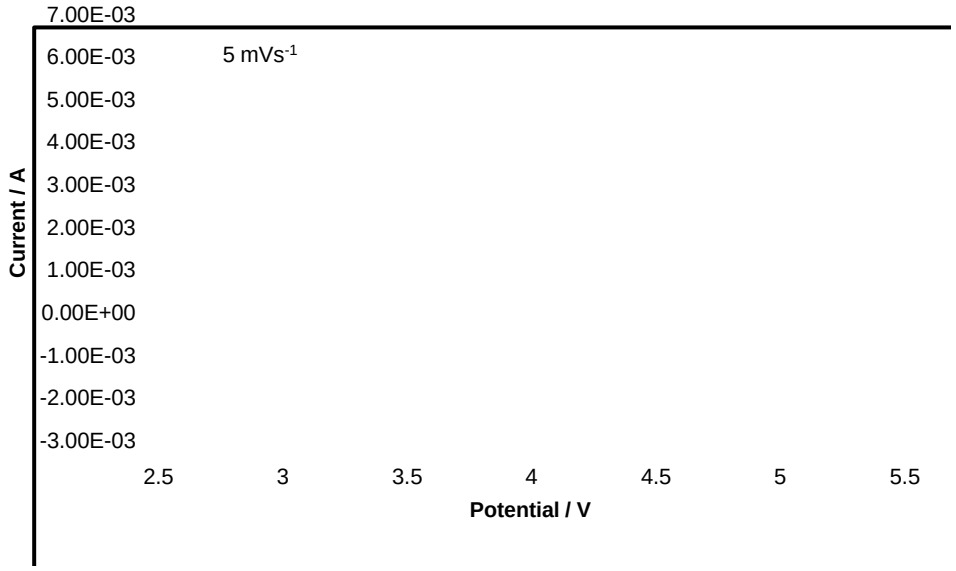

Figure 5.26. Cyclic voltammogram of $LiNiPO_4$ at 5 mVs^{-1} scan rate.

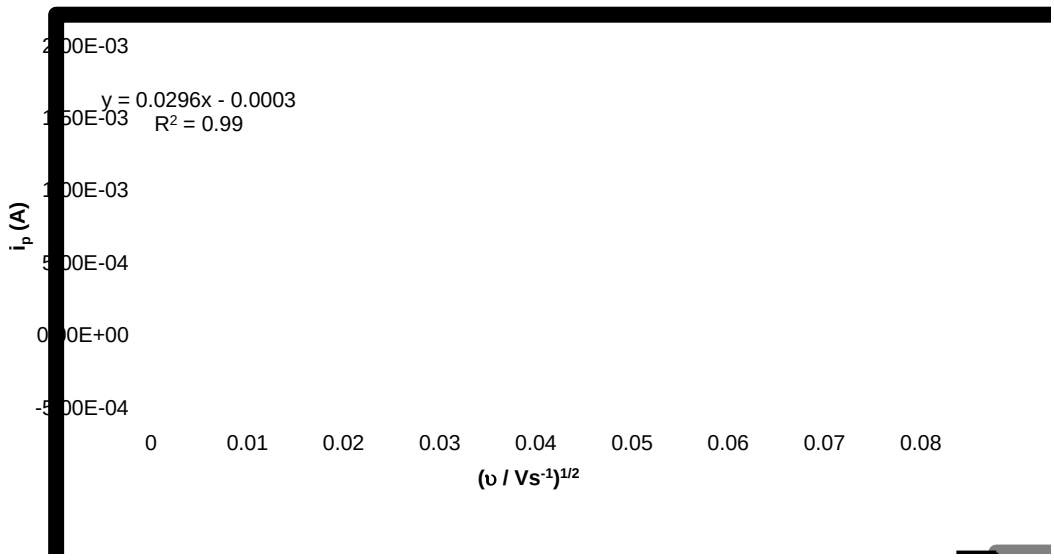

Figure 5.27. Relationship between the peak currents (i_p) and $\upsilon^{1/2}$ for a positive scan of sample $LiNiPO_4$.

5.5.4 Diffusion coefficient , D_{Li}^{+}

Since peak currents, i_p is proportional to $\upsilon^{1/2}$, the diffusion coefficient of the the Li^+ ions in the present cathode materials can be estimated from the Randles –Sevcik

equation (Equation 4.14) which was described in Chapter 4. $LiNiPO_4$ has a bulk density of 3.9 g cm^{-3} with a molar mass of 160 g mol^{-1} which corresponds to a Li concentration of 0.024 mol cm^{-3}. A, the area of electrode is 0.785cm^2. Figure 5.27 revealed that the slope of the straight line is 0.030 $As^{1/2}V^{-1/2}$. Table 5.10 lists the data used for the calculation of the diffusion coefficient for sample B4 i.e $LiNiPO_4$. The calculated value for the diffusion coefficient for $LiNiPO_4$ is 3.50x 10^{-11} cm^2s^{-1}.

Table 5.10 . List of data used for the calculation of the diffusion coefficient and the calculated diffusion coefficient value for $LiNiPO_4$.

Sample	**Slope $As^{1/2}V^{-1/2}$**	**Density, gcm^{-3}**	**Molar mass $gmol^{-1}$**	**C_{Li}^{+} $molcm^{-3}$**	**D_{Li}^{+} cm^2s^{-1}**
$LiNiPO_4$	0.030	3.79	160	0.024	3.50x 10^{-11}

Similar to $LiMnPO_4$, diffusion coefficient values of $LiNiPO_4$ in the literature are also rare and thus no comparison can be made.

5.5.5 Cell capacity

Table 5.9 shows the density of charge (Q), recorded, capacity and the specific capacity of $LiNiPO_4$. Sample $LiNiPO_4$ could only deliver 44.8 $mAhg^{-1}$. The mass of the active material used was 0.025 g.

Table 5.11. The charge density, capacity and specific capacity for $LiNiPO_4$.

Sample	Scan rate (mVs-1)	Q (As)	Capacity (mAh)	Specific capacity (mAh/g)
$LiNiPO_4$	0.1	4.01	1.12	44.8

The results above is comparable to the value obtained by Wolfenstine and Allen (2004) who obtained 4 mAh/g for the discharge capacity for $LiNiPO_4$. The $LiNiPO_4$ powders in their work was prepared by the solid state reaction method. As for Ruffo et al. (2005) the $LiNiPO_4$ powders in their study was prepared via the polymeric precursor method and no deintercalation process occurred in the $LiNiPO_4$ sample.

5.6 Summary

$LiNiPO_4$ were successfully synthesized by the sol-gel method with tartaric acid as the chelating agent. The firing of the precursor was carried out in air ambient and is of low cost. TGA studies showed that the weight of the precursor material stabilizes at temperatures above 725 ^oC. The weight loss obtained from the thermogram supports the mechanism of reactions proposed. Literature survey shows that the reactions mechanism suggested in this work has not been reported.

The XRD results revealed that the $LiNiPO_4$ which firing took place at 1000 ^oC was pure. By using information obtained from the FWHM, the crystallite size of the pure $LiNiPO_4$ was found to be 66 nm. Nanosized $LiNiPO_4$ was successfully prepared in this work. FTIR results confirmed the presence of PO_4^{3-} anions.

The voltammograms obtained show the presence of redox peaks corresponding to the intercalation and deintercalation of lithium ion. The calculated diffusion coefficient and the specific capacity value for $LiNiPO_4$ is 3.50 x 10^{-11} cm^2s^{-1} and 44.8 $mAhg^{-1}$ respectively. Specific capacity calculated from charge/ discharge curves for $LiNiPO_4$ reported are 4 mAh g^{-1} or none. The results obtained in this work are comparable to the values reported.

CHAPTER 6

RESULTS

LITHIUM IRON PHOSPHATE

6.1 Introduction

Lithium iron phosphate is an excellent candidate for cathode material in rechargeable lithium batteries. Among the phospho-olivine, $LiMPO_4$ (M=Fe, Mn, Co, Ni) cathode materials for Li-ion battery, $LiFePO_4$ has attracted particular attention due to its low cost , high energy density, non-toxicity and high theoretical specific capacity of 170 mA h g^{-1} (Takahashi, 2002; Padhi et al., 1997). It also exhibits a small capacity fade after several hundreds cycle (Park et al., 2003). Although $LiFePO_4$ has lots of advantages, it is difficult to synthesize since the Fe^{2+} ions are easily oxidized to Fe^{3+}. Several kinds of synthesis have also been employed, including solid-state reaction, sol–gel, mechanochemical, hydrothermal, coprecipitation and more recently microwave (MW) synthesis (Kwon et al., 2006; Hsu et al., 2004; Yang et al., 2002; Franger et al., 2003; Arnold et al., 2003; Higuchi et al., 2003).

At present almost all techniques used in preparing $LiFePO_4$ had to control the oxidation state of Fe^{2+} by the use of a reductive or inert gas flow. Besides that most methods would also employ a reducing agent to prohibit the conversion of Fe^{2+} to Fe^{3+}. The use of inert gas will increase the synthesis cost of $LiFePO_4$ (Guo et al., 2007). In this study, the $LiFePO_4$ was prepared by the chemical precipitation and low temperature sterilization method in the absence of both inert gas and reducing agent.

The preparation does not involve any heating steps at high temperatures in inert or reducing atmosphere as is usually required in other methods. This method was found to be simple and of low cost.

Structural and morphological characterizations were investigated by X-ray diffraction (XRD), and Energy Dispersive X-rays Analysis (EDX) while the electrochemical properties of $LiFePO_4$ in non aqueous electrolytes were investigated by cyclic voltammetry. The results of the investigations are presented in this chapter.

6.2 X-Ray Diffraction (XRD)

X-ray diffraction analysis was carried out on the $LiFePO_4$ sample synthesised by the chemical precipitation and low temperature sterilization heating method. Figure 6.1 shows the X-ray diffraction patterns of the prepared $LiFePO_4$. The XRD pattern showed very distinct peaks for the sample which clearly indicates the crystalline nature of the material. The XRD pattern are dominated by (011),(111), (121) and (131) lines with peaks at 2θ =20.7 ^{o}, 25.5 ^{o}, 29.6 ^{o} and 35.5 ^{o} respectively. The diffractogram can be indexed to a single-phase material having an orthorhombic ordered olivine structure with space group Pnmb, due to its similarity with the JCPDS No.40-1499 data file. The comparison between the experimental results and the JCPDS are found to be in good agreement. This result is also similar to the previous reports (Hsu et al., 2004; Liu et al., 2006; Jin et al., 2008) on the XRD patterns of $LiFePO_4$ powder prepared by the conventional method of synthesis.

Table 6.1 lists the peaks of the sample and the peaks in the JCPDS for $LiFePO_4$ (No 40-1499) for comparison. Thus olivine phase $LiFePO_4$ with minor impurities was successfully synthesized in this work.

Table 6.1. XRD peaks for lithium iron phosphate as compared to the JCPDS (No .40-1499)

Sample F, 2θ(°)	Intensity (%)	JCPDS for $LiFePO_4$ 2θ (°) (40-1499)	Intensity (%)	hkl
17.1	23	17.1	34	020
20.7	35	20.8	76	011
22.6	7	22.6	26	120
24.0	4	24.0	10	101
25.6	100	25.5	70	111
26.9	21	IMPURITIES		
27.4	15			
29.8	62	29.7	100	121
32.2	33	32.2	34	031
35.6	91	35.5	81	131
36.6	40	36.5	25	211
37.8	12	37.8	16	140
39.3	11	39.3	9	012
39.6	3	39.6	14	221
39.7	27	39.7	19	041
42.1	8	42.2	16	112
49.3	7	49.1	8	202
50.2	5	50.2	11	311
52.4	11	52.4	23	222
52.6	22	52.6	13	042
54.9	10	54.8	12	142
55.4	10	55.4	13	160
56.8	11	56.5	14	331
58.3	11	58.1	8	340

Two low intensity peaks around 2θ = 26.9 ^{o} and 27.2 ^{o} are also observed. These peaks are thought to be pyrophosphate which is probably due to the polymerization of the phosphoric acid used in the synthesis as shown in the equation below. Lithium pyrophosphate, $Li_4P_2O_7$ is then formed (Franger et al., 2003). These impurity peaks were also observed by Franger and co-workers who prepared $LiFePO_4$ via the co-precipitation technique and heat treated the sample at 550 ^{o}C for 12 hours under inert atmosphere.

$$2H_3PO_4 \longrightarrow H_4P_2O_7 + H_2O \qquad (6.1)$$

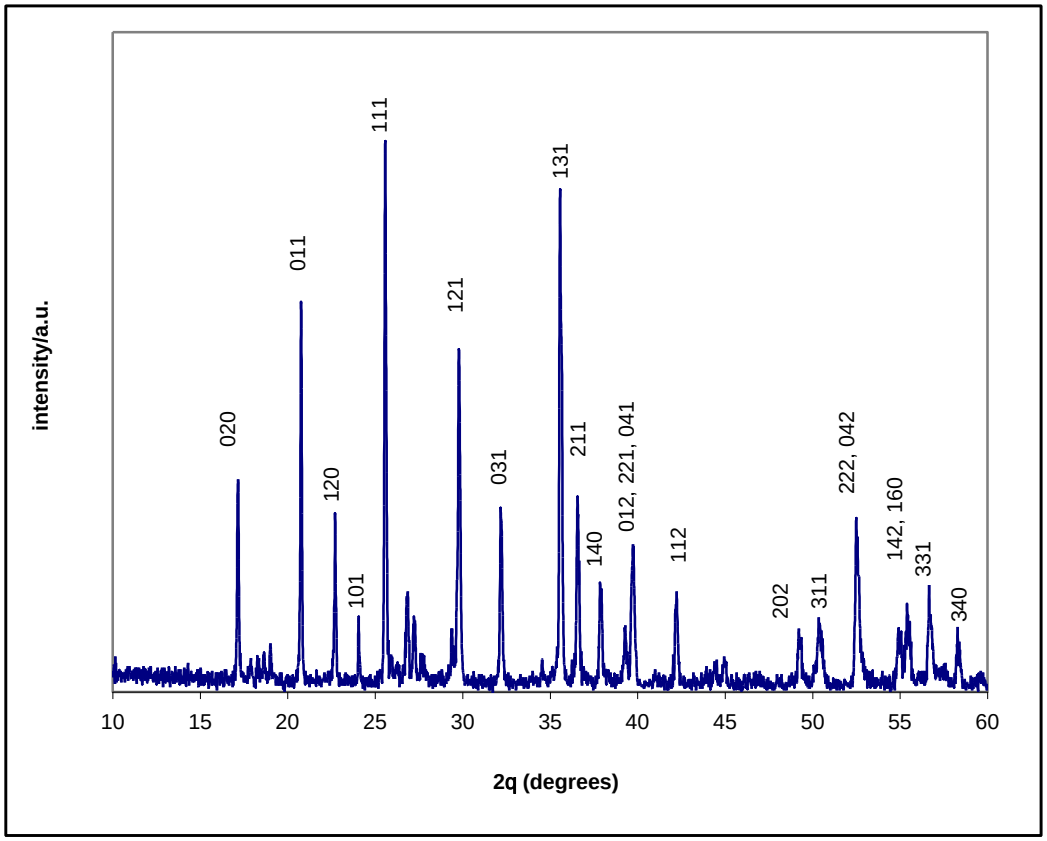

Figure 6.1. X-ray diffractogram of $LiFePO_4$.

6.2.1 Crystallite size

The crystallite size (L) was estimated by measuring the width of the the three highest peaks in the diffractograms using the conventional Scherrer equation (Equation 4.12) as shown in Chapter 4. The mean value of L computed from the (011), (111), (121) and (131) diffraction peaks is 58 nm. Yonemura et. al (2004) estimated the average particle size for $LiFePO_4$ to be 95 nm using the conventional Scherrer equation while Prosini et al. (2003) obtained the grain size of $LiFePO_4$ to be 85 nm after 1hour heating at 550 ^oC to 90 nm after 5 hours heating at 550 ^oC (Prosini et al., 2003). Hsu et al. who prepared $LiFePO_4$ via sol gel method with citric acid as the chelating agent calculated the sample grain size to be between 47, 48, 50 and 51 nm for the sintering time of 2,10, 20 and 30 hours respectively. The sample was sintered after drying for one week (Hsu et al., 2004).

6.3 Fourier Transform Infrared Spectroscopy (FTIR)

FTIR absorption measurements were carried out in order to determine the main features of the $LiFePO_4$ under study. Spectral assignments for IR bands of $LiFePO_4$ vibrations have already been reported in earlier works and those assignments are adopted here (Burba and Frech, 2006; Salah et al., 2005).

The vibrational spectroscopic data available from these measurements provide important information on the structure. Figure 6.2 show the FTIR spectra in the wave number range 850 to 1400 cm^{-1}. It was reported that in the region of the internal modes of the phosphate anion (high-wavenumber region), the asymmetric stretching mode as identified at ν_1 = 965 cm^{-1}, the doublet ν_2 = 466 to 503 cm^{-1}; and the triplets ν_3 and ν_4 in the regions 1051 to 1093 cm^{-1} and 578 to 645 cm^{-1} respectively (Salah et al., 2006).

Infrared absorption spectra of the intramolecular stretching vibrations (ν_1 and ν_3) for the synthesised $LiFePO_4$ sample, are shown in Figure 6.2 and compared with IR bands of $LiFePO_4$ from previous researchers (Salah et al., 2006; Salah et al., 2005; Burba and Frech., 2004). No extra line is observed with respect to pure $LiFePO_4$. The bands at 1055, 1065, and 1134 cm^{-1} are assigned to ν_3 vibrations and the ν_1 modes are identified at 988 cm^{-1}. Table 6.2 showed the comparison with the reported positions for crystalline $LiFePO_4$. The IR bands appear exactly at the same positions as were reported (Salah et al., 2006).

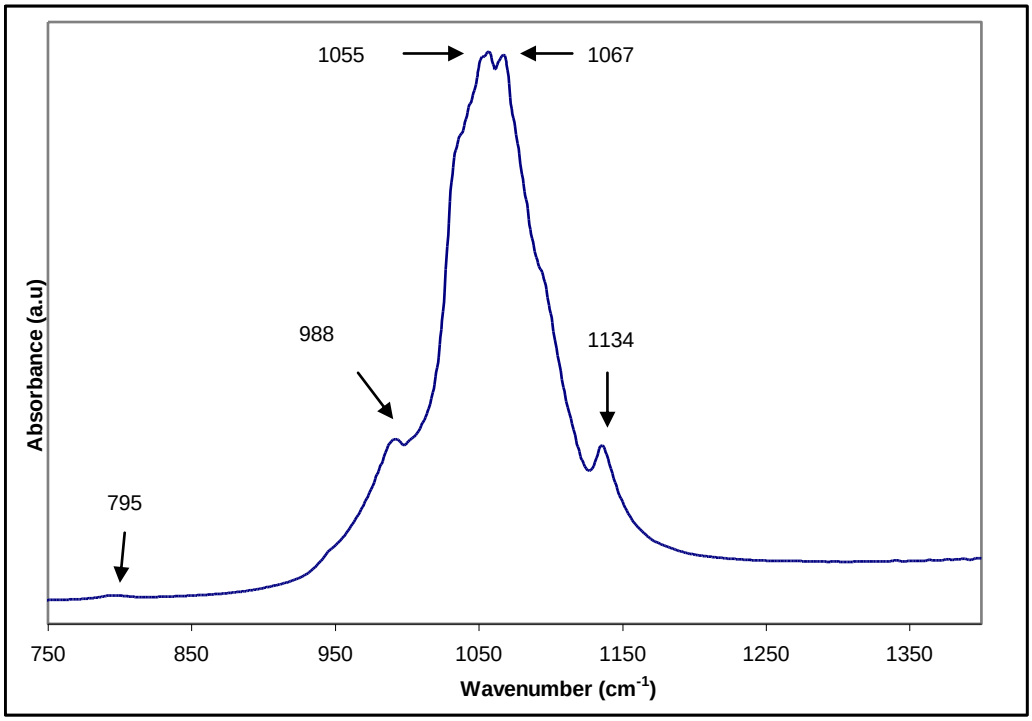

Figure 6.2 Infrared spectrum of $LiFePO_4$ in the wavenumber 750 cm^{-1} to 1400 cm^{-1}.

Figure 6.3 shows infrared spectra of $LiFePO_4$, between 400 to 750 cm^{-1}, where the intramolecular PO_4^{3-} bending modes (ν_2 and ν_4) occur. The bands in the spectral range 400–550 cm^{-1} are sensitive to the local lithium environment (Salah et al., 2006). Isotopic substitution studies on $LiMPO_4$ (M = Fe, Mg, and Ni) have suggested that the bands at 506 and 470 cm^{-1} might be Li^+ ion "cage modes" (Burba and Frech, 2006). In these modes, Li^+ ions undergo translatory vibrations in a potential energy environment determined by the nearest neighbour oxygen atoms (Burba and Frech, 2007). The FTIR spectrum of the sample indicates the presence of characteristic vibrational bands of olivine structure as shown in Table 6.2.

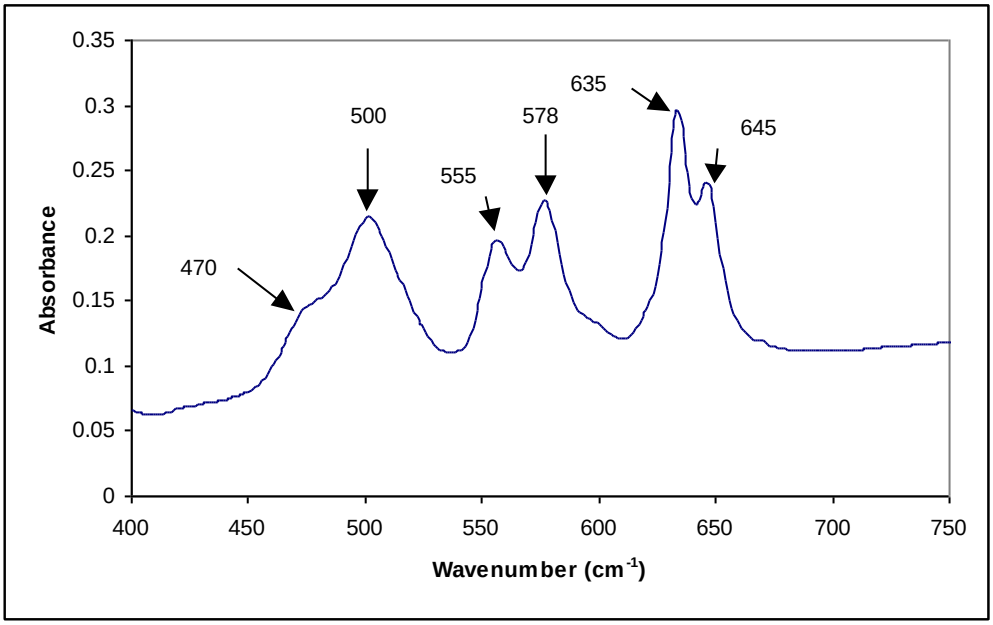

Figure 6.3. Infrared spectrum of $LiFePO_4$ in the wavenumber 400 cm^{-1} to 750 cm^{-1} .

Table 6.2 Wavenumbers and assignments of the FTIR bands of $LiFePO_4$.

Sample	Experiment	Wavenumber (cm^{-1}) reported	Assignments	References
$LiFePO_4$	988	965 (singlet)	ν_1	Jozwiak et al., 2008 Burba and Frech, 2007
	506,556	466–503 (doublet)	ν_2	
	1134,1065,1055	1051–1093 (triplet)	ν_3	
	578,634,646	578–645 (triplet)	ν_4	

The lack of bands at 1020, 990, 890 and 470 cm^{-1} discard the presence of FeOOH, $Fe_3(PO_4)_2$, α-FeOOH and ∂–FeOOH respectively in the sample (Borras et al., 2000). A new peak was observed at 795 cm^{-1}. This peak is attributed to the asymmetric vibrations of P–O–P bridging bonds in $P_2O_7^{-4}$ units and are characteristic for pyrophosphate materials (Jozwiak et al., 2008) which was the impurity found in this sample.

6.4 Energy Dispersive X-rays Analysis (EDX)

Figure 6. 4 shows the EDX spectra of $LiFePO_4$. The expected atomic percentages and EDX atomic percentages of the elements are listed in Table 6.3. It has been found that the Fe: P ratio to be 1:1 which agree with the $LiFePO_4$ stoichiometry.

Table 6.3 Atomic % of elements and mole ratio between elements in lithium iron phosphate.

Sample		Li	Fe	P
$LiFePO_4$	Starting mass(g)	10.07	22.24	7.86
	No of moles	0.24	0.08	0.08
	No of atoms	1.44×10^{23}	4.82×10^{22}	4.82×10^{22}
	Atomic % expected	-	50	50
	Atomic % in EDX	-	49.8	50.2

In this sample the total number of Li, Fe and P atoms is 2.40×10^{23}. The atomic percentage of Li, Fe and P is 60 %, 20 % and 20 % respectively. The total number of Fe and P atoms is 9.64×10^{22} atoms. The atomic percentage of Fe and P is 50 % and 50 % respectively which agrees with the results obtained from EDX. Hence the formula $LiMnPO_x$ can be assigned to the prepared sample. By the same argument as discussed in Chapter 4 and Chapter 5 the formula $LiFePO_4$ is assigned to this sample. Here the analysis shows that the iron +2 oxidation state is maintained after preparing the sample in the absence of inert gas.

In the preparation of $LiFePO_4$, the reacting materials were mixed according to the equation below,

$$3LiOH + FeSO_4 + H_3PO_4 \longrightarrow LiFePO_4 + Li_2SO_4 + 3H_2O \quad (6.2)$$

Although the starting mole ratio of LiOH: $FeSO_4$: H_3PO_4 is 3:1:1, the final product is $LiFePO_4$ as can be seen from the EDX results that the ratio of Fe: P is 1:1 . The excess Li formed Li_2SO_4 as a by product as shown in Equation 6.2. As Li_2SO_4 is soluble in water, it can be removed by washing with distilled water. The $LiFePO_4$ formed was then washed several times with distilled water and the filtrate was tested with barium chloride solution ($BaCl_2$) until no more SO_4^{2-} ions could be detected. In the presence of SO_4^{2-} ion the $BaCl_2$ solution will turn cloudy. The identity of the sample is also confirmed by XRD in Section 6.2 of this Chapter.

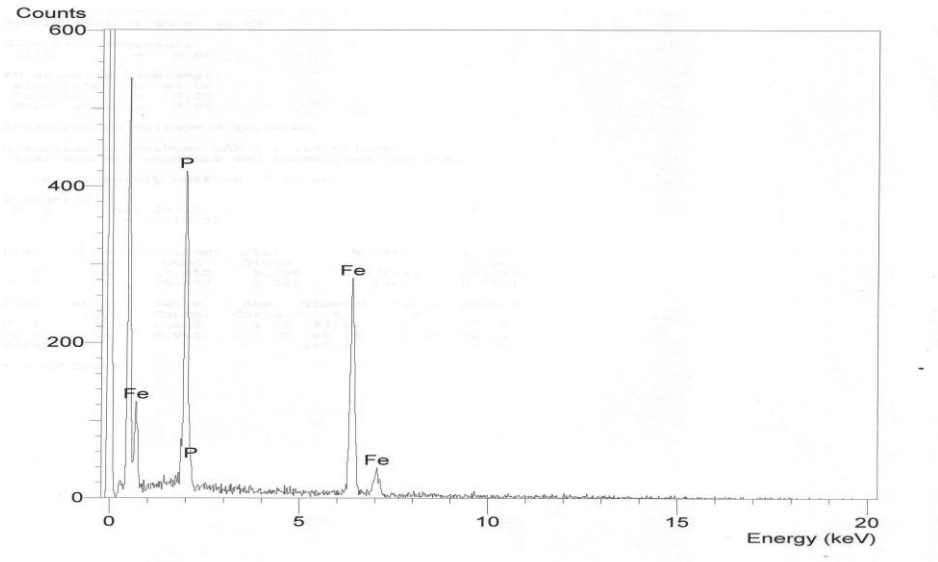

Figure 6.4. EDX spectra of $LiFePO_4$.

6.5 Cyclic Voltammetry

Cyclic voltammetry is the most widely used technique for acquiring qualitative information about electrochemical reactions. Study on the cyclic voltammogram behavior of lithium iron phosphate is essential in order to determine the extent of electrochemical reversibility of a redox reaction and to evaluate the feasibility of the material as an active battery electrode (Mi et al., 2007).

Cyclic voltammetry experiments were done at room temperature using Li foil as the reference and counter electrode. The working electrode was the synthesized $LiFePO_4$ and experiments were carried out with scan rates at the range of 0.1 to 50 mVs^{-1}. The potential was scanned from 2.5 V to 4.2 V.

6.5.1 Redox behaviour

In Figure 6.5 the cyclic voltammogram exhibited a pair of a pair of redox peaks due to the gaining and withdrawal of electrons by the iron species in $LiFePO_4$. It can be seen that during the anodic sweep, lithium ions are extracted from the $LiFePO_4$ structure. An oxidation peak is located at 3.80 V versus Li^+/Li. The anodic peak is due to the oxidation of Fe^{2+} to Fe^{3+} in $LiFePO_4$ When the potential was scanned from 4.20 V to 2.50 V a reduction peak occurred at 3.20 V corresponding to lithium insertion into the $LiFePO_4$ structure. The pairs of peaks corresponded to the two phase charge-discharge reaction of the Fe^{3+}/Fe^{2+} redox couple.

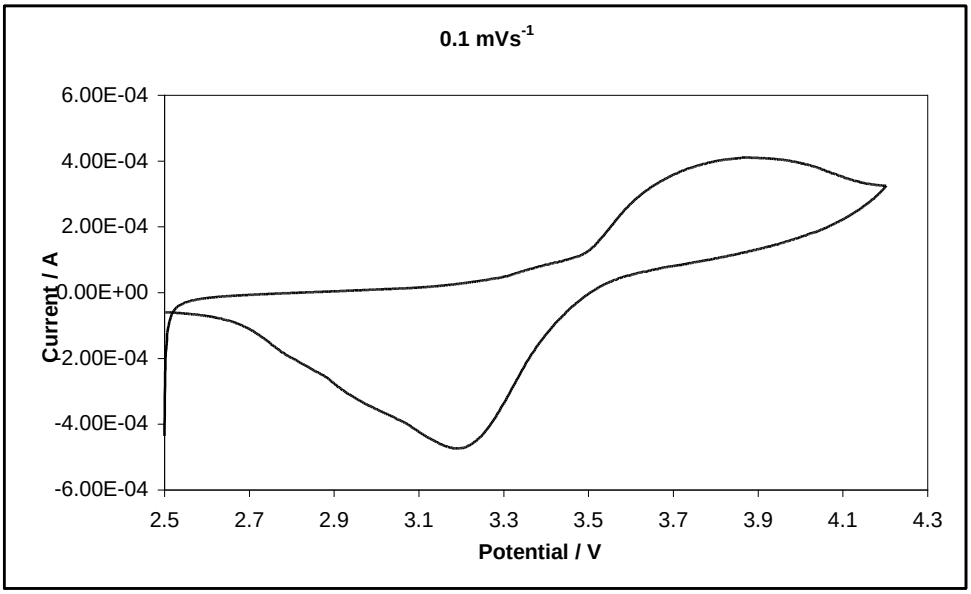

Figure 6.5. Cyclic voltammogram of $LiFePO_4$ at scan rate 0.1 mVs^{-1}.

The appearance of the redox peaks is due to the electron accepting and electron donating of the iron species in $LiFePO_4$. Iron is the primary electron donating or accepting centre. The absence of other peaks is indicative that there are no electroactive iron impurities (Palomares et al., 2007).

In Figure 6.6 the cyclic voltammogram taken at scan rate 0.25 mVs^{-1} is depicted. The cyclic voltammogram revealed that, at scan rate 0.25 mVs^{-1} an oxidation peak at 3.78 V and a reduction peak at 3.13 V are observed.

From Figure 6.7, it can be deduced that at scan rate 0.5 mVs^{-1}, overall there is an increase in anodic current with a small hump at 3.83 V and a decrease in cathodic current with a small hump at 3.08 V. These humps are taken to be the anodic and cathodic peaks respectively.

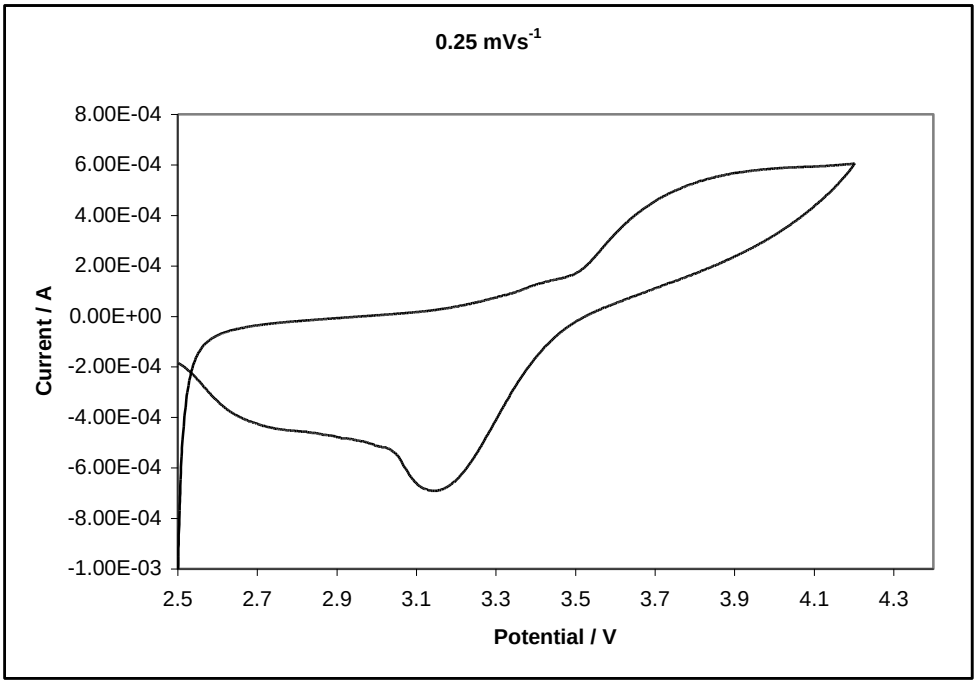

Figure 6.6. Cyclic voltammogram of $LiFePO_4$ at scan rate 0.25 mVs^{-1}.

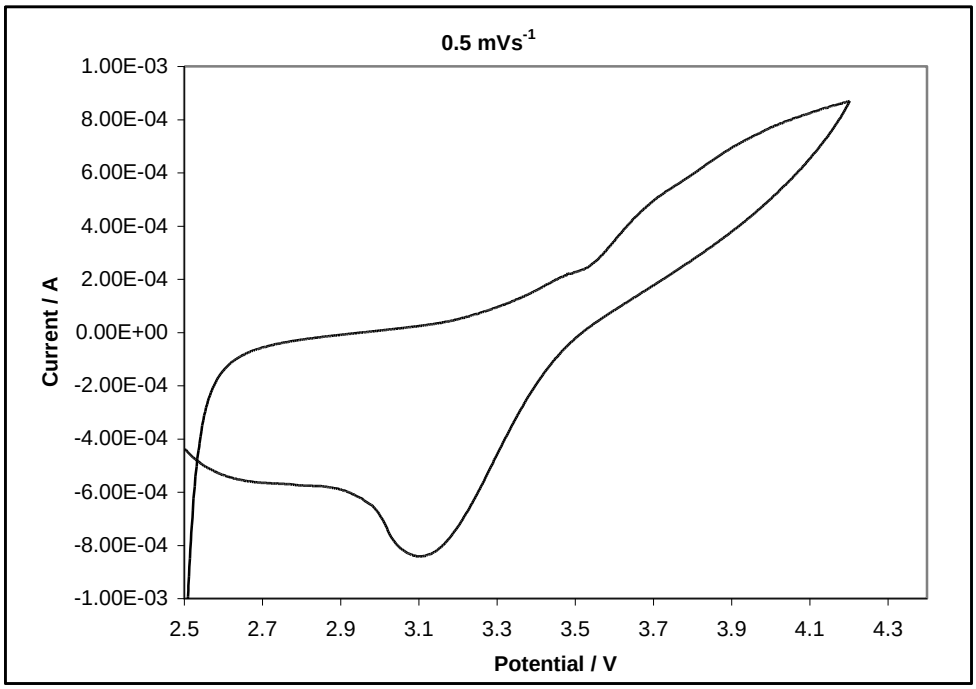

Figure 6.7. Cyclic voltammogram of $LiFePO_4$ at scan rate 0.5 mVs^{-1}.

The ratio of the anodic to cathodic peak currents are found to be 0.93, 0.93 and 0.90 for scan rates 0.10, 0.25 and 0.50 mVs^{-1} respectively which is close to one i.e $i_{pa} / i_{pc} = 1$ which is a characteristic of a reversible system.

The effect of scan rates on the redox behaviour of $LiFePO_4$ was also investigated. Figures 6.8 shows the six cyclic voltammograms taken at scan rates 5 mVs^{-1}, 10 mVs^{-1}, 20 mVs^{-1}, 30 mVs^{-1}, 40 mVs^{-1} and 50 mVs^{-1}.

The cylic voltammogram shown in Figures 6.5, 6.6, 6.7 and 6.8 reveal that the peak potential difference, ΔE (E_{pa} - E_{pc}) between the two peaks increases as scan rate increases. Table 6.4 shows (E_{pa} - E_{pc}) at various scan rates calculated from Figures 6.5, 6.6, 6.7 and 6.8 for $LiFePO_4$ cathode material.

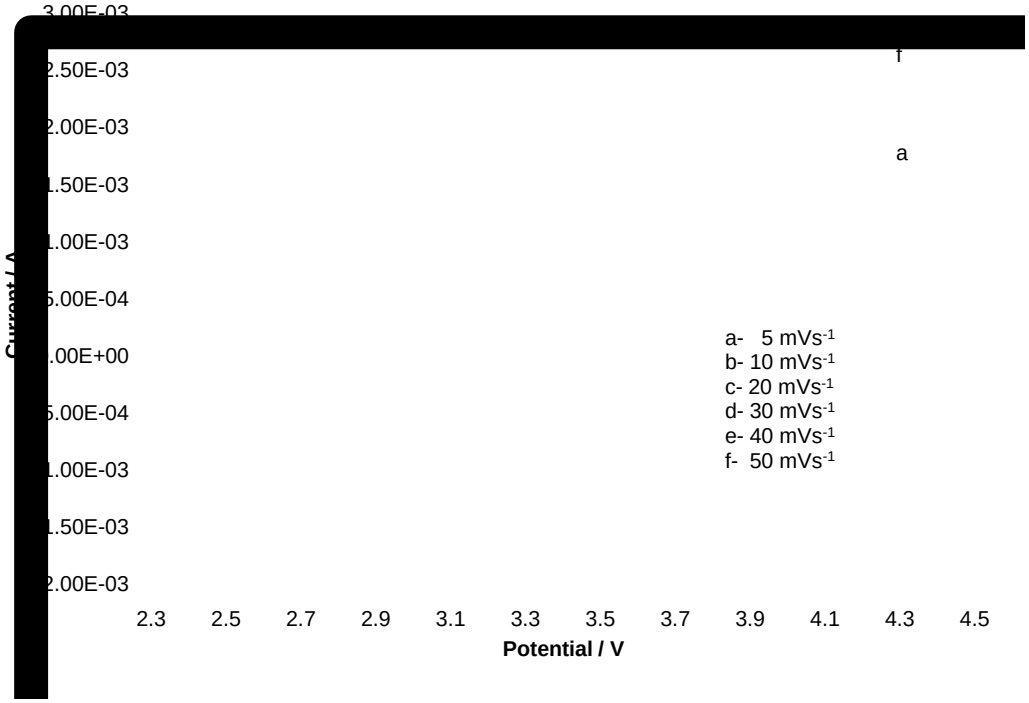

Figure 6.8. Cyclic voltammogram of $LiFePO_4$ at scan rate 5 mVs^{-1}, 10mVs^{-1}, 20 mVs^{-1}, 30 mVs^{-1}, 40 mVs^{-1} and 50 mVs^{-1}.

At small scan rates, system may yield reversible waves, while at large scan rates, irreversible behaviour is observed (Bard and Faulkner, 2001), revealing that kinetic effects depends on the scan rates.

Nevertheless, the redox peaks at lower scan rates (Figure 6.5,6.6 and 6.7) are better defined than that at medium scan rates (Figure 6.8), because the Li^+ ions cannot completely extract/insert from/into the bulk during the time interval of a high rate scan. This trend also observed by other researchers (Mi et al., 2007; Ma and Qin, 2005; Franger et al., 2004).

Table 6.4. Peak potential difference (E_{pa} - E_{pc}) at various scan rates for sample $LiFePO_4$.

(a)Peak potential difference for scan rates shown in Figure 6.5 to 6.7.			
Scan rate mVs^{-1}	Anodic/Oxidation peak (E_{pa})	Cathodic/Reduction Peak (E_{pc})	(E_{pa} - E_{pc}) = ΔE
0.50	3.83	3.08	0.75
0.25	3.78	3.13	0.65
0.50	3.80	3.20	0.60
(b)Peak potential difference for scan rates shown in Figure 6.8			
50	3.82	2.85	0.97
40	3.75	2.90	0.85
30	3.67	2.93	0.74
20	3.68	2.96	0.72
10	3.62	2.99	0.63
5	3.56	3.01	0.56

6.5.2 Formal electrode potential

The formal electrode potential can be calculated from the redox peaks potential. Therefore, the identity of the cation which extract and insert from and into $LiFePO_4$ compound upon the redox reaction of Fe^{2+}/Fe^{3+}couple can be identified. The corresponding equations for the redox reactions represented by redox peaks of $LiFePO_4$ can be written as

Oxidation: $LiFePO_4 - xLi^+ - xe \longrightarrow xFePO_4 + (1-x)\ LiFePO_4$

Reduction: $FePO_4 + x\ Li^+ + xe^- \longrightarrow xLiFePO_4 + (1-x)\ FePO_4$

Thus the formal potential (E_f) can be calculated from the delithiation / lithiation peak potentials of 3.80 V (E_{pa}, anodic peak potential) and 3.20 V (E_{pc}, cathodic peak potential) versus Li^+/Li based on Equation 4.13 shown in Chapter 4. The calculated E_f value was 3.50 V versus Li^+/Li. This value agrees with the previous results reported (Ma and Qin, 2005) indicating that the typical feature of $LiFePO_4$ is obtained here.

6.5.3 Relationship between i_p and $\upsilon^{1/2}$

.

In a reversible reaction the peak current, i_p increases linearly to the square root of the scan rate $\upsilon^{1/2}$. To determine the reversibility in the $LiFePO_4$ cathode material, a graph of peak current, i_p versus square root of the scan rate, $\upsilon^{1/2}$ for the cylic voltammograms in Figure 6.8 were plotted. The graph depicted in Figure 6.9 revealed that the regression, R^2 is 0.96 and thus the peak current is proportional to square root of the scan rate which is a characteristic of a reversible reactions. Since the peak current is proportional to square root of the scan rate this implies that only the

materials at the surface of the $LiFePO_4$ particles contribute to the reaction and the anodic peak of the cyclic voltammogram is related to the reaction of the diffusing species (Takahashi et al., 2002) .

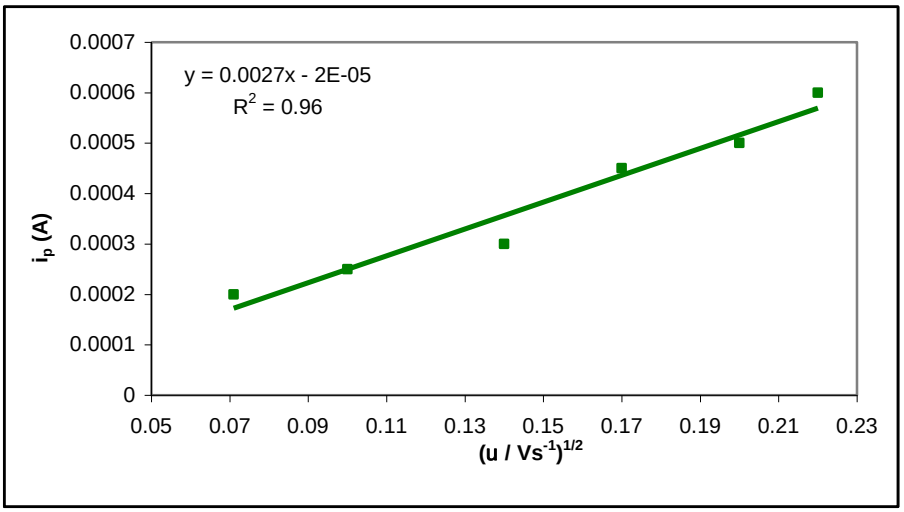

Figure 6.9. Relationship between *ip* and $\upsilon^{1/2}$ at various scan rates for a positive scan of sample $LiFePO_4$.

6.5.4 Diffusion coefficient, D_{Li}^{+}

Since peak currents, i_p is proportional to the square root of the scan rate, $\upsilon^{1/2}$, the Randles –Sevcik equation (Equation 4.14) which was described in Chapter 4 is again applied to determine the diffusion coefficient of Li^+ ion in $LiFePO_4$. In this experiment the electrode area was 0.785 cm^2. $LiFePO_4$ has a bulk density of 3.6 g cm^{-3} (Yu et al., 2007) with a molar mass of 158 g mol^{-1}. This corresponds to a Li concentration of 0.023 mol cm^{-3}. The data used for the calculation of the diffusion coefficient (D_{Li}^{+}) of Li^+ ion in $LiFePO_4$ are listed in Table 6.5 and the estimated D_{Li}^{+} value is 3.09 x 10^{-13} cm^2s^{-1}. For comparison the diffusion coefficient of Li^+ in $LiPF_6$ in EC:PC:DMC=1:1:1 is found to be close to the diffusion coefficient of Li^+ in $LiPF_6$ in EC:DEC=3:7 as listed in Table 6.6. The calculated D_{Li}^{+} in this work is slightly higher

than that measured by Prosini et al (2002) ($1.8x10^{-14}$ cm^2s^{-1}) and values calculated by Yu et al (2007) (~ $10^{-14}cm^2 s^{-1}$).

Table 6.5 . List of data used for the calculation of the diffusion coefficient and the calculated diffusion coefficient values for $LiFePO_4$.

Sample	Slope $As^{1/2} V^{1/2}$	Density/ gcm^{-3}	Molar mass g mol^{-1}	C_{Li}^{+}/ $molcm^{-3}$	D_{Li}^{+}/ $cm^2 s^{-1}$
$LiFePO_4$	0.0027	3.6	158	0.023	3.09×10^{-13}

Table 6.6 . Comparison of diffusion coefficient of $LiFePO_4$ in different electrolytes.

	Electrolytes	Diffusion coefficient, cm^2s^{-1}	References
1	$LiPF_6$ in EC:DEC=3:7	$2.2x10^{-14}$	Yu et al., 2007
2	$LiPF_6$ in EC:DEC=7:3	$5x10^{-15}$	Yu et al., 2007
3	$LiPF_6$ in EC:DME=3:7	$1.3x10^{-14}$	Yu et al., 2007
5.	$LiPF_6$ in EC:DMC=1:1	$1.8 x10^{-14}$	Prosini et al., 2002
4	$LiPF_6$ in EC:PC:DMC=1:1:1	3.09×10^{-13}	this work

6.5.5 Cell capacity

In order to investigate the capacity of the cell, the specific capacity values was calculated from the electrical charge density value, Q, recorded. Table 6.7 shows the specific capacity of $LiFePO_4$ / Li cell using 1M $LiPF_6$ / (EC + PC+ DMC) (v/v/v =1) as the electrolyte. The finding in this work is consistent with the work done by Ma and Qin (2005). In their work the initial charge capacity for $LiFePO_4$ was estimated to be ~ 65 $mAhg^{-1}$.

Table 6.7. Specific capacity of $LiFePO_4$.

Sample	Scan rate (mVs^{-1})	Q (C)	Capacity (mAh)	Specific capacity (mAh/g)
$LiFePO_4$	0.1	3.94	1.09	44

6.6 Summary

The phospho-olivine $LiFePO_4$ was successfully prepared by chemical precipitation and sterilizer heating in the absence of nitrogen gas and reducing agent as often used by researchers. The author literature survey showed that sterilizer has not been used for preparing $LiFePO_4$ powders. This method also allow mass production to be produced. The XRD results demonstrate that $LiFePO_4$ powder with an orthorhombic olivine-type structure and a space group of Pnmb was synthesized. Olivine phase $LiFePO_4$ with minor impurities such as pyrophosphate was successfully synthesized. The crystallite size of the $LiFePO_4$ was found to be 58 nm by Scherrer equation. Nanosized powder $LiFePO_4$ was successfully prepared by this method.

From cyclic voltammetry studies the mean redox potential is 3.53V, which is typical of $LiFePO_4$. The cyclic voltammograms at various scan rates show that the peak current (i_p)increases linearly to the square root of the scan rate ($\upsilon^{1/2}$) indicating Li^+ intercalation/deintercalation processes are diffusion controlled.

The calculated diffusion coefficient (D_{Li}^+) of F is 3.09 x 10^{-13} cm^2s^{-1}. The diffusion coefficient of Li^+ in $LiPF_6$ in EC:PC:DMC=1:1:1 which was investigated in this work is found to be close to the diffusion coefficient of Li^+ in $LiPF_6$ in EC:DEC=3:7 (D_{Li}^+ = 2.2 x $10^{-14}$$cm^2s^{-1}$). The calculated specific capacity for $LiFePO_4$ from the charge density i.e from the cyclic voltammogram curves is 44 $mAhg^{-1}$.

CHAPTER 7

DISCUSSION

Lithium transition metal phosphate, $LiMPO_4$ (M=Mn, Ni, Fe) have attracted much interest because of their use as cathodes in rechargeable batteries. Method of synthesis is known to give great impact on the electrochemical characteristics of cathode materials. Since the performance and cost of the lithium batteries are often decided by the properties of the cathode material, much effort has been directed to develop the synthesis techniques of olivines, $LiMPO_4$ cathode material to improve their electrochemical performance. These include solid-state (Liu et al., 2006), sol-gel (Hsu et al., 2005; Piana et al ., 2004; Yang and Xu, 2004) hydrothermal (Lee and Teja, 2006) and aqueous precipitation techniques (Arnold et al., 2003). Many of the sol-gel methods reported used citric acid as chelating agent and argon or nitrogen ambient during calcinations of precursor powders. Ma and Qin (2005) calcinated the $LiMnPO_4$ deposited on the substrate under pure argon ambient. Dominko and co workers (2006) fired the obtained $LiMnPO_4$ xerogel in pure argon atmosphere. The use of inert gas and a reducing agent will increase the synthesis cost of the material.

In the solid state reaction it is very difficult to control the stoichiometry and grain size distribution. Therefore the solution methods have been developed to overcome these problems. The sol-gel method, one of the solution methods, was selected for the present study. Comparing it to the solid state reaction, the sol-gel method has several advantages such as, easier to control stoichiometry and possible achievement of submicron-size particles and good homogeneity. In addition, shorter-time and lower temperatures are used for the process (Liu et al., 2004) The sol–gel synthesis

technique also offers a convenient means of producing particles of small size from homogeneous mixing of reagents on an atomic scale (Drezen et al., 2007)

In this work, lithium manganese phosphate was prepared based on the synthetic procedure of a sol-gel reaction and lithium hydroxide (LiOH) is used as one of the starting reagents. LiOH is cheap and chemically stable materials and use of the compounds does not involve the production of any harmful side-products during the synthesis process. Lithium acetate, $Li(CH_3COO)_2$ on the other hand will decompose to harmful gases on heating. Thus, it appears better to use LiOH which is more environmental friendlier. As for industrial preparation LiOH will be more favourable since it is cheaper (Yang et al., 1999). Reports discussing on the preparation of $LiMnPO_4$ with sol-gel method based on tartaric acid as complexing agent are also very rare. Tartaric acid has only four carbon atoms in its structure and therefore formed a ring structure which is small compared to other chelating acids.

$LiNiPO_4$ in this work is also prepared by the tartaric acid assisted sol-gel technique. Literature survey shows that there is not many reports available on the preparation method of $LiNiPO_4$. $LiNiPO_4$ is prepared for the first time via tartaric acid based sol-gel method in this work.

$LiFePO_4$ has become a very promising cathode material for lithium batteries since it was first proposed by Padhi et al (1997). $LiFePO_4$ has attracted particular attention due to its low cost, high energy density, excellent thermal stability, non-toxicity and high theoretical specific capacity of 170 mAh g^{-1} (Padhi et al., 1997; Takahashi et al., 2002) as well as small capacity fade even after several hundreds cycles (Park et al., 2003). Similar to $LiMnPO_4$ and $LiNiPO_4$ it has low electronic conductivity and low lithium diffusitivity (Dominko et al., 2006; Zhang et al., 2005; Andersson and

Thomas, 2001). Besides that $LiFePO_4$ is difficult to synthesize since the Fe^{2+} ions are easily oxidized to Fe^{3+}. Several kinds of synthesis have also been employed, including, solid-state reaction where repeated grinding and a longer period of heating at high temperatures in inert conditions are required (Kim et al., 2004, Kwon et al., 2004). In the sol–gel method the precursor is obtained by subsequent evaporation of the solvent and then decomposed in a furnace in inert atmosphere (Hsu et al., 2004; Dominko et al., 2006). In the hydrothermal method solutions of raw materials were mixed quickly and transferred to a Parr reactor (Yang et al., 2001). Co-precipitation method to synthesize $LiFePO_4$ requires heat treated for 12 hours at temperatures ranging from 550 to 800 ^oC in a nitrogen flow (Franger et al., 2003; Arnold et al., 2006). Higuchi et al.(2003) prepared $LiFePO_4$ by solid state mixing and calcining it with the microwave under inert atmosphere.

Almost all of the techniques mentioned earlier used a reducing agent or inert gas to prevent the conversion of Fe^{2+} to Fe^{3+} and this increases cost. Therefore in order to be able to produce $LiFePO_4$ at a reasonable cost, intensive research on its preparation method are essential.

In this work for the synthesis of $LiFePO_4$, the solution method was adopted. The $LiFePO_4$ was prepared using a chemical precipitation and low temperature sterilization heating method in the absence of both inert gas and reducing agent. It is the first time the sterilizer is being selected to prepare $LiFePO_4$. The preparation does not involve any heating step with high temperature in inert or reducing atmosphere as is usually required in other methods. The absence of inert gas and reducing agent reduce the cost of this method. This method requires only a low heating temperature

of 121 ^{o}C and 5 hours heating time. This method was found to be simple and of low cost and is suitable for mass production.

In order to realize the formation of $LiMnPO_4$ and $LiNiPO_4$ the precusors must be heated. TGA experiments was carried out to determine the suitable heating temperatures. The precursor of $LiMnPO_4$ showed two distinct weight losses at different temperature regions. The TGA studies revealed that the total weight loss for this system is 68% and that the material is composed of lithium manganese phosphate at 550 ^{o}C. Therefore the overall proposed decomposition of the precursor in air atmosphere i.e.

$$Li((H_2PO_4)_2(NH_4)_2C_4H_5O_6)\,Li\,C_4H_5O_6.(Mn\,C_4H_4O_6)_2 + 10O_2 \longrightarrow 2LiMnPO_4 + 16CO_2 + 12H_2O + 2NH_3 \quad (4.7)$$

The thermogram of $LiNiPO_4$ precursor showed four discrete weight losses regions and the total weight loss is 67.9 %. The results showed that the temperature is constant at 729 ^{o}C and it is assumed that complete formation of $LiNiPO_4$ took place at this temperature. With the aid of the thermogravimetric analysis, the equations for the synthesis of $LiNiPO_4$ has been proposed as shown below.

$$Li((H_2PO_4)_2(NH_4)_2C_4H_5O_6)\,Li\,C_4H_5O_6.(Ni\,C_4H_4O_6)_2 + 10\,O_2 \longrightarrow 2LiNiPO_4 + 16CO_2 + 12H_2O + 2NH_3 \quad (5.7)$$

To confirm the identity of the three cathode materials produced, X-ray diffraction analysis were carried out on the samples. The $LiMnPO_4$ prepared by the sol-gel method was subjected to X-ray diffraction analysis. Generally, the peaks intensity increased as firing temperature increases indicating improved crystallization and particle growth. The diffraction peaks of the precursor (Figure 4.5) exhibit the

presence of $LiMnPO_4$ peaks and peaks due to impurities. This is expected as the precursor was only heated to 60 ^oC and therefore most of the starting materials are still present. X-ray diffraction studies revealed that $LiMnPO_4$ fired for 15 hours at 350 ^oC has low crystalinity as broad peaks with low intensities are present from $2\Theta = 10^o$ to 80^o. On heating the sample to 450 ^oC peaks with higher intensities but still with high background noise was produced. The sample was then further heated at 550 ^{o} C, 650 ^{o} C, 750 ^{o} C, 850 ^{o} C and 1000 ^{o} C in a muffle furnace in air. The XRD patterns of sample fired at 550 ^{o} C, 650 ^{o} C and 750 ^{o} C showed no impurities and the peaks were well crystalline and sharp. All the three XRD patterns are dominated by the (131), (121), (021) and (011) planes at around $2\theta = 35.2^0$, 29.2^o, 25.1^0 and 20.5^0 respectively. The XRD peaks of the samples exhibit reflections that matches with the standard (JCPDS No:33-0803) for orthorhombic $LiMnPO_4$. Hence pure and crystalline $LiMnPO_4$ was successfully prepared in this study. The firing temperatures agrees with the TGA results in this work which showed complete formation of $LiMnPO_4$ at temperatures above 550 ^oC.

It was observed that for samples fired at 850 ^oC the relative peak intensities changes and that the peaks in the (011) and (021) planes has higher intensity than the peak in the (121) plane. However the peak at the (131) plane remained the most intense. The peaks ratio is shown in the table below.

From Table 7.1 it can be seen that temperatures of 850 ^{o} C and 1000 ^{o} C are not a suitable firing temperature for $LiMnPO_4$. At 1000 ^oC the intensity of the peaks dropped tremendously. On the other hand the A3, A4 and A5 intensities ratios of $I_{(011)} / I_{(131)}$, $I_{(021)} / I_{(131)}$ and $I_{(121)} / I_{(131)}$ are very close to 0.55, 0.70 and 0.90 respectively

showing that the degree of crystallinity of $LiMnPO_4$ is very high. Calculation from Scherrer Equation showed that nanosize particles are obtained in this work

Table 7.1. Peaks ratio for $LiMnPO_4$

Samples	Peaks Ratio		
	$I_{(011)} / I_{(131)}$	$I_{(021)} / I_{(131)}$	$I_{(121)} / I_{(131)}$
JCPDS	0.55	0.70	0.90
A3 (550 ^oC)	0.65	0.77	0.86
A4 (650 ^oC)	0.83	0.88	0.95
A5 (750 ^oC)	0.64	0.77	0.77
A6 (850 ^oC)	0.82	0.87	0.74
A7(1000 ^oC)	0.15	0.24	0.09

As for $LiNiPO_4$ the precursor was first fired at 750 ^oC for 15 hours but the XRD pattern showed the presence of impurities. These impurities are thought to be Li_2CO_3 (Arof, 2007; Song, 1997; Chang, 1998) and NiO (Arof, 2007). This is possible as during heating, lithium hydroxide and nickel acetate might decompose and reacted in the presence of oxygen as shown in the equation below,

$$2LiOH + Ni(CH_3COO)_2 + \frac{5}{2} O_2 \longrightarrow Li_2CO_3 + NiO + 4H_2O + 3CO \quad (7.1)$$

Apparently 750 ^oC firing temperature and 15 hours firing time is not sufficient to prepare pure $LiNiPO_4$. The firing temperature was then increased to 850 ^oC and peaks at $2\theta=33.9^o$ and 43.8^o still exist. This is indicating that NiO and Li_2CO_3 were present. When the sample was heated at 1000 ^oC for 15 hours the peak attributed to Li_2CO_3 disappears but the peak attributed to NiO still remained. This indicates that firing process eliminates the presence of impurities. Hence the sample was further fired at

1000 ^{o}C for 24 hours and the XRD pattern for the sample fired at 1000 ^{o}C for 24 hours showed no impurities and sharp and intense diffraction lines are observed indicating the crystalline nature of the materials as represented by Figure 5.7. All the lines in the XRD pattern of the sample fired at 1000 ^{o}C for 24 hours exhibit the characteristic diffraction lines of the olivine $LiNiPO_4$ without any impurities and matches the orthorhombic structure listed in JCPDS pattern number 32-0578. This observation was also reported by Ruffo and co-workers (2005). The above observations confirmed that a pure compound of $LiNiPO_4$ was successfully synthesized in the present work and calculation from Scherrer Equation showed that nanosize particles of $LiNiPO_4$ are obtained in this work.

The XRD pattern (Figure 6.1) of the $LiFePO_4$ sample prepared in this work is the same as those of pure orthorhombic ordered olivine phase $LiFePO_4$ with space group Pnmb (JCPDS No.40-1499). Two low intensity peaks around 26.88 ^{o} and 27.18 ^{o} are also observed. These peaks are attributed to the pyrophosphate due to the dimerisation of the phosphoric acid used in the preparation. These minor impurities was also observed by Franger et al. (2003) who prepared $LiFePO_4$ via the co-precipitation technique and heat treated the sample at 550 ^{o}C for 12 hours under inert atmosphere. The $LiFePO_4$ sample in the present work utilizes lower temperature, lower duration of heating and in the absence of inert gas meaning to say that the method employed in the present work is a simpler synthetic pathway for the preparation of $LiFePO_4$ cathode material.

Hence $LiFePO_4$ with minor impurities was successfully synthesized. This proved that the chemical precipitation and low temperature sterilization heating method provide a reliable synthetic pathway for the production of $LiFePO_4$. The whole synthetic

process, performed in the absence of inert gas and reducing agent is economical and environmentally benign.

In this work the average crystallite size of the samples prepared were calculated using Scherrer equation. Many researchers used Scherrer equation to estimate the crystallite size of the material they produced (Jin and Gu., 2008; Drezen et al., 2007; Piana et al., 2004). The smaller particles, which shortened the diffusion path for Li^+ ions will have a great influence on the electrochemical properties of the cathode materials (Shin et al., 2006). The comparison between the average crystallite size of $LiMnPO_4$ obtained in this work and of those reported are listed in the table below.

Table7.2. Comparison of crystallite size of $LiMnPO_4$ calculated by Scherrer Equation

Preparation methods	**Synthesis conditions**	**Grain size /nm**	**References**
Solid state	600 ^oC, 6 hours in Argon gas	79	Yonemura (2004)
Sol-gel	600 ^oC, 18 hours, citric acid, in Argon gas	82	Piana (2004)
Sol-gel	550 ^oC,15 hours, tartaric acid, in air	38	This work

The calculated crystallite size shows that the particle size increases as firing temperature increases. The powders calcinated at temperatures below 750 ^oC shows similar average crystallite size. The reason why the $LiMnPO_4$ sample has less average crystallite size shows that the tartaric acid have played a dual role in the synthesis, it functioned as a chelating agent as well as preventing the growth of the crystals. Tartaric acid is a carboxylic acid with four carbon atoms in its chain with formula $C_4H_6O_6$. The structure of tartaric acid is shown below in Figure 7.1.

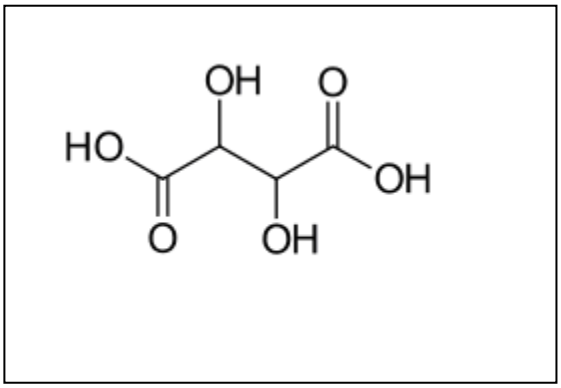

Figure 7.1 Structure of tartaric acic

During the sol-gel synthesis of $LiMnPO_4$ and $LiNiPO_4$, colloid particles are formed and there are a great deal of free hydroxyls i.e OH group on the surface of the colloid particles. The oxygen atoms in the tartaric acid then formed hydrogen bond with the free hydroxyls on the surface of colloid particles. The colloid grains are then embedded in the tartaric acid molecules and thus inhibit the particle growth. During heating the tartaric acid which acted like a coat to the particles controls the growth of the $LiMnPO_4$ and $LiNiPO_4$ particles, limiting the growth of the particle. Previous literature survey indicates that no reports have been published in the last 10 years on the crystallite size of $LiNiPO_4$. Therefore no comparison can be made.

The calculated average crystallite size for $LiFePO_4$ was found to be 58 nm. For $LiFePO_4$, small particle size and well-shaped crystal are important for enhancing the electrochemical properties. In particles with a small diameter, the lithium ions may diffuse over smaller distances between the surfaces and center during lithium intercalation and de-intercalation, and the $LiFePO_4$ on the particle surfaces contributes mostly to the charge/discharge reaction (Choi and Prashant, 2007).

The FTIR spectra of $LiMnPO_4$, $LiNiPO_4$ and $LiFePO_4$ all show intense peaks over the range of 700 to 1400 cm^{-1} and weaker bands between 700 and 450cm^{-1} indicating

the presence of phosphate anion in the samples. For both $LiMnPO_4$ and $LiNiPO_4$ peaks at 1305 to 1130 cm^{-1} due to the tartarate group were seen in the IR spectrum of the precursor. When the sample was fired at 350 ^oC the peaks due to the tartarate group disappear and peaks in the region 570 to 460 cm^{-1} due to the metal-oxide bond and 1100 to 1134 cm^{-1} due to the phosphate bond are seen. However their intensity is low which agree with the XRD spectra for the sample fired at 350 ^oC. On further heating the characteristic peaks become much sharper, but the shape of the peak remained the same.

FTIR spectra also showed that the absorption peaks become more intense as temperature for $LiMnPO_4$ formation increases. However, the absorption peaks at 965cm^{-1} (singlet), 1051 to 1093 cm^{-1} (triplet) and 578 to 645 cm^{-1} (triplet) get less intense for the sample fired at 850 ^oC and 1000 ^oC for $LiMnPO_4$ sample. With these observations it can be said that the sample $LiMnPO_4$ structure is not stable or the structure might start to decompose at 850 ^oC. This observation is consistent with the results shown by X-ray diffraction studies where the X-ray diffraction peaks intensity reduces drastically for the samples fired at 850 ^oC and 1000 ^oC. Therefore it can be concluded that for $LiMnPO_4$ the suitable heating temperature is between 550 ^oC and 750 ^oC and 15 hours firing duration.

As for $LiNiPO_4$, there is a small peak at ~881 cm^{-1} for the sample fired at 750 ^oC and this can be said to be due to the presence of carbonates in the sample. This peak disappears at higher firing temperature. The presence of the carbonates is confirmed by the X-ray diffraction diffractogram. The X-ray diffraction studies revealed that for $LiNiPO_4$ material only the sample fired at 1000 ^oC for 24 hours is free of impurities. The FTIR spectra of this sample is dominated by a singlet at ν_1= 965 cm^{-1}, a doublet

at ν_2= 415 to 464 cm^{-1} and two triplets at υ_3 in the region 1050 to1140 cm^{-1} and υ_4 in the range 500 to 560 cm^{-1} which are characteristic peaks of phosphate anion. This means that the temperature required to prepare impurities free $LiNiPO_4$ cathode material is 1000 ^oC for sintering time of 24 hours.

The $LiFePO_4$ sample has PO_4^{3-} group in its structure as such it is expected that all the peaks due to the phosphate anion to appear at~965 cm^{-1} (singlet), at~466 to 503 cm^{-1} (doublet), at~1051 to 1093 cm^{-1}(triplet) and at~578 to 645 cm^{-1} (triplet) in the absorption peaks. A new IR peak at 795 cm^{-1} which is due to the P-O-P bridging bonds in $P_2O_7^{4-}$ (pyrophosphate) unit was recorded. Their presence was also detected in the X-ray diffraction diffractogram. Peaks at $2\theta \sim 26.9^o$ and 27.2^o are attributed to pyrophosphate.

The EDX data show peaks attributable to Mn,Ni, Fe and P and it was found that the ratio of Li : Metal : P is 1:1:1 which is consistent with the stoichiometric amount of the $LiMPO_4$ (M= Mn, Ni and Fe) prepared in this work. This suggest that the stoichiometry of the prepared materials agree with the calculated values and thus the material obtained in this work are of the calculated stoichiometries. By conservation of charge, the calculation between positive and negative charges of the cathodic material shows that there are 4 moles of oxygen in one mole of lithium metal phosphate.

The redox properties of the $LiMnPO_4$/Li, $LiNiPO_4$/Li and $LiFePO_4$/Li cells were investigated by carrying out the cyclic voltammetry experiments at various scan rates. At 10 mVs^{-1} scan rate all samples (A3, A4, A5, $LiNiPO_4$ and $LiFePO_4$) produced redox peaks which are small and not well defined. This is expected as Li^+ ion cannot

intercalate and deintercalate completely into and from the bulk as the scan rate is too fast. At 1.0 mVs^{-1} better oxidation and reduction peaks were seen.

At 0.1 mVs^{-1} scan rate the samples produced one distinct anodic peak (charge) and one cathodic peak (discharge) which correspond to the reversible two phase charge/discharge reactions in $LiMnPO_4$, $LiNiPO_4$ and $LiFePO_4$. This indicates that Mn^{3+}/ Mn^{2+}, Ni^{3+}/ Ni^{2+} and Fe^{3+}/ Fe^{2+} redox pairs contribute to the gain and loss of electron in $LiMnPO_4$, $LiNiPO_4$ and $LiFePO_4$ crystal structures respectively during the lithium insertion /extraction process. The anodic peaks is probably due to the oxidation of M^{2+} to M^{3+}(M= Mn, Ni and Fe) accompanied by a loss of electron and the cathodic peak is due to the reduction of M^{3+} to M^{2+} accompanied by a gain of electron. The well defined peaks in the CV curves of the samples indicate the high reactivity and good reversibility of the materials as cathode. The redox peaks of all samples are shown in Chapters 4, 5 and 6. These results indicate that all three samples are able to undergo oxidation and reduction and are thus good cathode materials.

The redox peaks appearance is due to the redox activities of the electron donating or accepting center which is Mn in $LiMnPO_4$, Ni in $LiNiPO_4$ and Fe in $LiFePO_4$. The cations which are responsible to the gain or loss of electron were identified in this work by calculating the formal electrode potential, E_f, using Equation (4.13). Results showed that E_f for $LiMnPO_4$, $LiNiPO_4$ and $LiFePO_4$ are 4.15 V, 4.88 V and 3.50 V respectively. The theoretical, E_f value can be calculated using data from data book (Stark and Wallace, 1982) as shown in Table 7.3.

Since the electrode potential values of $Ni^{3+} + e^- \rightarrow Ni^{2+}$ is not known, therefore for comparison the value for $LiNiPO_4$ is taken from the work of Deniard et al. (2004) where the intercalation potential was predicted to be 5.3 V for $LiNiPO_4$ / Li system.

It is realized that, according to literature (Ruffo et al., 2005; Okada et al., 2001) the peaks for $LiNiPO_4$ in the cyclic voltammogram will not be able to be observed when the $LiPF_6$ electrolytes used is not able to withstand voltage above 5.0 V range. But Okada et al., (2001) in his work, showed that the $LiPF_6$ electrolyte system can withstand up to 5.5 V. An electrolyte system that can withstand up to 6V was used by other researchers (Wolfenstine and Allen, 2004), however peaks of oxidation or reduction of $LiNiPO_4$ were still not observed in their work. It was suggested by the researchers (Wolfenstine and Allen, 2004) that perhaps reducing the particle size to nano-scale and/ or carbon doping and/ or lattice doping may allow the Ni^{3+}/ Ni^{2+} redox potential to be seen. So in this work $LiNiPO_4$ has been prepared and the crystallite size obtained from XRD data and calculated using Scherrer equation show that it is nanosize as shown in Chapter 5. The cyclic voltammetry experiments results of the prepared $LiNiPO_4$ are also shown in Chapter 5. However we note that the suggested anodic and cathodic peaks are quite small. So, if these peaks are true then the diffusion coefficient of $LiNiPO_4$ is as calculated in Chapter 5.

Table 7.3. Calculated E_f values for $LiMnPO_4$ and $LiFePO_4$ and experimental E_f values for $LiMnPO_4$, $LiFePO_4$ and $LiNiPO_4$.

Sample	Reduction	Electrode potential, (V)	Oxidation	Electrode potential, (V)	Theoretical potential, (V)	Experimental electrode potential (V)	References
$LiFePO_4$	$Fe^{3+} + e^- \rightarrow Fe^{2+}$	+0.77	$Li^+ + e^- \rightarrow Li$	-3.04	+3.81	3.50	this work
						3.41	Ma and Qin, 2005
$LiMnPO_4$	$Mn^{3+} + e^- \rightarrow Mn^{2+}$	+1.51	$Li^+ + e^- \rightarrow Li$	-3.04 V	+4.55	4.15	this work
						4.10	Chang et al.,2005
$LiNiPO_4$	$Ni^{3+} + e^- \rightarrow Ni^{2+}$	Not known	$Li^+ + e^- \rightarrow Li$	-3.04 V	Not available	4.88	this work
						5.30	Deniard et al.,2004

The effect of scan rates on the redox behaviour of the $LiMPO_4$ systems was studied by varying the scan rates between 0.1 mV s^{-1} to 50 mV s^{-1}. The CV curves showed that the peak potential difference (E_{pa} - E_{pc}) increases with increasing scan rates. The same pattern was also reported by other researchers (Takahashi et al; 2002). Reversibility is greatest at the slowest scan rate where there is ample time for the reacting species to reach equilibrium (Yu et al., 2007). This behaviour showed that the appearance of kinetic effects depends on the scan rates. At small scan rates, system may yield reversible waves, while at large scan rates irreversible behaviour is observed (Bard, 2001). This observation might make researchers assume that the electrochemical lithium ion intercalation-deintercalation process changes from being kinetically quasi–reversible to irreversible when scanning rate increases.

The diffusion coefficient values for samples A3, A4 and A5 were 9.37 x 10^{-13} cm^2 s^{-1} 8.57 x 10^{-13} cm^2 s^{-1} and 2.97 x 10^{-14} cm^2 s^{-1} respectively. The diffusion coefficient values for A3 is the highest. Sample A5 on the other hand has the lowest diffusion coefficient This is expected as sample A5 has the largest crystallite size among the three samples. The diffusion coefficient values for $LiNiPO_4$ is 3.50 x 10^{-11} cm^2 s^{-1} .

In $LiMnPO_4$ samples it can be seen that sample with the smallest crystallite size gave the highest diffusion coefficient values. The reduction in size is believed to shorten the diffusion length for the lithium ions. Unfortunately, diffusion coefficient values from CV curves and Randles-Sevcik equation for $LiMnPO_4$ and $LiNiPO_4$ are very rare in the literature and no further comparison is possible to be made between the result of this work and those already published. As for $LiFePO_4$ the diffusion coefficient value obtained was 3.09×10^{-13} $cm^2 s^{-1}$.

Due to the above results and explanations, the $LiMPO_4$ diffusion coefficients values can be improved by reducing the particle size. Diffusion coefficient values of $LiMnPO_4$ and $LiNiPO_4$ in the literature are rare. The known diffusion coefficient values of lithium ion in the $LiFePO_4$ olivines cathodes is 10^{-14} to 10^{-16} cm^2s^{-1} (Prosini et al., 2002). To the best of our knowledge reports on diffusion coefficient constant of $LiMnPO_4$ and $LiNiPO_4$ by cyclic voltammetry studies has not been published elsewhere. Diffusion coefficient constant can also be calculated by Impedance spectroscopy (IS) and Galvanostatic intermittent titration technique (GITT) (Prosini et al., 2002). However CV has an advantage over IS and GITT because complicated model fitting is not necessary as long as the active area of the particle is known and analysis of CV profiles does not require the knowledge of differential capacity with potential (dQ/dE) as in GITT (Yu et al., 2007). CV is then a more straight forward and less time consuming method. Therefore diffusion coefficient constant can be obtained with a higher accuracy using CV (Yu et al., 2007).

The specific capacity was calculated from the Q values obtained from the CV curves and it is obvious that the smaller size particle gave higher specific capacity.

CHAPTER 8

CONCLUSIONS AND SUGGESTIONS

In this study lithium manganese phosphate, $LiMnPO_4$ and lithium nickel phosphate, $LiNiPO_4$ have been successfully synthesized by the sol-gel method while the lithium iron phosphate, $LiFePO_4$ has been synthesized by the chemical precipitation and low temperature sterilization method. Both methods have proven to produce nano-size particles which is able to increase the diffusion coefficient values of the cathode materials and shortens the pathway for Li^+ ion diffusion.

The precursors of $LiMnPO_4$ and $LiNiPO_4$ was subjected to thermogravimetric analysis (TGA and DTGA) where the firing temperature of the sample was determined. The thermal stability of the compounds were analysed by the TGA curves. There are two weight losses in the system but the largest weight was seen at 220 ^{o}C to 550 ^{o}C for $LiMnPO_4$ and at 150 ^{o}C to 275 ^{o}C for $LiNiPO_4$. The materials were generally stable at temperatures above 550 ^{o}C for $LiMnPO_4$ and around 725 ^{o}C for $LiNiPO_4$. Therefore 550 ^{o}C and 750 ^{o}C was chosen as the firing temperatures for $LiMnPO_4$ and $LiNiPO_4$ respectively. Firing of samples were done in air which is environmental friendly compared to firing in inert gas. The absence of inert gas and reducing agents also made the synthesis low cost which is one of the objectives of this work.

The X-ray diffraction diffractograms of all three cathode systems revealed that the samples prepared in this work are orthorhombic olivine structure cathode materials. XRD analysis confirmed the formation of $LiMnPO_4$ at temperature 550 ^{o}C to 750 ^{o}C without impurities. Below 550 ^{o}C and at 850 ^{o}C although there are no impurities

detected, the peaks intensity are rather low. The formation of $LiNiPO_4$ at 1000 ^{o}C was confirmed also by XRD but the sintering time is 24 hours. $LiFePO_4$ with minor impurities formation was cofirmed in the preparation. The XRD analysis reveal the purity and the crystalline nature of the $LiMPO_4$ prepared in this work due to the presence of sharp peaks in their diffractograms.

The suggested decomposition reaction for the synthesis of $LiMnPO_4$ was proposed from the thermogravimetric analysis. The calculated total weight loss of the overall proposed decomposition process which is is 65.9 % shows agreement with the percentage weight loss from the TGA curves which is 68 %. Similar to $LiMnPO_4$, the suggested decomposition reaction for the synthesis of $LiNiPO_4$ was also proposed from the thermogravimetric analysis. The calculated total weight loss of the overall proposed decomposition process which is 67 % shows agreement with the percentage weight loss from the TGA curves which is 68 %.

The crystallite size from Scherrer equation (Equation 4.12) was found to be in the range of 31 nm to 46 nm for $LiMnPO_4$, a mean crystallite size of 66 nm for $LiNiPO_4$ and 58 nm for $LiFePO_4$.

The FTIR structural analysis indicate the presence of characteristic vibrational bands for olivine orthorhombic structure for all samples prepared. The FTIR spectra also indicates that the phosphate bond is present in all samples.

The elemental composition of the samples was confirmed by EDX analysis and showed that the prepared samples have stoichiometries which agreed with the calculated values.

The cyclic voltmmetry curves showed that all $LiMnPO_4$, $LiNiPO_4$ and $LiFePO_4$ systems exhibit oxidation and reduction peaks. It can be concluded that in all samples the Li^+ ion can undergo intercalation and deintercalation. The $LiMnPO_4$ samples exhibited a peak around 4.4 V versus Li/Li^+ which is the typical redox potential of Mn^{+2}/Mn^{+3} in olivine manganese phosphate while the $LiNiPO_4$ samples redox peaks are found around 4.8 V suggesting the Ni^{3+}/Ni^{2+} redox couple are taking place in the cells. The $LiFePO_4/Li$ cell showed a charge/discharge plateau at 3.8 V/3.2 V and a mean redox potential of 3.5 V was calculated confirming the typical feature of $LiFePO_4$ cathode material.

All samples showed a linear relationship between peak current and $(\text{scan rates})^{1/2}$ indicating that the samples are reversible. Formal electrode potential indicates that the cation responsible for the gain and loss of electrons in the cathode materials are Mn^{+2} in $LiMnPO_4$ system, Ni^{+2} in $LiNiPO_4$ system and Fe^{+2} in $LiFePO_4$. The diffusion coefficient for $LiMnPO_4$ are 9.37×10^{-13} cm^2s^{-1} 8.57×10^{-13} cm^2s^{-1} and 2.97×10^{-14} for sample A3, A4 and A5 respectively indicating that smaller particles at lower heating temperature has shortened the path length and intercalate faster. The diffusion coefficient for $LiNiPO_4$ is 3.50×10^{-11} cm^2s^{-1}. As for $LiFePO_4$ the diffusion coefficient is 3.09×10^{-13} cm^2 s^{-1}.

It was found that the best diffusion coefficient was given by the samples with small crystallite size and low firing temperature. For $LiMnPO_4$ the highest diffusion coefficient was given by the sample fired at 550 ^oC.

A study of diffusion coefficient is important for the coating and doping of the cathode materials. The diffusion coefficient values of the $LiMnPO_4$ in this work are relatively

low when compared to the diffusion coefficient of other active materials in lithium battery and thus coating of these materials are recommended before using them as cathode materials.

The present work also showed that for $LiMnPO_4$ the sample with firing temperature of 550 ^oC and 650 ^{o} C showed similar specific capacity. This indicates that the best $LiMnPO_4$ can be obtained by firing between 550 ^oC and 650 ^oC. Thus the present work showed that reduce particle size does increase diffusion coefficient values. Since the diffusion coefficient values in this work are calculated using CV where no complicated model fitting and knowledge of differential capacity with potential (dQ/dE) are required, therefore the diffusion coefficient constant can be obtained with a higher accuracy.

From the work done in this study it can be concluded that both $LiMnPO_4$ and $LiNiPO_4$ can be prepared via the sol-gel method with tartaric acid as the chelating agent and the firing of samples can be carried out in air i.e in the absence of inert gas. Nanosize $LiMnPO_4$ and $LiNiPO_4$ were obtained in the present work indicating that the tartaric acid has successfully inhibit the growth of the particle due to its small size as expected.

Reactions for decomposition of $LiMnPO_4$ and $LiNiPO_4$ precursors are suggested in this work. The reactions are accepted since the calculated weight loss from the suggested decomposition reactions and the TGA curves agree closely.

Nanosize $LiFePO_4$ are also obtained from the chemical precipitation and low temperature sterilization method where no inert gas and reducing agent are used

making the technique simple and cost effective. EDX analysis of $LiMnPO_4$, $LiNiPO_4$ and $LiFePO_4$ show that ratio of Li: metal: is 1:1 . Hence it can be concluded that there is no difference in the electronic configuration of the manganese, nickel and iron before and after the preparation implying that inert gas is not necessary during firing or preparation of the samples.

All CV in this work shows redox peaks indicating that the prepared samples ($LiMnPO_4$, $LiNiPO_4$ and $LiFePO_4$) are potential cathode materials. The diffusion coefficient of Li^+ in $LiMnPO_4$, $LiNiPO_4$ and $LiFePO_4$ are calculated from CV since diffusion coefficient is a key factor that determines the rate at which a battery can be charged or discharged. No comparison could be made for $LiMnPO_4$ and $LiNiPO_4$. The diffusion coefficient of Li^+ in $LiFePO_4$ is slightly higher than the diffusion coefficient of $LiFePO_4$ prepared by solid state or hydrothermal method.

The cell capacity of the samples ($LiMnPO_4$, $LiNiPO_4$ and $LiFePO_4$) prepared are comparable to the data available in literature for uncoated material. However at present better cell capacity values are obtained for these material since the materials are now coated but it is not the intention of this work to study this parameter.

Further studies should be aimed at investigating the influence of cell temperature on the lithium diffusion process to allow the diffusion coefficient at different temperatures to be calculated. The cathode materials investigated in this work can also be improved by adding other substituents to the system and by altering the stoichiometries.

Andersson, A. S. and Thomas J.O., 'The source of first-cycle capacity loss in $LiFePO_4$', Journal of Power Sources (2001) 498-502.

Arnold, G., Garche J., Hemmer, R., Stro¨bele, S.,Vogler C.and Wohlfahrt-Mehrens M., 'Fine-particle lithium iron phosphate $LiFePO_4$ synthesizedby a new low-cost aqueous precipitation technique', Journal of Power Sources., 119–121 (2003) 247–251.

Arof A.K., 'Characteristics of $LiMO_2$ (M = Co, Ni, $Ni_{0.2}Co_{0.8}$, $Ni_{0.8}Co_{0.2}$) powders prepared from solution of their acetates', Journal of Alloys and Compounds Journal of Alloys and Compounds 449 (2008) 288–291.

Bae, J-S. and Pyun, S-I., ' Electrochemical lithium intercalation into and deintercalation from vanadium oxide electrode by using potentiostatic current transient technique', Solid State Ionics 90 (1996)251-260.

Balakrishnan, P.G., Ramesh, R. and Kumar, T.P., 'Safety mechanisms in lithium-ion batteries', Journal of Power Sources 155 (2006) 401–414.

Bao, S-J., Liang, Y-Y., Li and H-L., 'Synthesis and electrochemical properties of $LiMn_2O_4$ by microwave-assisted sol–gel method', Materials Letters 59 (2005) 3761 – 3765.

Bard, A.J and Faulkner,L.R., ' Electrochemical Methods: Fundamentals and Applications', second ed., John Wiley and Sons, New York, 2001.

Bewlay, S. L., Konstantinov, K., Wang, G. X., Dou, S. X. and Liu H. K., 'Conductivity improvements to spray-produced $LiFePO_4$ by addition of a carbon source', Materials Letters 58 (2004)1788-1791.

Borrás, C.A., Romagnoli, R. and Lezna, R.O., ' In-situ spectroelectrochemistry (UV–visible and infrared) of anodic films on iron in neutral phosphate solutions', Electrochimica Acta, 45 (2000)1717-1725.

Bramnik, N.N. and Ehrenberg H., 'Precursor-based synthesis and electrochemical performance of $LiMnPO_4$', Journal of Alloys and Compounds 464 (2008) 259–264.

Broadhead J. and Kuo H.C. 'Electrochemical principles and reactions' in 'Handbook of Batteries' , David Linden, McGraw Hill, Inc,USA,2.1-2.35 (1994).

Burba C., Frech R., 'Vibrational spectroscopic investigation of structurally-related $LiFePO_4$, $NaFePO_4$, and $FePO_4$ compounds', Spectrochimica Acta Part A 65 (2006) 44–50.

Burba C., Frech R., 'Vibrational spectroscopic studies of monoclinic and rhombohedral $Li_3V_2(PO_4)_3$',Solid State Ionics 177 (2007) 3445–3454.

Burba C.M., and Frech, R. 'Raman and FTIR Spectroscopic Study of $LixFePO_4$ ($0 \leq x \leq 1$)',J. Electrochem. Soc. 151 (2004) A1032– A1038.

Chang C.C., Scarr N., Kumta P.N., 'Synthesis and electrochemical characterization of LiMO (M=$Ni_{0.75}$ $Co_{0.25}$) for rechargeable lithium ion batteries, 'Solid State Ionics 112 (1998) 329–344.

Chang, X.Y., Wang, Z.X., Li, X.H., Zhang, L., Guo, H.J and Peng, W.J., 'Synthesis and performance of $LiMn_{0.7}Fe_{0.3}PO_4$ cathode material for lithium ion batteries', Materials Research Bulletin 40 (2005) 1513–1520.

Chen, J. and Whittingham, M.S., 'Hydrothermal synthesis of lithium iron phosphate', Electrochemistry Communications 8 (2006) 855–858.

Choi, D. and Prashant, N.,'Surfactant based sol–gel approach to nanostructured $LiFePO_4$ for high rate Li-ion batteries', Journal of Power Sources163 (2007) 1064–1069.

Cushing, B.L. and Goodenough, J.B. ' Influence of carbon coating on the performance of a $LiMn_{0.5}Ni_{0.5}O_2$ cathode', Solid State Sciences, Volume 4, Issues 11-12, November-December 2002, Pages 1487-1493.

Danielewski, M. and Kucza, W., 'Modeling of the transport processes in electrodes showing composition-dependent diffusivity', Solid State Ionics 172 (2004) 13–17.

Delacourt, C., Poizot,P., Levasseur, S. and Masquelier ., 'Size Effects on Carbon-Free $LiFePO_4$ Powders The Key to Superior Energy Density', Electrochemical and Solid-State Letters, **9 (**7) (2006) A352-A355

Delacourt,C., C. Wurm, P. Reale, M. Morcrette, and C. Masquelier, *Solid State*
Dell R.M., 'Batteries fifty years of materials development', Solid State Ionics 134 (2000) 139–158.

Dell, R.M., 'Batteries fifty years of materials development', Solid State Ionics 134 (2000)139–158.

Deniard, P., A.M. Dulac, A.M.,Rocquefelte, X.,Grigorova, V., Lebacq O., Pasturel A. and Jobic, S., 'High potential positive materials for lithium-ion batteries:transition metal phosphates', Journal of Physics and Chemistry of Solids 65 (2004) 229–233

Dominko R., Bele M., Gaberscek M., Remskar M., Hanzel D.,Goupil J.M., Pejovnik S., Jamnik J., 'Porous olivine composites synthesized by sol–gel technique ', Journal of Power Sources 153 (2006) 274–280.

Dompablo, A. and Ceder, G. C., 'First-principles calculations on $LixNiO_2$: phase stability', Journal of Power Sources 119–121 (2003) 654–657.

Drezen, T., Kwon, N.H., Bowen, P., Teerlinck, I., Isono, M. and Exnar, I.,'Effect of particle size on $LiMnPO_4$ cathodes', Journal of Power Sources 174 (2007) 949–953.

Eriksson, T.A. and Doeff, M., 'A study of layered lithium manganese oxide cathode materials', Journal of Power Sources 119–121 (2003) 145–149.

Fang, H., Pan, Z., Li, L., Yang, Y., Yan, G., Li, G., Shiqiang, G. and Wei, S., ' The possibility of manganese disorder in $LiMnPO_4$ and its effect on the electrochemical activity', Electrochemistry Communications 10 (2008) 1071–1073.

Fang, H.,Wang Z., Zhang, B., Li X., Li, G .,'High performance $LiNi_{0.5}Mn_{1.5}O_4$ cathode materials synthesized by a combinational annealing method', Electrochemistry Communications 9 (2007) 1077–1082.

Ferracin, L.C., Fa´bio, A. A. and Nerilso, B., 'Characterization and electrochemical performance of the spinel $LiMn_2O_4$ prepared from ε-MnO_2', Solid State Ionics 130 (2000) 215–220.

Fey, G.T-K., Lin, Y.Y. and Prem Kumar, T. 'Enhanced cyclability and thermal stability of $LiCoO_2$ coated with cobalt oxides', Surface & Coatings Technology 191 (2005) 68– 75.

Franger, S., Bourbon, C. and Le Cras, F., 'Optimized Lithium Iron Phosphate for High-Rate Electrochemical Applications', Journal of The Electrochemical Society, 151(7) (2004) A1024-A1027.

Franger, S., Le Cras, F., Bourbon, C. and Rouault, H., 'Comparison between different $LiFePO_4$ synthesis routes and their influence on its physico-chemical properties', Journal of Power Sources 119–121 (2003) 252–257.

Fu, L.J., Liu, H., Li, C., Wu, Y.P., Rahm, E., Holze, R. and Wu, H.Q., 'Surface modifications of electrode materials for lithium ion batteries', Solid State Sciences 8 (2006) 113–128.

Fu, L.J., Liu, H.,Li, C., Wu, Y.P., Rahm, E., Holze, R. and Wu, H.Q., 'Electrode materials for lithium secondarybatteries prepared by sol–gel methods', Progress in Materials Science 50 (2005) 881–928.

Gaberscek, M., Dominko, R., Bele, M., Remskar, M., Hanzel, D. and Jamnik, J., 'Porous carbon-decorated $LiFePO_4$ prepared by sol–gel method based on citric acid', Solid State Ionics 176 (2005) 1801-1805.

Gao, F. and Tang, Z., 'Kinetic behavior of $LiFePO_4$/C cathode material for lithium-ion batteries', Electrochimica Acta 53 (2008) 5071–5075.

Gao, X.G., Hu, G.R., Peng, Z. and Du, K., '$LiFePO_4$ cathode power with high energy density synthesized by water', Electrochimica Acta 54 (2009) 4777–4782.

Gopukumar, S., Jeong, Y. and Kim, K.B., 'Synthesis and electrochemical performance of tetravalent doped $LiCoO_2$ in lithium rechargeable cells', Solid State Ionics 159 (2003) 223– 232.

Guo Rong Hu, Xu Guang Gao , Zhong Dong Peng, Ke Du, Yan Jun Liu
Synthetic $LiFePO_4$/C without using inert gas', Chinese Chemical Letters 18 (2007) 337–340.

Higuchi, M., Katayama, K., Azuma Y.,Yukawa, M.and Suhara M., 'Synthesis of $LiFePO_4$ cathode material by microwave processing', Journal of Power Sources 119–121 (2003) 258–261.

Hsu, K.F., Tsay ,S-Y. and Hwang, B.J., 'Synthesis and characterization of nano-sized $LiFePO_4$ cathode materials prepared by a citric acid-based sol–gel route', Journal of Materials Chemistry 14 (2004) 2690-2695T.

Huang X., Ma J., Wu P., Hu Y., Dai J., Zhu Z., Haiyan Chen H., Wang H., ' Hydrothermal synthesis of $LiCoPO_4$ cathode materials for rechargeable lithium ion batteries', Materials Letters 59.,(2005)) 578– 582.

Hui Xie H., Zhou Z., 'Physical and electrochemical properties of mix-doped lithium iron phosphate as cathode material for lithium ion battery', Electrochimica Acta 51 (2006) 2063–2067

Hyung-Sun Kim, H-s., Cho, B-W.and Cho W-I., 'Cycling performance of $LiFePO_4$ cathode material for lithium secondary batteries', Journal of Power Sources 132 (2004) 235–239.

Jin, E.M., Jin, B., Jun, D.K., Park, K-H.,Gua, H-B. and Kim, K-W., ' A study on the electrochemical characteristics of $LiFePO_4$ cathode for lithium polymer batteries by hydrothermal method', Journal of Power Sources 178 (2008) 801–806

Jozwiak. P.,Garbarczyk J.E.,Wasiucionek. M.,Gorzkowska I.,Gendron F.,Mauger A, and Julien C.M., ' DTA, FTIR and impedance spectroscopy studies on lithium–iron–phosphate glasses with olivine-like local structure', Solid State Ionics 179 (2008) 46–50.

Julien C., '4-Volt Cathode Materials for Rechargeable Lithium BatteriesWet-Chemistry Synthesis, Structure and Electrochemistry', Ionics 6 (2000) 30-47

Julien C.M., Jozwiak P., Garbarczyk J., ' Vibrational Spectroscopy of Electrode Materials For Rechargeable Lithium Batteries', Proceedings of the International Workshop Advanced Techniques for Energy Sources Investigation and Testing 4 – 9 Sept. 2004, Sofia, Bulgaria.

Kim, B-H., Kim, J-H., Kwon, I-H., and Song, M-Y., 'Electrochemical properties of $LiNiO_2$ cathode material synthesized by the emulsion method', Ceramics International 33 (2007) 837–841.

Kim, H.S., Cho, B.W. and Cho, W., 'Cycling performance of $LiFePO_4$ cathode material for lithium secondary batteries', Journal of Power Sources 132(2004) 235–239.

Kim, J., Kim, B., Lee, J.G., Cho, J. and Park, B., 'Direct carbon-black coating on $LiCoO_2$ cathode using', Journal of Power Sources 139 (2005) 289–294.

Kim, J.K., Choi, J.W., Cheruvally, G., Kim, J.U., Ahn, J.H., Cho, G.B., Kim, K.W. and Ahn, H.J., 'A modified mechanical activation synthesis for carbon-coated $LiFePO_4$ cathode in lithium batteries', Materials Letters 61 (2007) 3822–3825.

Kim, S-W. and Pyun, S-I., 'Thermodynamic and kinetic approaches to lithium intercalation into a $Li_{1-\delta}Mn_2O_4$ electrode using Monte Carlo simulation', Electrochimica Acta 46(2001) 987-997.

Kwon, N.H., Drezen, T., Exnar, I., Ivo, T., Motoshi, I. and Michael, G., 'Enhanced Electrochemical Performance of Mesoparticulate $LiMnPO_4$ for Lithium Ion Batteries', Electrochemical and Solid-State Letters 9 (6) (2006) A277-A280.

Lai, Q.Y., Lu, J.Z., Liang, X.L., Yan, F.Y., Ji, X.Y.,'Synthesis and electrochemical characteristics of Li–Ni vanadates as positive materials', International Journal of Inorganic Materials 3 (2001) 381–385.

Lee, J. and Teja, A.S., 'Synthesis of $LiFePO_4$ micro and nanoparticles in supercritical water', Materials Letters 60 (2006) 2105–2109.

Lee, Y.S., Yang, K.S. and Nahm, K.S., 'Synthesis of spinel $LiMn_2O_4$ cathode material prepared by an adipic acid-assisted sol–gel method for lithium secondary batteries', Solid State Ionics 109 (1998) 285–294.

Lee, Y.S., Sun, Y.K. and Nahm, K.S., ' Synthesis and characterization of $LiNiO_2$ cathode material prepared by an adiphic acid-assisted sol–gel method for lithium secondary batteries', Solid State Ionics 118 (1999) 159–168.

Leftheriotis, G, Papaefthimiou, S. and Yianoulis, P., 'Dependence of the estimated diffusion coefficient of $LixWO_3$ films on the scan rate of cyclic voltammetry experiments', Solid State Ionics 178 (2007) 259–263.

Levi, M.D., Wang, C., Aurbach, D. and Chvoj, Z.,'Effect of temperature on the kinetics and thermodynamics of electrochemical insertion of Li-ions into a graphite electrode', Journal of Electroanalytical Chemistry 562 (2004)187-203.

Liang, Y.Y., Bao, S.J. and Li, H.L., 'A series of spinel phase cathode materials prepared by a simple hydrothermal process for rechargeable lithium batteries', Journal of Solid State Chemistry 179 (2006) 2133–2140.

Liu, H., Li C., Zhang H.P., Fu L.J., Wu Y.P., Wu H.Q., 'Kinetic study on $LiFePO_4$/C nanocomposites synthesized by solid state technique', Journal of Power Sources 159 (2006) 717–720.

Liu, H., Wu, Y.P.,Rahm, E.E., Holze, E.R. and Wu, E.H.Q., 'Cathode materials for lithium ion batteries prepared by sol-gel methods', J Solid State electrochem 8 (2004)450–466.

Liu, H. and Tang D., 'The low cost synthesis of nanoparticles $LiFePO_4$/C composite for lithium rechargeable batteries', Solid State Ionics 179 (2008) 1897–1901.

Liu, R.S. and Shen, C., 'Structural and electrochemical study of cobalt doped $LiMn_2O_4$ spinels', Solid State Ionics 157 (2003) 95– 100.

Lu, Z., Levi, M.D., Salitra, G., Gofer,Y., Levi, E. and Aurbach, D., 'Basic electroanalytical characterization of lithium insertion into thin, well-crystallized V_2O_5 films', Journal of Electroanalytical Chemistry 491 (2000) 211-221.

Ma, J. and Qin Q.Z., 'Electrochemical performance of nanocrystalline $LiMPO_4$ thin-filmsprepared by electrostatic spray deposition', Journal of Power Sources 148 (2005) 66–71

Markevich, E., Levi, M.D. and Aurbach, D., 'Comparison between potentiostatic and galvanostaticintermittent titration techniques for determination ofchemical diffusion coefficients in ion-insertion electrodes', Journal of Electroanalytical Chemistry 580 (2005) 231–237.

Meligrana, G., Gerbaldi, C.,Tuel, A., Bodoardo, S. and Penazzi, N., 'Hydrothermal synthesis of high surface $LiFePO_4$ powders as cathode for Li-ion cells', Journal of Power Sources 160 (2006) 516–522.

Mi, C.H., Zhang, X.G. and Li, H.L., 'Electrochemical behaviors of solid $LiFePO_4$ and $Li_{0.99}Nb_{0.01}FePO_4$ in Li_2SO_4 aqueous electrolyte', Journal of Electroanalytical Chemistry 602 (2007) 245–254.

Mi, C.H., Zhang, X.G. and Li, H.L., 'Low-cost, one-step process for synthesis of carbon-coated $LiFePO_4$ cathode', Materials Letters 59 (2005) 127–130.

Molenda, J., Ojczyk, W., Świerczek, K., Zając, W., Krok, F., Dygas, J. and Liu, R.S., 'Diffusional mechanism of deintercalation in $LiFe_{1-y}Mn_yPO_4$ cathode material', Solid State Ionics 177 (2006) 2617–2624.

Morgan, D., Van der Ven, A. and G. Ceder., 'Li Conductivity in Li_xMPO_4 (M= Mn, Fe, Co, Ni) Olivine Materials', Electrochemical and Solid-Stat eletters, 7 (2) (2004)A30-A32.

Murali, K.R., Saravanan,T., Anand, S. and Ganesh,V., 'Synthesis and characterization of Li–Mn–V–O spinel as cathode material for lithium battery applications', Materials Research Bulletin 35 (2000) 2287–2294.

Nakamura,T., Sakumoto, K.,Okamoto, M.,Seki, S., Kobayashi, Y.,Takeuchi T., Tabuchi M. and Yoshihiro Yamada Y., 'Electrochemical study on Mn^{2+}substitution in $LiFePO_4$ olivine compound',Journal of Power Sources 174 (2007) 435–441.

Ni, J.F., Zhou, H.H., Chen, J.T. and Zhang, X.X., '$LiFePO_4$ doped with ions prepared by co-precipitation method', Materials Letters 59 (2005) 2361 – 2365.

Okada, S., Sawa, S., Egashira, M., Yamaki, J-i., Tabuchi, M., Kageyama, H., Konishi, T. and Yoshino, A., 'Cathode properties of phospho-olivine $LiMPO_4$ for lithium secondary batteries', Journal power sources 97-98 (2001) , 430-432.

Padhi, A.K., Nanjundaswamy, K.S., Goodenough, J.B., Journal . Electrochem. Soc.144 (1997) 1188.

Palomares, V., a, Go˜ni, A., Gil de Muroa, I., Meatza, I., Bengoechea, M., Miguel, O. and Rojo, T., 'New freeze-drying method for $LiFePO_4$ synthesis',Journal of Power Sources 171 (2007) 879–885.

Park, K.S., J.T. Son J.T., Chung, H.T., Kim S.J., Lee C.H., Kim H.G., 'Synthesis of $LiFePO_4$ by co-precipitation and microwave heating', Electrochemistry Communications 5 (2003) 839–842.

Peng, Z.S., Wan, C.R. and Jiang, C.Y., 'Synthesis by sol–gel process and characterization of $LiCoO_2$ cathode materials', Journal of Power Sources 72 (1998) 215–220.

Prabaharan, S. R. S., Saparil N B., Micheal S. S., Massot M., Julien C., Soft-chemistry synthesis of electrochemically-active spinel $LiMn_2O_4$ for Li-ion batteries", Solid State Ionics 112 (1998) 25-34.

Piana, M., Cushing, B.L., Goodenough, J.B. and Penazzi, N., 'A new promising sol–gel synthesis of phospho-olivines as environmentally friendly cathode materials for Li-ion cells ', Solid State Ionics 175 (2004) 233–237.

Predoan˘a, L., Bar˘au, A., Zaharescu, M., Vassilchina, H.,Velinova, N., Banov, B., Momchilov, A., 'Electrochemical properties of the $LiCoO_2$ powder obtained by sol-gel method', Journal of the European Ceramic Society, 27(2007)1137-1142.

Prosini, P.P., Carewska, M., Scaccia, S., Wisniewski, P. and Pasquali M., 'Long-term cyclability of nanostructured $LiFePO_4$', Electrochimica Acta 48 (2003) 4205–421.

Prosini, P.P., Daniela, Z. and Mauro, P., 'Improved electrochemical performance of a $LiFePO_4$-based composite cathode', Electrochimica Acta 46 (2001) 3517–3523.

Prosini, P.P., Marida, L., Zane, D. and Pasquali M., 'Determination of the chemical diffusion coefficient of lithium in $LiFePO_4$',Solid State Ionics 148 (2002) 45– 51.

Reidinger, F., Sanjeeva,N. and Correale, S.T., in 'A guide to Materials Characterization and Chemical Analysis', eds John P. Sibilia.VCH Publishers, Inc U.S.A.,115-119 (1988).

Ritchie, A and Howard W.,' Recent developments and likely advances in lithium-ion batteries', Journal of Power Sources 162 (2006) 809–812.

Ruffo, A., Huggins, R.A., Mari, C.M., Piana, M. and Weppner, W., 'Phosphate Materials for Cathodes in Lithium ion secondary Batteries', Ionics 11 (2005) 213-219.

Roberts, M.R., Girts, V., John, R and Owen, G.V., 'High-throughput studies of $Li_{1-x}Mg_{x/2}FePO_4$ and $LiFe_{1-y}Mg_yPO_4$ and the effect of carbon coating', Journal of Power Sources 179 (2008) 754–762.

Salah, A., Jozwiak, P., Zaghib, K ., Garbarczyk, J., Benkhoujac, K., Zaghib, K., Gendron, F. and Julien, C.M.,' Local structure and redox energies of lithium phosphates with olivine- and Nasicon-like structures', Journal of Power Sources 140 (2005) 370–375.

Salah, A., Jozwiak, P., Zaghib, K ., Garbarczyk, J ., Gendron, F ., Mauger A. and Julien, C.M., 'FTIR features of lithium-iron phosphates as electrode materials for rechargeable lithium batteries', Spectrochimica Acta Part A 65 (2006) 1007–1013.

Savitha, T., Selvasekarapandian, S., Ramya, C.S., Bhuvaneswari, M.S., Hirankumar, G., Baskaran, R. and Angelo, P.C., 'Structural and ionic transport properties of $Li_2AlZr[PO_4]_3$', Journal of Power Sources 157 (2006) 533–536.

Scrosati, B., 'Recent advances in lithium ion battery materials', Electrochimica Acta 45(2000) 2461–2466.

Shin, H.C., Cho, W. and Jang, H., 'Electrochemical properties of carbon-coated $LiFePO_4$ cathode using graphite, carbon black, and acetylene black', Electrochimica Acta 52 (2006)) 1472–1476.

Shin, H-C and Pyun, S-I., 'An investigation of the electrochemical intercalation of lithium into a $Li_1-\delta CoO_2$ electrode based upon numerical analysis of potentiostatic current transients', Electrochimica Acta 44 (1999) 2235-2244.

Shin, H-C and Pyun, S-I., 'The kinetics of lithium transport through $Li_{1-\delta}CoO_2$ by theoretical analysis of current transient', Electrochimica Acta 45 (1999) 489-501.

Sibilia, J.P., Hammond,W.B. and Szobota, J.S., in "A guide to Materials Characterization and Chemical Analysis", eds John P. Sibilia.VCH Publishers, Inc U.S.A.,137-144 (1988).

Song, M.Y. and Lee R., 'Synthesis by sol–gel method and electrochemical propertiesof $LiNiO_2$ cathode material for lithium secondary battery', Journal of Power Sources 111 (2002) 97–103.

Stark, J.G. and Wallace, H.G., 'Chemistry Data Book', Second Edition, John Murray Publishers (1982).

Subramania, A., Angayarkanni, N., Karthick, S.N., Vasudevan, T., 'Combustion synthesis of inverse spinel $LiNiVO_4$ nano-particles using gelatine as the new fuel', Materials Letters 60 (2006) 3023–3026.

Suresh, P., Rodrigues, S., Shukla A.K., Vasana, H.N. and Munichandraiah, N., 'Synthesis of $LiCo_{1-x}MnxO_2$ from a low-temperature route and characterization as cathode materials in Li-ion cells', Solid State Ionics 176 (2005) 281–290.

Tajimi, S.,Yosuke, I., Kazuyoshi, U., Kenji, T. and Mineo, S., 'Enhanced electrochemical performance of $LiFePO_4$ prepared by hydrothermal reaction', Solid State Ionics 175 (2004), 287–290.

Takahashi, M., Tobishima S.,Takei, k.,Sakurai, Y., 'Reaction behavior of $LiFePO_4$ as a cathode material for rechargeable lithium batteries', Solid State Ionics 148 (2002) 283– 289.

Takahashi, M., Tobishima, S., Takei, K. and Sakurai, Y., 'Characterization of $LiFePO_4$ as the cathode material for rechargeable lithium batteries', Journal of Power Sources 97-98 (2001) 508-511.

Tang, X.C, Pan, C.Y., He, L.P., Li, L.Q. and Chen, Z.Z., 'A novel technique based on the ratio of potentio-charge capacity togalvano-charge capacity (RPG) for determination of the diffusioncoefficient of intercalary species within insertion-host materials:theories and experiments', Electrochimica Acta 49 (2004) 3113–3119.

Tang, X.C., Song, X.W., Shen, P.Z. and Zeng, D.J., 'Capacity intermittent titration technique (CITT): A novel technique for determination of Li^+ solid diffusion coefficient of $LiMn_2O_4$', Electrochimica Acta 50 (2005) 5581–5587.

Tang, X.C., Xing, Li, L., Qiong, L.L., Song X-W. and Jiang L.H., 'Investigation on diffusion behavior of Li^+ in $LiFePO_4$ by capacity intermittent titration technique (CITT)', Electrochimica Acta 54 (2009) 2329–2334.

Turi, E.A., Yash, P. and Taylor, K., in 'A guide to Materials Characterization and Chemical Analysis', eds John P. Sibilia.VCH Publishers, Inc U.S.A., 205-208 (1988)

Vincent, C. A., 'Lithium batteries: a 50-year perspective, 1959–2009', Solid State Ionics 134 (2000) 159–167.

Walton, R.I., Smith, R.I., and O'Hare, D., 'Following the hydrothermal crystallisation of zeolites using time-resolved in situ powder neutron diffraction', Microporous and Mesoporous Materials 48 (2001) 79-88.

Wang, G.X., Bewlay, S.L., Konstantinov, K., Liu, H.K., Dou, S.X., Ahn, J-H. and Wang, X., 'Physical and electrochemical properties of doped lithium iron phosphate electrodes', Electrochimica Acta 50 (2004) 443–447.

Wang, D., Buqa, H., Michael, C., Gianluca, D., Drezen, T.,Ivan, E., Kwon, N.H., James, H. M., Laetitia, P. and Michael, G., 'High-performance, nano-structured $LiMnPO_4$ synthesized via a polyol method', Journal of Power Sources 189 (2009) 624–628.

Wang, G.X.,Yang, L., Bewlay, S.L., Chen, Y., Liu, H.K. and Ahn, J.H., 'Electrochemical properties of carbon coated $LiFePO_4$ cathode materials', Journal of Power Sources 146 (2005) 521–524.

Wang, Q., Li, H., Chen, L. and Huang X., 'Novel spherical microporous carbon as anode material for Li-ion batteries', Solid State Ionics 152–153 (2002) 43– 50.

Whiston,C., 'X-ray methods', John Wiley & sons, Great Britain, 29-33 (1987).

Wolfenstine J. and Allen J., 'Ni^{3+}/Ni^{2+} redox potential in $LiNiPO_4$', Journal of Power Sources 142 (2005) 389–390.

Wolfenstine, J., Allen J., 'LiNiPO$_4$–LiCoPO$_4$ solid solutions as cathodes', Journal of Power Sources 136 (2004) 150–153.

Wolfenstine, J., 'Electrical conductivity of doped LiCoPO$_4$', Journal of Power Sources 158 (2006)1431–1435.

Wolfenstine, J., Read, J. and Allen J.L., 'Effect of carbon on the electronic conductivity and discharge capacity LiCoPO$_4$', Journal of Power Sources 163 (2007) 1070–1073.

Xia, H., Lu, L. and Ceder, G., 'Li diffusion LiCoO$_2$ thin films prepared by pulsed laser deposition', Journal of Power Sources 159 (2006) 1422–1427.

Xia,Y., Takeshige, H., Noguchi, H. and Yoshio, M., 'Studies on an Li-Mn-0 spine1 system (obtained by melt-impregnation) as a cathode for 4 V lithium batteries Part 1. Synthesis and electrochemical behaviour of Li$_x$Mn$_2$O$_4$', Journal of Power Sources 56 (1995) 61-67.

Xu, Z, Xu, L., Lai, Q. and Xiaoyang J., 'A PEG assisted sol–gel synthesis of LiFePO$_4$ as cathodic material for lithium ion cells', Materials Research Bulletin 42 (2007) 883–891.

Yamada, A., Hosoya, M., Chung, S.C.,Yoshihiro, K., Koichiro, H., Kuang, Y.L. and Yoshio, N., 'Olivine-type cathodes Achievements and problems', Journal of Power Sources 119–121 (2003) 232–238.

Yang, H.X., Dong, Q.F., Hu, X.H., Ai, P. and Li, S.X, 'Preparation and characterization of LiNiO$_2$ synthesized from Ni(OH)$_2$ and LiOH. H$_2$O',Journal of Power Sources 79 (1999) 256–261.

Yang, S., Song, Y., Zavalij, P. and Whittingham, S., ' Reactivity, stability and electrochemical behavior of lithium iron phosphates', Electrochemistry Communications 4 (2002) 239–244.

Yonemura, M.,Yamada, A., Takei, Y., Sonoyama, N. and Kanno, R., 'Comparative Kinetic Study of Olivine Li$_x$MPO$_4$', Journal of The Electrochemical Society, 151(9)(2004) A1352-A1356.

Young, H. R., Kanamura K., 'Fabrication of thin film electrodes for all solid state rechargeable lithium batteries', Journal of Electroanalytical Chemistry 559 (2003) 69-75.

Yu, Y., Denis, W., Christopher ,F., Wolfgang, W., Kazunori, D., Takao, I., Hiroshi, K. and Shin F., 'Study of LiFePO$_4$ by Cyclic Voltammetry', Journal of The Electrochemical Society, 154 (4) (2007) A253-A257.

Zhang, J., Xiang, Y.J., Yu, Y., Xie, S., Jiang, G.S. and Chen, C.H., 'Electrochemical evaluation and modification of commercial lithium cobalt oxide powders', Journal of Power Sources 132 (2004) 187–194.